Out-of-field dose measurements in radiotherapy

Dosismessungen außerhalb des Zielvolumens in der Strahlentherapie

Zur Erlangung des Grades eines Doktors der Naturwissenschaften (Dr. rer. nat.)
genehmigte Dissertation von Dipl.-Phys. Robert Kaderka aus Offenbach am Main
2011 — Darmstadt — D 17

TECHNISCHE
UNIVERSITÄT
DARMSTADT

Fachbereich Physik
Institut für Festkörperphysik

Out-of-field dose measurements in radiotherapy
Dosismessungen außerhalb des Zielvolumens in der Strahlentherapie

Genehmigte Dissertation von Dipl.-Phys. Robert Kaderka aus Offenbach am Main

1. Gutachten: Prof. PhD. Marco Durante
2. Gutachten: Prof. Dr. Gerhard Kraft

Tag der Einreichung: 5. Mai 2011
Tag der Prüfung: 13. Juli 2011

Darmstadt — D 17

"Tumour is the target; there is no advantage to the patient in irradiation of normal tissue." **Herman Suit**

Contents

Zusammenfassung

Das Ziel dieser Arbeit war es, die Dosis außerhalb des Zielvolumens in der Strahlentherapie zu messen, welche verantwortlich ist für Langzeitschäden nach der Therapie. Diese Dosis wurde für eine Bestrahlung mit Photonen, Protonen und Kohlenstoff mit passiver und aktiver Applikation verglichen. Hierfür wurden Experimente mit einfacher Geometrie mit Hilfe eines Wasserphantoms durchgeführt. Für ein weiteres Experiment wurde ein anthropomorphes Phantom benutzt, um einen Vergleich unter patientennahen Bedingungen zu ermöglichen.

Fast zeitgleich mit der Entdeckung der Röntgenstrahlung wurde die Strahlentherapie an Tumoren begonnen. Heute werden etwa 50% aller Patienten, die unter lokalen bösartigen Tumoren leiden, bestrahlt. Die Fortschritte in der Strahlentherapie der vergangenen Jahrzehnte verbessern die Erfolgswahrscheinlichkeit der Behandlung, die gestiegenen Überlebensraten machen gleichzeitig aber auch Spätfolgen der Behandlung wahrscheinlicher. Diese Spätfolgen resultieren aus der unumgänglichen Bestrahlung von normalem Gewebe. Klinische Studien zeigen einen Zusammenhang zwischen bestrahltem normalen Gewebe und dem Auftauchen eines neuen Tumors Jahre nach der Bestrahlung. Das Ziel der Strahlentherapie muss es deshalb sein, die Dosis außerhalb des Zielvolumens für die Bestrahlungsplanung zu berücksichtigen und zu minimieren. Neue Behandlungen wie die Ionentherapie mit Protonen und Kohlenstoff ermöglichen eine bessere Schonung des normalen Gewebes bei der Bestrahlung und lassen auf verminderte Spätfolgen hoffen.
Im Rahmen des EU Projekts ALLEGRO, das die Spätfolgen der Tumortherapie untersucht, werden in dieser Arbeit Dosismessungen in der Strahlentherapie beschrieben. Um das Risiko von Spätfolgen genau bestimmen zu können, müssen physikalische, biologische und klinische Aspekte berücksichtigt werden. Ohne die physikalischen Basisdaten, die deponierte Dosis, fehlt aber die Grundlage für die weitere Analyse. An dieser Stelle muss jedoch festgehalten werden, dass die Dosisverteilung im Körper nicht allein verwendet werden kann, um das Krebsrisiko zu bestimmen.
Bei der Dosismessung wurde ein systematischer Vergleich zwischen konventioneller Photonentherapie (IMRT) und neueren Therapieansätzen wie der Bestrahlung mit Protonen sowie Kohlenstoffionen mit verschiedenen Applikationssystemen angestrebt. Während bei der konventionellen Strahlentherapie viele Studien durchgeführt wurden, halten sich bislang auf dem Gebiet der Ionentherapie entsprechende Untersuchungen vergleichsweise in Grenzen. Diese unterscheiden sich zudem häufig im Aufbau und erschweren den Vergleich.
Im Hinblick auf diese Problematik wurden zwei Experimente entworfen, um unter möglichst ähnlichen Bedingungen einen Vergleich durchführen zu können. Im ersten Experiment wurde eine einfache Geometrie verwendet und ein Wasserphantom mit einem quadratischen Feld bestrahlt. Zur Bestimmung der Dosis außerhalb des Zielvolumens wurde in der Tiefe des Dosis-

maximums ein laterales Dosisprofil mithilfe mehrerer Detektoren vermessen. Für dieses Experiment wurden Bestrahlungen mit Photonen, passiv modulierten Protonen, aktiv modulierten Protonen und Kohlenstoffionen durchgeführt. Im Rahmen der Bestrahlungen galt es zum einen die Therapien systematisch zu vergleichen und zum anderen für jede Therapie nach der Veränderung mehrerer Parameter den entsprechenden Einfluss auf das Dosisprofil zu untersuchen.
Inhalt der zweiten Experimentserie war die Untersuchung eines komplexeren Falles: An die Stelle des Wasserphantoms trat ein anthropomorphes Phantom. Für dieses wurde ein dreidimensionales Zielvolumen im Kopf definiert, um einen Hirntumor zu simulieren. Die Behandlung sollte dabei einem realen Patienten so ähnlich wie möglich sein. Dafür wurde zunächst ein CT Bild für die Bestrahlungsplanung aufgenommen, anschließend wurden Marker definiert, mit deren Hilfe das Phantom ausgerichtet und anschließend bestrahlt werden konnte. Eine IMRT Bestrahlung (Photonen) sowie Bestrahlungen mit passiv modulierten und gescannten Protonen und Kohlenstoffionen diente zum Vergleich der Therapiearten. Die Dosis wurde für alle Therapien entlang einer Körperachse sowie in ausgewählten Körperebenen vermessen. Zudem wurden Messungen durchgeführt, die eine qualitative Abschätzung der durch niederenergetische Neutronen deponierten Dosis ermöglichen.
Da Neutronen potentiell eine hohe Gefahr für Patienten darstellen, wurde zusätzlich für die Photonentherapie eine Messung der Neutronendosis durchgeführt. Sowohl im Wasserphantom, als auch im anthropomorphen Phantom konnte das Neutronenspektrum mit hoher Orts- und Energieauflösung gemessen werden, was weitere Informationen zur Berechnung des Spätfolgerisikos liefert.

Insgesamt wurde der Ansatz des systematischen Vergleichs der Therapien erfolgreich umgesetzt. Die Wasserphantom Messungen zeigen den Einfluss aller Parameter auf die Dosisverteilung und ermöglichen den systematischen Vergleich der Therapien. Dieser Vergleich unter identischen Bedingungen konnte zum ersten Mal auch für ein anthropomorphes Phantom gemessen werden. Das Risiko der Spätfolgen wird nun weiter unter biologischen und klinischen Aspekten analysiert. Insbesondere die Umrechnung der Dosis zu einem Risiko erfordert weitere Untersuchungen. Während diese Arbeit einen Vergleich aller Therapien unter physikalischen Gesichtspunkten liefert, ist es offensichtlich, dass das Gebiet in den nächsten Jahren Forschungsfelder bietet, von denen viele Krebspatienten in der Zukunft profitieren können.

Motivation

The motivation of this work was to measure a profile of the absorbed dose in different radiotherapy techniques. The main aim was to provide a systematic analysis of radiotherapy techniques to help evaluating whether a specific treatment type causes a lower risk of inducing a secondary cancer than the others. Both simple and complex geometries have been investigated, shedding light on the major differences of the parameters influencing the out-of-field dose. These data represent the base for future evaluations of the clinical hazard around the target and in the low dose region and will provide an improved determination of the secondary cancer risk. The final goal is to develop a treatment planning optimized not only for the target region, but also for organs at high risk of secondary cancer. A translation from the absorbed dose to cancer incidence and mortality is necessary for this purpose. Picture (courtesy of Wayne Newhauser) depicts the steps to consider in future treatment plannings. While the first step, the absorbed dose, is addressed in this work, the translation to cancer incidence requires an effort from the biological and clinical side. Finally, the knowledge gained from physical dosimetry measurements during radiotherapy will help optimizing both the design of new treatment facilities and the treatment planning, resulting in lower secondary cancer incidence after radiotherapy.

Around 50% of all patients with localized malignant tumours are treated with radiotherapy, making it one of the most common types of cancer treatment along with surgery and chemotherapy. Modern radiotherapy using photons has seen large improvements over the decades that have passed since the first use of X-rays for cancer treatment. Furthermore, new technologies have emerged such as the use of charged particles for radiotherapy that has moved from trials at nuclear research facilities to clinical practice.
The World Health Organisation expects an increase of global cancer deaths from 7.9 million in 2007 to 11.5 million in 2030 caused by an increasing and aging population. At the same time, technological improvements have enabled more people to benefit from radiotherapy. Nowadays many cancer entities can be treated with radiation with increasing chance of being cured. Even if the probabilities for a successful treatment still have a wide range depending on tumour type, position and many other factors, the amount of people treated with radiation will continually increase in the next years, as well as the tumour control probability and overall survival.
The increased number of patients receiving radiotherapy together with the growing individual survival rate have led to an elevated concern of long-term effects from radiotherapy. The normal tissue in the vicinity of the tumour receives a high dose and a high secondary cancer incidence is observed in this region (Dörr and Herrmann, 2002). Data obtained from the follow-up of atomic bomb survivors in Japan also imply an increased risk of cancer incidence after exposure to low doses (Pierce et al., 1996), (Preston et al., 2003). The incidence of treatment-related cancers far from the treatment site after radiotherapy is also well observed in several clinical

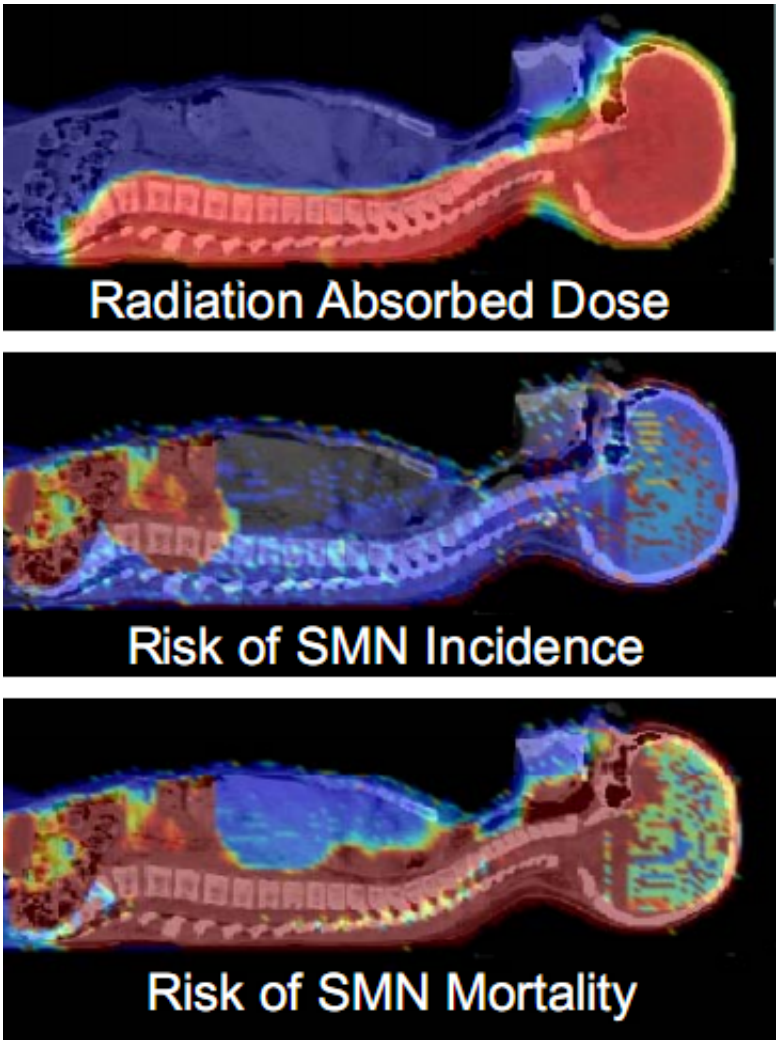

Figure 1: Desired translation of absorbed dose to resulting second malignant neoplastoma (SMN) incidence and mortality in a human model, courtesy of (Newhauser and Durante, 2011).

studies, for example (de Vathaire et al., 1989) and in publications from the Childhood Cancer Survivor Study (for example (Oeffinger et al., 2006; Friedman et al., 2010)). As it is not possible to irradiate only the tumour and completely spare the tissue surrounding it, patients in radiotherapy receive some dose also outside the target volume. Even though typical symptoms from radiation sickness are often observed shortly after treatment, the tissue far from the target absorbs a dose low enough to not produce immediate effects. However, as implied by the atomic bomb survivors, radiotherapy follow-ups and biological studies, exposure to low dose can cause long-term effects such as induction of secondary cancer.

One of the main improvements in radiotherapy is the optimization of the target conformality to minimize the dose in the region close to the target, while the regions far from the target have received comparably little attention. Increasing the difference between the dose in the target and the surrounding tissue is vital for improving the tumour control probability, since the target

dose deliverable is limited by the normal tissue complications in target vicinity. In the last years an increasing number of studies on the characterization of the far out-of-field dose distribution were published for therapy with photons, but for charged particles only a few publications are available so far, many relying on Monte Carlo methods rather than measurements. Furthermore a systematic comparison of the dose delivered outside the target volume after irradiation with photons and charged particles is lacking. Also, studies comparing different types of ion therapy often use different setups making the comparison difficult.

To address the issue of side effects following radiotherapy the ALLEGRO project was designed and funded by the European Community under grant agreement number 231965. The 2-year project is a first step for a systematic evaluation of the health risks associated with radiotherapy. The risk of secondary cancer induction is not determined only by the absorbed dose, but also influenced by other parameters such as the organ specific radiosensitivity, age, gender, fractionation scheme and so on. To account for all these aspects the ALLEGRO project approached the study from a physical, biological and clinical point of view.

Clinical data imply a secondary cancer risk both in the high dose region around the target and the region far away. To account for this the aim of the physical task was a systematic evaluation of both the dose gradient around the target and the dose in the far out-of-field region. This goal was achieved with measurements, the data collected will be provided for Monte Carlo simulations. This thesis deals with the experimental investigation of the out-of-field dose profile in conventional radiotherapy and particle therapy within the ALLEGRO project.

The biological approach focuses on translating the physical dose to a clinical risk. Several groups have investigated the effects of low doses on biological systems.

The clinical approach of the project deals with retrospective analysis of the health risk. An extensive collection of patient data and follow-up will allow an analysis of therapies performed in the past 50 years and tries to correlate the treatment parameters with the incidence of secondary cancer.

The thesis deals with the physical approach of health effects following radiotherapy and describes measurements of the absorbed dose delivered by different radiotherapy modalities. Two types of experimental setups were chosen. In an experiment with a simple geometry, a standard water phantom was irradiated to measure the basic factors determining the out-of-field dose. This simple setup is ideal for evaluating the dose delivered by different irradiation techniques and simulation with Monte Carlo codes, enabling a comparison and verification of the models in a dose region neglected so far. Effects measured in the simple setup can also be used to extrapolate the dose in more complex geometries.

The second experiment used a complex setup where an anthropomorphic phantom was irradiated under conditions as close as possible to a real patient. The phantom underwent clinical treatment planning based on a CT and was positioned and irradiated like a patient. This ex-

periment represents the first comparison of the three dimensional out-of-field dose distribution delivered from different radiation therapy techniques.

As the main aim of this study is to provide basic physical data, the translation from absorbed dose to secondary cancer risk is beyond the scope of this work. Especially for ion therapy the health risk assessment is difficult because it depends on many parameters and only a small amount of clinical data is available so far. The radiation protection community is continuously revising the risk factors associated to a certain dose. The effect of low doses from ionizing radiation on humans is heavily discussed and still poses many questions (Hall, 2004).
The physical dose measured in this study however can be used as a starting point for the evaluation of the long term health risks following radiotherapy. The results will be provided for comparison with Monte Carlo predictions prepared by several groups that also give other parameters such as the LET spectrum and particle distribution. Together with the dose, the LET and particle types represent the main input data necessary for deriving the biological risk. If agreement between Monte Carlo predictions and experimental data is observed, the model can provide a solid ground for risk evaluation.

Publications of this work

Kaderka, R.; Schardt, D.; Durante, M.; Berger, T.; La Tessa, C.: Out-of-field dose measurements in a water phantom using different radiotherapy modalities. *Radiother. Oncol.* (2011), paper in preparation

La Tessa, C.; Berger, T.; Kaderka, R.; Schardt, D.; Körner, C.; Licher, J.; Ramm, U.; Matsufuji, N.; Dahlgren, C. V.; Grusell, E.; Lomax, A.; Reitz, G.; Durante, M.: Out-of-field dose studies with an anthropomorphic phantom. I. Comparison of X-rays and particle therapy treatments. *Radiother. Oncol.* (2011), paper in preparation

La Tessa, C.; Berger, T.; Kaderka, R.; Schardt, D.; Körner, C.; Martino, G.; Matsufuji, N.; Yamashita, W.; Burmeister, S.; Reitz, G.; Durante, M.: Out-of-field dose studies with an anthropomorphic phantom. II. Radiation quality measurements *Radiother. Oncol.* (2011), paper in preparation

Non-reviewed publications:

Kaderka, R.; La Tessa, C.; Schardt, D.; Ramm, U.; Licher, J.; Durante, M.: Out-of-field dose measurements in radiotherapy for ALLEGRO. Oral presentation at the "PTCOG49". *PTCOG49 Abstract book* (2010), 14

Kaderka, R.; Schardt, D.; Durante, M.; La Tessa, C.: Out-of-field dose measurements in a water phantom using different modalities. Poster presentation at the "PTCOG50". *PTCOG50 Abstract book* (2011), in press

Kaderka, R.; La Tessa, C.; Schardt, D.; Ramm, U.; Licher, J.; Durante, M.: Out-of-field dose measurements in radiotherapy for ALLEGRO. *GSI scientific report 2009* (2010), 495

Kaderka, R.; La Tessa, C.; Ramm, U.; Licher, J.; Safai, S.; Meer, D.; Vallhagen Dahlgren, C.; Grusell, E.; Brons, S.; Schardt, D.; Durante, M.: Dose profile in MATROSHKA for a standard cancer treatment with carbon. *GSI scientific report 2010* (2011), in press

La Tessa, C.; Berger, T.; Kaderka, R.; Schardt, D.; Reitz, G.; Durante, M.: Dose profile in MATROSHKA for a standard cancer treatment with carbon. *GSI scientific report 2009* (2010), 494

La Tessa, C.; Schardt, D.; Kaderka, R.; Durante, M.: Out-of-field dose contribution of secondary particles: comparison between measurements and Monte Carlo simulations. Poster presentation at the "Heavy Ions in Therapy and Space Symposium 2009". *Heavy Ions in Therapy and Space Symposium 2009 Abstract book* (2009), 77

1 Radiation interactions

To understand applications and possible risks of ionizing radiation it is essential to know the basic interactions with matter. An overview of these processes is the topic of this chapter. An introduction to the physics relevant for radiotherapy is given for example in (Knoll, 2010) and (Podgorsak, 2005).

1.1 Photons

Several processes describe the interaction of photons with matter of interest in this work: Photoelectric absorption, Compton scattering and pair production. In all cases the energy of the photon is partially or completely transferred to electrons. Further photon interactions are the Rayleigh scattering with low relevance for therapy and the giant resonance that leads to a neutron dose in the patient. The probability of each process is dependent on the energy of the photon (Fig. 2) and the absorber.

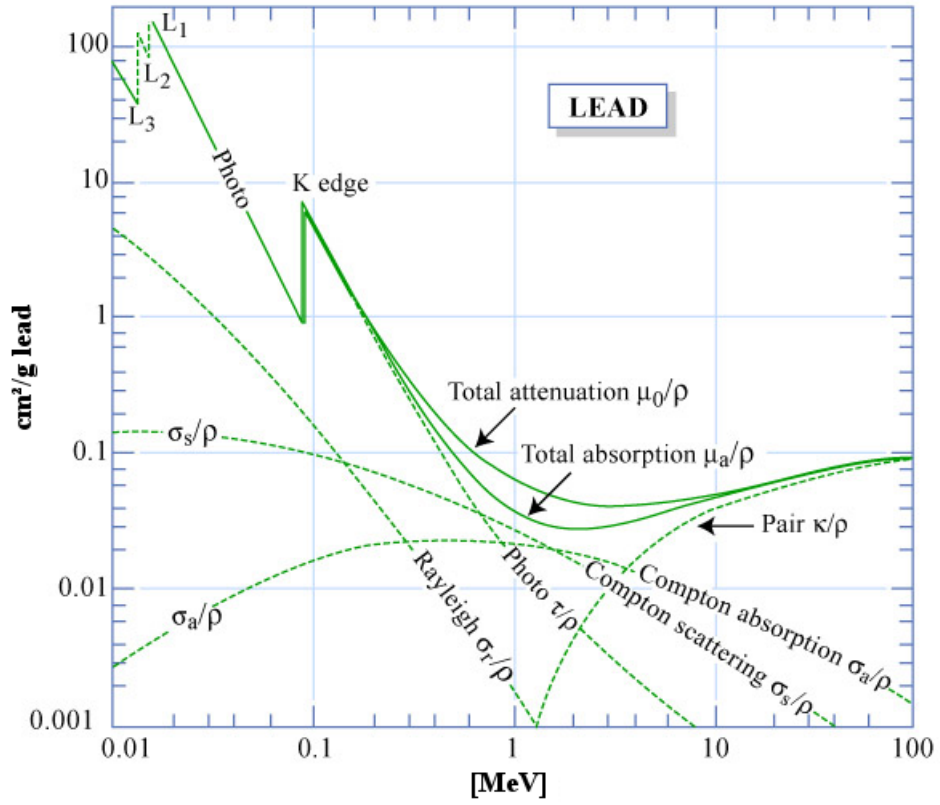

Figure 2: Energy dependence of gamma-ray interactions in lead, picture provided by (MIT).

Photoelectric absorption

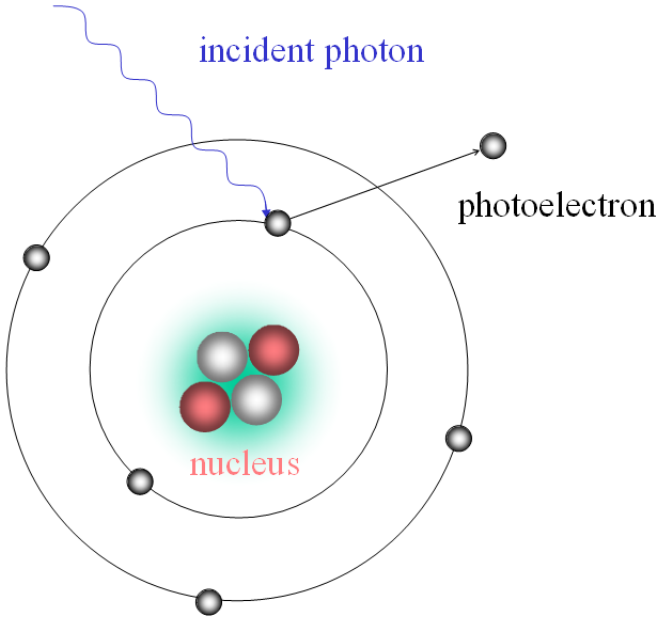

Figure 3: Sketch of the photoelectric absorption where the incident photon is absorbed under ejection of a photoelectron.

In photoelectric absorption the photon undergoes an interaction with the absorber atom and completely disappears. The absorption leads to an ejection of a photoelectron from the atom's bound shells (Fig. 3). The energy of the photoelectron is given by

$$E_{e^-} = h\nu - E_b \tag{1}$$

with E_b being the binding energy of the electron in its original shell, h the Planck constant and ν the photon frequency. The energy of the photon is completely transferred to the photoelectron if its value is higher than a few hundred keV.

The interaction not only creates a photoelectron but also leaves an ionized atom with a vacant spot in one of the bound shells behind. The atom either captures a free electron and/or rearranges the electrons from other shells. The excitation energy following the rearrangement can be lost either by emitting a new photon or an electron (Auger electron).

The photoelectric effect is the main process for low energetic photons and is enhanced by ab-

sorber materials with high atomic number Z. No analytical expression for the probability of photoelectric absorption exists for all energy ranges, however an approximation is given by

$$\tau = \text{constant} \times \frac{Z^n}{E_\gamma^{3.5}} \tag{2}$$

where n varies between 4 and 5 for the photon energy of interest. The high dependency of absorption on Z immediately identifies high-Z-materials as gamma-ray shields.

Compton scattering

Compton scattering is a reaction occurring between the incident photon and an electron of the absorber. The incoming photon is scattered to a different direction and part of its energy is transferred to an electron (Fig. 4). This so-called recoil electron can have a wide range of energies since all scattering angles are possible.
Since Compton scattering is an interaction of photons with electrons, the probability depends on the number of electrons in the target and thus increases linearly with Z. The cross section of Compton scattering decreases with increasing photon energy.

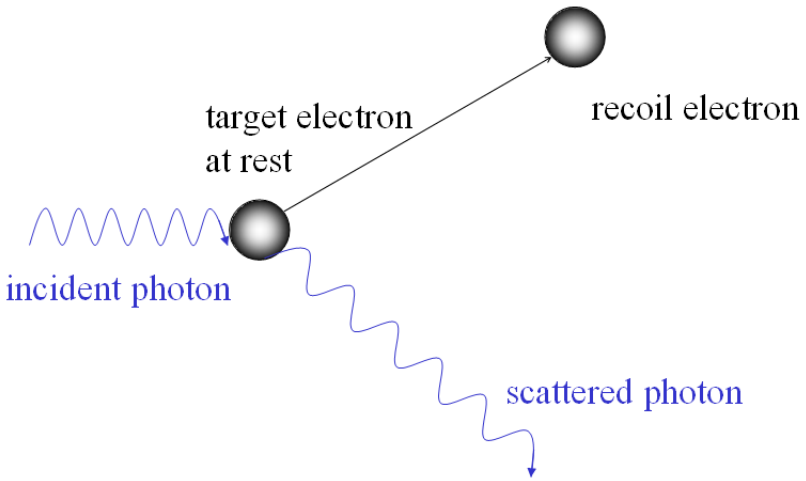

Figure 4: Sketch of Compton scattering, where the incident photon transfers some energy to an electron and changes its direction.

Pair production

When a photon has at least twice the energy of the electron rest mass (1.022 MeV) pair production becomes energetically possible. The cross section of pair production increases with energy making it the dominant process in the energy region of several MeV. The interaction takes place in the Coulomb field of a nucleus where the photon disappears and creates an electron-positron pair (Fig. 5). The energy exceeding 1.022 MeV represents the kinetic energy of the positron-electron pair. Secondary photons are produced by the annihilation of the positron. The probability for this process increases approximately as $\sqrt{Z}$ of the absorber material.

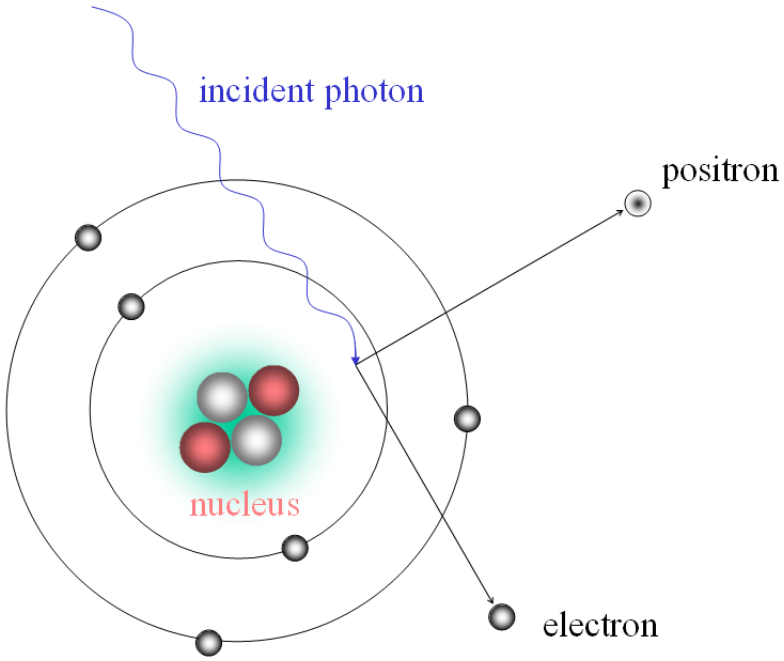

Figure 5: Sketch of pair production. A high energetic photon disappears in the Coulomb field of a nucleus and creates an electron-positron pair.

Rayleigh scattering

Another interaction for photons with an energy below several hundred keV is Rayleigh scattering where almost no energy is transferred between the atom and the photon and only the direction of the latter changes. The cross-section for Rayleigh scattering increases for high-Z absorbers. The deflection angle decreases for higher photon energies, further reducing the relevance for the interaction with tissue.

Giant nuclear resonance

Another reaction of large importance for this work is the giant nuclear resonance which is energetically possible for photons above around 6 MeV. In the interpretation by (Goldhaber and Teller, 1948) the nuclear excitation following photon absorption causes a collective vibration of the nucleus. Most likely is the dipole vibration but also higher multipole vibrations contribute significantly. Protons and neutrons move collectively against each other producing a shift of the center of mass and charge creating a dipole moment. The energy imparted can be sufficient to exceed the binding energy of a proton or neutron. The kinetic energy enables only a short range of the former, while the latter can travel large distances since it does not interact via Coulomb force. The photon energy necessary for the giant resonance to occur was approximated by (Berman and Fultz, 1975) to be

$$E_{\mathrm{GDR}} = 31.2 \times A^{-1/3} + 20.6 \times A^{-1/6} \quad [\mathrm{MeV}] \tag{3}$$

where A is the atomic mass number of the absorber. Therefore the photon energy necessary for neutron emission decreases with the atomic mass number of the target. The giant nuclear resonance is possible for a wide photon spectrum. In literature one can find that the reaction threshold is 16 MeV for Oxygen with the highest cross section at 22 MeV (Bramblett et al., 1964). For calcium the values are 15 and 20 MeV (Min et al., 1963), for Tungsten around 8 and 15 MeV (Goryachev et al., 1973). These materials are relevant for therapy because of their abundance in tissue or the accelerator components.

Absorption law

In every process described above the photon is absorbed or scattered away. The attenuation of a monoenergetic photon beam passing through an absorber can be described by an exponential function:

$$\frac{I}{I_0} = e^{-\mu d} \tag{4}$$

where I_0 is the number of photons incident and I the number of photons transmitted through an absorber of thickness d. The *linear attenuation coefficient* μ describes the probability per unit path length of losing the photon from the initial beam and can be written as:

$$\mu = \tau(\text{photoelectric}) + \sigma(\text{Compton}) + \kappa(\text{pair}) \tag{5}$$

The reciprocal of μ is the mean free path length λ which is defined as the average length travelled in an absorber until an interaction takes place.
In practice instead of the linear attenuation coefficient μ the mass attenuation coefficient is used:

$$\text{mass attenuation coefficient} = \frac{\mu}{\rho} \tag{6}$$

where ρ represents the density of the matter. This quantity is used since μ varies with the density of the absorber even when the material is the same. The mass attenuation coefficient on the other hand is independent of the physical state of the absorber.
To obtain the mass attenuation coefficient of an absorber consisting of a compound or a mixture of materials, the relation

$$\left(\frac{\mu}{\rho}\right)_c = \sum_i w_i \left(\frac{\mu}{\rho}\right)_i \tag{7}$$

is used, where w_i is the weight fraction of an element in the absorber.
Using the mass attenuation coefficient the gamma-ray attenuation of (4) can now be described as

$$\frac{I}{I_0} = e^{-(\mu/\rho)\rho d} \tag{8}$$

The term ρd is known as mass thickness and can be used to determine the attenuation. The mass thickness is often used in radiation measurements instead of the linear attenuation coefficient since it is a more fundamental quantity.

The primary interactions of charged particles in energy ranges relevant for therapy are through Coulomb force or nuclear interactions such as fragmentation.
A charged particle incident on an absorber interacts simultaneously with many electrons. The Coulomb force can be sufficient to raise the electron to a higher shell in the absorber atom (excitation) or even remove it completely (ionization). The particle transfers only a small fraction of its energy to the electron and thus loses only a small amount of its velocity, therefore many interactions are necessary to stop the particle completely.
Until the end of their path ions travel in a relatively straight track: this is caused by the large mass difference, small deflection and the simultaneous interaction in all directions. Therefore, the path length of a particle is almost identical to the range which is defined as the average distance travelled in an absorber before stopping.
An electron might receive enough kinetic energy to produce further ionizations. These highly energetic electrons are called δ-electrons and represent an indirect way of transferring energy from a charged particle beam to an absorber. The majority of the energy loss of a charged particle is usually through δ-electrons. Since the range of the δ-electrons is small compared to the range of the primary particle, the ionization occurs close to the straight track of the particle. The track structure of ions leads to a forming of many clusters of ion pairs close to the track, rather than randomly distributed ionizations caused by photon interactions.

Stopping power

The *linear stopping power* S (for charged particles) represents the differential energy loss of a particle within a material divided by the corresponding differential path length and is defined as:

$$S = -\frac{dE}{dx} \tag{9}$$

The term $-dE/dx$ along the particle track is also called the specific energy loss.
S increases when the particle velocity decreases. To describe the specific energy loss the *Bethe-Bloch formula* (Bethe, 1930; Bloch, 1933a,b) is used:

$$-\frac{dE}{dx} = \frac{4\pi e^4 z^2}{m_0 v^2} NB \tag{10}$$

where

$$B \equiv Z \left[\ln \frac{2m_0 v^2}{I} - \ln \left(1 - \frac{v^2}{c^2} \right) - \frac{v^2}{c^2} \right]$$

The specific energy loss is dependent on the velocity v and the charge z of the primary particle, the number density N and the atomic number Z of the absorber. The electron mass is denoted by m_0 and the electronic charge by e. The average excitation and ionization potential is represented by the parameter I. Only the first term in B is relevant for small velocities as the further terms are relativistic corrections. The behavior of dE/dx is mostly determined by the velocity of the particle. For a nonrelativistic particle the energy loss varies as $1/v^2$ or the inverse of the particle energy. This trend can be easily explained when considering that the charged particle spends a longer time in the vicinity of an electron when the velocity is low, therefore the momentum transfer to the electron is higher and thus the energy transfer.
For different particles with the same velocity the specific energy loss increases with higher charge. The influence of z^2 on the specific energy loss is easily seen from (10).
The product NZ represents the electron density of the absorber. From the Bethe-Bloch formula it is deducted that high electron density absorbers (high atomic number, high density) have the largest linear stopping power.
The Bethe-Bloch formula does not describe the specific energy loss correctly anymore when the particle energies become low (for lighter ions below about 10 MeV/u). The charge z then has to be replaced in (10) by z_{eff} to account for the charge state changes through ionization and recombination processes. The effective charge z_{eff} can be calculated by using Barkas' formula (Barkas, 1963).

Bragg curve

The Bragg curve depicts the depth-dose profile of charged particles in matter. The curve is named after Sir William Henri Bragg who performed an investigation of α particles slowed down in air (Bragg, 1905). An example of Bragg curves for a beam of ions with the same range is shown in Fig. 6. In the Figure one can see an initial increase of $-dE/dx$ with $1/E$ for protons and carbon ions. At the end of the track the particles start to pick up electrons and the curve falls off. The position of the highest specific energy loss is called Bragg peak.

Range straggling

While for a single ion the Bragg curve would result in a very sharp peak at the end of the track, a beam of particles undergoes statistical fluctuations of the energy loss in the absorber. The statistical nature of this process leads to a broadening of the Bragg peak as shown in Fig. 6. The expression

$$\frac{\sigma_R}{R} = \frac{1}{\sqrt{M}} f\left(\frac{E}{Mc^2}\right) \tag{11}$$

can be used to describe the ratio of the straggling width σ_R and the mean range R. Here f is a function depending on the absorber, E is the particle energy and M its mass (Rossi, 1952).

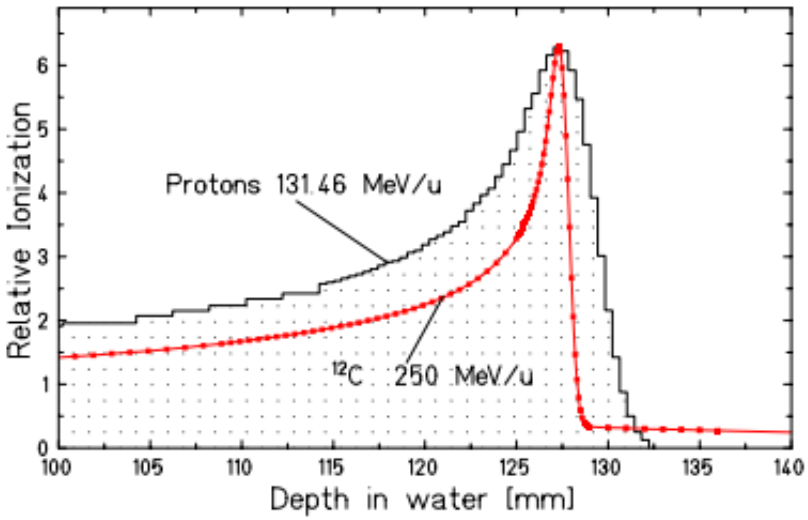

Figure 6: Bragg curve of protons and carbon ions, taken from (Schardt et al., 2010)

It is the σ_R dependence on $1/\sqrt{M}$ that shows that the energy straggling is greater for lighter particles. For therapy purposes, it is advantageous to use a broadened Bragg peak rather than the very sharp peak to reduce treatment times and improve homogeneity. In scanning delivery systems the ripple filter has been designed for this purpose (Weber and Kraft, 1999).

Lateral spreading

When applying the ions for therapy, not only the energy straggling but also the lateral deflection of particles has to be taken into account. The smaller lateral deflection of heavier ions represents a clinical advantage over protons. The spreading of the beam is caused by elastic Coulomb interactions with the target nuclei and can be analytically calculated using the Molière theory (Molière, 1948).

For ions of clinical relevance calculations are shown in (Weber and Kraft, 2009). The effect is roughly proportional to $Z_{\text{proj}}/A_{\text{proj}} \times \nu_{\text{proj}}$. In comparison the lateral straggling is more than three times higher for protons than for carbon ions. A factor 2 is given by the different A/Z and an additional factor of around 1.7 is given by the fact that for the same range in an absorber protons have a smaller velocity than carbon ions.

Lateral spreading in therapy is also largely dependent on the beam line and the setup in the treatment room. Scattering is caused by the materials in front of the patient but also inside the patient. While the latter cannot be reduced, the design of the beam exit window and beam monitors can be optimized to minimize the lateral spreading. The patient lies up to 1 m away from the beam exit and thus the particles travel quite a long distance in air after scattering in the material close to the window. This consideration is especially important for protons as their straggling is higher as discussed above. To conserve the high spatial precision of the particle beam the nozzle material should therefore be kept as thin as possible and not use heavy

elements. For protons, the patient should be positioned as close as possible to the nozzle to ensure a small beam spot; for carbon ions the air gap is less critical, furthermore when using a ripple filter a larger air distance is required so to achieve a homogeneous field.

Nuclear fragmentation

Another important process shaping the Bragg curve is nuclear fragmentation. The stopping process of particles is dominated by collisions with atomic electrons while the probability of nuclear reactions are much smaller. Nevertheless, for high energies and thus long particle ranges significant effects can be observed. The traversal of fast particles in matter can result in a partial or complete disintegration of projectile and target. The loss of nucleons of the beam particle can be well described by the abrasion-ablation model (Serber, 1947) in a two step process.
In the abrasion, which is the first step of the process, nucleons are abraded in the overlapping reaction zone (the "fireball") whereas the outer nucleons are only slightly affected. In the second step (ablation) the remaining projectile and target fragments deexcite through evaporation of nucleons or clusters.
Studies summarized in (Schardt et al., 2010) have shown several aspects of fragmentation relevant to radiotherapy:

- the number of fragmentation increases with penetration depth and causes a loss of primary ions while lower-Z fragments increase
- secondary (or higher order) projectile-like fragments travel at approximately the same speed as the projectile ions and because of their lower charge they possess a longer range than the primary ions producing a dose tail behind the Bragg peak
- fragments are generally forward directed, however the angular distribution is much broader than the lateral straggling of primary ions caused by multiple Coulomb scattering

The dose tail has to be taken into account for treatment planning. On the other hand, fragmentation of projectile and target can be exploited for monitoring of the irradiation. In the case of carbon ions, ^{10}C and ^{11}C emit positrons that can be monitored via positron emission tomography (PET) for quality assurance purposes (Enghardt et al., 2004). PET monitoring is also possible for other heavy ion beams, but the β^+-activity profile is more complex in these cases. While a β^+-activity profile can also be measured for a proton beam, no peak structure is observed, caused by the lack of projectile fragments (Parodi et al., 2005).

The type of interaction a neutron undergoes is mostly dependent on the energy of the neutron as discussed below. As neutrons are not affected by Coulomb force, they may travel larger distances than ions in matter without interacting. Neutron interactions are between the neutron and the nuclei of the absorbing material. The neutron can disappear in the process or cause secondary radiation. Furthermore the energy and direction of the neutron can be changed.
The interaction of neutrons often result in secondary heavy charged particles. As stated above the interaction occurring is largely dependent on the neutron energy and can be neutron-induced nuclear reactions or energy transfer to target nuclei.

Slow neutron interactions

The term slow neutrons denotes neutrons below an energy of 0.5 eV (the cadmium cutoff energy). The interactions of slow neutrons are the elastic scattering with the absorber nuclei and neutron-induced nuclear reactions. In the former, only small amounts of energy are deposited making the detection difficult. Elastic scattering slows the neutrons down and brings them to a thermal equilibrium with the absorber. The thermalized neutrons have an energy of about 0.025 eV at room temperature. In the thermal energy region many reactions become possible for example neutron capture reactions (n,γ),(n,α),(n,p) and (n,fission).

Fast neutron interactions

While for neutrons above 0.5 eV the neutron-induced reactions become less probable, the energy transfer to the recoil nuclei in the collisions increases. The neutron can lose its entire energy in a single collision with hydrogen nuclei whereas in case of heavier nuclei only a partial energy transfer is possible.
Inelastic scattering can occur when the energy of the fast neutron is high enough. The recoil nucleus is elevated to an excited state and deexcites emitting a photon, then the neutron loses a greater fraction of energy compared to an elastic collision.

To evaluate the exposure of matter to radiation the quantity *absorbed dose* is defined as the mean energy absorbed by a material per unit mass (ICRU51, 1993). The SI unit of the absorbed dose D is the Gray (Gy) [1 Gy=1 J/kg]. According to the definition, the absorbed dose is determined only by physical attributes and represents a measure of the physical effects from radiation in an absorber. The absorbed dose is typically also simply called dose or physical dose. The most direct way to determine the absorbed dose is a calorimetric measurement where the temperature rise in a medium after irradiation is recorded. However, this type of measurement is rather difficult and complex and is mainly used for calibration of other detectors.

Equivalent dose

The ionization of radiation in matter may cause a damage to cells. The effect on a cell is not only dependent on the absorbed dose but also on the type of radiation and the linear energy transfer LET which is the local amount of energy deposition along a particle track. The LET is very similar to the specific energy loss $-dE/dx$ but does not take the energy lost via bremsstrahlung into account. Generally the biological damage from radiation increases with the LET but decreases after a maximum.
The biological hazard from different types of ionizing radiation is expressed as the equivalent dose instead of absorbed dose for radiation protection purposes as proposed by (ICRP60, 1990). The equivalent dose is defined as the dose averaged over an organ or a tissue multiplied by a radiation weighting factor depending on the type or radiation. The equivalent dose for an organ is represented by $H_{T,R}$ and it is calculated as:

$$H_{T,R} = w_R \times D_{T,R} \tag{12}$$

where $D_{T,R}$ is the dose averaged over a tissue or an organ and w_R the radiation weighting factor for the given type of radiation. The unit of the equivalent dose is the Sievert (Sv). Values of w_R for all radiation types are given in Table 1.4. The values for neutrons are taken from (ICRP103, 2008), the other data come from (ICRP60, 1990).

The weighting factor for photons and electrons is 1. For heavy charged particles the LET increases and therefore the biological effect, the energy dependence however is not taken into account for the equivalent dose. Neutrons deliver their energy mostly through protons and heavy particles and therefore the weighting factor is correspondingly higher than one and varies greatly with energy.
The equivalent dose is a convenient quantity in radiation protection but uses a conservative

Table 1: Radiation weighting factors from (ICRP60, 1990; ICRP103, 2008)

Type	Energy range	Radiation weighting factor w_R
Photons	all energies	1
Electrons	all energies	1
Neutrons	≤ 1 MeV	$2.5 + 18.2e^{-(\ln(E_n))^2/6}$
	$1 - 50$ MeV	$5.0 + 17.0e^{-(\ln(2E_n))^2/6}$
	≥ 50 MeV	$2.5 + 3.25e^{-(\ln(0.04E_n))^2/6}$
Protons	≥ 2 MeV	5
Alpha particles, heavy nuclei		20

estimate of the risk and therefore represents the upper limit rather than an exact deterministic value of the biological risk. Based on the concept of the equivalent dose, the effective dose is used as a convenient way of evaluating the risks after an irradiation of the whole body. However, for establishing the risks following radiotherapy treatment the concept of the effective dose is not precise enough. The concept is further limited by the very localized dose in radiotherapy opposed to the risk determined from a whole-body irradiation using the effective dose. The probability of cancer incidence following radiation is shortly discussed in 1.6.

1.5 Relative biological effectiveness

An accurate treatment planning requires precise knowledge of the biological effect of radiation. The *relative biological effectiveness* is used for this purpose and represents a more precise and powerful tool for determining the biological effect than the equivalent dose. The latter uses the upper limits of the RBE and represents an easy tool for radiation protection. While this work only investigated the absorbed dose, the implications of the RBE should be considered when comparing different techniques. The relative biological effectiveness is defined as the ratio of the dose of a reference radiation (250 kV x-rays) divided by the dose of an ion irradiation that yields the same biological effect (such as cell inactivation):

$$\mathrm{RBE}_{\mathrm{iso}} = \frac{D_{\mathrm{ref}}}{D_{\mathrm{ion}}} \tag{13}$$

The RBE changes with many different parameters. It is dependent on the biological endpoint, the dose, particle type, particle energy and also the tissue irradiated. Consequently the RBE has complex dependencies in the treatment field and different models have been developed to account for these. For radiotherapy purposes the most interesting end points are tumor control (determined by cell survival) and normal-tissue complication. The former describes the response of the tumour, the latter is used to determine the radiation tolerance of surrounding

tissue. A qualitative explanation of the increased effect of heavy ions is given below, an overview of the models with a more detailed description as well as many references are given in (Schardt et al., 2010).

The main difference between photons and ion irradiation is observed in the microscopic spatial energy deposition. Photons transfer their energy via photo effect, Compton effect or pair production. The cross sections for these processes are small, therefore a large number of photons is needed to achieve a particular dose. The energy deposition of photons occurs via electrons and is randomly distributed, the ionization density in a cell can therefore be assumed to be homogeneous over the entire cell volume.

The radial dose distribution around an ion track on the other hand behaves differently. A spectrum of secondary δ-electrons is emitted by Coulomb interaction of the projectile nucleus and the target electrons. The liberated electrons further undergo frequent interactions with the medium and scatter. Energetic electrons are also liberated by the Auger effect. The electrons are transported through the absorber in elastic and inelastic collisions. The latter process leads to an energy transfer to the medium by ionization or excitation. For energies below 50 eV excitation dominates whereas for larger energies ionization becomes more important. Ionization creates an additional spectrum of electrons adding to the energy deposition. The mean free path of 100 eV electrons in water is in the order of a few nm. Since the opposite strands of DNA are 2 nm apart there is a high probability of ionization events in both strands by one electron of this energy. The passage of heavy ions creates a dense cluster of secondary electrons increasing the damage to the DNA (Fig. 7).

This explains qualitatively the elevated radiation damage in cells from ions. The radiation damage in a cell is assumed to be mostly caused by DNA damage. While the random distribution of photons leads to damage in distant parts of the DNA, heavy ions have a more localized effect increasing the probability of correlated DNA damage. The cell repair capability is reduced for more complex DNA damage as in the case of low-energy heavy ions explaining the reduced cell survival.

The RBE is dependent on many parameters, for this work most important is the difference of photons, protons and carbon ions. By definition the RBE in photon therapy is one. The review by (Paganetti et al., 2002) states that for protons a single RBE of 1.1 can be used for the clinical target, however an increase of the RBE observed in the terminal millimeters of the volume should be considered for treatment planning. In the case of carbon-ions the situation becomes more complex because of the LET variation as well as fragmentation of primary ions. To account for these, the Local Effect Model was developed for treatment planning in heavy ion therapy (Scholz and Kraft, 1996).

In principal an increase of the local ionization density and thus the LET raises the RBE. However a maximum RBE is reached at a certain LET level. At this LET level a high reduction of the cell survival probability is observed. For the same particle fluence, a further increase of the LET will

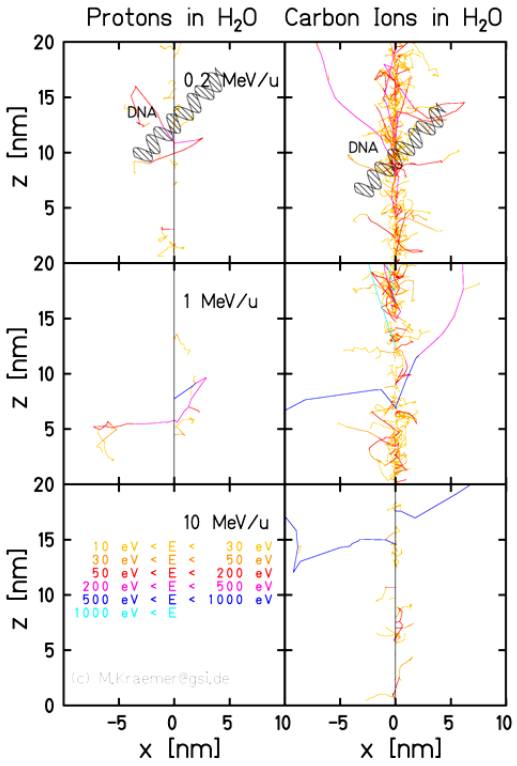

Figure 7: Track structure of protons and carbon ions with several energies together with a sketch of the DNA. The simulation depicts the paths of individual secondary electrons. Figure courtesy of Michael Krämer.

therefore lead to the same effect as lower LET particles, reducing the ratio of high LET over low LET radiation. Hence the RBE is reduced from this so called overkill effect. Additionally, less ions with high LET are needed to achieve the same dose as low LET ions. This reduces the probability to hit a cell which also results in a lower RBE for cell killing.
The RBE is not only determined by the LET but also by the particle type. For protons and carbon ions with the same LET, the carbon ions are faster and therefore have a reduced ionization density in the track center. The RBE for cell killing of carbon ions is therefore lower than for protons at the same LET. For exploiting the RBE for therapy, the position of the RBE maximum must coincide with the Bragg peak, to combine the highest physical dose with the biological effect. For carbon ions the position of the RBE maximum is almost at the Bragg peak giving a major clinical advantage of carbon ions in contrast to some other ions. In clinical practice for chordomas and chondrosarcomas the RBE values are determined to be around 2 to 5 in the target with only slightly elevated values in the entrance channel (Weber and Kraft, 2009).

In summary, only a rough introduction to the importance of the RBE was given. The concept of the RBE will not be used for the results obtained with this work, only the physical dose is given. The constant RBE of photons and protons enables a direct transfer of physical data to

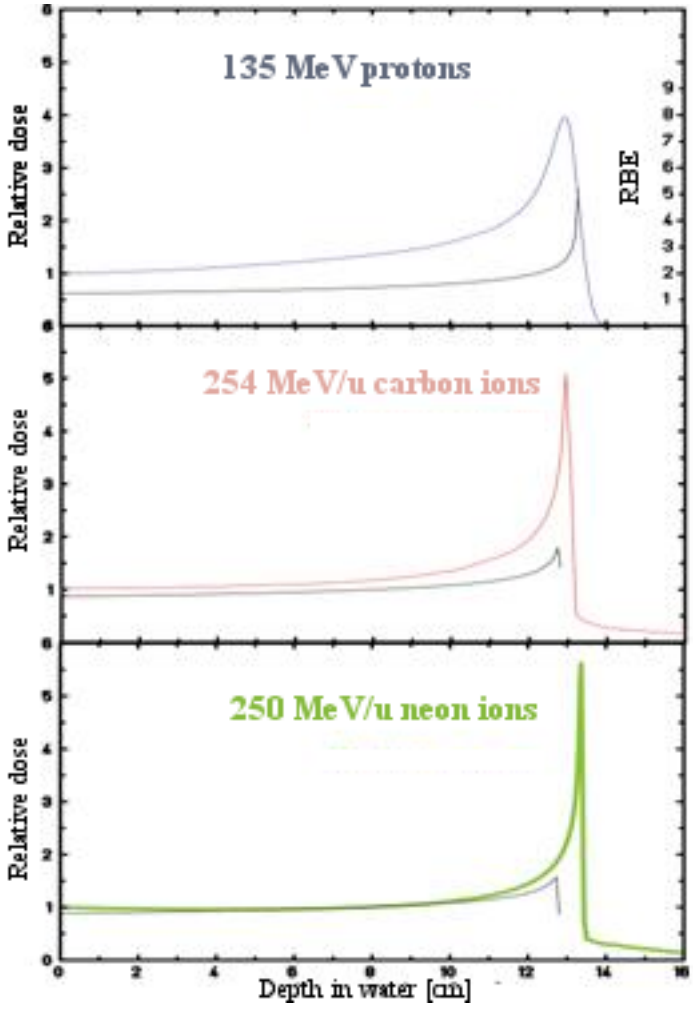

Figure 8: Comparison of the Bragg curve (colored line) and the RBE (black line) for protons, carbon ions and neons. Figure courtesy of Wilma Kraft-Weyrather.

the clinically relevant biological dose. However for carbon ions the RBE is dependent on too many parameters such as fractionation scheme, dose, tissue type and biological end point under consideration. It is not possible to make a comparison of the biological dose in the tumour – where cell survival is the important value – and the biological dose in the normal tissue where a different biological endpoint can be important. Even if the RBE is not applied in this work, one should keep in mind that the RBE for carbon ions in the target is in the order of 2 to 5 whereas it is only 1.2 to 1.5 in the entrance channel. This improves the ratio of the biological dose in the target over the surrounding tissue, an effect that should be considered when comparing the results of carbon ions with photons and protons.

1.6 Radiotherapy and associated risks

In 2007 worldwide 7.9 million deaths were attributed to cancer representing around 13% of death causes (WHO). The number of deaths from cancer is expected to increase over the next years because of an increasing and aging world population. Cancer treatments can have curative or palliative aims. Treatment consists of surgery, radiotherapy, chemotherapy or a combination of these. Palliative treatments intend to reduce the pain of patients and improve their life quality. Around 50% of patients with localized malignant tumours receive radiotherapy.

The effect of cell inactivation through radiation can be used for therapeutical purposes as it is essential for tumour shrinkage. The quality of a tumour treatment can be described by the parameters tumour control probability (TCP), overall survival and normal tissue complication probability (NTCP). The latter describes the probability of developing secondary malignancies after a treatment. From atomic bomb survivors, early radiation accidents and clinical follow-ups it can be well observed that exposure to radiation results in health risks.

In an ideal treatment, the tumour control probability would be 100% with no NTCP, in other words the tumour is cured without any side-effects. The TCP and NTCP both increase with increasing (biological) dose in the tumour respectively in normal tissue. Fig. 9 shows a dose response curve for both effects, the gap between both is known as the therapeutic window (Holthusen, 1936) where a high probability for cure with a low probability of side effects is given. Developments in radiotherapy aim at increasing the therapeutic window, i.e. increasing the dose in the target while minimizing the dose in the surrounding tissue. In radiotherapy, it is common to display the dose received by a threedimensional target and organs at risk in dose volume histograms (DVH) (Fig. 10) which show the volume that has received a certain dose. In the ideal treatment, a rectangle would be seen for the target and a flat line at zero for organs at risk.

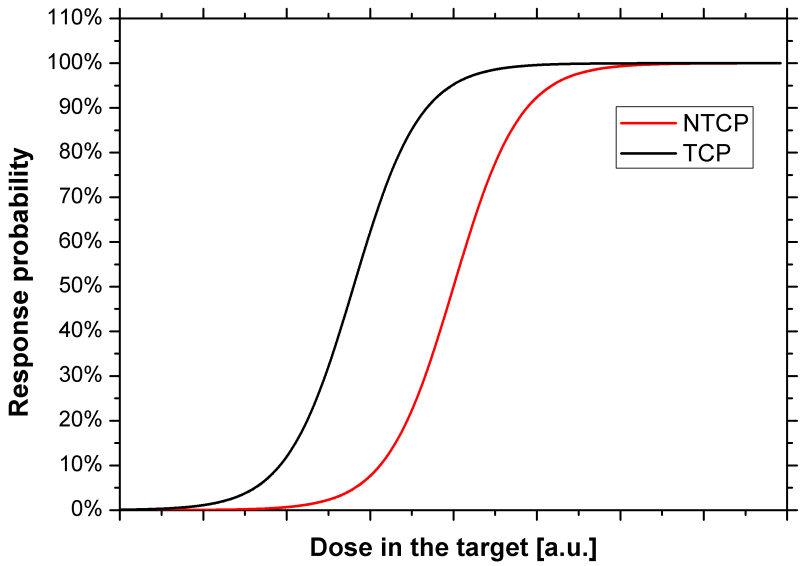

Figure 9: Dose-response curves for tumour control probability and normal tissue complication probability. The gap between both gives a high probability of tumor control with a small chance of side effects, the gap is known as the therapeutic window (Holthusen, 1936).

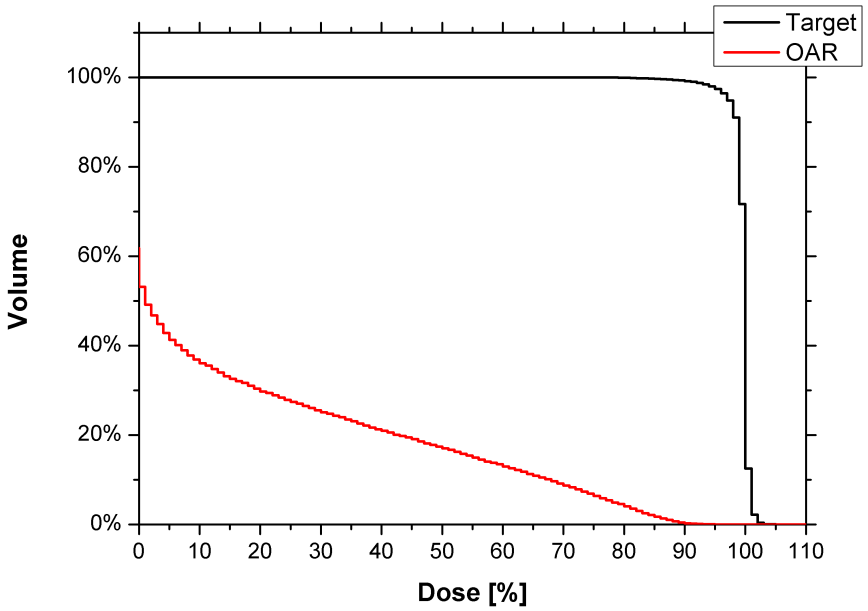

Figure 10: Dose volume histogram for the target and an organ at risk.

Normal tissue complications can occur in a variety of ways. Acute health effects generally come from the exposure to high doses and include for example skin burns. High doses in surrounding organs have a high risk of developing subsequent malignancies, but also low doses far from the tumour are at risk of late health effects. Among these late health effects is the induction of secondary cancer, the term is defined in (Cahan et al., 1948) as follows:

- the secondary cancer is located in a region exposed to a therapeutic beam
- the tumour has a different histology than the original tumour, which means it is not a metastasis
- several years of time pass between treatment and occurrence of the new tumour
- the tumour was not present during the treatment
- no cancer-prone syndrome is known in the patient

Several studies found an increase of cancer risk following radiotherapy even 40 years after treatment (Chaturvedi et al., 2007). A review of studies dedicated to secondary cancer induction is found in (Xu et al., 2008) with a focus on photon treatments, but also some studies for proton therapy. An important conclusion to consider is that both organs close to the target irradiated with a high dose and organs far from the target receiving a low dose have increased secondary cancer incidence (Dörr and Herrmann, 2002).
The different cell response associated with early and late effects are caused by the different underlying biological reactions. In a simplified picture early effects are caused by cell-killing whereas long term effects come from cell mutations, caused by non lethal DNA damage and misrepair.
The relationship of dose and cancer incidence is heavily discussed. While in the intermediate dose range of approximately 0.05 to 2.5 Sv a linear dose-response is accepted after evaluation of the atomic bomb survivors (Hall, 2004), the validness of the linear model outside the range is unclear. Further uncertainties arise from the transfer of whole-body irradiations as in the case of the atomic bomb survivors to the risk of localized irradiations as in radiotherapy. Organs close to the tumour may receive a dose well above 2.5 Sv during a treatment, an improved understanding of the high dose region is therefore necessary for risk evaluation. On the other hand a low dose is delivered to organs far away from the tumour. Hypotheses are illustrated in Fig. 11 and range from a steep decrease of cancer risk for low doses, over to an extrapolation of the linear dose response from the intermediate range, up to a large increase of the dose response. In the intermediate dose range described above a solid tumour mortality of 10% per Sievert (Pierce et al., 1996) (Preston et al., 2003) is derived from the atomic bomb survivors. Many studies (summarized in (Xu et al., 2008)) show that an equivalent dose above 0.1 to 0.2 Sv increases

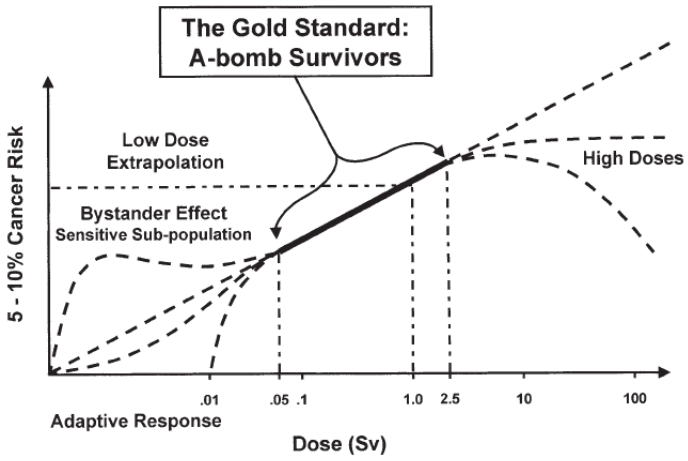

Figure 11: Qualitative illustration of cancer risk from irradiation, the solid line represents data obtained from atomic bomb survivors from 0.05 to 2.5 Sv. Dashed lines represent hypotheses for the dose response outside the known range. Picture taken from (Hall, 2004).

carcinogenesis. The BEIR committee (BEIR, 2006) and (ICRP60, 1990) recommend a linear-no-threshold model below 0.1 Gy, however further investigation is necessary. The evaluation of the dose response in the low dose region is difficult because of the large amount of data necessary to gain statistically significant results. Moreover not only the dose but also organ-specific risk factors, fractionation schemes and individual sensitivity need to be investigated. The individual risk is also largely determined by the age of the patient, therefore paediatric patients have a substantial risk because of their long lifetime after treatment.

While the exact response in the low dose region and in the high dose region is under discussion, it is clear that a patient does not gain any advantage by an irradiation of healthy tissue. The risk both in the vicinity of the tumour and far away from the target need to be considered for treatments. Therefore the aim of future treatment planning in radiotherapy should be minimizing the dose in healthy tissue not only close to the target but also at large distances.

2 Radiotherapy techniques

The delivery techniques of the radiotherapy modalities investigated in this work are all described in this chapter. All irradiation techniques presented here fall in the category of teletherapy which means irradiation from an external source. In contrast, brachytherapy delivers the dose by a radioactive source inserted directly through seeds or grains in the tissue to be treated.

2.1 Conventional radiotherapy

In conventional radiotherapy with photons major developments have taken place since the first use of X-rays in cancer treatment. In the 1950s first linear accelerators based on bremsstrahlung have been employed in radiotherapy rather than radioactive sources such as ^{60}Co. Photons of higher energies are characterized by a more favourable depth dose distribution, i.e. the dose maximum is deeper and the decrease after the maximum is slower (Fig. 12); but, on the other hand above about 10 MeV photoneutron production becomes possible raising additional concern for the out-of-field dose.

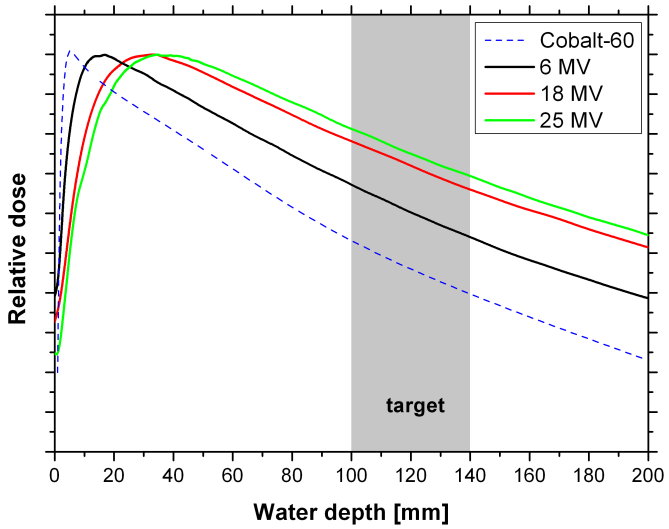

Figure 12: Depth dose curves of photons in water from a Cobalt-60 source and from linear accelerators in 6,18 and 25 MV mode. Dashed line redrawn from (Podgorsak, 2005), solid lines represent own measurements. The gray area illustrates a possible tumour position.

Modern radiotherapy machines produce bremsstrahlungs photons in the energy range between 4 and 25 MeV for treatment with a linear electron accelerator. Accelerated electrons impinging on a target produce a continuous spectrum of photon energies. The bremsstrahlungs spectrum is dependent on the treatment head design of the accelerator. To compare different machines

the ratio of ionization in different water depths under standardized conditions is used. This ratio determines the depth dose profile of the photon beam produced by an accelerator. The depth dose profile of a photon beam is defined by the accelerator potential and is given in megavolts (MV). While the electron energy (in MeV) is close to the potential given in MV, it can be different for each accelerator while still generating the same depth dose profile which is the relevant parameter for therapy. It is important to note, that even if accelerators have the same depth dose profile, they do not necessesarily have the same bremsstrahlungs spectrum giving one reason why a different out-of-field dose is observed for different machines.

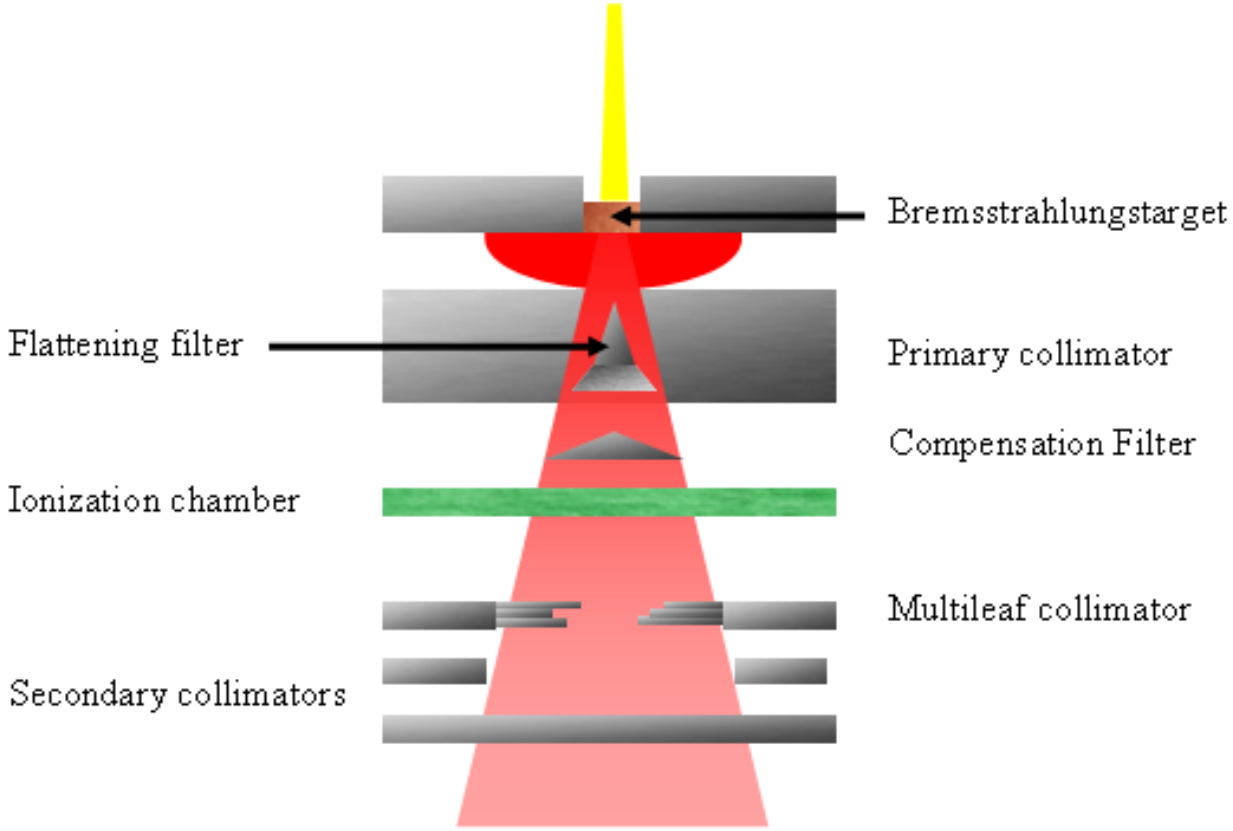

Figure 13: Scheme of the treatment head of a linear accelerator for photon therapy.

The treatment head of the linear accelerator (linac) where the experiments were performed is sketched in Fig. 13. The design of these components determines the beam-shaping and the out-of-field dose characteristics. While the details of the design vary for each machine the setup is similar for all linacs used in radiotherapy.

After acceleration the electrons are guided into a gantry which can be rotated by almost 360 degrees. Then the electron beam is transported through a bending magnet onto a target producing the bremsstrahlungs photons. In many linear accelerators, the target can be removed for a treatment with electrons. The photons first hit the primary collimator where most of them are absorbed except the forward directed beam. The collimator is usually made out of a tungsten al-

loy or another high-Z material with a high cross section for photon reactions as described in 1.1. To flatten the beam profile a compensation filter is used and sometimes an additional flattening filter is built in the primary collimator. The beam is continuously monitored with an ionization chamber placed below the compensation filter. In the case of the Elekta SL 25 machine used in this work, the beam is shaped by a multileaf collimator (MLC) which consists of 40 leaves that can be moved separately and allow the irradiation of irregular targets. Also the MLC is usually made of tungsten. The beam is further collimated by X and Y secondary collimators which are orthogonal to each other and are also known as jaws. In some machines, the positions of the MLC and secondary collimators are interchanged.
The MLC is a relatively new development for shaping the beam. Previously patient specific collimators in tumour-shape were used. Once the MLC was implemented, this individual collimator became obsolete. The MLC plays a major role in intensity-modulated radiotherapy (IMRT) which has led to an improved tumour conformality. In a classical 3D-CRT (three dimensional conformal radiotherapy) treatment the MLC is fixed in one position. For deep-seated tumours the dose maximum of photons typically lies before the tumour. Therefore, to deliver the highest dose in the target while sparring the normal tissue, the patient must be irradiated from several angles using different MLC settings; a typical treatment uses 4 to 9 fields.
In an IMRT treatment, the target conformality is further optimized by modulating the fluence with the MLC during the treatment. The term intensity modulating is slightly misleading since it is actually a fluence modulation. The irradiation is still performed using several angles, typically up to 9 fields.

Several components contribute to the out-of-field dose in photon therapy. Photons produced in the bremsstrahlungs target are initially shaped with the primary collimator, but a small amount of photons leak through it. The MLC and lower collimators shape the treatment field, but also here a small amount of photons passes through the material resulting in unwanted dose to the patient. The primary photons might also undergo scattering in the patient.
At photon energies above roughly 10 MeV the giant resonance interaction contributes significantly. Photoneutrons are mostly produced in the primary collimator (55-60%) and the lower collimators (15-30%) as calculated with a Monte Carlo simulation (Garnica-Garza, 2005). The high-Z elements do not shield effectively against neutrons which then leak through the head. As most neutrons are produced in the primary collimator, the photoneutron production is mostly dependent on the time the beam is on rather than the treatment field characteristics.
The photoneutrons produced are composed of a direct component dominant in the forward angle and an isotropic component from an evaporation process (Ongaro et al., 2000). As the average energy of the neutrons is in the order of about 1 MeV, they may represent a major contribution to the equivalent dose because of the high radiation weighting factors. Furthermore, the dose delivered by the isotropic component is almost independent of the distance from the

target and therefore the patient might receive an additional dose even very far from the treatment site.
Neutron production is highly dependent on the energy of the photons. A simulation with GEANT4 from (Saeed et al., 2009) found a two-fold increase of the neutron yield when increasing from 18 to 20 MV for a Varian Clinac 2100C.

IMRT improves the tumour conformality, but the collimator cuts off a larger fraction of the primary beam enlarging the out-of-field dose. The ion chamber built in the treatment head monitors the photon beam in terms of monitor units. The monitor unit (MU) is usually defined as 1 cGy at the depth of maximum dose under reference dosimetry conditions. By definition, the conversion of MU to Gy in the target is dependent on the energy. The out-of-field dose is often normalized to the monitor units since the leakage of photons is dependent on the time electrons impinge on the target. The risk from the out-of-field dose for different tumours can therefore be calculated when the amount of MU for each treatment is known.
For a specific prostate tumour case an almost threefold increase of monitor units was found by (Howell et al., 2005) for an IMRT treatment compared to a conventional treatment. The higher number of leaked photons and neutrons produced increase the secondary malignancy risk for an IMRT treatment.

2.2 Particle therapy

The use of charged particles for radiotherapy was suggested as early as 1946 by Robert R. Wilson (Wilson, 1946). As described earlier, charged particles undergo different reactions than photons and therefore show a different depth dose curve (Fig. 14). The trend of the energy loss of ions in matter can be exploited fruitfully in radiation therapy because of the Bragg peak, whose position can be changed through variation of the particle energy. The first treatment of patients with proton and helium beams started in 1954 at LBL Berkeley (Chu et al., 1993; Chen et al., 1981; Petti and Lennox, 1994). An overview of the strategies applied to achieve dose conformality in particle therapy is given in (Schardt et al., 2010) and will be also described here. As described

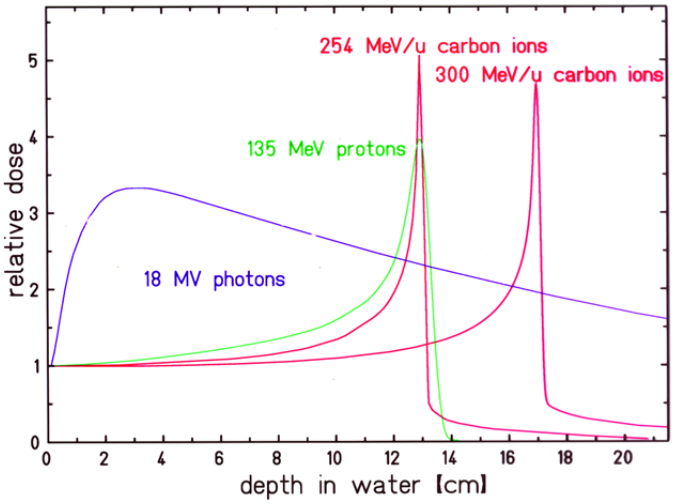

Figure 14: Depth dose curves for photons, protons and carbon ions in water for several energies. Figure courtesy of Dieter Schardt.

in the first chapter both protons and carbon ions undergo lateral scattering, though this effect is larger for the former than for the latter. The spreading occurs in the nozzle and the patient itself. After spreading in the nozzle the beam diverges in the air gap infront of the patient. The out-of-field dose in therapy with ions is the result of a complex mixed radiation field. In proton therapy, the scattering of primary protons and secondary neutron production both in the beam line and the patient contribute to the out-of-field dose. Carbon ions undergo fragmentation that leads to a build-up of secondary particles depositing dose outside the treatment field (Haettner et al., 2006). All these effects are increased when more material has to be passed by the beam, i.e. in passive delivery techniques which are described later.

Accelerators

To reach particle energies required to penetrate up to around 30 cm of tissue accelerators of comparably large size are needed. While linacs for use in photon therapy are compact enough to fit in a single room, accelerators for particle therapy are much larger, especially for carbon ions.
The first treatments with charged particles started in facilities focussed on nuclear research. Dedicated accelerators for radiotherapy were designed later with a focus on reliability rather than flexibility as needed in research facilities. Accelerators based on the cyclotron and synchrotron design are in use today and each of them offers advantages and suffers some disadvantages. While cyclotrons are popular for their reliability and ease of operation, they lack the feature to actively regulate the beam energy and thereby its penetration depth in tissue. To achieve this purpose, passive degraders have to be used. Synchrotrons are more complex in operation but the energy of the beam can be modulated from pulse to pulse. On the other hand, the passive degrader in cyclotrons allows for a fast change of the beam energy.
Both synchrotrons and cyclotrons are currently used for providing proton therapy. For irradiation with heavy ions only synchrotrons have been employed so far. The high cross section for breaking carbon ions in three α-particles limits the use of passive degraders in the beamline for energy selection in contrast to proton therapy using cyclotrons.

Passive beam delivery

Two basic techniques have been developed to deliver the beam to the target. In passive beam delivery, the beam is shaped with a set of fully passive systems.
The focussed beam coming from the accelerator is broadened through a scattering device which generates a flat transversal profile. The sharp Bragg peak characteristic of a monoenergetic ion beam is not suited for radiotherapy and has to be widened to cover a larger volume. The so-called spread-out Bragg peak (SOBP) is produced by placing a range modulator in the nozzle. An example of a range modulator is a circular rotor moving different material thicknesses. The fast movement of the rotor causes the beam to traverse different depths adjusting the penetration in the patient.
After spreading the Bragg peak, its position is adjusted with a range shifter which may consist of plates of plastic. Afterwards, the particles travel through the collimator and the bolus. These devices are specific for each patient and tumour. The collimator has an opening in the shape of the target. It is made out of a heavy metal to stop the particles outside the tumour projection. The bolus is made of a tissue equivalent plastic of different thicknesses and changes the distal distribution of ions. A high dose conformality can be achieved with the bolus, but for some tumour geometries the shaping of the field on the distal part results in a high dose to normal tissue in the proximal part. This dose can be reduced with some effort (a dynamic MLC for

example), but not as much as with the scanning technique.
Passive delivery technique requires the presence of several devices placed along the beam line and in front of the patient. Thus, the beam travels through several centimeters of matter that increase the neutron production and fragmentation in front of the patient.

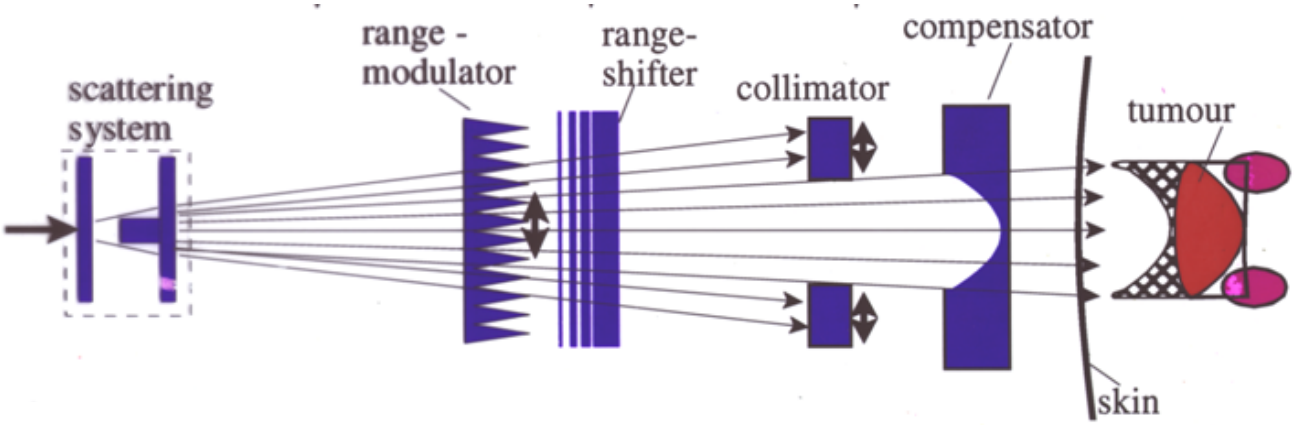

Figure 15: Schematic of a fully passive beam delivery system, the black and white pattern in front of the target represents irradiated normal tissue in the proximal part. Figure courtesy of Uli Weber.

Scanning systems

The second method for delivering the beam on the target is the scanning technique, often also called an active system. In this case the planned target volume (PTV) is divided into a grid of voxels. The delivery system scans the pencil beam with fixed energy using horizontal and vertical deflection magnets over one iso-energy slice and then changes to the next energy.
Fully active systems provide several benefits:

- no need for manufacturing specific hardware for each patient (like the collimator and bolus)
- the build up of secondary fragments in front of the patient is reduced
- even tumours with complex geometries can be irradiated with a high dose conformality in the PTV
- the dose for each layer can be modulated to compensate for preirradiation of higher energies as well as biological effectiveness

On the other hand, the scanning technique demands higher quality assurance processes.
Scanning allows an intensity and thus dose modulation of the beam in contrast to passive techniques. For a single field in IMRT the dose can only be modulated in two dimensions. The energy variation in scanning provides a third degree of freedom for the dose modulation. Thereby a

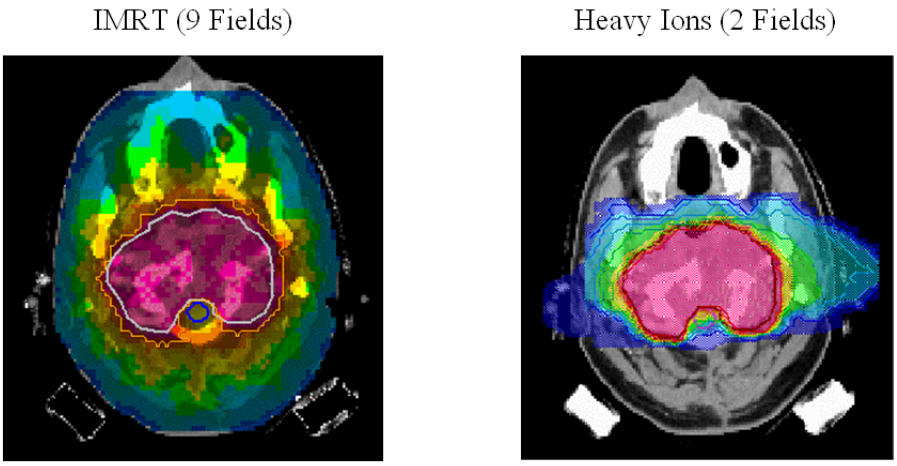

Figure 16: Treatment planning for a target in the head. The left side shows the dose distribution by an IMRT treatment, the right side depicts the same target irradiated by two fields of carbon ions. Picture courtesy of Oliver Jäkel.

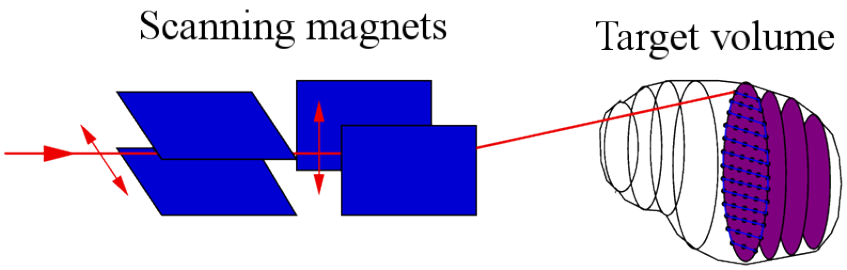

Figure 17: Sketch of the raster-scanner used at GSI, from (Haberer et al., 1993).

single scanned field of charged particles can provide a high dose conformality whereas photon IMRT uses several fields (Fig. 16). In practice, a tumour irradiation with charged particles is most often performed using two fields.

Different types of scanning techniques are in use. The *Paul-Scherrer-Institute* (PSI) was the pioneer of *spot-scanning* (Pedroni et al., 1989, 1995). The PSI system uses circular-shaped pencil beams with a Gaussian profile produced by a cyclotron and positioned by a sweeper magnet on a spot. Once the selected spot is irradiated, the fast kicker magnet switches the beam off. Then the sweeper magnet is changed to irradiate the next spot and the beam is switched on again. A dynamic range shifter is used to adjust the penetration depth of the beam.

The faster scanning approach is the *raster-scanner* (Haberer et al., 1993), where each isoenergy slice is divided into a number of raster points (Fig. 17). Without switching the beam off, the raster-scanner moves the beam to the next position when the planned dose in one raster point is delivered. To achieve a homogeneous dose distribution, the raster points are chosen so to be

apart one-third of the full width at half maximum of the beam. Typically, raster points are 2 mm apart compared to the 5 mm used in spot-scanning. When the slice is completely irradiated, the beam extraction is immediately interrupted and the next energy is selected. By using more raster points, the raster-scanning system makes the treatment less sensitive to intensity fluctuations of the synchrotron spills.

2.3 Radiotherapy facilities

This section introduces the facilities involved in the experiments and gives further details on the strategies employed for dose delivery.

KGU

The University Clinic of Frankfurt am Main (*Klinikum Goethe Universität – KGU*) is a hospital employing a total of four linear accelerators as well as several brachytherapy units for radiotherapy. One of the linacs in use for patient treatment is an Elekta SL 25. It is equipped with an MLC and can deliver IMRT using dedicated treatment planning. A sketch of the setup is shown in Fig. 13 from section 2.1.
The SL25 has two operating modes: it can be used for electron treatments or for photon treatments by inserting the bremsstrahlungs target in the beamline.
Electrons can be accelerated to two different energies yielding a different bremsstrahlungs spectrum. Until the middle of 2010 the accelerator used modes of 6 and 25 MV. While 6 MV is an energy very common in photon therapy, 25 MV is comparably high and on the upper limit of photon energies used for radiotherapy. In fall 2010 the accelerator was modified to reduce the maximum voltage to 18 MV. The accelerator is mounted on a gantry that enables irradiations from 0 to almost 360 degrees. The source-to-surface distance (SSD) is usually in the order of 100 cm.
Quality assurance measurements are performed with a SSD of 100 cm in a PTW water phantom. The temperature and pressure in the treatment room are continuously monitored and used for an automatic correction of the ion chamber readings. The output of the ion chambers integrated into the treatment head is given in monitor units. At KGU, the monitor units are calibrated so that 200 MUs correspond to 2.120 Gy in the energy dependent depth dose maximum with a source detector distance of 100 cm. Since the calibration is done in the depth dose maximum, the SSD for the calibration is energy dependent. In literature, a calibration of 1 MU = 1 cGy in the depth dose maximum is commonly used. For an easier comparison with previous studies, this convention is adapted and the number of MUs given in the results is renormalized so that 1 MU = 1 cGy in the depth dose maximum.

TSL

The university of Uppsala in Sweden houses the *The Svedberg Laboratory* (TSL). The facility uses a cyclotron for therapy and research purposes. The largest fraction of beam time available at TSL is used for delivering proton therapy. Treatments at this facility started in 1957 (the facility was called Gustav Werner Institute at the time). The treatment room consists of a fixed horizontal beam line and a chair or a table for the patient. The maximum proton energy used for treatments is 180 MeV and can be reduced with a degrader to 130 MeV.
The proton beam produced by the cyclotron has a FWHM between 8 and 10 mm when injected into the treatment beam line. Then, the beam is broadened by a first scatterer, which is also defined as the source point. The beam traverses several transmission chambers and a second scatterer placed 50.5 cm after the source. At 89.1 cm, a collimator made of Pb and Fe with a thickness of 3.5 and 2.0 cm stops the beam outside an opening of a 5 cm diameter. At approximately 105 cm from the source, an exchangeable rotating wheel made of PMMA produces the SOBP. Another collimator made of iron with a thickness of 5.0 cm and an opening of 9.7 cm in diameter is positioned at 168 cm. The final collimator is placed at around 210 cm from the source. The collimator is made of rose's metal, an alloy consisting of 25% Pb, 25% Sn and 50% Bi. It has a thickness of 5 cm and is produced specifically for every patient allowing irradiation of targets up to 7 cm in diameter. As protons are strongly affected by lateral spreading, the distance between the exit window and the patient st be reduced as much as possible to preserve the beam focus and thus produce sharp edges. A plastic bolus is positioned in front of the patient for compensating the different depths of the target volume. The isocenter of the treatment is at 230 cm from the source.

PSI

Measurements with scanned protons were performed at the PROSCAN facility at PSI which is described in (Schippers et al., 2007). Successful treatments of cancer patients with protons starting in 1996 have led to the construction of the PROSCAN facility that began treatment in 2007.
The PROSCAN facility was built into the existing experimental halls of PSI. A superconducting cyclotron was built by ACCEL Instruments GmbH in cooperation with PSI. A scheme of the facility is shown in Fig. 18. Protons are accelerated to a fixed energy of 250 MeV with an extraction rate of over 80%. Beam losses are small minimizing the activation of the machine parts reducing waiting times for service. The proton energy can be modulated to a range of 70-238 MeV with a degrader consisting of carbon wedges and magnets that allow to change the range in water by 5 mm in 50 ms. It is located shortly after the cyclotron exit and far away from the patient eliminating the exposure to secondary particles from degrading.

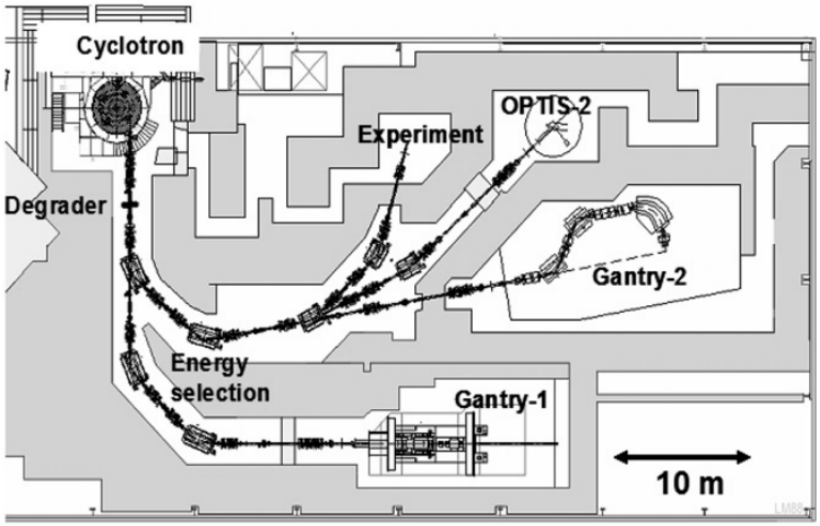

Figure 18: Sketch of the PROSCAN facility, taken from (Schippers et al., 2007).

Figure 19: Photograph of the treatment room Gantry 2 at PSI, taken in February 2010.

Several beam lines are available for treatment or experiments. The experiments described in this work took place at Gantry 1 and Gantry 2 where the beam can be delivered with the spot-scanning technique described above.

The former is an eccentric gantry system: the patient couch rotates together with the gantry while a counter rotater keeps the table in a horizontal position. The beam is scanned horizontally with the sweeper magnet and vertically by a slow movement of couch. Gantry 1 was used for patient treatments before the construction of the PROSCAN facility. The beamline was connected to the new cyclotron and treatments started again in 2007. The eccenctric gantry allowed for a compact design but showed flaws in clinical practice. For example, the movement of the couch makes it inaccessible at times, but quick access to patients is desired by the medical staff.

Gantry 1 only uses three energies from the degrader, further depth modulation is achieved by a range shifter integrated into the treatment nozzle. The passive energy modulation in the nozzle spreads the beam and increases the neutron yield in front of the patient. Furthermore, the slow mechanical vertical scanning prolongs the irradiation time and might make future treatments of moving organs difficult.
To overcome several limitations, Gantry 2 was designed as a new isocentric gantry using a double magnet system for two dimensional scanning as well as full energy modulation by the degrader far from the patient. The isocentric design moves the treatment nozzle around the patient, only for energies below 70 MeV a preabsorber made of carbon is inserted in the nozzle to enable irradiations of proximal targets. A photo of Gantry 2 as it was during the experiment is shown in Fig. 19. Patient treatments are expected to start in 2012.

HIMAC

The *Heavy Ion Medical Accelerator* (HIMAC), belonging to National Institute of Radiological Sciences (NIRS) in Chiba, Japan, started treating patients with carbon ions in 1994. A detailed description of the facility can be found in (Torikoshi et al., 2007). The facility uses two synchrotrons and was designed for medical purposes. Three treatment rooms are available at HIMAC, one with a horizontal beam line, one enabling a vertical irradiation and one room with both. Up to the present, irradiations are performed using the passive scattering technique. Currently, scanning is implemented and treatments are expected to start soon in the new HIMAC facility.
Carbon ions provide two main advantages compared to protons: the reduced lateral beam spread and the elevated biological effectiveness in the Bragg peak.
The two accelerators of HIMAC are positioned on top of each other: the former provides the beam for horizontal irradiation with energies of 170, 290 or 400 MeV/u while the latter delivers beam energies of 140, 290 and 350 MeV/u to the vertical irradiation ports. The beam is monoenergetic, has a spotlike beam profile and must be spread in depth and width to cover a three-dimensional target. Instead of a fully passive scatterer HIMAC uses the wobbling technique, where two wobbling magnets are positioned so that their fields are orthogonal to each other and the beam profile is enlarged by using a phase shift in the excitation of the magnets and a small scatterer placed behind the them. A maximum field size of 22 cm in diameter can be produced with this delivery technique. The correct choice of the magnet excitation, scatterer material and thickness yields a highly uniform field. An inhomogeneity of $\leq \pm 2.5\%$ is accepted for treatment. Compared to a fully passive scatterer, the wobbling method reduces the material in the beam path and the range loss.

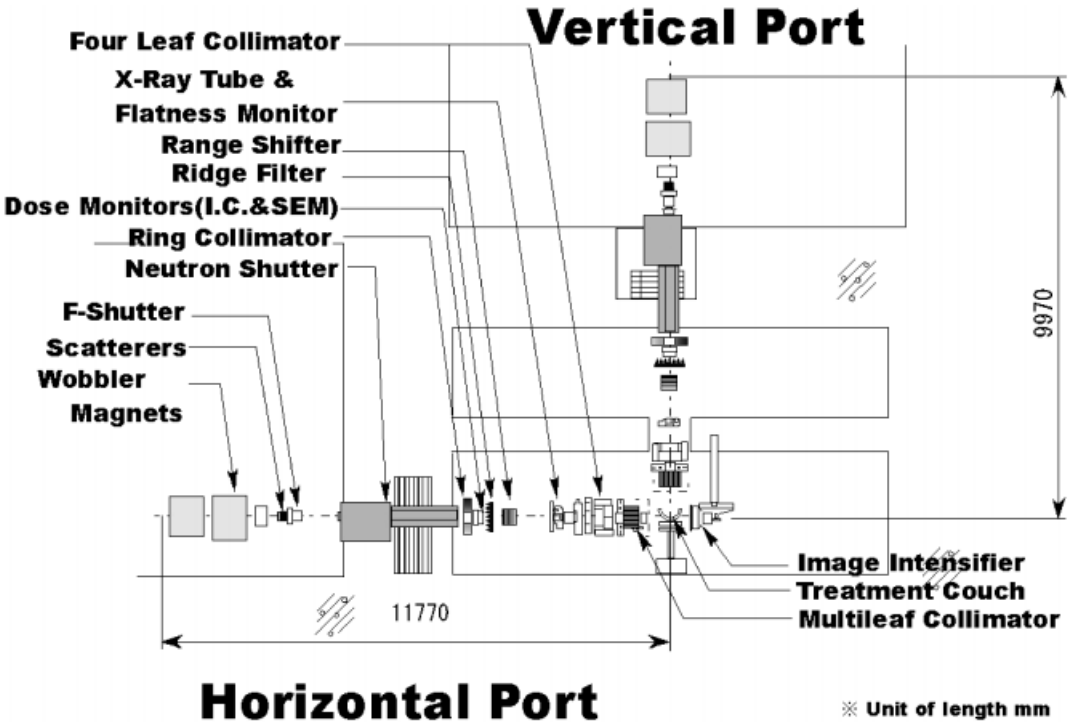

Figure 20: Sketch of the HIMAC beamline for cave B, taken from (Torikoshi et al., 2007).

A sketch of the treatment cave B at HIMAC is shown in Fig. 20. Instead of a rotating wheel bar ridge filters are used for creating a SOBP. The particles traverse the filters at different positions and therefore pass through different thicknesses so that the monoenergetic beam becomes spread-out. The bar ridge filters are designed to deliver a homogeneous biological dose and are made either of aluminium or brass. HIMAC uses a set of PMMA plates as range shifter. The required range can be adjusted with a set of 10 PMMA plates each one having twice the thickness of the previous. The combination of the plates produces a thickness between 0.25 and 255.75 mm.

After the range shifter the beam passes the four-leaf collimator (FLC) and the multileaf collimator (MLC), the former is located upstream of the latter so to reduce its activation. The FLC is made of aluminium while the MLC consists of 23 pairs of iron leaves with a thickness of 6.5 mm each. The MLC is used for most treatments except for tumours in the head and neck. In these cases, the collimators are produced of brass as those used at TSL.

For every patient an individual compensator (or bolus) made of polyethylene is used to adjust the distal part of the SOBP to the exact position and is placed at the end of the nozzle. When a collimator is used, it is attached to the compensator. The nozzle can be moved close to the patient so to achieve a sharp penumbra.

GSI

GSI started patient treatment with carbon ions in 1997 after the raster-scan method was developed and implemented in 1993 (Haberer et al., 1993). A pencil beam is deflected in horizontal and vertical directions by fast scanning magnets. The PTV is divided into rasterpoints and energy slices. One spill is used to irradiate several spots (mostly a full energy slice) without turning the beam off. When the energy slice is completed the irradiation is aborted and the next energy is set. A combination of ion chambers and position-sensitive multiwire chambers is used for monitoring the beam position and the dose. In case a measured quantity is outside the tolerable values, the irradiation is stopped immediately.
The beam energy is changed with the synchrotron instead of using a passive range modulator. A set of 250 energies ranging from 80 to 430 MeV/u with 15 intensities and 7 focus widths is stored for the synchrotron and magnets in the beam line. To reduce treatment time and to widen the sharp Bragg peak of carbon ions in longitudinal direction, a ripple filter is placed upstream of the exit window. This device is a thin piece of plastic with different thickness in the order of 2 mm which spreads the beam accordingly (Weber and Kraft, 1999). Around 1 meter of air gap is needed between the ripple filter and the patient so that the carbon ions with slightly different energies mix again and form a homogeneous field. It is important to note that this is a large air gap compared to that used and required in proton therapy.
From 1997 to 2008 a total of 440 patients were treated mostly for radioresistant tumours in the skull base, along the spinal cord and for prostate. The project was a collaboration of GSI with the Heidelberg University Clinic, the German Cancer Research Center (DKFZ) and the Research Center Rossendorf in Dresden. The raster-scan method has now moved into clinical practice at HIT.
Cave M was built at GSI for medical purposes and patient treatment. The cave contains a horizontal beam port. A movable and rotatable couch was used to position patients. After patient treatments have stopped, Cave M is still used for research purposes and irradiations in full therapy conditions are possible after careful beam-tuning. Machine tests for the irradiation of moving targets and the irradiation of biological targets are among others the experiments taking place in Cave M.
Before the start of patient treatments in Cave M, the system was developed in the research Cave A, which is also equipped with a raster scanner but cannot provide irradiations of three dimensional targets. Cave A is still in operation and can deliver all particles available at GSI from protons to uranium.

HIT

Following the successful trial of treating patients with heavy ions delivered with an active system, a dedicated particle therapy facility was built in Heidelberg. The design and the construction of the Heidelberg Ion Therapy Center (HIT) was performed by GSI and is described in (Combs et al., 2010). The requirements for a clinical accelerator are quite different from those for a research facility. At HIT, a linac-synchrotron combination was built with a focus on a compact and reliable design.

HIT is designed for both clinical purposes and therapy-related research. The synchrotron delivers the beam to two horizontal treatment lines, a heavy-ion gantry and the quality assurance and research cave QA. The first patient was treated in November 2009 in one of the horizontal-line rooms. The QA cave can be used parasitically during patient treatments for quality assurance and therapy-related experiments. The second patient room was completed in 2010, the gantry is still under commissioning. When fully operational, HIT will be able to irradiate with protons, carbon, helium-3 and oxygen. Currently (April 2011), protons and carbon ions are available for patient treatments. The desired ion species can be selected from spill to spill.

The design of the beamline at HIT is very similar to GSI, details can be found in (Parodi et al., 2010). HIT uses the raster-scanning technique described earlier in section 2.2. The particle beam is deflected with vertical and horizontal magnets and, after the vacuum window, travels through the Beam Application and Monitoring System (BAMS, Siemens AG) which consists of a multiwire chamber, three ionization chambers and another multiwire chamber. If the measured parameters are not within the tolerated limits an interlock stops the beam within 250 μs.

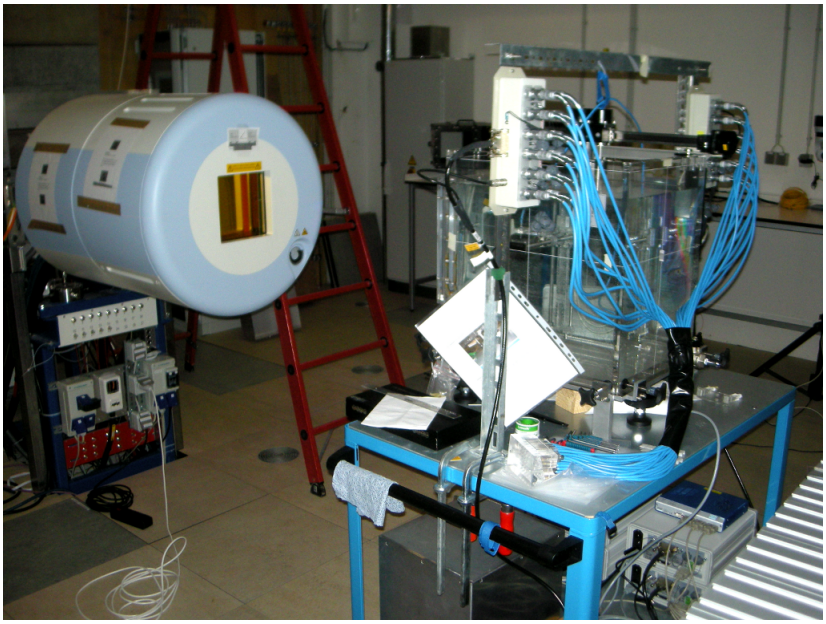

Figure 21: Photograph of the QA cave at HIT.

3 Detectors

Several detectors were used for this work. Their properties which are described in this chapter account for the demands of the experiment. A photograph of all detector types used is shown in Fig. 22.

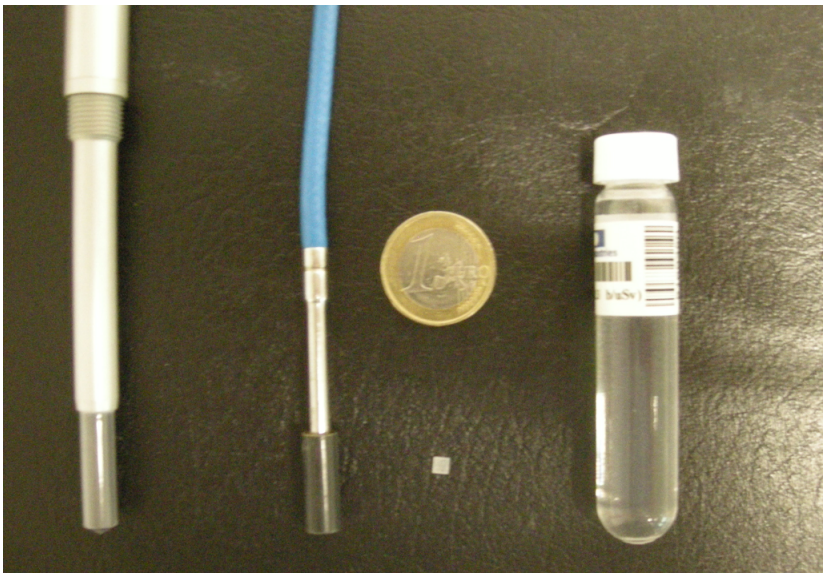

Figure 22: The picture shows from left to right a PTW Farmer Chamber type 30013, a PTW diamond detector type 60003, a Harshaw TLD 600 and a bubble detector from BTI together with a 1 €-coin for comparing the size.

3.1 Diamond detector

The PTW Diamond detector type 60003 was used for measurements in the water phantom as well as the anthropomorphic phantom. Diamond detectors are solid state detectors suitable for use in radiotherapy for several reasons. Made of carbon, the detector is nearly tissue equivalent and has a high sensitivity to radiation as well as a low leakage current (Kozlov et al., 1975); a further advantage is the high radiation hardness (Planskoy, 1980).
The general properties of diamond are described in (Tapper, 2000) and (Fowler, 1963) while details on the PTW diamond detector are given in (Hoban et al., 1994). Pure diamond has a high resistivity in the order of 10^{13} to 10^{16} Ω cm determined by the bandgap of 5.45 eV. While from an electrical point of view diamond is an insulator, it is often considered a semiconductor for its properties similar to silicon or germanium.
The detection of radiation is achieved by measuring an electrical signal in an external circuit. Radiation passes the sensitive material generating excited and ionized atoms and thus electron-hole pairs, which recombine quickly if not separated. When an electrical field is applied, the electrons and holes drift away from each other and generate a detectable current (Fig. 23).

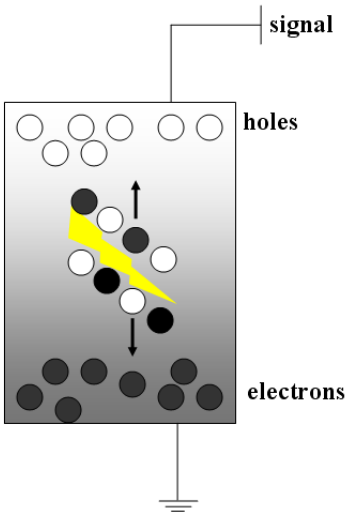

Figure 23: Principle of the detection of ionizing radiation by a diamond detector. The applied voltage causes electron-hole pairs to drift apart when hit by ionizing radiation. The movement of charge generates a signal in the external circuit.

Because of its high resistivity, the current in the detector is practically zero for a set bias voltage without radiation. An almost linear signal is produced after passage of ionizing radiation. The slight deviation from the linear response is caused by the recombination time of charge carriers. This effect is more significant for solid-state detectors than for ion chambers because of their higher density. Moreover, the typical charge collection time of ion chambers is shorter if the bias voltage is set high enough. At increasing dose rate, the number of vacant holes in diamond increases thus reducing the recombination time. The recombination time may then be shorter than the time needed to collect the electron by the anode. As a result, this leads to incomplete charge collection and thus an underestimate of the dose for high dose rates.
To reduce this effect, commercial diamond detectors have impurities which create metastable states that trap electrons and prevents them from recombining. In case of a high amount of impurities, the increase of vacant holes is almost independent of the dose rate yielding an almost linear response independently of the dose rate. However the impurities must not become dominant, since the increased number of vacant holes decreases the recombination time. Moreover, trapped electrons form a space charge that creates an electric field of opposite sign to the external field. This effect is called polarization.
To correct for the dose-rate dependent response the following expression is used:

$$I \propto \dot{D}^{\Delta} \tag{14}$$

I denotes the detector current, $\dot{D}$ the dose rate and Δ the fitting parameter for the sublinearity. Studies with a PTW diamond detector were performed by several groups. The experimental

Table 2: Properties of the diamond detectors used for the experiments

Serial number	1-008	1013	3-004
Dark current [fA]	≤ 1	≤ 0.5	≤ 1
^{60}Co sensitivity [C/Gy]	1.90E-7	2.340E-7	1.83E-7
Sensitive volume [mm^3]	1.7	2.99	1.8
Sensitive area [mm^2]	4.2	8.8	8.6
Thickness of sensitive volume [mm]	0.40	0.34	0.21

results for Δ values range from 0.91 to 0.98 (Hoban et al., 1994; Laub et al., 1997; Planskoy, 1980). The conclusion from their studies was that an individual calibration for each diamond detector is needed. The Δ value was found to be constant for a given detector.

The PTW diamond detector requires a preirradiation after it has been connected to the external field. Without preirradiation, the response decreases with absorbed radiation. The filling of traps lead to an increasing polarization and therefore a decrease of the electric field (Kozlov et al., 1975). Also, the number of vacant holes increases with absorbed dose, reducing the recombination time. PTW recommends a preirradiation of up to 10 Gy with applied voltage before measurements. In this way equilibrium in the number of traps and therefore a stable response is achieved. If the detector is unused for several months, studies have found that a preirradiation of up to 20 Gy is necessary (Hoban et al., 1994; Planskoy, 1980).

A total of three diamond detectors were used for the experiments. The detector 1-008 was used for the photon measurements with 6 and 25 MV linacs, the diamond detector 1013 was used for the measurement in charged particle therapy while for the measurements with photons of 6 and 18 MV the diamond detector 3-004 was used. The properties of the detectors are summarized in table 2. All detectors have the same operating bias of +100 V. As reported in the table, the sensitive volume of the diamond detector is characterized by a very small thickness. Therefore, measurements with high spatial resolutions are possible if the detector is turned so to show the flat side towards the desired direction.

Diamond shows a sensitivity to neutrons of several MeV through the ^{12}C(n,α)^{9}Be reaction (Foulon et al., 2002). Own tests with 14 MeV neutrons produced by a d-t generator at the Fraunhofer Gesellschaft in Euskirchen showed a response in the order of $3*10^{-7}$ C/Gy (the dose was calculated for water using Kerma factors) and therefore slightly higher compared to a ^{60}Co irradiation as reported in Table 2. A neutron efficiency measurement for several energies was planned at PTB in Braunschweig but could not be performed for lack of beamtime. A technical study of the detector's response to neutrons could enable a routine use of the detector in quality assurance measurements in radiotherapy. Knowing the neutron efficiency in the high-energy region would be especially beneficial for passively delivered particle therapy.

3.2 Thermoluminescent detector

Thermoluminescent detectors (TLDs) have a wide range of applications in personal dosimetry, medical physics and space-related research. The basic principles and properties can be found in (Knoll, 2010), (Berger and Hajek, 2008) and (McKeever, 1985). A collaboration of the German Aerospace Center DLR and GSI enabled to use TLDs for this study. DLR has a high expertise on TLDs based on several calibration studies as well as space-related experiments with TLDs.
Radiation passing through a thermoluminescent crystal deposits energy in the crystal. While a large fraction of the energy is quickly spent for heating the material, the rest is stored by moving electron-hole pairs to "traps" below the conduction band. When the material is subsequently heated, the imparted energy is released as TL light. The absolute TL efficiency of this process is called α and is written as:

$$\alpha = \frac{\epsilon_0}{\epsilon} \tag{15}$$

where ϵ_0 denotes the energy emitted as TL light and ϵ the mean energy imparted to the material.

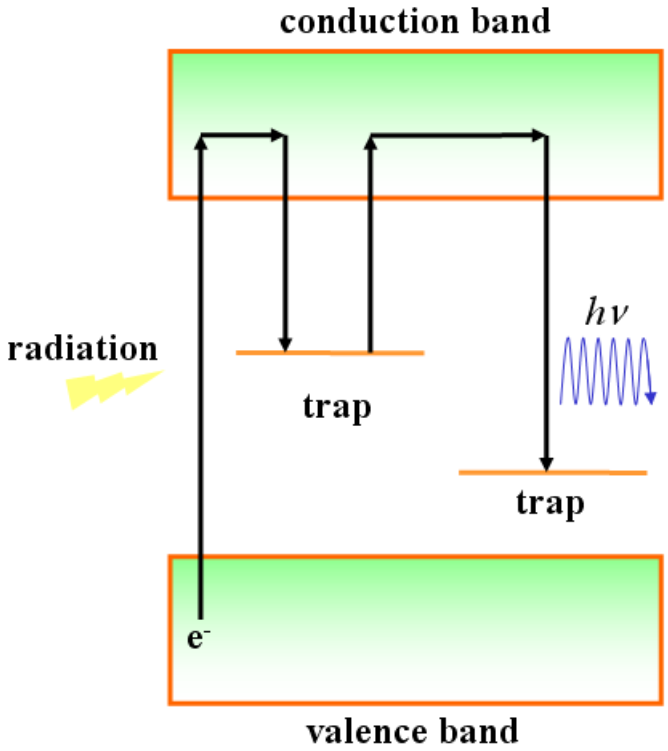

Figure 24: Simplified model of thermoluminescence: ionizing radiation stores some electron-hole pairs in traps below the conduction band. Subsequent heating releases electrons from the traps enabling recombination at deeper states under emission of a TL photon. In the detectors used, traps at several energies exist.

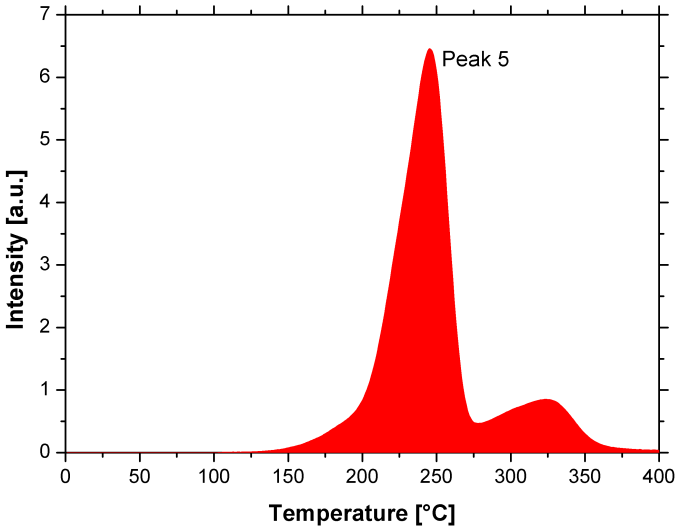

Figure 25: Typical glow curve from the read out of a TLD showing several peaks.

The theory of thermoluminescence is rather complex and not yet fully understood. A simple theory uses a band model, is described in (Ranogajec-Komor, 2002) and shown in Fig. 24. The crystal is an insulator, therefore the electrons reside in the valence band which is separated from the conduction band through the forbidden band gap. Natural impurities or doping introduce electron traps within the forbidden gap. Electrons can be excited to the valence band by radiation. Some electrons quickly deexcite to the valence band and emit a photon according to a process called radioluminescence. Other electrons get trapped in the forbidden gap and may be released again with a probability described by the Arrhenius equation:

$$p = s \cdot e^{-\frac{E}{k_b T}} \tag{16}$$

with p being the probability per time, s the frequency factor (constant in the simple model), E the activation energy, the Boltzmann constant k_b and T the absolute temperature. The equation shows that the probability for release is mainly dependent on the temperature of the crystal as well as the energy between the forbidden trap and the conduction level.
Different materials are suitable for dosimetry. The detectors used in this work consist of ^{6}LiF:Mg, Ti and ^{7}LiF:Mg, Ti known commercially as TLD 600 and TLD 700. The main difference of these detectors is the concentration of ^{6}Li which is sensitive to thermal and epithermal neutrons up to around 200 keV via the (n, α) reaction. Enriching a thermoluminescent material with ^{6}Li increases its sensitivity to low energetic neutrons.
When used as a dosimeter, the TLD is irradiated during the experiment and later heated up for readout. The light emitted in this process is recorded and the intensity is compared to a

reference value measured with a well known source. Usually the light intensity is shown as a function of temperature or time for a constant heat up process in a so-called glow curve. An example is shown in 25.

A glow curve usually shows several peaks corresponding to the electrons released from different traps. The ideal candidate for dosimetry is the so called peak 5 marked in Fig. 25 because of its linear dose response on a dose range from 100 μGy up to around 10 Gy (Knoll, 2010) for the TLD 600 and TLD 700 detectors. Above this dose, a supralinear followed by a sublinear dose response is observed (McKeever, 1985).

The absolute TL efficiency is very difficult to determine (Bos, 2007) and therefore a focus has been put on the relative TL-efficiency, defined as the light signal produced per mass and dose of the radiation under study versus the light signal produced by a reference radiation with the same dose. Usually the reference radiation comes from ^{60}Co or ^{137}Cs sources. The relative efficiency must be carefully considered when using TLDs for dosimetry in charged particle therapy and was investigated by (Geiß, 1997). The relative efficiency $\eta_{CP,\gamma}$ is defined as:

$$\eta_{CP,\gamma} = \frac{R_{CP}/D_{CP}}{R_{\gamma}/D_{\gamma}} \tag{17}$$

where R stands for the TL response per unit mass and D for the dose levels. The underscore denotes the radiation under study with CP for charged particles and γ for the reference radiation. Theoretical models predicted that the efficiency of peak 5 to charged particles depends on LET and on the particle species (Waligórski and Katz, 1980a),(Waligórski and Katz, 1980b)(Horowitz, 1981). The models were confirmed experimentally by (Berger, 2003; Geiß, 1997). A summary of efficiencies can be found in the review paper from (Berger and Hajek, 2008). For carbon ions the relative efficiency changes from 0.940 for an LET_{∞} in H_2O of 11.2 keV/μm to 0.505 for 49.6 keV/μm.

The change of efficiency is explained by the local energy deposition of secondary electrons. The energy, and thus the range of these electrons varies greatly. The electron density can lead to a local energy deposition in the sublinear, linear, or supralinear dose response range in the TL material. Therefore, the relative TL-efficiency may have values below 1 but also above 1. The reference radiation (photons) has a homogeneous distribution of secondary electrons causing the energy to be deposited in the same response range, whereas the localized effects from the track structure of charged particles leads to different responses chaning the relative efficiency. Several different theoretical models exist for the prediction of the TL-efficiency. Several models are based on the radial distribution of dose around ion tracks (Waligórski and Katz, 1980a,b; Kalez-Ezra and Horowitz, 1982). The efficiency was also calculated by (Geiß, 1997; Bassler, 2006) using the Local Effect Model. Another model is based on microdosimetric considerations, where the energy deposition in a volume (of nanometer or micrometer dimension) is related to

the observable effect (Olko et al., 2002; Olko, 2004). All models show some agreement with experimental results but are still under development and need to be validated for the entire range (Horowitz et al., 2006).
As reported above, the relative TL efficiency is found to depend not only on the LET but also on the particle species. In agreement with the theoretical models based on track structure, this behavior is explained by the fact that for the same LET a particle with a higher charge has a higher velocity leading to a lower ionization density and ultimately to a higher efficiency (Olko, 2007)
It is important to use the same procedure for the evaluation of results collected in different experiments. (Berger and Hajek, 2008) summarize the following parameters responsible for TLD results:

- TL material (manufacturer, batch, form)
- reference radiation (^{137}Cs, ^{60}Co, X-rays)
- calibration
- readout system
- heating rate
- annealing cycle
- data evaluation (single peak, region of interest, composite peak)

The cited review states that an intercomparison of data taken from different groups is difficult but possible. However, it is clearly stated that for a given group with a given protocol a comparison of results from different radiation experiments is valid. The same protocol was applied to all the experiments reported in this work. The analysis of the results was performed in close collaboration with the experts from DLR. The protocol for the evaluation of TLDs at DLR is also described in the review.

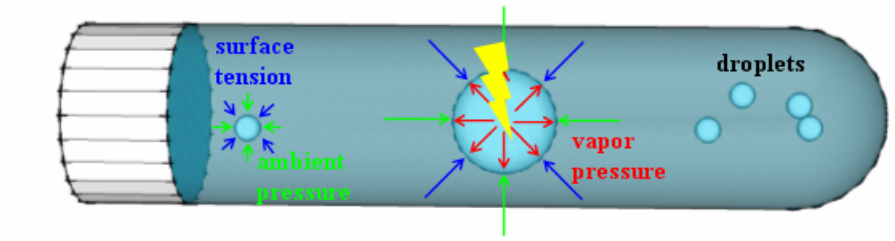

Figure 26: Model of the detection mechanism of bubble detectors. While in the unirradiated state the droplets are kept pressurized, the energy deposition of radiation increases the vapor pressure increasing the size of the droplets making them visible by the eye.

Bubble detectors were used to measure neutron fluences and energy spectra in photon therapy. A description of the basic physics of bubble detectors is based on (d'Errico and Matzke, 2003). A bubble detector is a detector consisting of metastable droplets that vaporize into visible bubbles when hit by a neutron or charged particle. Bubble detectors are often referred to as superheated emulsions because of these properties. They are passive dosimeters, popular in personal dosimetry because of the easy handling. An advantage of the detector is the discrimination of neutrons and photons as it is completely insensitive to photons. The response to neutrons of different energies can be varied by changing the composition of the droplets or the temperature and pressure. Hence, with different detectors a complete neutron spectrum can be unfolded mathematically in the range of about 10 keV to 25 MeV.

The detector itself is a vial filled with an emulsion in a liquid contained in a steady-state superheated condition. Usually a bubble detector is filled with halocarbon. The term superheated means that the liquid is kept above its boiling point through pressure. When a neutron interacts with the emulsion, a charged particle generates a trail of submicroscopic vapour cavities in the droplet. When the droplet reaches a critical size, the expansion becomes irreversible and the droplet evaporates reaching a size visible by the eye (Figs. 26 and 27).

Figure 27: Photograph of bubble detectors after irradiation, bubbles are clearly visible by eye.

The energy necessary for the formation of a visible bubble depends on the composition and degree of superheat of the emulsion. To determine the nucleation energy necessary for bubble formation the following theoretical approach can be used (Skripov, 1974):

$$W_\sigma = \frac{16p\gamma^3}{3(p_s - p')^2(1 - v'/v'')^2}\left(1 + \frac{2\Delta H}{(p_s - p')(1 - v'/v'')} - 3\frac{T}{\gamma}\frac{d\gamma}{dT}\right) \tag{18}$$

where W_σ is the nucleation energy necessary, the prime and double prime denote the liquid and vapour phases, γ the surface tension, p the pressure, p_s the saturation value, v the specific volume and ΔH the latent heat of vaporisation of the fluid.

It is possible to parametrise the properties of the superheated emulsion with the dimensionless quantity reduced superheat (d'Errico, 1999):

$$s_T = \frac{T - T_b}{T_c - T_b} \tag{19}$$

It represents the normalised operating point of an emulsion within the temperature and pressure range corresponding to the metastable state. Instead of varying the temperature, the pressure may also be changed and the reduced superheat can be expressed as

$$s_p = \frac{p - p_s}{p_c - p_s} \tag{20}$$

with p_c being the critical pressure (Sawamura et al., 2003). The advantage of this property is that for all relevant superheated emulsions a correlation of superheat and neutron detection thresholds was found. Hence, when the normal boiling point and critical temperature of a halocarbon are known, it is possible to predict the neutron threshold of a detector for a given ambient temperature. Not only the neutron threshold can be calculated, but also its sensitivity to photons and electrons. For example, a big difference between the operating temperature and the boiling point enables the detection of sparsely ionizing radiation of photons and electrons, whereas a smaller difference of both quantities only enables the detection of energetic heavy ions produced by neutrons. The detectors are also sensitive to charged particles, but for example for protons in the range up to 70 MeV the sensitivity is one order of magnitude lower than for neutrons Takada et al. (2004).

A neutron spectrometer set based on this knowledge is commercially available from Bubble Technology Industries (BTI) in Chalk River, Canada. Different liquids are used to enable a complete spectral measurement. The liquids are dispersed in a polymer of aqueous gel. The emulsifier matrix must be chosen so that the droplets neither dissolve nor lose their properties. The neutron spectrometer BDS consists of a set of 36 bubble detectors with six different thresholds providing a measurement of neutrons with energies between 10 keV and approximately 25 MeV. The sensitivities to each neutron energy range are provided for unfolding of the results (Fig. 28). The BDS is insensitive to photons making them an ideal candidate for neutron measurements in photon therapy. The spectral unfolding is another important feature of this detector since the RBE of the neutrons is greatly dependent on their energy.

The neutron thresholds and sensitivities of the BDS system are only known for a temperature of 20 ± 0.5°C. Since the response of the detectors is based on a thermodynamical process and is therefore highly dependent on temperature, this parameter must be strictly controlled. It is not possible to extrapolate the response from a different temperature since both the overall sensitivity and the threshold of a detector change. To keep the detectors at the desired temperature for the experiment, they were placed in a water bath where the water temperature was controlled with an accuracy of ± 0.03°C. According to the manufacturer, the detectors reach water temperature within 10 to 15 minutes. For the experiments, the detectors were removed from the water bath and put in foam pipe insulation, which was found to keep the detectors at the original temperature for several minutes.

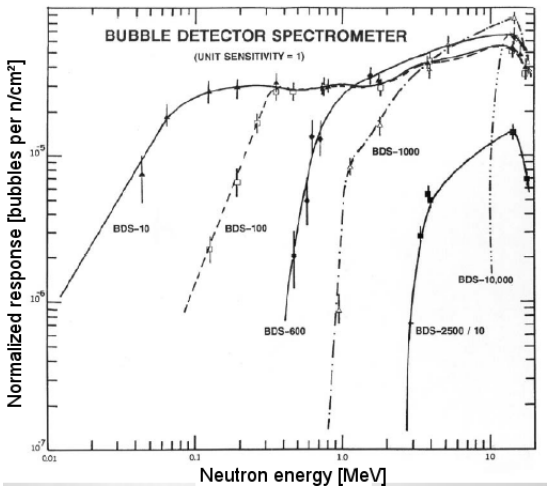

Figure 28: Response function of detectors used in the bubble detector spectrometer. Figure provided by BTI.

The irradiation causes the immediate formation of bubbles which are counted with an automatic reader system also commercially available from BTI. The ratio of the sensitivities at different energies is assumed to be constant, the overall sensitivity is different for each detector. The results from each individual detector are normalized with the sensitivity specified by the manufacturer from exposure to an AmBe-source.

The bubble detectors can be reused several times, after each measurement they are placed in a recompression chamber where a pressure of over 25 bar recondenses the bubbles into the liquid phase. Since the bubbles slowly grow over time, the recompression takes longer the more time has elapsed after exposure. Immediate recompression after irradiation reduces the time to about 10 minutes, therefore the same detector can be used several times during the same experiment. The recompression chamber is also used between experiments to recompress bubbles formed by background radiation. As the readings of detectors underlie large statistical fluctuations, it is highly recommended to measure each position at least three times and with a dose producing around 100 to 150 bubbles in a detector for proper statistics.

When produced, the detectors are insensitive to neutrons, as they are kept pressurized by a volatile liquid. When the cap of the detector is opened for the first time, the liquid vaporizes and releases the pressure thus making it ready for detection. The detectors have a lifetime of three to six months once they are activated. The matrix in the detector destabilizes over time reducing its sensitivity.

Spectrum unfolding

The BDS is primarily used for low-resolution neutron spectroscopy. The raw data are converted into an energy spectrum with a simple unfolding algorithm provided by the manufacturer. The main assumption of this algorithm is that the spectrum can be represented as a 6-bin histogram.

The unfolding starts with the highest threshold (10 MeV) and assumes that all bubbles observed were caused by neutrons in the highest bin. Additional bubbles from the next lower threshold are attributed to the next lower bin, taking into account the sensitivity to different neutron energies. The process is reiterated until the lowest threshold (10 keV) is reached. This method suffers from large error propagation as the unfolding comes to the lower thresholds and may even lead to negative fluence values in some bins. These are set zero for the following unfolding, but indicate the limitations of the algorithm. It was not used after a first trial and was discarded in favour of a more reliable algorithm.

BUNTO

BUNTO is an unfolding code for passive neutron dosimeters including bubble detectors. The code is described and applied in (Ongaro et al., 2000, 2001; Zanini et al., 2005).
The principle behind the algorithm is that the read out of a bubble detector is represented by its response curve folded with the number of neutrons of a given energy. In mathematical terms this can be formulated as a set of Fredholm integral equations:

$$M_i = \int R_i(E)\Phi(E)dE \tag{21}$$

where i is the number of the detector, M_i the number of bubbles in this detector, $R_i(E)$ its response curve and $\Phi(E)$ the spectral fluence. The approximated discrete version of (21) is given by

$$M_i = \sum_{j=1}^{N_g} R_{ij}\Phi_{E_j}\Delta E_j \tag{22}$$

where j denotes the number of energy intervals the spectrum is divided into. The equation set (22) can be written in a compact matrix form:

$$M = \mathbf{F}\Phi \tag{23}$$

M and Φ denote the respective vectors and F a matrix. When the total number of energy intervals N_g is higher than the number of detectors used, (23) has an infinite number of solutions. (For the experiments with bubble detectors, 5 or 6 detectors are used and the spectrum is logarithmically divided into 34 intervals from 10 keV to 25 MeV). Several strategies are applied to receive the "best" solution, i.e. a physically plausible solution. As a first requirement the resulting Φ should be non-negative in all entries and not produce artificial peaks.
BUNTO uses an iterative method to calculate the spectrum and unlike most other codes, is not

dependent on a-priori knowledge of the latter. Instead, a flat guess spectrum can be used for the first iteration. The experimental results of M_i are used for a random sampling, where M_i is used as expectation value of a normal distribution with σ equal to the associated experimental uncertainty. For each i, a total of k values is derived from M_i and a solution ϕ_{i_k} is calculated by perturbation of the starting spectrum. The spectrum Φ is then obtained as the mean of all ϕ_{i_k} weighted on the mean standard deviation.
The Φ obtained in this way is then inserted in all equations of type (22). If the spectrum can reproduce the experimental reading (i.e. the number of bubbles in each detector) better than the previous spectrum, Φ is used as guess spectrum for the next iteration. The iteration is repeated until a convergence criterion is met.

A simple example illustrated in Fig. 29 shows the basic idea of the algorithm. In a hypothetical experiment, a 2 MeV neutron source is considered and the BDS10 and BDS1000 are assumed to have a homogeneous sensitivity of 1 above their threshold. Once exposed to the source, both detectors read 100 bubbles. For this example the spectrum is divided into 4 energy regions. The solutions ϕ_i from the flat guess spectrum will be a flat distribution with 25 neutrons per interval for the BDS 10 and 50 bubbles in the higher two intervals for the BDS1000. The mean of both distributions results in a histogram with 12.5 neutrons each in the lower intervals and 37.5 in the higher intervals. Further iterations will lead to an increase of the neutrons in the higher intervals together with a decrease in the lower intervals. The algorithm will converge at the end in a spectrum with 50 bubbles each in the higher intervals. Using more detectors with non-flat sensitivities will then be able to resolve the peak position more precisely and will also calculate spectra more complex than this example.

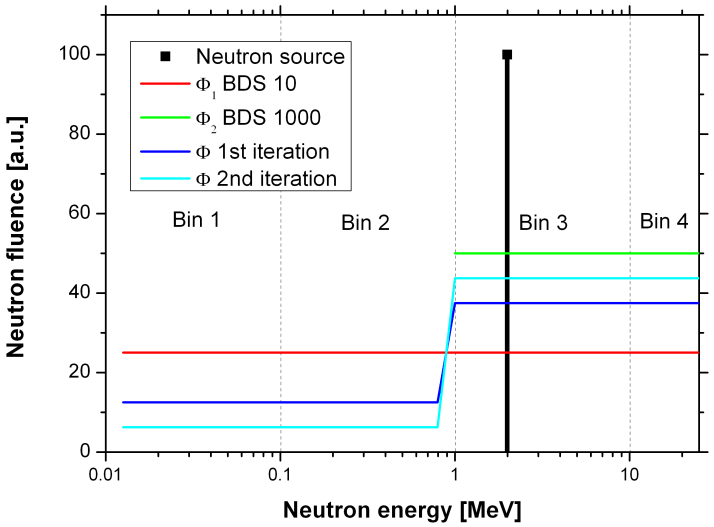

Figure 29: Simplified illustration of the iteration process of BUNTO.

4 Single field measurements

The thesis describes two basic sets of experiments for characterizing the out-of-field dose in radiotherapy. This chapter explains the setup of the experiment with a simple geometry.

In the first set of measurements, a water phantom was irradiated with a single field of a photon or particle beam. The measurements investigated the lateral dose profiles in the water phantom to help understanding the effect of the irradiation technique chosen. The simple geometry also makes this experiment ideal for comparison with Monte Carlo simulations.
There are many studies on lateral dose profiles in the literature, most of these concentrated on characterizing the region close to the field edge because the dose fall-off is crucial for target conformality and effects in neighbouring organs. The measurements presented in this study focused both on the dose decrease close to the edge as well as on the far out-of-field region where side effects are possible in radiosensitive organs many years after treatment.

In clinical practice water is often used as tissue-equivalent medium for this kind of studies as well as for daily quality assurance measurements. Several types of water phantoms with similar properties were used in this work, all were manufactured by PTW in different sizes, except for the experiment at TSL where a Scanditronix-Wellhöfer model was used. The walls of the water phantoms are made of PMMA which is also nearly tissue-equivalent and has a density of 1.19 g/cm^3. The PTW phantoms had a wall thickness of 2 or 1 cm, the Scanditronix model had a wall thickness of 1 cm. The water phantoms are equipped with a three-dimensional linear drive that can move an object in three dimensions with sub mm precision.
One of the main points addressed when designing the setup of this study was the lack of data in literature comparing different radiation and irradiation modalities under similar conditions. Thus, for all measurements a fixed field size of 5×5 cm^2 was chosen and the lateral dose fall-off was measured at the depth of maximum dose for photons or at the Bragg peak for charged particles. All results are normalized to 1 Gy in the field at the depth of maximum dose.
To compare protons and carbon ions, their energies were chosen so to have the same range in water. A range value of 12.5 cm in water was selected for several measurements with a monoenergetic beam as it represents a typical tumour depth in ion therapy. For photons, measurements were also performed at 10 cm water depth for comparison with data from literature and at 12.5 cm depth for comparison with charged particles. In all irradiations with charged particles a dose of 1 or 2 Gy in the field was delivered. The accuracy of the in-field dose is ensured by the daily quality assurance routines required for medical purposes. The absolute dosimetry was done by the therapy control system operated by the local staff.

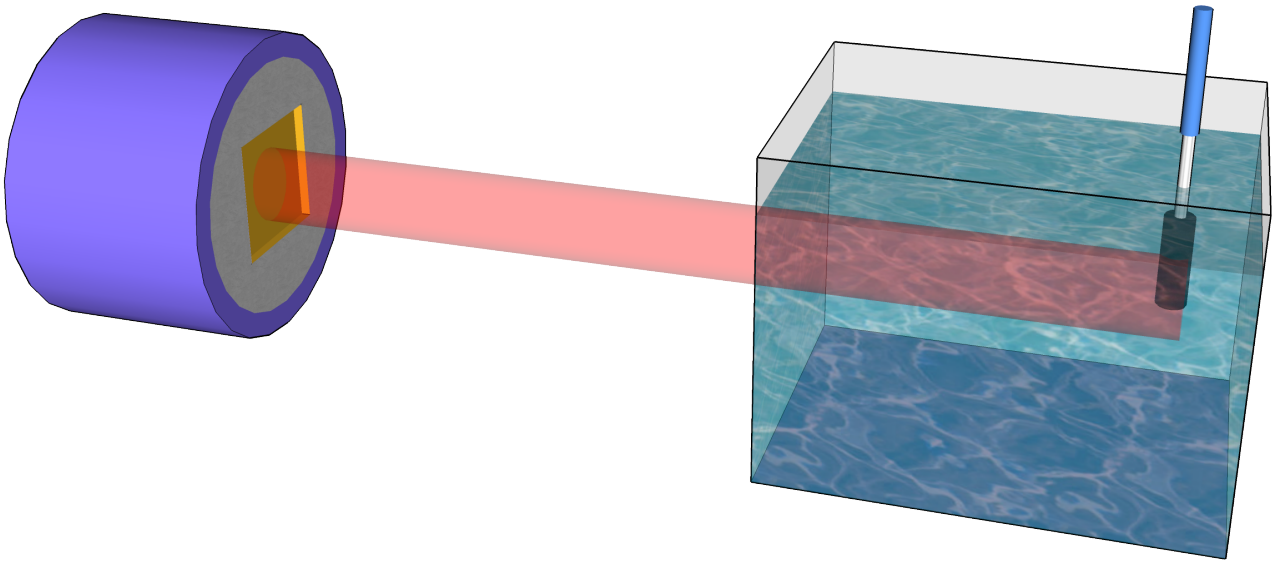

Figure 30: Experimental setup for dose fall-off measurements with charged particles.

For the comparison of the 5×5 cm^2 field in the dose maximum the following irradiations were performed:

- 6, 18, 25 MV linac energy for photon therapy at KGU, Frankfurt, Germany
- 130 MeV passively delivered protons at TSL, Uppsala, Sweden
- 130 MeV scanned protons at PSI, Villigen, Switzerland
- 130 MeV scanned protons at HIT, Heidelberg, Germany
- 250 MeV/u scanned carbon ions at HIT
- 250 MeV/u scanned carbon ions at GSI, Darmstadt, Germany

The irradiation with charged particles was performed at horizontal beam lines as illustrated in Fig. 30. In Frankfurt, photons were delivered vertically without passing the PMMA walls of the phantom as shown in Fig. 31. The alignment of the water phantom was achieved using laser grids available at the facility.

A diamond detector, TLD 600 and 700 and an ion chamber were used in the experiments. As described in section 3.1, the diamond detector is characterized by measuring a current induced from charged particles, photons and, to some extent, neutrons with a high spatial resolution and a wide dose range. Therefore, it offers best conditions for an accurate measurement of the fall-off as well as the low dose far out-of-field. The detector was attached to the 3D linear drive of the water phantom with a special holder made of PMMA. A calibration measurement was performed against an ion chamber to account for the dose-rate dependence.

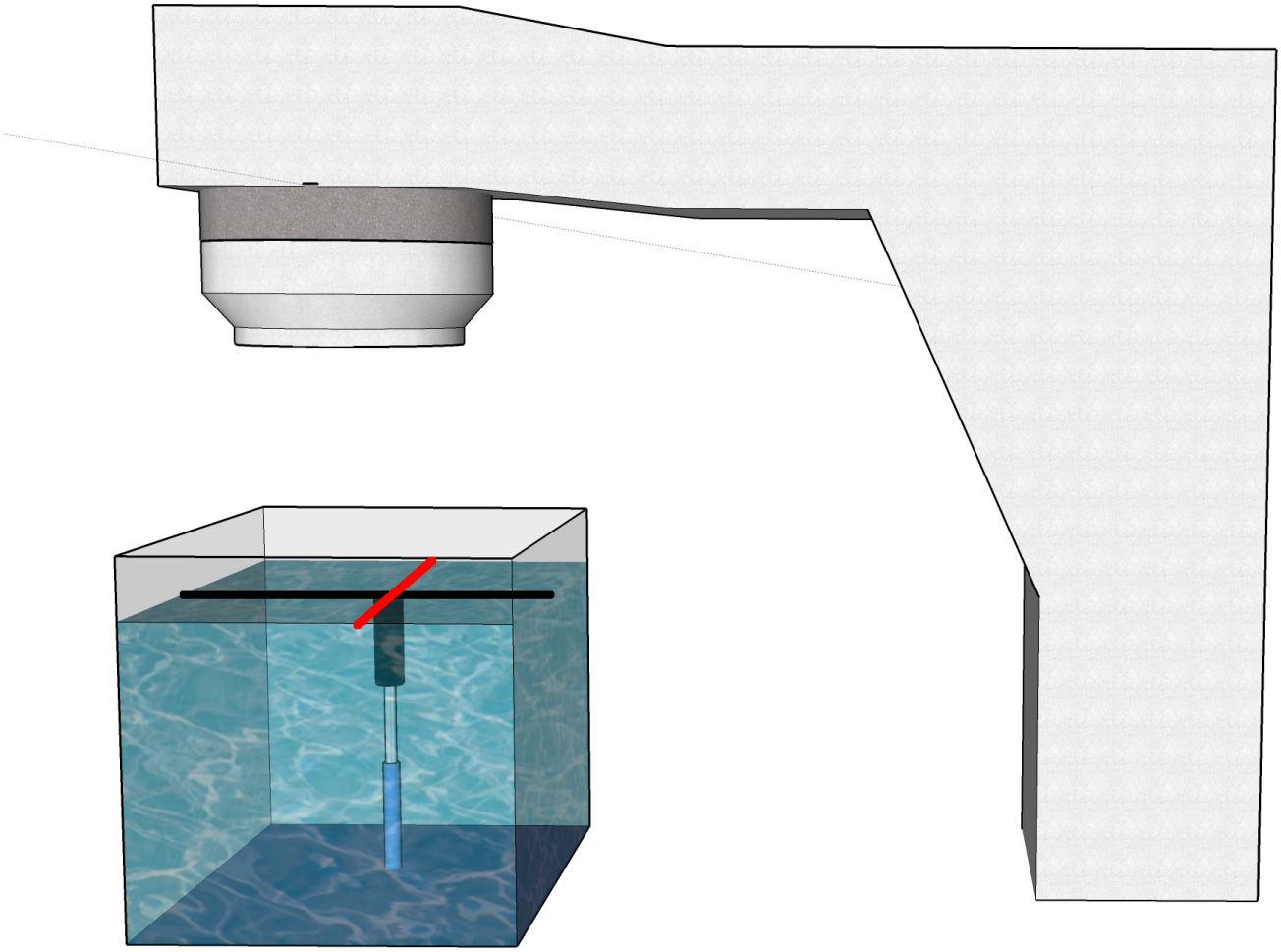

Figure 31: Experimental setup for dose fall-off measurements with photons. The black line shows the GT direction and the red one the AB direction.

TLDs can be used for comparison with the diamond detector measurements, but their response to charged particles must be taken into account; moreover, they give a qualitative measure of the low-energy neutron fluence. The TLDs were fixed to a holder shown in Fig 32 which contained up to 104 TLDs in 26 positions each 7 mm apart.
Additionally, bubble detectors were used for the detection of neutrons during the experiments with photons at KGU.

KGU

The linear accelerator Elekta SL 25 in Frankfurt can be operated at 6 and 25 MV. The higher energy was reduced to 18 MV in summer 2010. As the experiments with photons were all performed at KGU using the same machine, the dependence of the out-of-field dose on the beam energy could be investigated without further influences coming from different geometries in the beam line.

Figure 32: Photograph of the TLD holder (transparent).

The experimental setup was the same for all experiments at KGU. A PTW water phantom was placed on the patient bed beneath the treatment head. The position was chosen so that the field irradiated was located in a corner of the phantom. The reason for this setup was to enable measurements further away from the field. In beam's eye view, the field was on all sides at least 3 cm away from the PMMA walls.
As all irradiations were performed from the top, the beam did not pass any PMMA but hit directly the water surface. The source-to-surface distance was 100 cm. Two directions are defined for linac experiments: the gun-target (GT) direction and the AB or cross plane direction (see Fig. 31). The former is parallel to the linac axis while the latter is orthogonal to the GT direction in the plane of the patient.
The out-of-field dose profile was investigated with the diamond detector in the dose maximum and at 10 cm water depth, the latter being a typical value in published data. For the 18 MV beam, a measurement was also performed in a water depth of 12.5 cm which is the position of the Bragg peak of ions investigated in this work at other facilities.
Together with the regular 5×5 cm^2 field, a 10×10 cm^2 field was also considered to evaluate the influence of the field size on the out-of-field dose.
The SL 25 was further used to calibrate the diamond detectors. The dose profiles were measured both with the diamond detectors and an ion chamber that shows no dose-rate dependence. The comparison of both data allowed an estimate of the factor Δ which corrects for the recombination effects of the diamond detector.

Most importantly, measurements of the dose delivered by photoneutrons were performed at KGU. Since neutrons may contribute significantly to the out-of-field dose in high-energy photon treatments, a separate investigation of this issue was conducted with the bubble detector spectrometer BDS described in section 3.3. The data were collected with the 18 MV beam along the GT direction which is the most common direction for patient positioning.

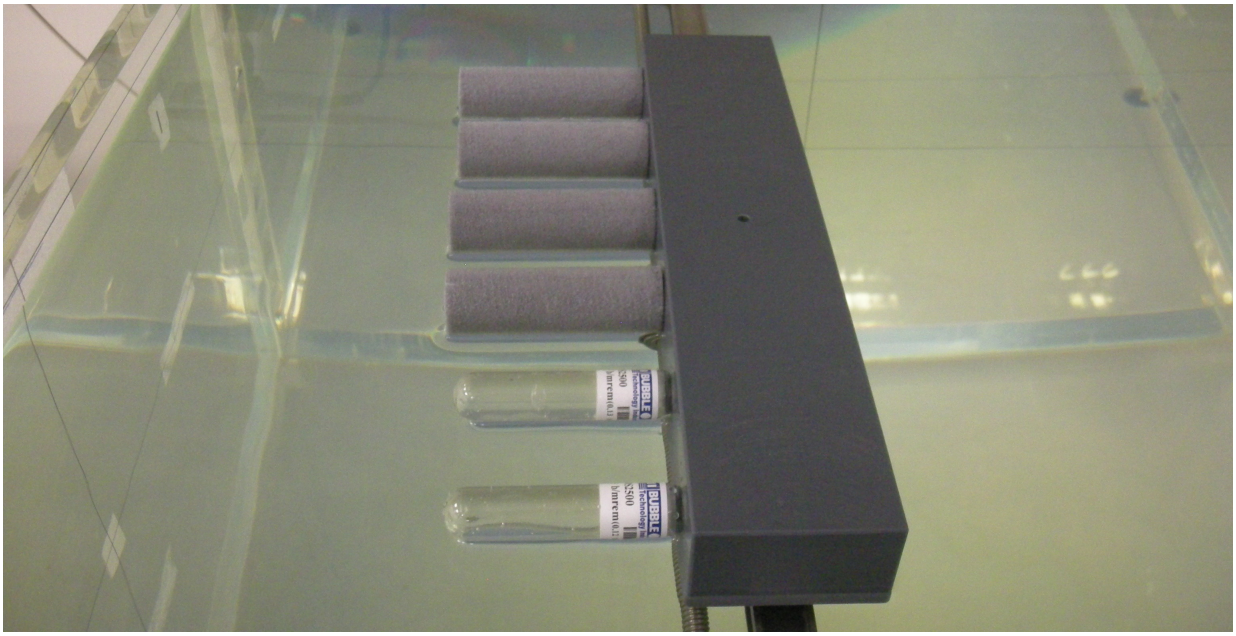

Figure 33: Bubble detectors fixed in a water phantom with a special holder. The four upper detectors are in foam pipe insulation keeping the detector temperature constant.

For this experiment, a holder was built to contain up to six bubble detectors at the same time (Fig. 33). The neutron out-of-field dose was measured at the water surface and at 10 cm water depth. In the former case, the detector touched the surface slightly, in the latter the center of the detector was at a depth of 10 cm. The compactness of the bubble detectors represents a major advantage to other photoneutron studies. Bonner-Sphere-Spectroscopy for example requires bulky hardware that prevents measurements in the phantom.
At both depths, six positions were measured per irradiation in the GT direction with increasing distance to the field. For each detector type and water depth three measurements were performed to reach satisfactory statistics. When repeating the measurements, the detectors were placed at different positions to avoid systematical errors. To eliminate the effects of temperature dependence, the detectors were cooled to 19.5°C and insulated in foam pipe for the irradiation on the surface. For the measurement in water, the phantom was cooled to 19°C and no additional insulation was used. The time elapsed between positioning the detectors and irradiating was less than 2 minutes. Previous tests with the insulation showed that this time was too short for temperature changes in the detector. The detectors were read out immediately with the automatic reader and recompressed so they could be used again. A total of approximately 100 irradiations in eight hours were achieved with the bubble detectors.

An additional measurement was performed in-field on the water surface. To determine the neutrons impinging on the surface, a single bubble detector was positioned in the center of the field. All detectors of each threshold were irradiated once; therefore 30 in-field irradiations were completed in total.

The out-of-field dose delivered by the 18 MV photon field was also measured with TLDs in the GT direction at a water depth of 3.1 cm (dose maximum) and 10 cm. The difference of TLD 600 and 700 gives an indication of the yield of low energy neutrons.

TSL

During the experiment at TSL, a Scanditronix Wellhöefer phantom was used for horizontal irradiation. Its composition is similar to the PTW water phantoms. The phantom was placed on the patient table that is used, for example, for prostate irradiations, while most patients are treated in sitting position. The seat and table are mounted on the same position and can be easily exchanged.
TSL uses passive beam shaping as portrayed in section 2.3. For the water phantom irradiations no bolus was used, only the collimator. The latter was made out of rose's metal and was fixed directly in front of the phantom wall.
Measurements with the diamond detector and TLDs were performed with the standard field size of 5×5 cm^2. For the diamond detector, the data were collected both without a range shifter and with the thinnest one available (18 mm SOBP).
In order to study the field size dependency additional measurements with 2×2 cm^2 field size were performed. Larger fields than 5×5 cm^2 were not available at TSL.
Additionally, measurements with a 3D volume were performed. The aim was to evaluate how the out-of-field dose changes when an extended field is used instead of a monoenergetic one. For the comparison, a 5×2 cm^2 field was irradiated with a range shifter generating a 5 cm SOBP at a mean depth of 10 cm.

PSI

Water phantom measurements for scanned protons at PSI were carried out at Gantry 2. The target was positioned on the movable patient couch. The nozzle of the treatment head was extended so that its edge had a distance of 80 mm to the water phantom wall. The lateral dose profiles of a 5×5 cm^2 and 10×10 cm^2 fields were investigated.

GSI

In a short experiment in cave A in August 2010 the field size dependency of the lateral dose profile was studied for carbon ion irradiations. The water phantom was positioned at a distance of 21 cm to the beam exit window. The dose distributions for field sizes from 2×2 cm^2 up to 10×10 cm^2 in steps of 1 or 2 cm were characterized with the diamond detector for a beam energy of 300 MeV/u. The measurements were repeated with the diamond detector turned by 180 degrees.
In a second beam time, the water phantom was irradiated in cave M with 250 MeV/u carbon ions. A 5×5 cm^2 field was used to compare the lateral dose profiles of HIT and GSI.

HIT

The radiotherapy facility in Heidelberg permits a direct comparison of protons and carbon ions since both are delivered through the same beamline. Thus, possible uncertainties of the phantom setup are minimized and differences in the out-of-field dose can be studied under optimal conditions. The lateral straggling of ions is energy dependent and the fragmentation of carbon ions increases for higher energies since the carbon ions traverse more material, therefore the out-of-field dose profile in the Bragg peak is also expected to be dependent on the energy. A systematic comparison of scanned protons and carbon ions was achieved for ranges of 5, 12.5 and 20 cm in water using a 5×5 cm^2 field in the QA cave of HIT. The middle range value was also measured at other facilities for comparison, while the other data were used mainly for understanding the dependency of the dose profile on the primary beam energy. The diamond detector was used for these experiments. As a first step, the Bragg peak position was determined experimentally. Then, the detector was moved laterally left and right from the beam direction to obtain the lateral dose fall-off. For the proton irradiations, no ripple filter was used. Unless stated otherwise, all irradiations with carbon ions were performed with the ripple filter inserted into the beamline.

A total of two days of beam time was used to investigate the influence of the particle species, energy and the distance from the target to the exit window on the lateral dose. For carbon, additional measurements with and without the ripple filter were performed. To check how the distance between the exit window and the target effects the lateral dose, the edge of the water phantom was placed at 104.0 and 10.6 cm from the BAMS. The larger distance is approximately the value used for treatment of patients with carbon ions. The short distance was chosen to reproduce the typical setup for proton irradiations.

The former data were all collected in May 2010 before a service shutdown of the accelerator. A further beamtime, focused on the investigation of the reproducibility of the experiment, was performed in July 2010. For this purpose, a lateral dose profile for carbon ions was measured three times, each time setting up the water phantom anew. In all cases, the distance from the edge of the BAMS to the edge of the water phantom was 104 cm.

Furthermore, an irradiation of TLDs with carbon ions was performed. The position of the Bragg peak was determined with the diamond detector and the TLD holder was placed in that position. An additional measurement focused on the comparison between the read out of the diamond detector and an ion chamber. The lateral dose profile delivered by carbon ions was recorded with the waterproof PTW farmer chamber 30013 as well as with the diamond detector.

5 3D volume measurements

The second main experiment consisted of the study of the out-of-field dose following irradiation of a three dimensional target volume. While the measurements in the water phantom with simple geometry provide good conditions for benchmarking Monte Carlo codes, the 3D irradiation aimed for an evaluation of the out-of-field dose in a more realistic case, i.e. with an irradiation process and geometry as close as possible to the case of a patient. Using an anthropomorphic phantom, the dose fall-off can be obtained as well as the spatial distribution of the dose. Such data are interesting for comparison with Monte Carlo simulations of complex geometries, since there appears to be a strong link between the secondary cancer risk and dose received in organs (Xu et al., 2008).

The 3D dose distribution was measured inside an anthropomorphic phantom treated with radiation for a hypothetical tumour in the head. The phantom was of the Rando type lent by the DLR, where it is used to assess the dose the astronauts are exposed to in space. It is part of the MATROSHKA facility (Reitz and Berger, 2006) which is an ESA project with a cooperation of more than 16 international partners. The phantom was sent to the international space station to evaluate the dose absorbed by an astronaut when staying in low-earth orbit.
The phantom simulates a human upper torso and is made of soft tissue (C, H, O, N and Sb) and bones. To simulate the different densities in a human body, the phantom has a varying density between 0.3 and 1.3 g/cm^3. It is sliced into 34 pieces with a height of 25.4 mm each, for a total of approximately 85 cm. Several regions are cut out of the slices to hold both active and passive detectors. Among other detectors, TLDs are used to determine the absorbed dose in a three-dimensional grid with a step size of 1 inch. The space bound phantom has more than 1600 TLD spots for collecting a detailed 3D dose distribution inside the body. Further details and results can be found in (Reitz et al., 2009).

5.1 Setup

For calibration purposes and biological experiments, a ground-based "twin" of the phantom used in the MATROSHKA experiment was produced. It is identical to the one used on the ISS except for less holes for detectors, and also consists of 34 slices numbered from 0 (top) to 33 (bottom). To compare the out-of-field dose delivered by different radiotherapies, a tumour treatment was performed with the most common irradiation types. A target volume of $5 \times 2 \times 5$ cm^3 was planned in the center of slice 4 to simulate a brain tumour. The phantom underwent the usual clinical routine for patients. First, a CT-scan was performed for treatment planning, then, before the irradiation, the phantom was fixed to the table and aligned at the isocenter.

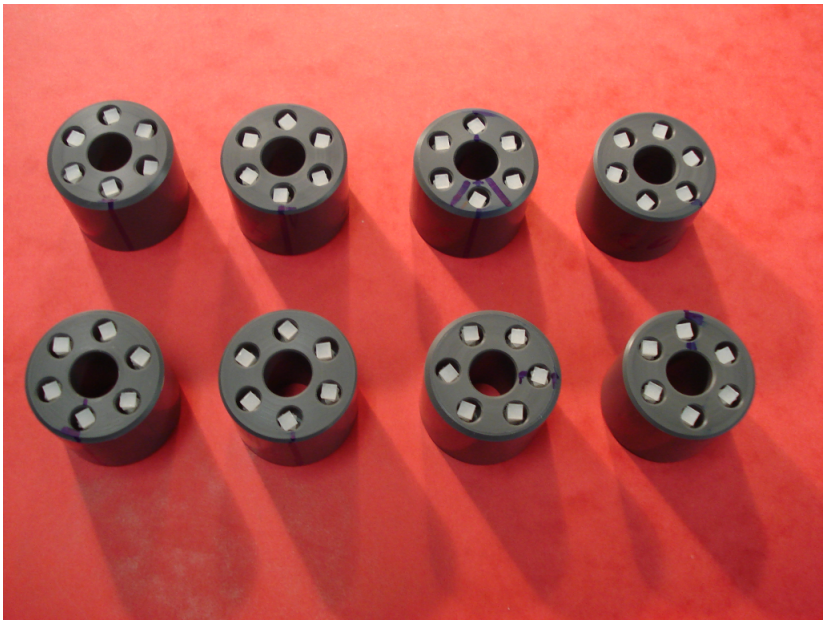

Figure 34: Picture of the rod pieces containing TLDs.

The dose was measured with TLD 600 and TLD 700 as in the space experiment. While the space phantom has holes for TLDs in all slices, the twin has only holes in the slices 3,4,5,14 and 20. To get a more detailed dose-fall off perpendicular to the beam direction, a special rod was constructed that could be inserted instead of a holder for the phantom. It was made out of small cylindrical pieces of 25 mm height. While most pieces were just blank, special rings with 6 little carvings every 60 degrees were produced. Each hole can hold eight TLDs and in this case four TLD 600 and four TLD 700 were used. The rings containing TLDs were placed at the position of slice 3,5,7,9,13,17 and 21. For slice 4 (the target slice), the 25 mm ring was divided into two smaller pieces of 12.5 mm height to improve the spatial resolution in the target. For the experiment with scanned carbon ions, the rod material was polyvinyl chloride ($\rho = 1.3$ g/cm^3), for the other experiments it was made of polyethylene ($\rho = 0.98$ g/cm^3). To compensate for the difference between the thickness of the rod pieces (25 mm) and the slices (25.4 mm), small rings with a height of 1.6 mm were produced. These were used for all experiments except the scanned carbon irradiation. A picture of the rod pieces filled with TLDs is shown in Fig. 34.

TLDs were also employed to evaluate the dose at the phantom surface. The detectors were contained in stripes of plastic bags. The stripes made out of thin plastic held 2 TLDs in one position. The surface dose was measured on the side of the entrance channel for charged particles, whereas for photons, the TLDs were placed on the frontal side of the phantom. The surface dose was measured along the phantom main axis shown in Fig. 35.

A total dose of up to around 200 Gy was delivered to the target in each experiment. Such a high value was required to deliver enough dose to TLDs far away from the treatment. However,

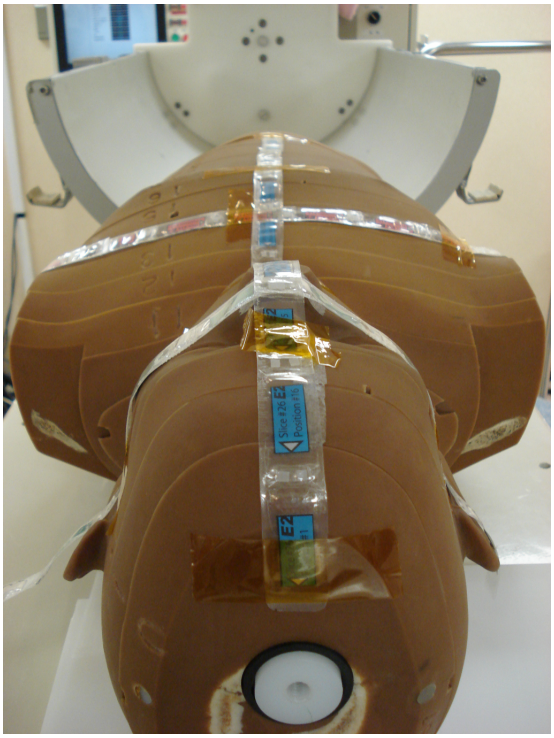

Figure 35: Photograph of the bags containing the TLDs for the surface dose evaluation.

Table 3: Parameters of the experiment with the anthropomorphic phantom. P-a and a-p stand for an irradiation in posterior-anterior and in anterior-posterior direction.

Radiation type	[AMeV]	Delivery type	Field	Facility
Photons	25	IMRT	7 fields	KGU Frankfurt, SL 25 linac
Protons	130	passive	p-a	TSL Uppsala, therapy beam line
Protons	88-136	scanned	p-a	PSI Villigen, Gantry 1
Carbon ions	350	passive	a-p	HIMAC Chiba, therapy beam line, room A
Carbon ions	165-260	scanned	p-a	GSI Darmstadt, Cave M

as this dose would surpass the linear response range of TLDs, those close to the target were removed after the first irradiation of a few Gy. The dose the detectors were exposed to during plane travels (for the experiments in Sweden and Japan) and / or natural radiation background with time were accounted for and subtracted from the results. All results shown are normalized to 1 Gy in the target region.
The experimental setup was as similar as possible in all measurements. However, the facilities caused slight deviations for every setup; for example the treatment could not always be delivered from the same direction. An overview of the facilities and the respective irradiation parameters is listed in Table 3.

For the IMRT treatment the bubble detectors were inserted in the rod to characterize the neutron field inside the body at the same position as the TLDs.

Data were also acquired with the diamond detector, placed both on the surface of the phantom and inside the rod. In the former case the detector was taped to the phantom surface, while for the latter a piece of the rod was used as a holder as the detector's diameter of 8 mm fitted well into the 10 mm hole of the ring.

IMRT at KGU

The anthropomorphic phantom received an IMRT treatment at KGU produced by the bremsstrahlungs spectrum generated in the 25 MV mode. The majority of clinical IMRT irradiations are performed at lower energies, therefore the results from this experiment represent the upper limit of the neutron dose expected in photon therapy.
Prior the experiment, a CT picture of the phantom was taken for treatment planning (Fig. 36). The markers necessary for an accurate positioning of the patient before irradiation were defined on a thermoplastic mask put over the phantom head.

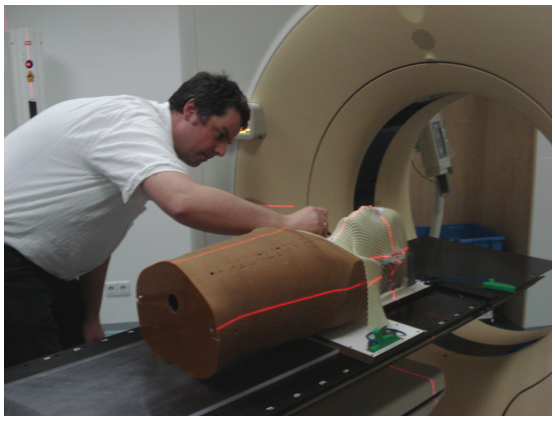

Figure 36: Preparation of the phantom for the CT-scan at KGU

For the treatment, the phantom was positioned lying on the patient table. One irradiation was delivered by 7 fields from different angles using the gantry. A treatment of 1 Gy in the target required a total of 117.2 MUs. The measurements were performed with the diamond detector, TLDs and bubble detectors; the sites where measurements were performed with the former two detectors are summarized together with the other treatments in Table 4.
The bubble detectors were placed inside a special rod made of polyethylene in 5 positions at increasing distance to the target. As the room temperature was 22 °C, the detectors were cooled to 19.5 °, insulated, placed inside the rod and irradiated immediately.

Charged particle irradiations

An overview of the data obtained from the irradiations is shown in Table 4. For the proton irradiation with passive modulation at TSL the phantom was standing on the patient seat and irradiated from the back. For the treatment, a combination of a range shifter, a collimator and

Table 4: Overview of the data obtained in the experiment of the anthropomorphic phantom. X marks the data available, DD stands for diamond detector.

Facility	Surface, TLD	Surface, DD	Inside, TLD	Inside, DD
KGU		X	X	X
TSL	X	X	X	
PSI	X		X	
HIMAC	X	X	X	X
GSI			X	

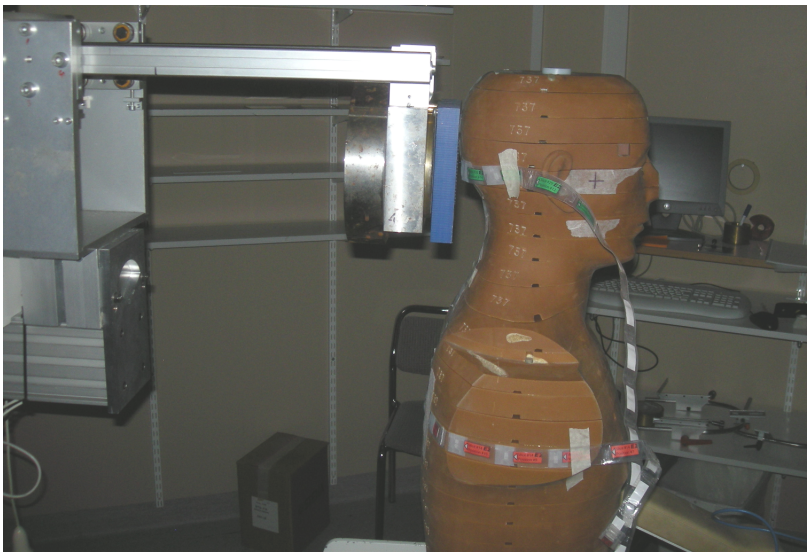

Figure 37: The irradiation of the anthropomorphic phantom at TSL; the picture shows the metal collimator and the bolus in blue plastic.

a bolus produced a homogeneous field of $5 \times 2 \times 5$ cm^3. The latter two devices were moved as close as possible to the head (Fig. 37). The beam energy used was 130 MeV after the 180 MeV beam had been degraded.

The scanned proton irradiation of the anthropomorphic phantom was performed at PSI Gantry 1. The phantom was positioned lying on the patient table and received a posterior-anterior irradiation.

The irradiation at HIMAC used a passively shaped carbon beam in the vertical treatment room A. The phantom was positioned lying on the patient table and was irradiated from above in the anterior-posterior direction. The carbon ions had an initial energy of 350 MeV/u and were collimated by the FLC and MLC. A bolus made of polyethylene was attached to the treatment head so to achieve a homogeneous field in the target (Fig. 38). No biological optimization was performed for the phantom in contrast to a patient treatment.

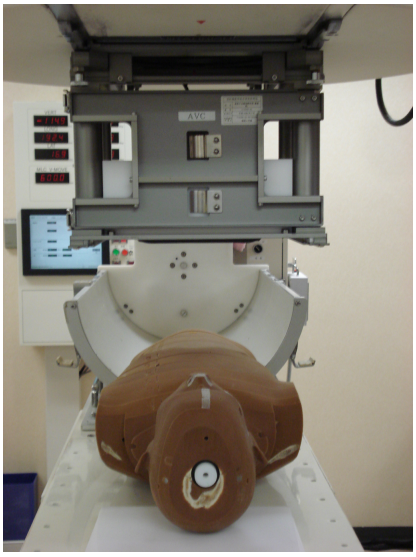

Figure 38: Experimental setup at HIMAC. The bolus can be seen in white above the phantom.

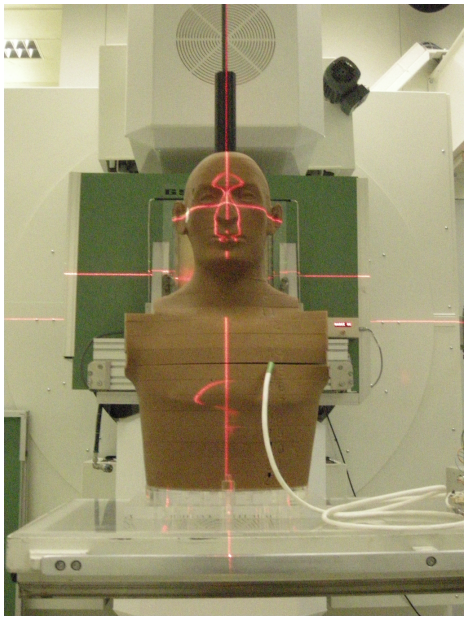

Figure 39: Experimental setup at GSI; the beam exit window is seen behind the phantom.

At GSI, the raster-scanning technique was applied for dose delivery. The phantom was positioned standing on the patient table in cave M for irradiation from the back (Fig. 39). The treatment planning program TRiP (Krämer and Scholz, 2000; Krämer et al., 2000; Jäkel et al., 2001) was used to produce a homogeneous physical dose distribution in the head. No biological optimization was performed.

Calibration of the diamond detector

The diamond detector is the primary detector used for the experiments with the single field. As reported in section 3.1, the detector shows a dose response slightly deviating from linearity and depending on the charge collected as: $I \propto \dot{D}^{\Delta}$. As a first step all diamond detectors were calibrated against an ion chamber to obtain the constant Δ, whose values will be then applied to correct all results.

The quantity Δ was measured using a 6 MV photon beam, which assured that no neutrons would affect the data. Measurements of lateral dose profiles in GT and AB direction were performed with different diamond detectors and compared to ion chamber data (reference) in the dose maximum. An example of these measurements is shown in Fig. 40 for the diamond detector 1-008. The ion chamber begins to give unreliable results for doses below 0.2% of the target dose. The values measured at the edge of the field have a large discrepancy between the two detectors because of their different sizes and thus spatial resolution. Therefore, only the region between 0.002 and 0.01 of the target dose is considered for obtaining Δ. From linear regression $\Delta = 0.961 \pm 0.002$ and $\Delta = 0.961 \pm 0.002$ were obtained from the measurements in GT and AB direction respectively. As expected, the results agree very well. The green line in Fig. 40 represents the corrected results of the diamond detector which show an excellent agreement with the ion chamber data.

With the same procedure Δ values of 0.979 ± 0.001 and 0.979 ± 0.002 were derived for diamond detectors 1013 and 3-004 respectively and used to correct the readings. Using the corrections for the non-linear response and the absolute dosimetry performed at each facility by the QA staff, the diamond detector results can be converted to absorbed dose.

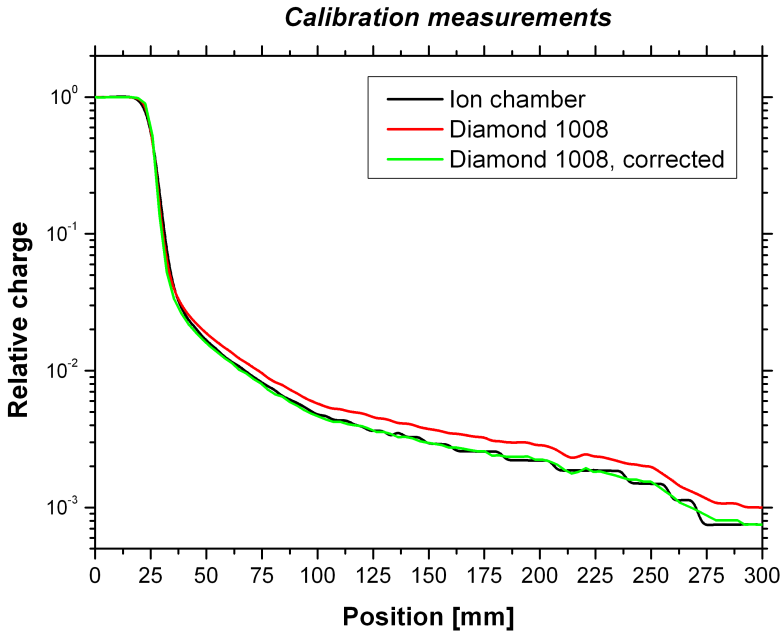

Figure 40: Collected charge measured at KGU for 6 MV photons in the GT direction at increasing distance to the field with an ion chamber and a diamond detector. The raw data obtained with the diamond detector were corrected for the nonlinearity (green line).

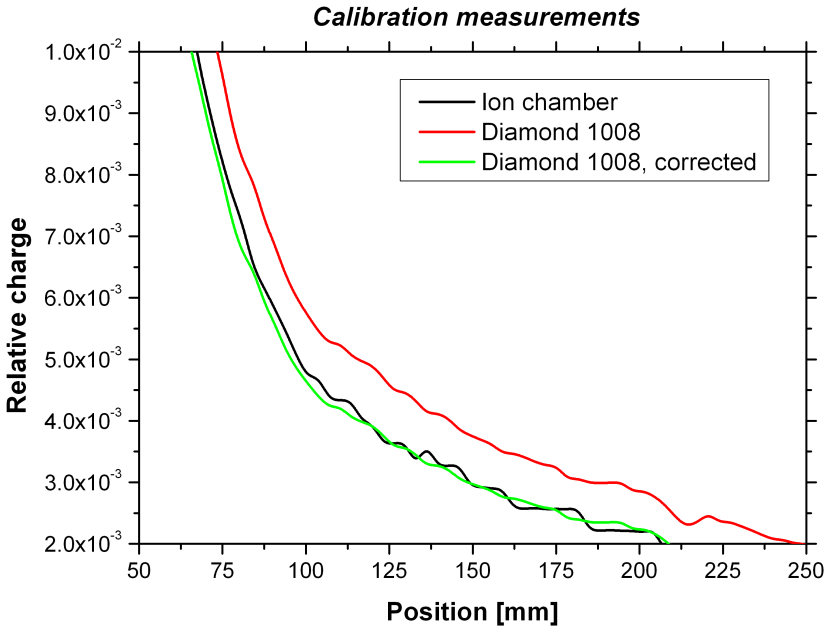

Figure 41: Linear plot of Fig. 40 in the region used for determining Δ.

Uncertainties of the diamond detector measurements

After correcting the systematic error due to the sublinearity of the diamond detector, the random errors of the experiment shall be investigated. These uncertainties come from fluctuations from the readout of the charge as well as positioning errors of the detector. Since all facilities are radiotherapy centers for patients and therefore satisfy strict requirements, the error from dose delivery fluctuations is negligible compared to other errors.
To evaluate the random errors the dose profile following carbon ion irradiation has been measured several times at HIT, each time repositioning the experimental apparatus (water phantom and detector). The fluctuation of the results for each position is used to estimate the random error of the measurement. Fig. 42 shows a comparison of three independent measurements of the dose profile. The standard deviation of the results was plotted as a function of the dose and a fit function with a focus on the low dose region was used to estimate the upper limit of the error. A linear regression of the standard deviation in a logarithmic plot shows that the errors can be estimated by b=-0.06±0.005 and a=0.09±0.01 for the linear equation $y = a + bx$. The linear regression of the semi logarithmic graph needs to be transformed and the error is then calculated as

$$D_{\mathrm{err}} = (0.09 - 0.06 \times \log D) \times D \tag{24}$$

The function is an estimate of the upper limit of the error and therefore overestimates largely the error in the field. However, the focus of this work is to characterize the dose far out-of-field, thus the error in this region was considered more important than an exact evaluation in field.

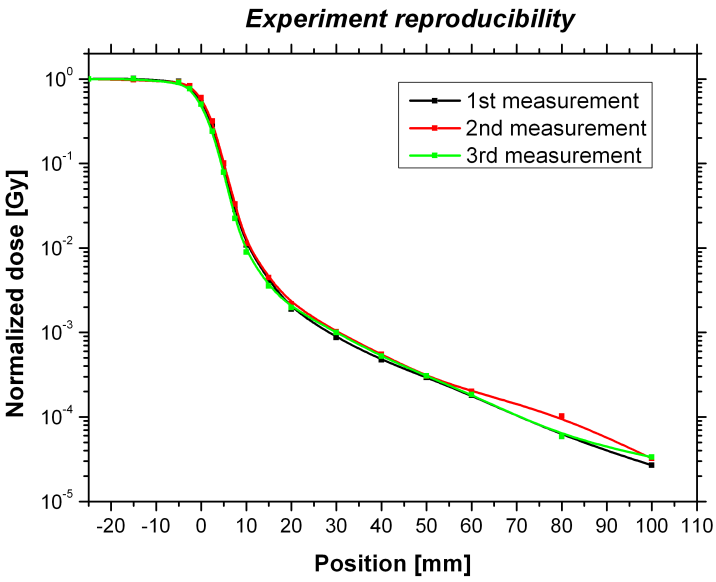

Figure 42: Lateral dose profile for a 5×5 cm^2 field of carbon ions measured at HIT with a diamond detector three times.

6.1 Photon irradiations at KGU

The main measurements were performed in the water depth of the dose maximum and the lateral dose profiles are normalized to 1 Gy in the field at the depth of maximum dose. As a first step the depth dose profiles were recorded with a diamond detector. The results are shown in Figs. 43-46. The distributions show an initial buildup of the dose until a maximum, after which the dose drops exponentially as expected. Higher photon energies show a more favorable depth dose deposition for use in radiotherapy, since the dose in the deeper parts is elevated. The position of the dose maximum was determined as 15 ±2 mm for the 6 MV beam, 31 ±2 mm for 18 MV and 35 ±2 mm for 25 MV. The corresponding lateral dose measurements were then collected at these depths.

The uncertainties in determining the dose maximum were caused by the measurement procedure. The irradiation was continuous and the electromotor moved the detector during the irradiation causing the formation of waves in the water and leading to uncertainties in the water depth.

For the larger fields a slightly slower dose fall-off with depth is observed. This behavior is likely explained by the increased number of photons that scatter in the field.

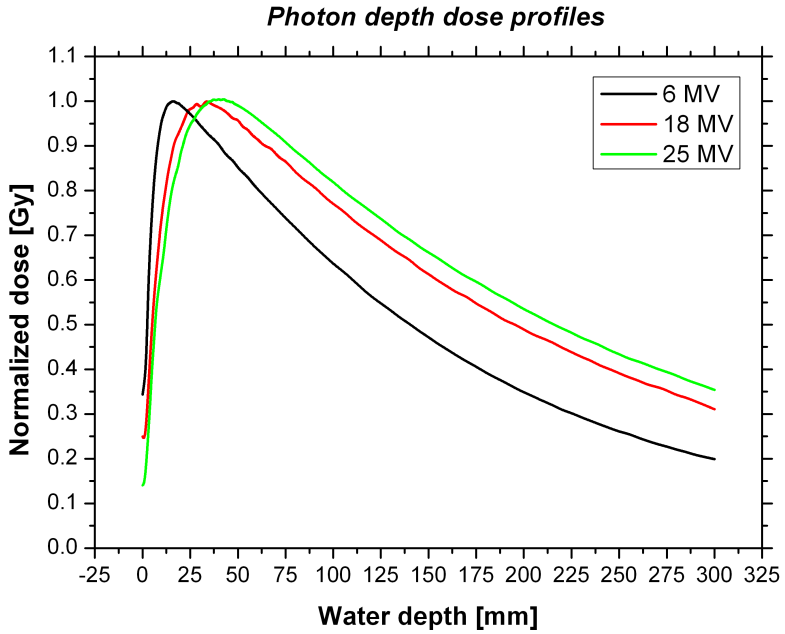

Figure 43: Depth dose profile in water measured at KGU with the diamond detector for a 5×5 cm^2 field using three different energies.

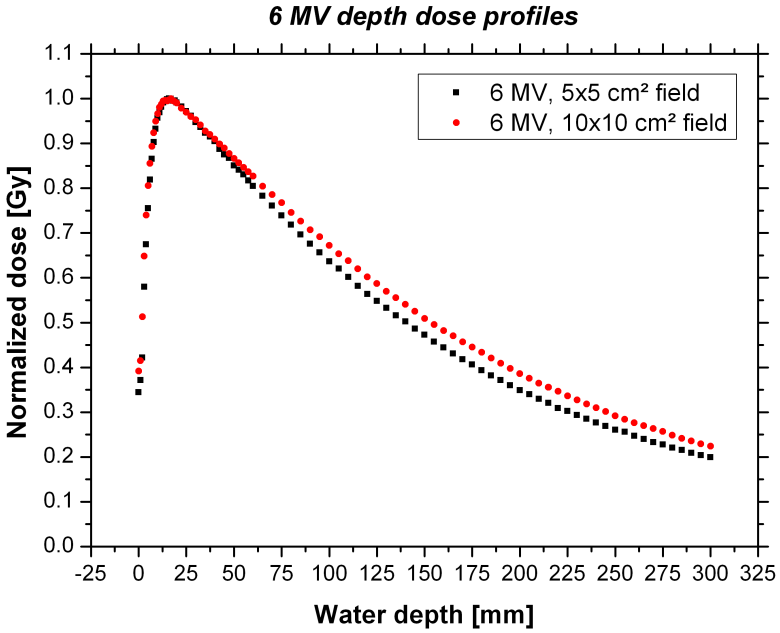

Figure 44: Depth dose profile in water measured at KGU with the diamond detector for a 6 MV photon field of size 5×5 and 10×10 cm^2.

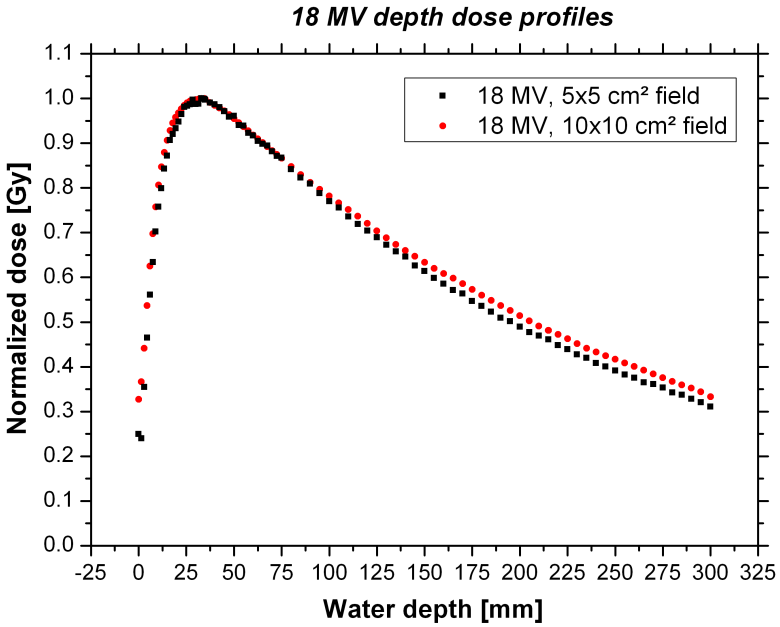

Figure 45: Depth dose profile in water measured at KGU with the diamond detector for a 18 MV photon field of size 5×5 and 10×10 cm^2.

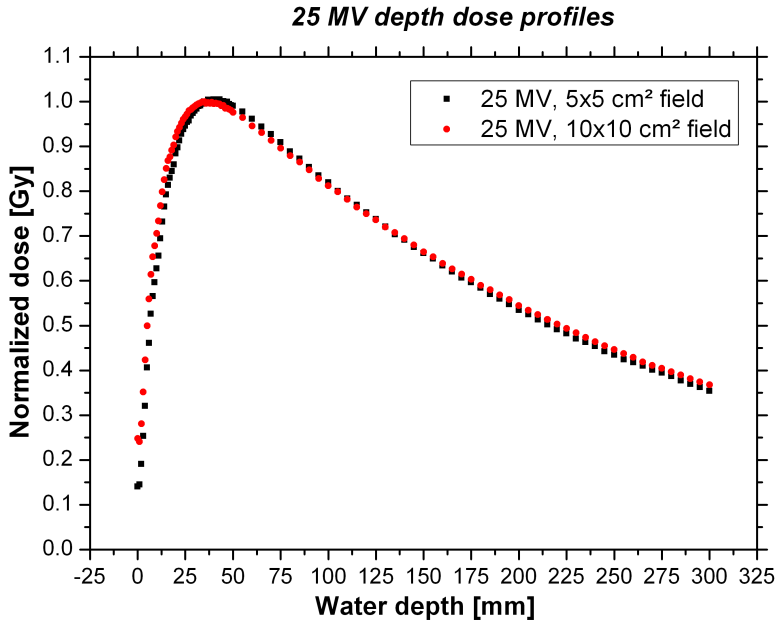

Figure 46: Depth dose profile in water measured at KGU with the diamond detector for a 25 MV photon field of size 5×5 and 10×10 cm^2.

Energy dependence

The out-of-field dose profiles for 6 MV, 18 MV and 25 MV are shown in the GT direction in Fig. 47 and in the AB direction in Fig. 48 for a 5×5 cm^2 field measured in the dose maximum. The data point raster is every 2-3 mm. The data are shown as solid lines connected with a spline interpolation for better visibility and to enable an easier comparison. The measurements with 6 and 25 MV were performed in 2009, whereas the data for 18 MV were collected in 2010 after modifications of the linac. Additionally, for the GT direction a measurement with 6 MV was performed in 2010 after the modification.

In the GT direction, a sharp dose drop is observed at around 200 mm from the isocenter. The reason for this behavior lies in the geometry of the accelerator head shown in Fig. 13 (section 2.1). The maximum field size that can be produced with the Elekta SL25 is 20×20 cm^2 and is limited by the opening in the primary collimator. Therefore, photons measured close to the field were produced in the bremsstrahlungstarget and leak through the MLC and secondary collimators. Photons contributing to the dose outside a 20×20 cm^2 field have the primary collimator as additional material along their path, which reduces the dose at these large distances.

For both directions, AB and GT, it appears that the penumbra of the field gets wider with higher photon energies, caused by an increased leakage for higher photon energies. However, at more than 200 mm away from the isocenter the 6 and 18 MV beam from 2010 deposit less dose than both 6 and 25 MV measured in 2009. This is probably caused by modifications of the accelerator geometry that apparently reduce the leakage at positions $>$ 200 mm.

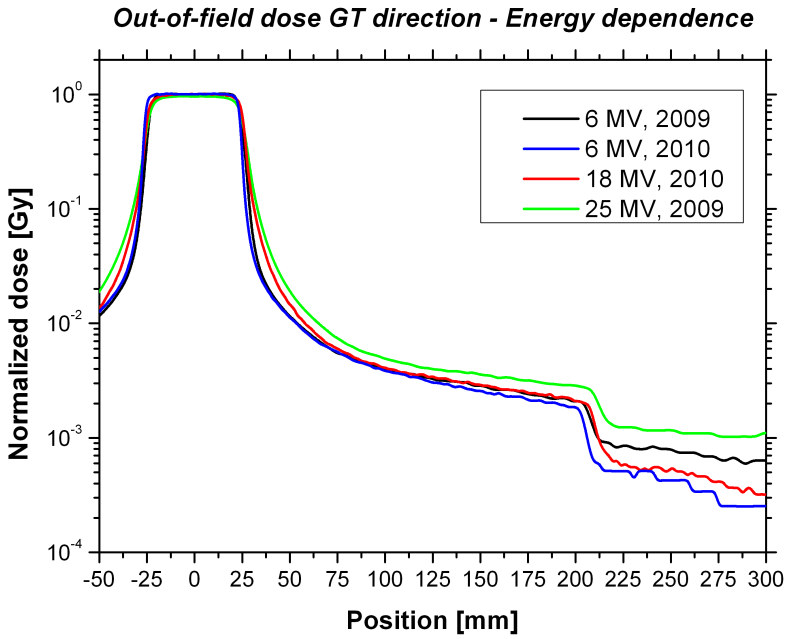

Figure 47: Lateral dose profile of a 5×5 cm^2 photon field measured at KGU in the GT direction for several accelerator energies in 2009 and 2010.

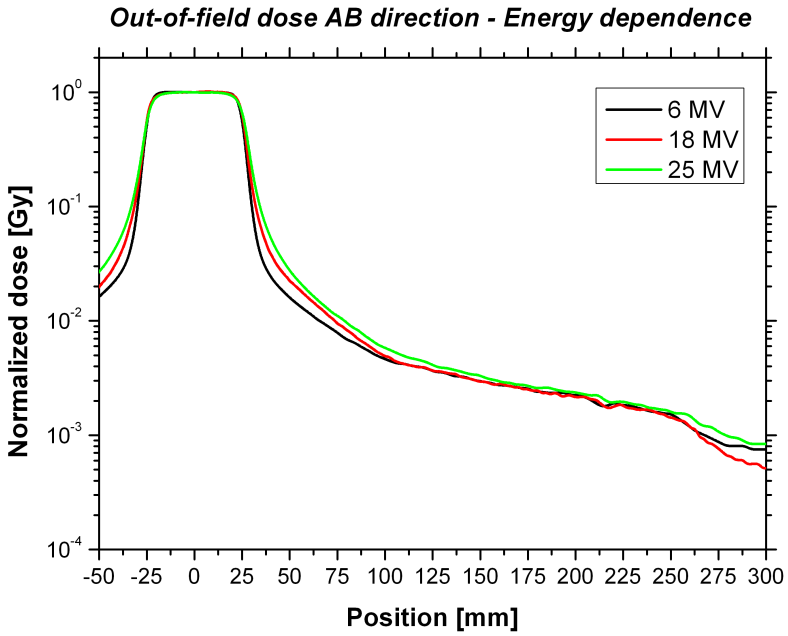

Figure 48: Lateral dose profile of a 5×5 cm^2 photon field measured at KGU in the AB direction for several accelerator energies.

Directional dependence

The out-of-field dose distribution for the Elekta SL25 is not uniform in all directions. A comparison of the profiles in both directions for a 5×5 cm^2 field delivered with 6,18 and 25 MV is shown in Fig. 49 to 51. The differences in the GT and AB direction are not negligible but very small. Therefore, the direction along which the patient is lying has little influence on the out-of-field dose caused by photons. The out-of-field dose in AB direction is generally a little higher than in the GT direction; the sharp drop at 200 mm is only seen in GT direction.

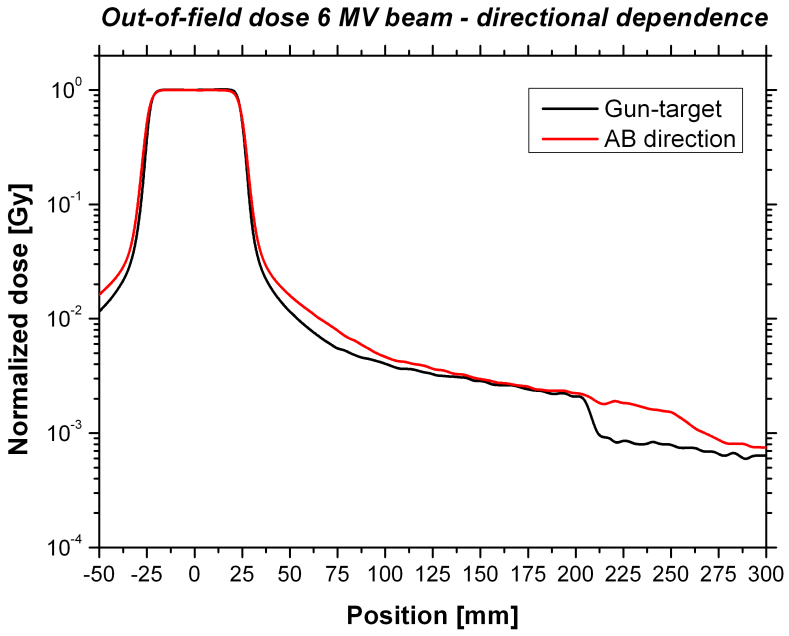

Figure 49: Comparison of the dose profile in the GT and AB direction for a 5×5 cm^2 6 MV photon beam at KGU measured with the diamond detector.

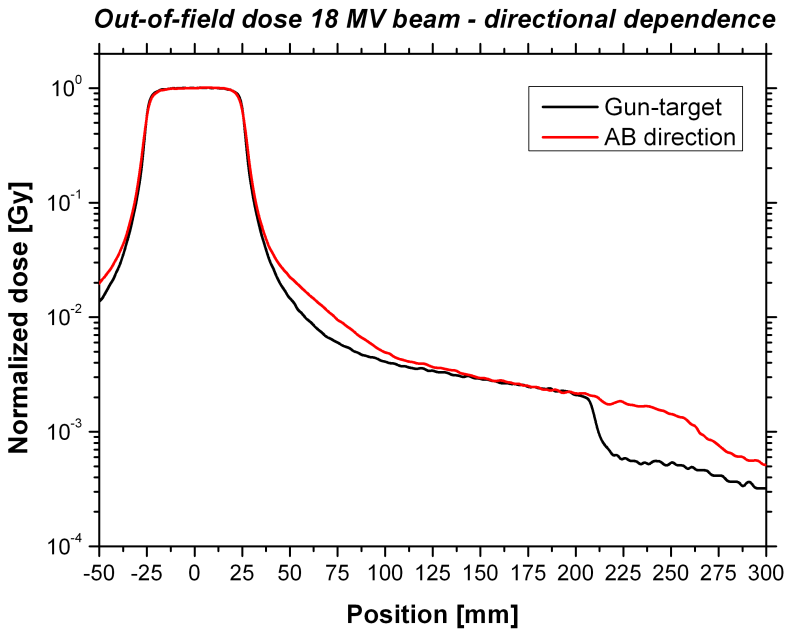

Figure 50: Comparison of the dose profile in the GT and AB direction for a 5×5 cm^2 18 MV photon beam at KGU measured with the diamond detector.

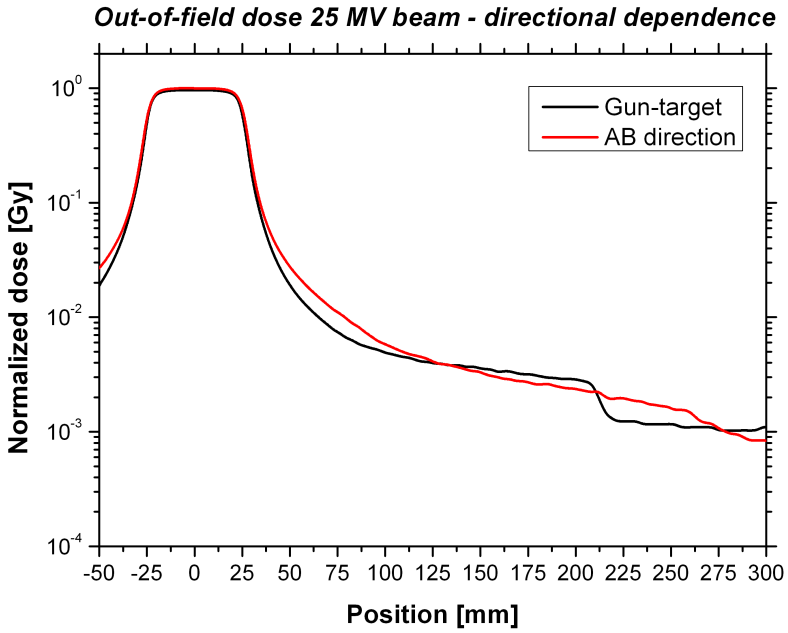

Figure 51: Comparison of the dose profile in the GT and AB direction for a 5×5 cm^2 25 MV photon beam at KGU measured with the diamond detector.

Field size dependence

The investigation conducted on the field size influence on the dose profile is shown in Fig. 52 to 57. For all energies and directions measured, an overall increase of the out-of-field dose with increasing field size can be observed. A higher number of photons are necessary to create larger fields and the increased scattering leads to larger out-of-field doses.

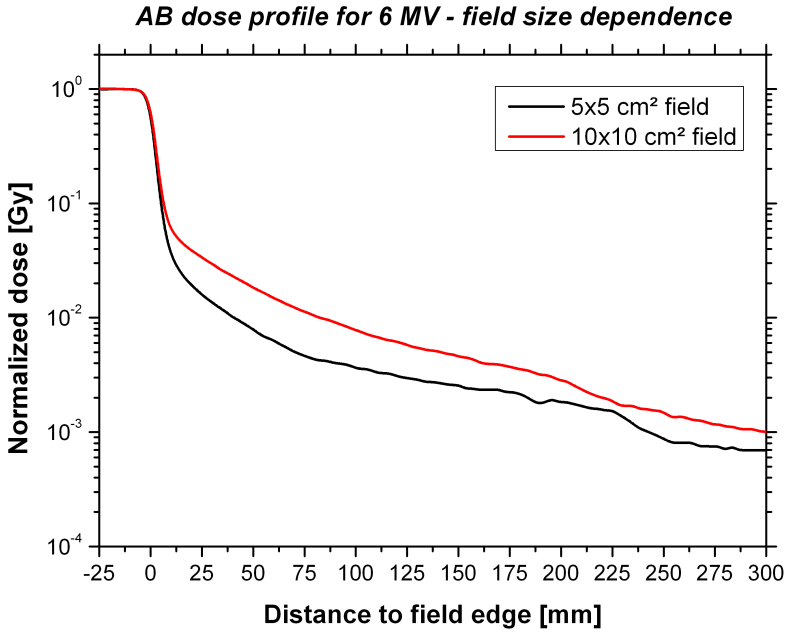

Figure 52: 5×5 and 10×10 cm^2 fields of 6 MV photons measured at KGU in AB direction with the diamond detector.

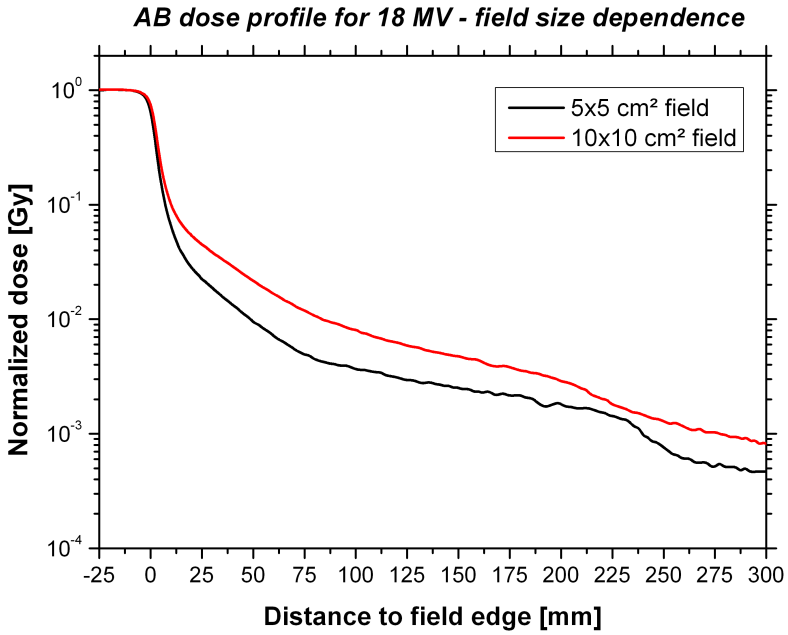

Figure 53: 5×5 and 10×10 cm^2 fields of 18 MV photons measured at KGU in AB direction with the diamond detector.

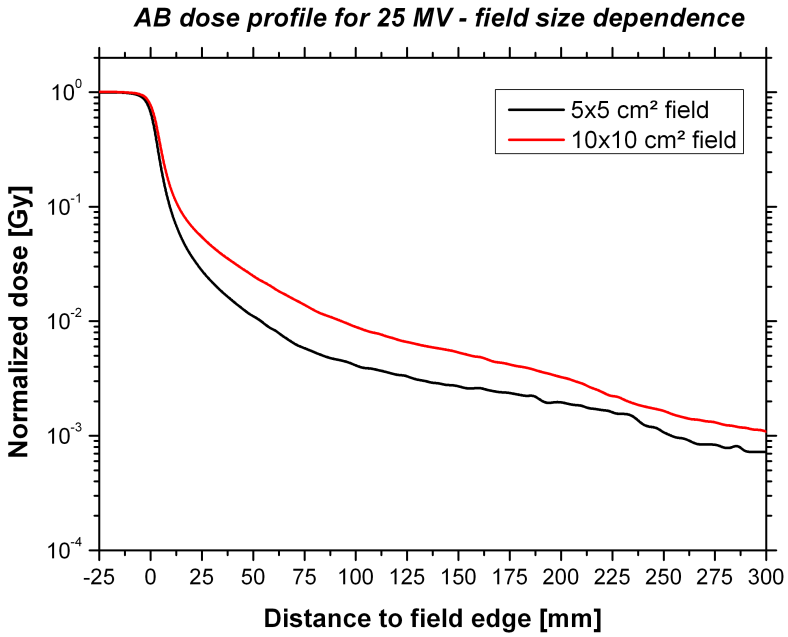

Figure 54: 5×5 and 10×10 cm^2 fields of 25 MV photons measured at KGU in AB direction with the diamond detector.

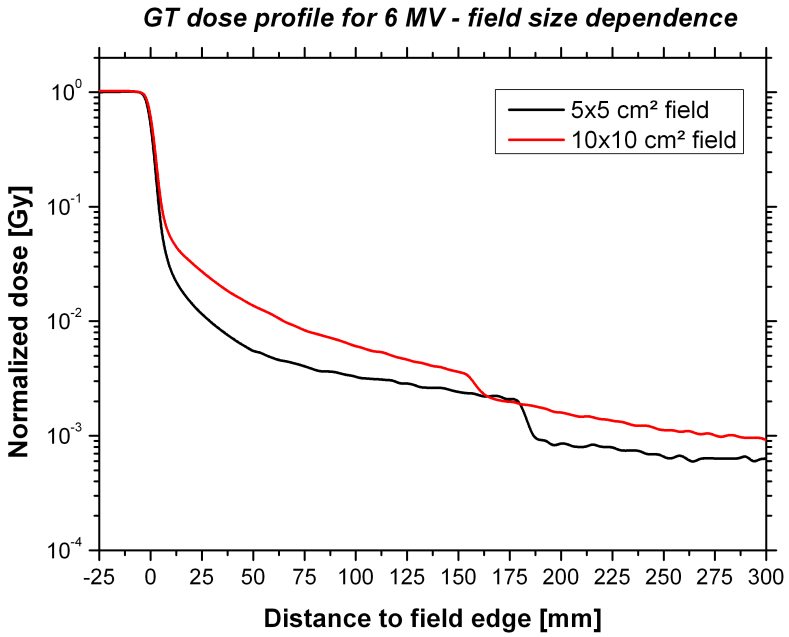

Figure 55: 5×5 and 10×10 cm^2 fields of 6 MV photons measured at KGU in GT direction with the diamond detector.

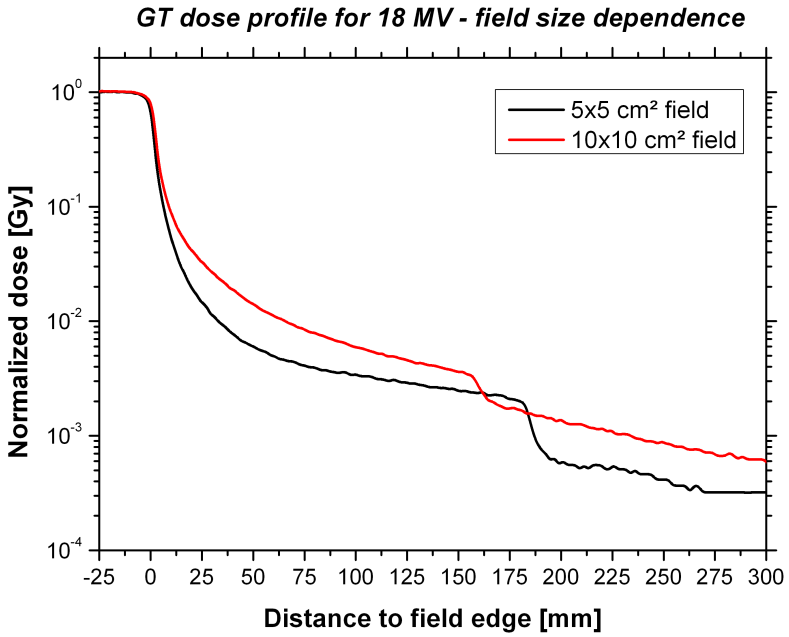

Figure 56: 5×5 and 10×10 cm^2 fields of 18 MV photons measured at KGU in GT direction with the diamond detector.

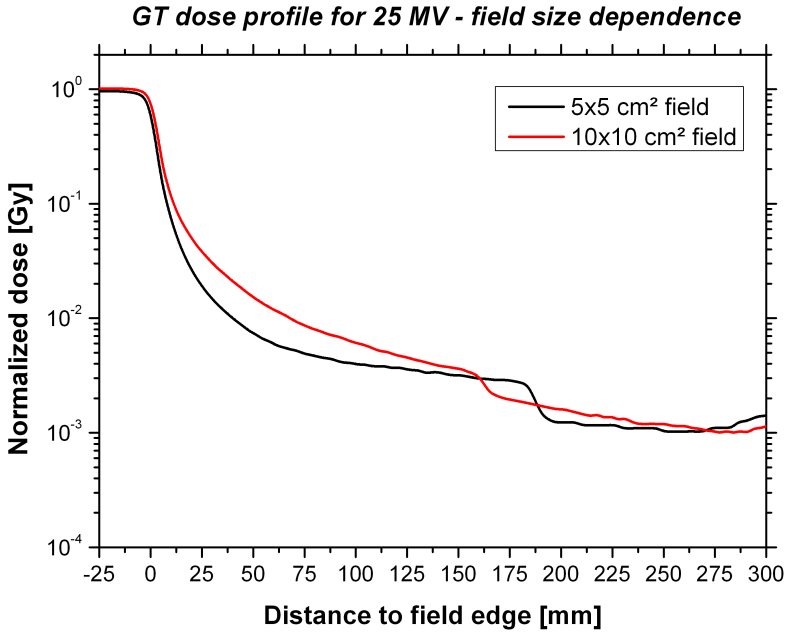

Figure 57: 5×5 and 10 × 10 cm^2 fields of 25 MV photons measured at KGU in GT direction with the diamond detector.

Depth dependence

The lateral dose distribution was measured in the dose maximum and at 10 cm water depth. In published works the out-of-field dose is often measured in a depth of 10 cm. Additionally, for comparison with the data from ion beams, the out-of-field dose was measured in a depth of 12.5 cm for the 18 MV beam. The results are shown in Fig. 58 to 63.

The larger penumbras at deeper depths are explained by the intercept theorem. In field, the dose drops with increasing depth as known from the depth dose profiles. However, only a small difference in the out-of-field dose can be observed for the different depths. In the GT direction, the dose drop caused by the primary collimator is shifted a little further away from the target, again because of the intercept theorem. No further significant changes in the out-of-field dose distribution can be observed in depths from the dose maximum to 10 cm.

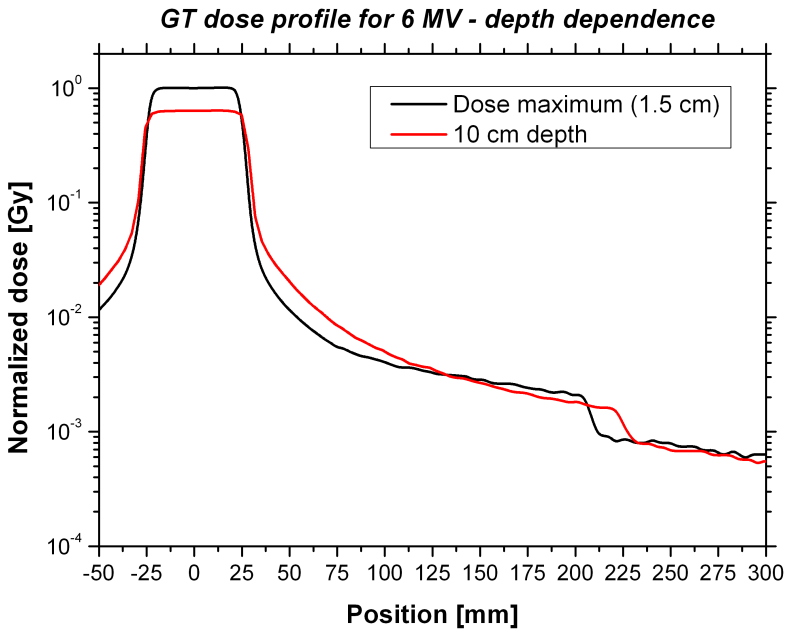

Figure 58: 5×5 cm^2 field of 6 MV photons measured with the diamond detector at KGU in the depth dose maximum and in 10 cm water depth in GT direction.

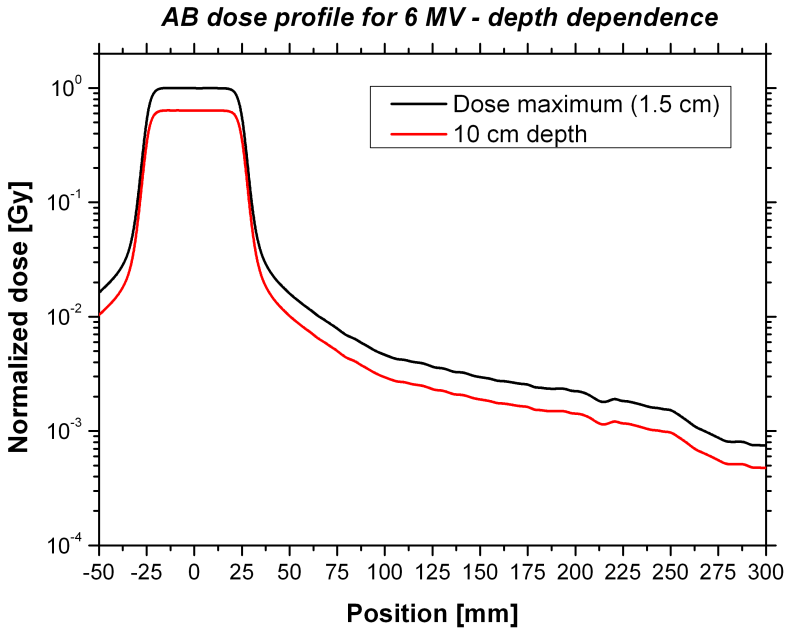

Figure 59: 5×5 cm^2 field of 6 MV photons measured with the diamond detector at KGU in the depth dose maximum and in 10 cm water depth in AB direction.

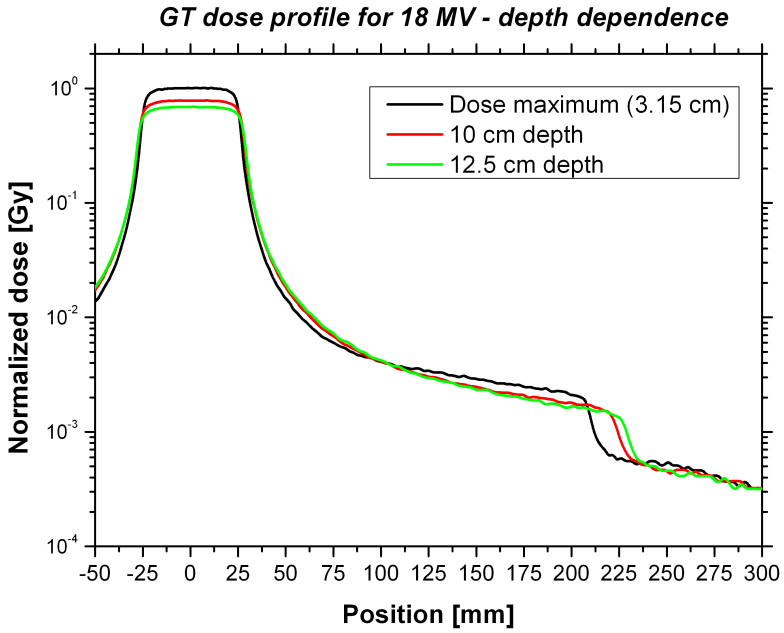

Figure 60: 5×5 cm^2 field of 18 MV photons measured with the diamond detector at KGU in the depth dose maximum, in 10 cm and 12.5 cm water depth in GT direction.

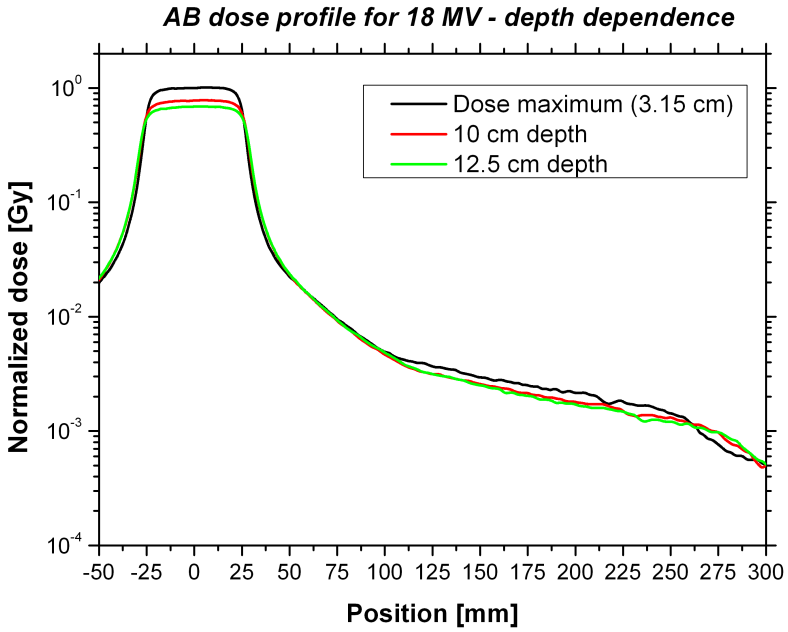

Figure 61: 5×5 cm^2 field of 18 MV photons measured with the diamond detector at KGU in the depth dose maximum, in 10 cm and 12.5 cm water depth in AB direction.

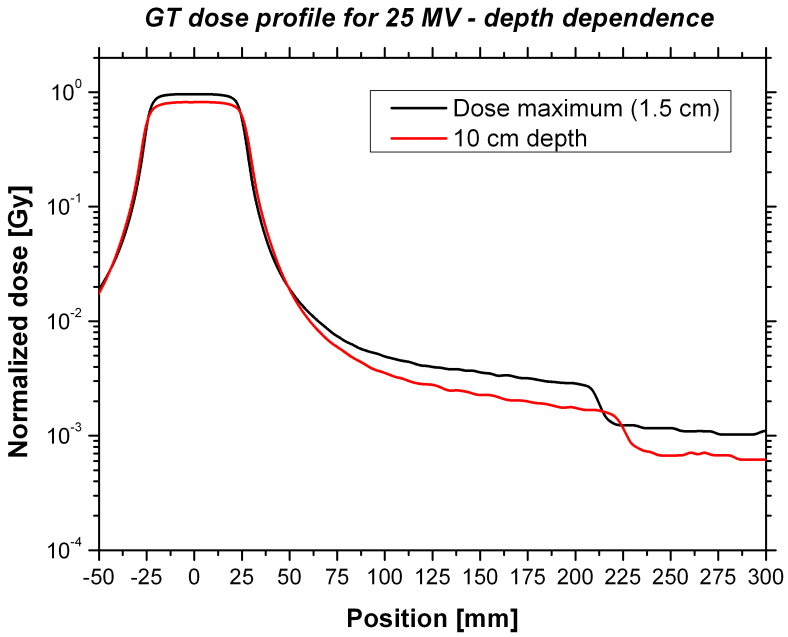

Figure 62: 5×5 cm^2 field of 25 MV photons measured with the diamond detector at KGU in the depth dose maximum and in 10 cm water depth in GT direction.

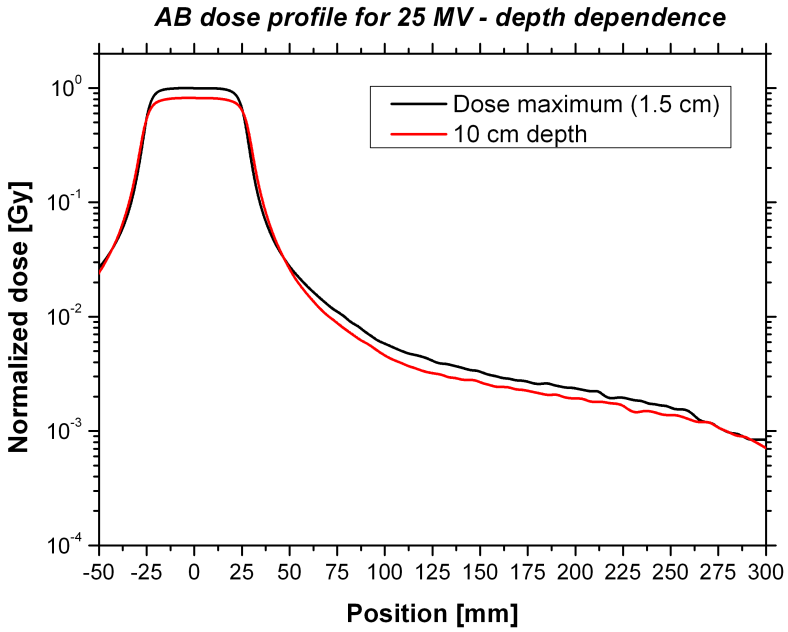

Figure 63: 5×5 cm^2 field of 25 MV photons measured with the diamond detector at KGU in the depth dose maximum and in 10 cm water depth in AB direction.

Thermoluminescence detectors

A comparison of the measurements with TLD 700 chips and the diamond detector is shown in Fig. 64. The TLD 700 chips are insensitive to neutrons and are calibrated to assess the absorbed dose. The results from the diamond detector and TLD 700 show an excellent agreement.
Fig. 65 and 66 show the thermoluminescence signal of the TLD 600 and the TLD 700 in the dose maximum and in 10 cm depth. The difference between both readouts can be used for a qualitative estimate of the abundance of low-energy neutrons but can not be directly converted to absorbed dose. It is significant only in the dose maximum, indicating that most of the low energy neutrons measured at a depth of 3.15 cm are absorbed before reaching a depth of 10 cm. The error bars represent the deviation of the signal measured by two detectors of same type.

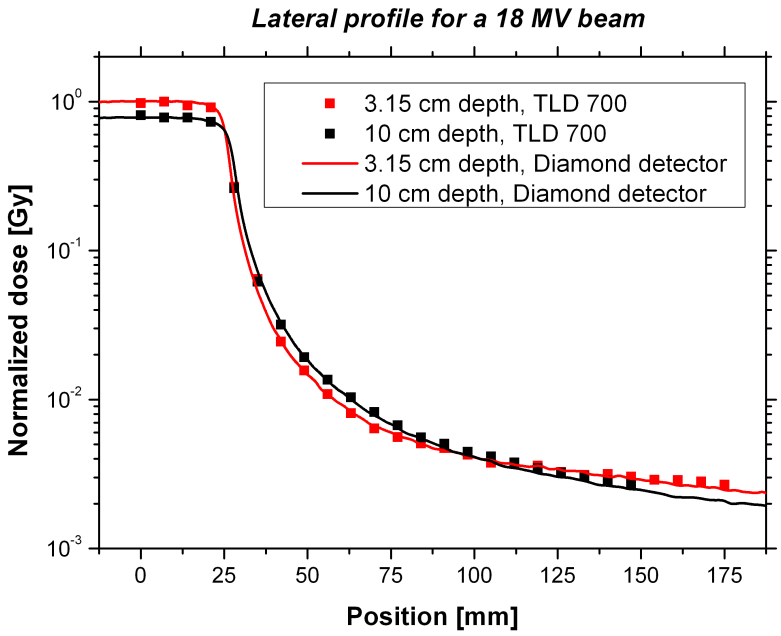

Figure 64: 5×5 cm^2 18 MV photon field measured with a diamond detector and TLD 700 at KGU in the depth dose maximum and in 10 cm water depth along the GT direction.

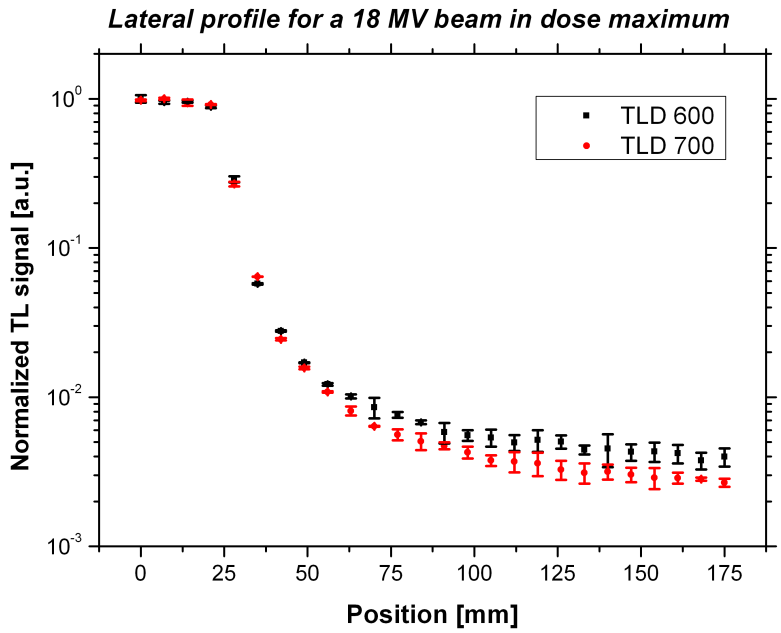

Figure 65: Thermoluminescence signal of TLD 600 and TLD 700 of a 5×5 cm^2 18 MV photon field measured at KGU in the depth dose maximum along the GT direction.

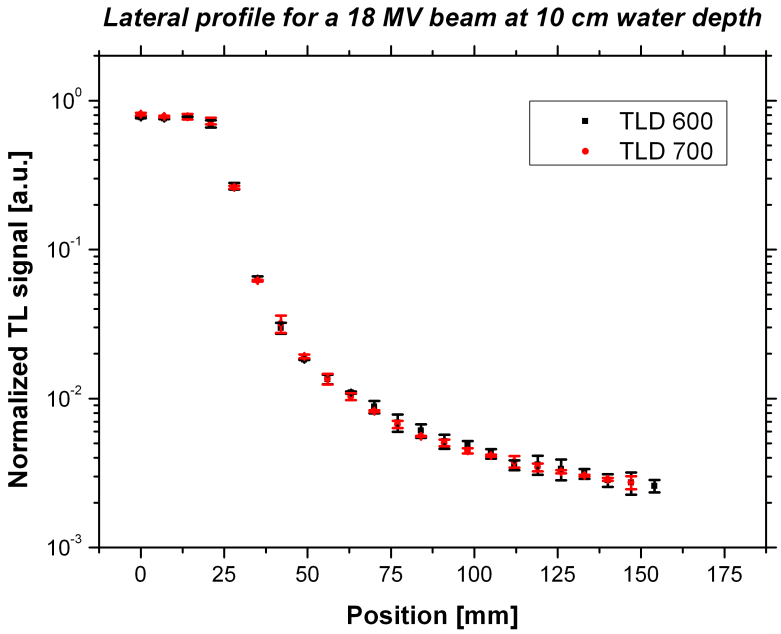

Figure 66: Thermoluminescence signal of TLD 600 and TLD 700 of a 5×5 cm^2 18 MV photon field measured at KGU in 10 cm depth along the GT direction.

Bubble detector results

This section shows the results collected after irradiation of the bubble detectors and unfolding with the BUNTO code. Bubbles were observed up to BDS2500 (with a threshold of 2.5 MeV), no bubbles were found in the BDS10000 detectors (threshold 10 MeV). However, when the BDS10000 were irradiated without prior cooling, bubbles could be seen in the detector confirming the influence of the temperature on the threshold.
The neutron fluence and energy spectrum measured directly on the water surface with increasing distance to the field along the GT direction is shown in Fig. 67. The water phantom was irradiated with a 5×5 cm^2 field and the results are normalized to monitor units.
A distinct peak at 1 MeV can be observed for all measurements outside the primary field. The shape and amplitude of the spectrum changes only slightly with increasing lateral distance. The peak in-field is shifted towards a higher neutron energy of 2 MeV.
The measurements confirmed the results from literature as well as theoretical considerations. The neutron spectrum is produced by two sources: nucleus evaporation and a direct reaction. The former shows a peak of approximately 1 MeV whereas the latter is shifted towards higher energies (Ongaro et al., 2000). Direct neutrons are mainly produced in forward direction, while neutrons coming from evaporation are emitted isotropically from the point of production. The geometrical behavior of the two components explains why the higher neutron energy peak can only be observed in-field. The isotropic emission of the evaporated neutrons leads only to small changes in the neutron fluence at different positions out-of-field.
The uncertainties on the bubble measurements are in the order of 20% and become rather large especially in the low energy region. Only one detector (the BDS10) is sensitive to neutrons in the region from 10 keV up to 100 keV. Large uncertainties in the unfolding arise therefore in this region. At higher neutron energies, several detectors contribute to the spectral unfolding improving the reliability of results in the high-energy region.
Fig. 68 shows the measurements at a water depth of 10 cm, where no data were collected in the field. Again, no significant difference can be observed with increasing distance to the field edge. As observed at the surface, the spectrum peaks at around 1 MeV but the absolute number of neutrons is much lower. The comparison of results for both water depths is shown in Fig. 69. The total fluences per MU are given in Table 5. Using kerma-factors for water, the absorbed dose has been calculated and the dose has been averaged over the detector and converted into equivalent dose per treatment Gray with weighting factors from (ICRP103, 2008). An ideal treatment of 100 MU = 1 treatment Gray has been assumed for this calculation. In a realistic case, a significantly higher amount of MUs will be necessary for completing a treatment.
A comparison of the absorbed dose measured by the diamond detector, the absorbed dose determined by the bubble detectors and the corresponding equivalent dose at a water depth of 10 cm is shown in Fig. 70. Photons measured by the diamond detector show a sharp dose fall-off,

Table 5: Overview of the total neutron fluence, absorbed dose and equivalent dose measured with the diamond detector for a 5×5 cm^2 field of 18 MV photons.

Position	Φ on surface [n/cm^2 per MU]	D on surface [Gy per MU]	$H_{T,R}$ on surface [mSv/treatment Gy]
in field	1.24E+05	4.77E-06	5.60
30 mm	4.30E+04	9.80E-07	1.88
80 mm	4.54E+04	9.42E-07	1.76
130 mm	3.97E+04	9.23E-07	1.85
180 mm	4.33E+04	9.17E-07	1.75
230 mm	4.03E+04	8.73E-07	1.67
280 mm	3.51E+04	8.38E-07	1.61
Position	Φ in 10 cm water [n/cm^2 per MU]	D in 10 cm water [Gy per MU]	$H_{T,R}$ in 10 cm water [mSv/treatment Gy]
30 mm	2.99E+03	7.19E-08	0.12
80 mm	3.04E+03	6.50E-08	0.11
130 mm	3.36E+03	6.35E-08	0.12
180 mm	2.48E+03	6.04E-08	0.11
230 mm	2.36E+03	5.45E-08	0.10
280 mm	2.45E+03	5.26E-08	0.09

whereas both the absorbed and equivalent dose from neutrons stay constant with increasing distance to the field. The equivalent dose from neutrons is lower than the dose delivered by photons for all positions measured at this depth. In table 5 it was shown that the dose from neutrons on the surface is higher, therefore, to determine the dose deposition by neutrons in a patient when irradiated with high energetic photons, an experiment or Monte Carlo simulation should be designed to track the neutron interactions.

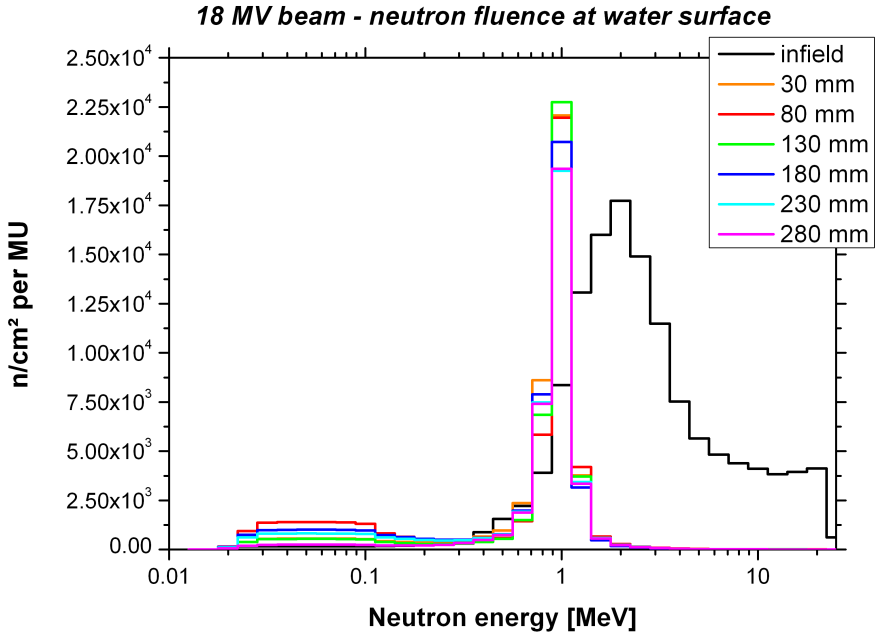

Figure 67: Neutron fluence per energy interval measured with bubble detectors on the water surface for a 5×5 cm^2 field of 18 MV photons with increasing distance to the field in GT direction.

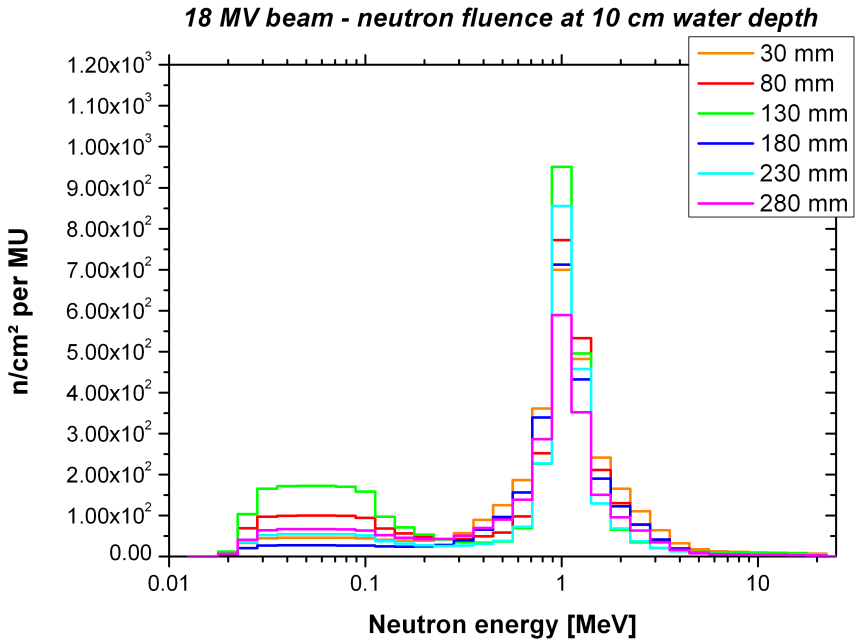

Figure 68: Neutron fluence per energy interval measured with bubble detectors at a water depth of 10 cm for a 5×5 cm^2 field of 18 MV photons with increasing distance to the field in GT direction.

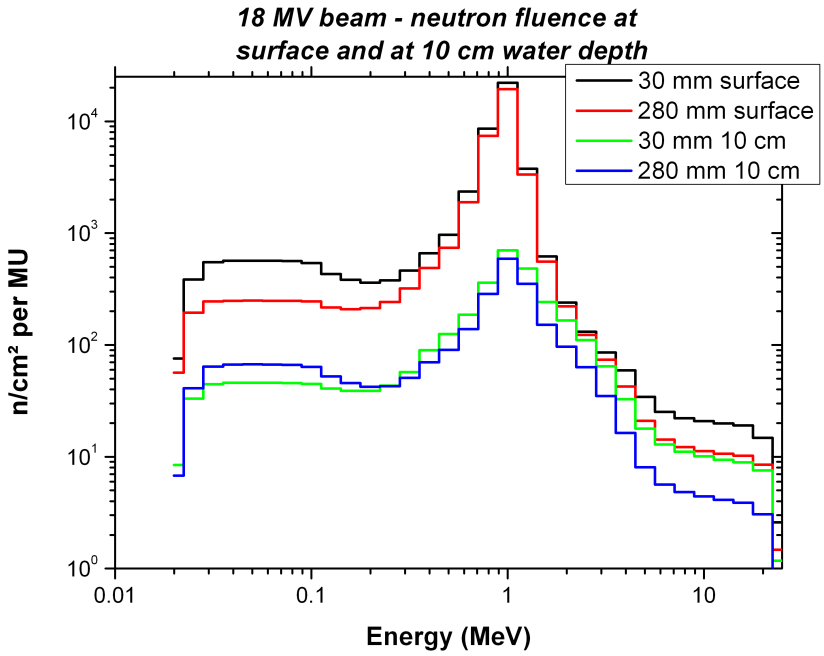

Figure 69: Neutron fluence per energy interval measured with bubble detectors at the surface and at a water depth of 10 cm for a 5×5 cm^2 field of 18 MV photons.

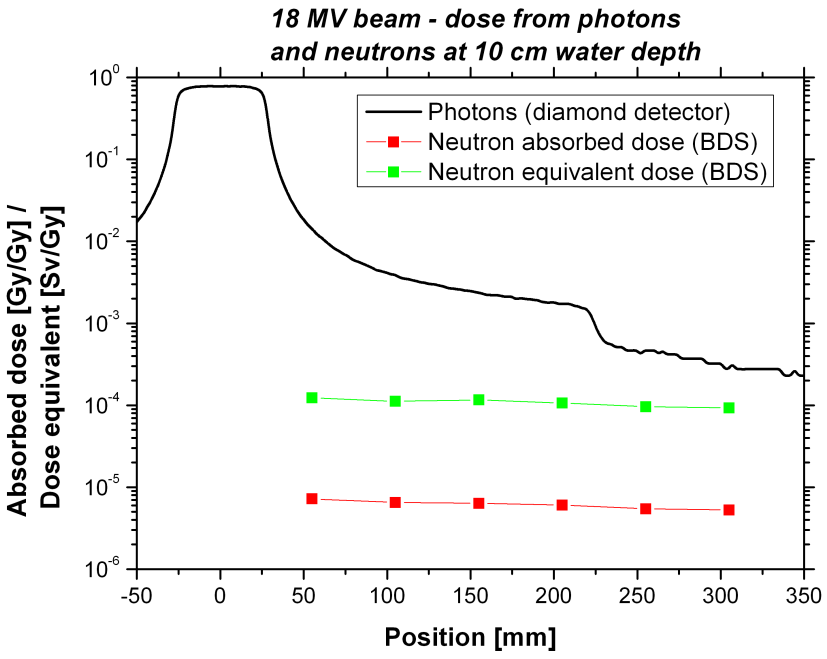

Figure 70: Absorbed and equivalent dose from photons (diamond detector) and neutrons (bubble detector) for a field of 5×5 cm^2 18 MV photons at KGU at a water depth of 10 cm normalized to 1 Gy in the dose maximum.

Comparison with literature

The photon experiments are compared with the review by (Xu et al., 2008), which summarizes data from several decades of dosimetry studies. Figure 2 of the review shows a comparison of the photon and neutron equivalent dose measured for an 18 MV beam by different groups. In all experiments, the dose for a 10×10 cm^2 field at a depth of 10 cm in a slab phantom was evaluated without specifying the direction of the measurement. When comparing the results with the present work, a reasonable agreement is observed even if the experimental setup chosen in this work consists of a water phantom irradiated with a 5×5 cm^2 field.

At a distance of 10 cm to the field edge the review reports dose values in the range of 5 to 9 mGy per treatment Gy and a high dependency on the machine; a value of 3 mGy was observed in this study. The difference is due to the smaller field; as observed in the comparison of field sizes in the dose maximum, the dose at this position increases up to a factor 2 for the 10×10 cm^2 field. At 20 cm doses between 1 to 3 mGy are shown in the review while a value of 0.9 mGy was measured in this investigation.

The neutron dose is compared with the literature data from several authors (Table 6). In the paper by (Ongaro et al., 2000) a surface neutron equivalent dose from 1 to 5 mSv/Gy is reported depending on the position and accelerator type; the measurements were completed with bubble detector spectrometers. The group of (Howell et al., 2009) used a Bonner-sphere system to evaluate the neutron dose at a distance of 40 cm from the isocenter. An equivalent dose of 0.84 mSv/Gy was found for an Elekta machine; moreover, the dose was clearly found to be highly dependent on the machine type. Despite the differences in the experimental procedures, the agreement with this study is satisfactory. The neutron contribution to the equivalent dose measured in this work was observed to be between 5.6 and 1.6 mSv/Gy, depending on the position (Fig. 71). The increase of the equivalent dose compared to (Howell et al., 2009) even though a lower total neutron fluence was found can be explained by the fact that the spectrum in this work peaks at an energy where the weighting factors are higher.

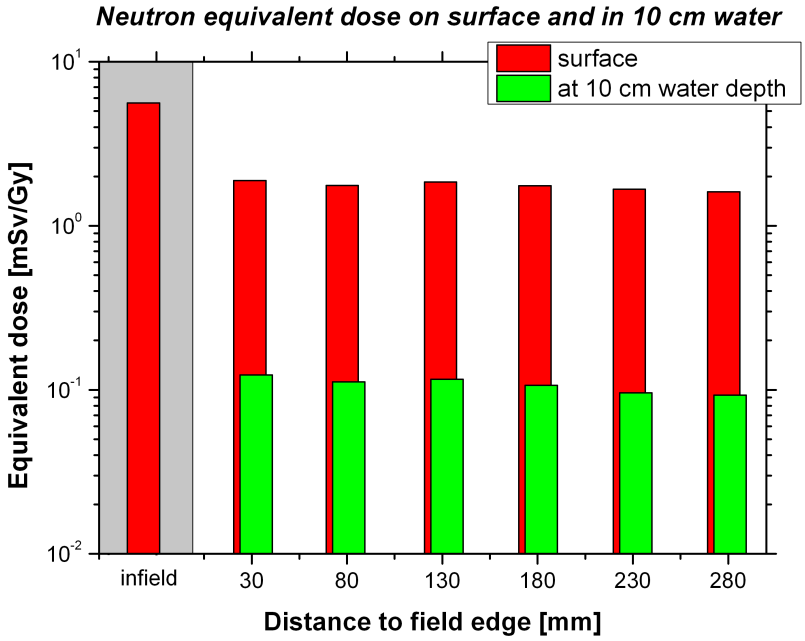

Figure 71: Equivalent dose from neutrons (bubble detector) for a field of 5×5 cm^2 18 MV photons at KGU measured on the surface and at a water depth of 10 cm. No data were collected in-field at a water depth of 10 cm.

Table 6: Comparison of the out-of-field neutron fluence and equivalent dose in-field and out-of-field obtained in this work and in literature.

	Linac-type	Field size	n-fluence out-of-field [n/cm^2 MU^{-1}]	$H_{T,R}$ in-field [mSv/Gy]	$H_{T,R}$ out-of-field [mSv/Gy]
This work	Elekta SL25 18 MV	5×5	3.73E+04 (33 cm to isoc.)	5.6	1.8
(Ongaro et al., 2000)	Elekta SL20i 20 MV	10×10	- (20 cm to isoc.)	4.7	2.6
(Howell et al., 2009)	Elekta Precise 18 MV	jaws closed	4.02E+04 (40 cm to isoc.)	-	0.8

Field-size-effect

The experiments were performed at TSL in April and October 2010. While the first set of measurements investigated the dose far away from the field, the second focused on a detailed characterization of the dose near the field edge. In the former experiment the irradiations were performed with 5×5 cm^2 and 2×2 cm^2 fields without a range modulator. Fig. 72 shows the lateral dose profiles measured with a diamond detector. Within 5 cm distance to the edge, the dose drops by four orders of magnitude. The presence of the collimator directly in front of the water phantom produces a very sharp penumbra of the proton beam. After the initial sharp drop, the dose decreases only very slightly with increasing distance to the field up to 30 cm. The out-of-field dose in this region arises from scattered primary particles and secondary neutrons produced in the beamline and in the water. The data for both field sizes agree within the error bars, thus there is no clear evidence for a field size effect at this beamline. However, a detailed experiment on the neutron yield may provide further insight.
The data collected in October are reported in Fig. 73. In this case the experiment was performed with a range modulator that produces a SOBP of 2 cm. The graph shows an improved spatial resolution close to the field edge. Also with this setup, the dose profile drops almost four orders of magnitude within 5 cm from the field edge and then decreases slowly by a further order of magnitude at 30 cm distance. The difference between the measurements with and without a range modulator is small and within the errors.

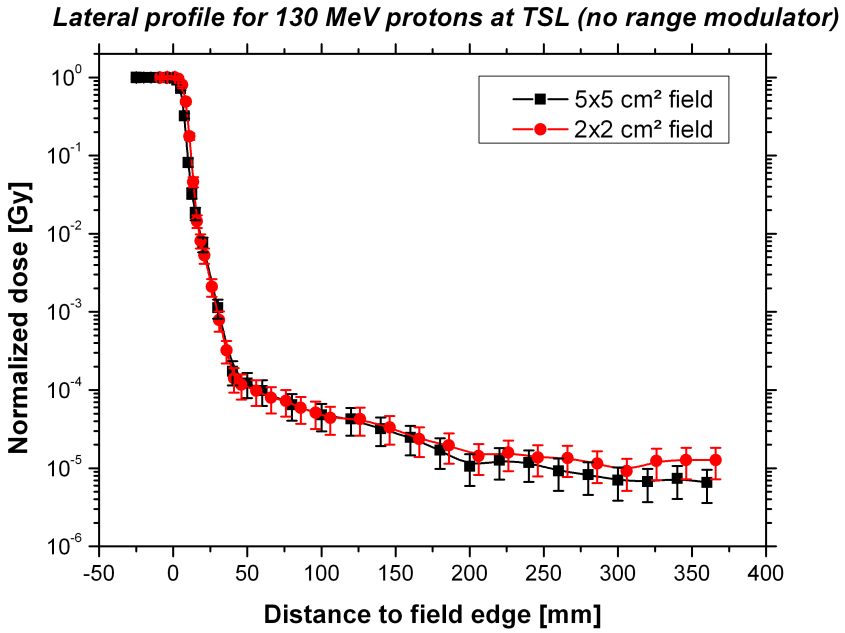

Figure 72: Lateral dose profile for 5×5 and 2×2 cm^2 fields of passively modulated 130 MeV protons beam without a range modulator measured at TSL with the diamond detector.

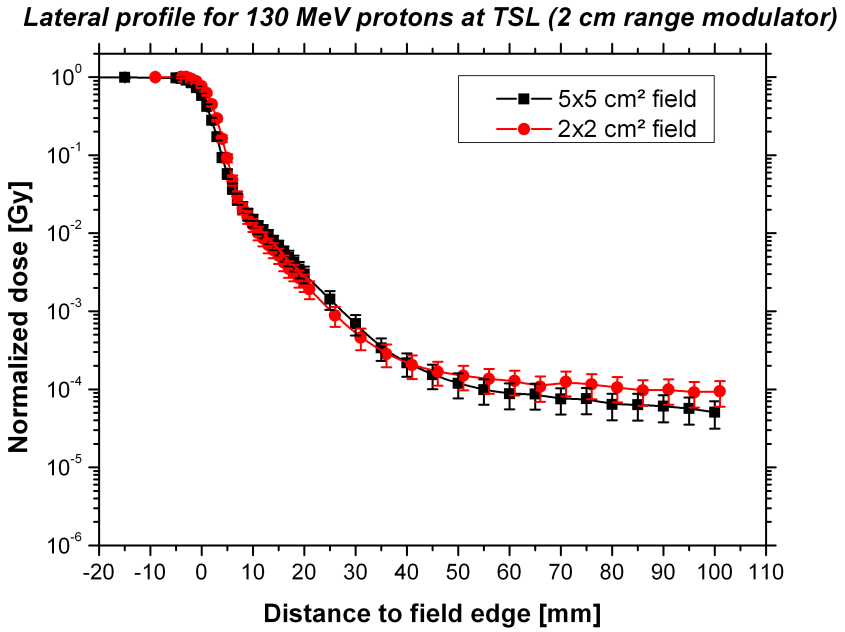

Figure 73: Lateral dose profile for 5×5 and 2×2 cm^2 fields of passively modulated 130 MeV protons beam with a 2 cm range modulator measured at TSL with the diamond detector.

Three-dimensional target

In October 2010 a further experiment was performed at TSL for the irradiation of the water phantom with a three-dimensional target volume. A target size of $5 \times 2 \times 5$ cm^3 was irradiated with a 5×2 cm^2 collimator and a 5 cm range modulator. Lateral dose profiles were acquired in the center of the SOBP as well as in the plateau and in the tail, located 15 mm in front and behind the target edge respectively (Fig. 74).

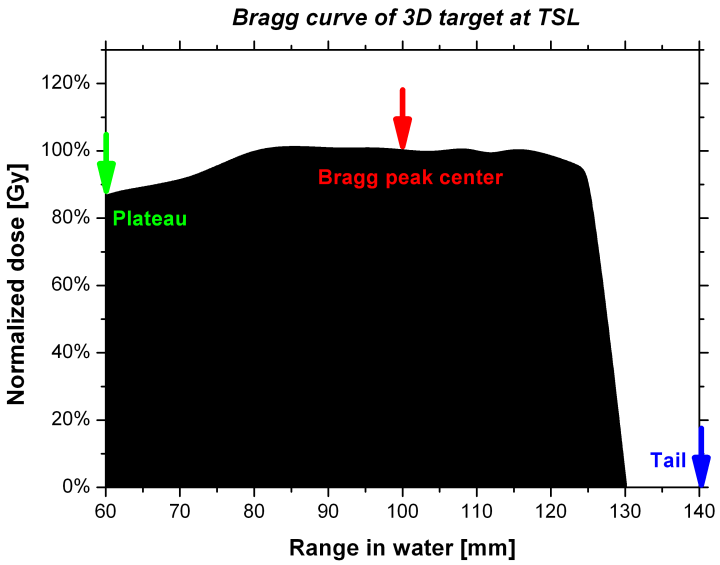

Figure 74: Depth dose curve for the three-dimensional target. The positions where lateral dose profile were measured are indicated with arrows.

The comparison of the data taken at different positions is shown in Figs. 75 and 76. The direction of the detector movement in beam's eye view is indicated in the Figure. As expected, the dose in the tail is much lower than in the Bragg peak. In all depths the lateral dose profile peaks in the field. The difference in the lateral dose profiles of the plateau and the Bragg peak region is small. An interesting increase of the dose can be observed in the plateau region at 10 cm distance from the field corresponding to the edge of the collimator. It appears that some primary particles scatter and travel outside the collimator depositing additional dose in positions not covered by the collimator. This increase is not seen in Bragg peak depth anymore.
The comparison of the 2D field without the range modulator and the 3D target (Fig. 77) shows that both fields are characerterized by a similar penumbra. At larger distances to the field edge, the dose increases when irradiating a three dimensional target. This is likely due to the larger amount of primary particles necessary to irradiate the threedimensional volume homogeneously. However, the difference is below 10^{-3} compared to the dose measured in the target.
The comparison of the lateral dose profiles corresponding to the right and up direction of the 3D target (Fig. 77) shows no significant differences.

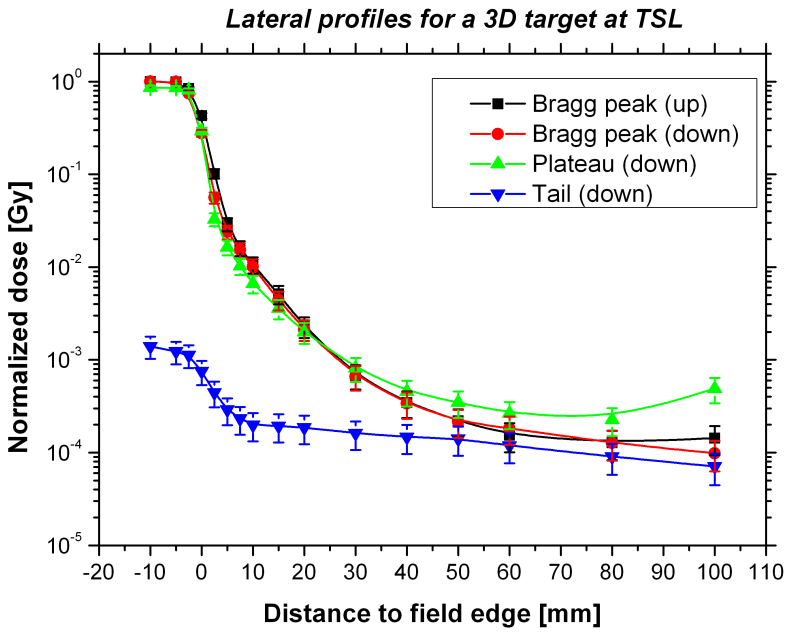

Figure 75: Lateral dose profile measured with the diamond detector at different depths for a three-dimensional target shaped by 130 MeV passively delivered protons. Indicated directions are in beam's eye view.

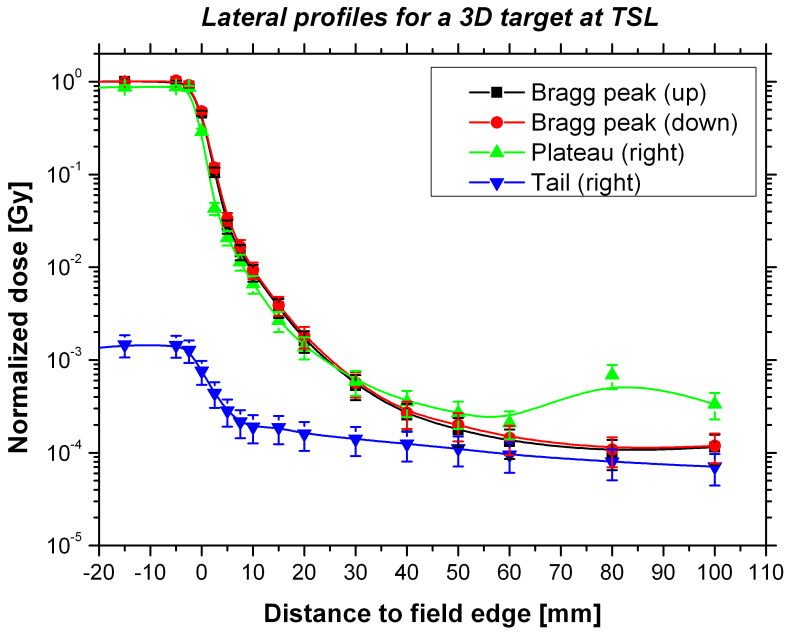

Figure 76: Lateral dose profile measured with the diamond detector at different depths for a three-dimensional target shaped by 130 MeV passively delivered protons. Indicated directions are in beam's eye view.

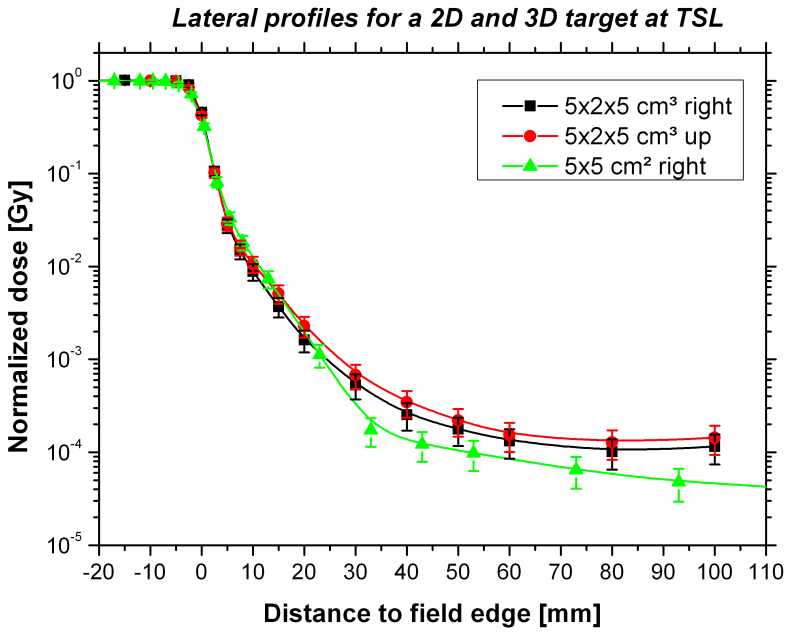

Figure 77: Lateral dose profile measured with the diamond detector for a three-dimensional and a two-dimensional target shaped by 130 MeV passively delivered protons. Indicated directions are in beam's eye view.

Results from TLD 600 and TLD 700

The results of the TLD irradiation are shown in Figs. 78 and 79. The first graph shows the data obtained with the TLD 700 and the diamond detector. The agreement is reasonable but not as perfect as for photons Fig. 64. The difference between both is attributed to positioning uncertainties caused by the lack of a laser alignment system at TSL.

In order to study the influence of slow neutrons on the out-of-field dose, the TLD 600 were used in combination with the TLD 700. The comparison of TLD 600 and TLD 700 in Fig. 79 shows a high increase of the thermoluminescence signal of TLD 600 at larger distances. This trend indicates a high production of low-energy neutrons, but the difference of both signals cannot be directly converted to a dose. The comparison of readings from TLD 600 and TLD 700 is for qualitative purposes and indicates that many high energy neutrons are produced in the beamline and then are moderated in water where they can be measured as thermal neutrons.

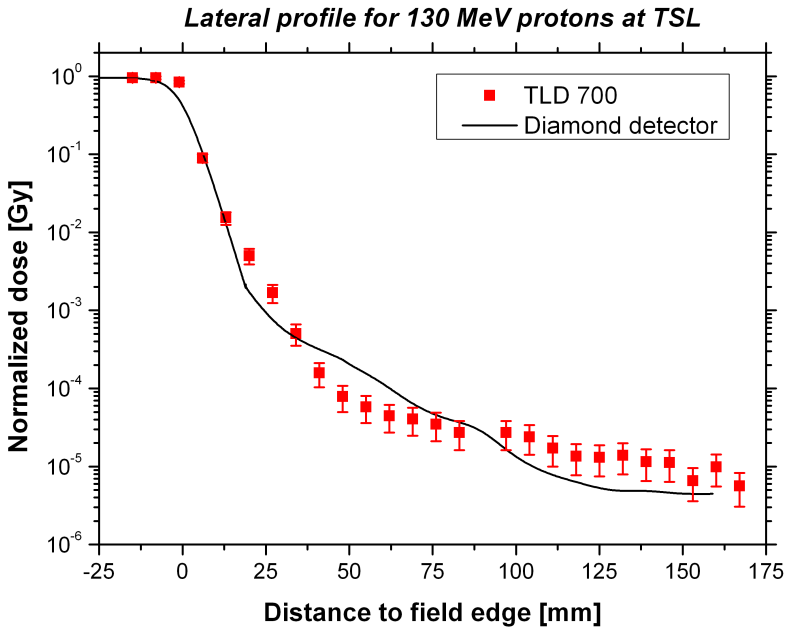

Figure 78: Lateral dose profile in the Bragg peak for a 5×5 cm^2 field of 130 MeV passively modulated protons measured with a diamond detector and with TLD 700.

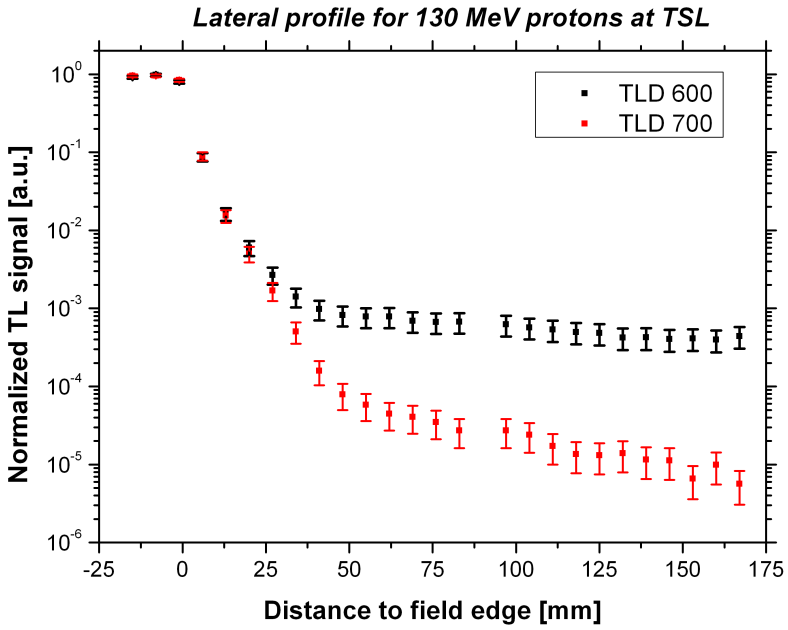

Figure 79: Thermoluminescence signal in the Bragg peak for a 5×5 cm^2 field of 130 MeV passively modulated protons measured with TLD 600 and TLD 700 showing the influence of slow neutrons at large distances.

Field-size-effect

The effect of the field size on the out-of-field dose measured at PSI is shown in Fig. 80. The initial dose drop is similar to the profile measured at TSL for both field sizes of 5×5 and 10×10 cm^2. At a distance of approximately 8 cm to the field edge the dose is significantly higher for the larger field size, the difference being larger than the errors. The result is not surprising, since a higher number of primary particles is necessary to produce a homogeneous field of bigger size leading to a higher amount of scattered protons. Note that for passive modulation, a change of the field size is achieved by adjusting the collimator, not the number of primary particles, whereas the scanning technique adjusts the number of primary particles according to the amount of spots irradiated.
Overall, the dose far out-of-field drops lower than for a passively modulated case at TSL, decreasing 6 orders of magnitude for a distance of 15 cm to the target edge for the 5×5 cm^2 field.

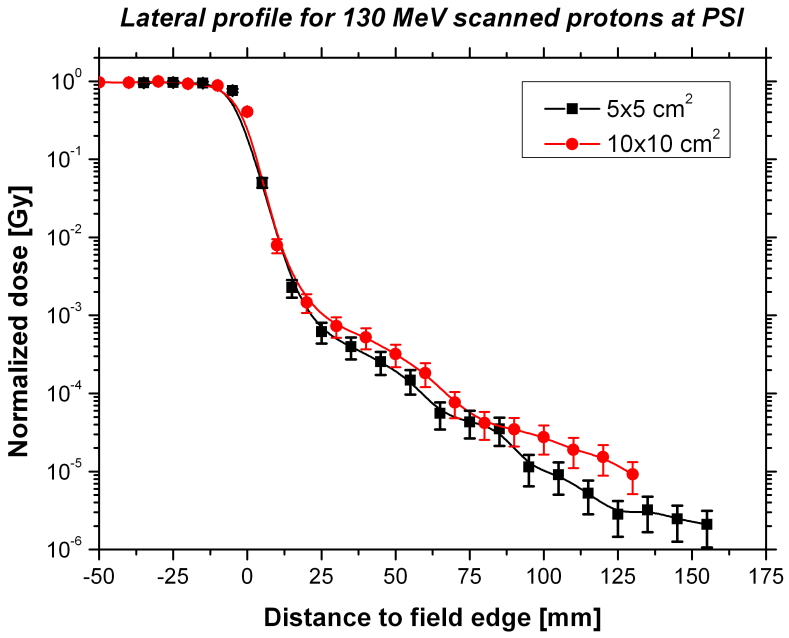

Figure 80: Lateral dose profile for a 5×5 and 10 × 10 cm^2 field measured with the diamond detector for 130 MeV scanned protons at Gantry 2, PSI.

Results from the TLD 600 and TLD 700 irradiation

The results from the TLD 700 are compared to the diamond detector data in Fig. 81. The agreement is very good within the errors of the measurement. The TLDs in-field were slightly saturated resulting in a supralinear response.
The slow-neutron yield is shown in Fig. 82. The comparison of TLD 700 and TLD 600 shows only a slightly higher thermoluminescence response for the latter in TLD 600 far away from the field. The comparison with the TLD 600 data measured for passively modulated protons in Fig. 79 shows that the TLD 600 in the scanning system collect a TL signal about two orders of magnitude lower, indicating a much lower neutron production for scanning systems.

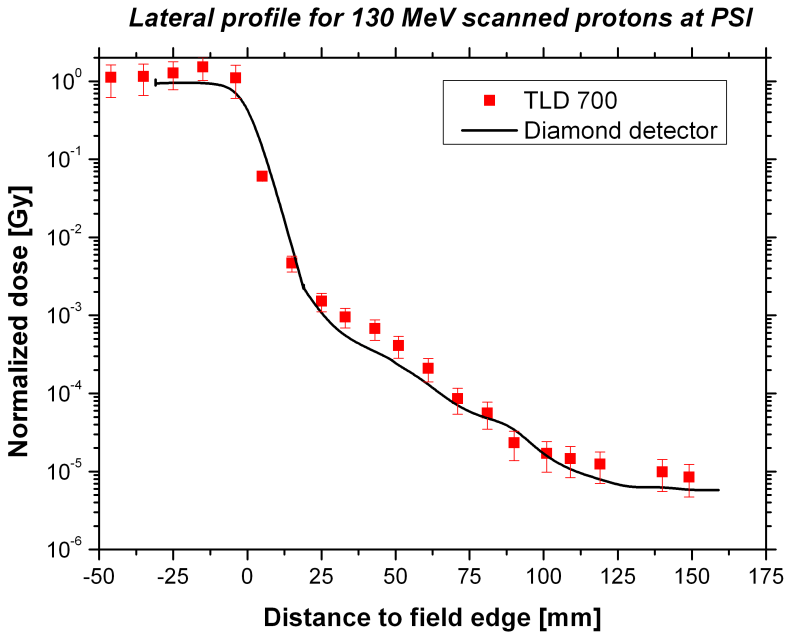

Figure 81: Lateral dose profile in the Bragg peak for a 5×5 cm^2 field of scanned protons measured with a diamond detector and with TLD 700.

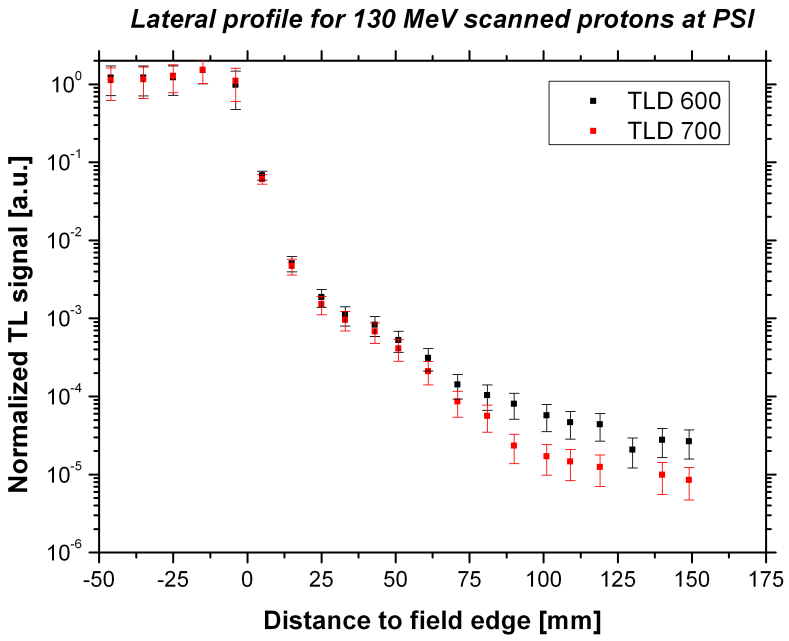

Figure 82: Thermolumniscence signal at Bragg peak depth for a 5×5 cm^2 field of scanned protons measured with TLD 600 and TLD 700.

6.4 Field-size-effect of carbon ions measured at GSI

An irradiation performed at GSI in Cave A focused on the evaluation of the field size influence on the out-of-field dose. Only little beamtime was available for the experiment and the pencil beam spot could not be optimized perfectly. A plot of the lateral dose profile for a 300 MeV/u carbon ion pencil beam is shown in Fig. 83. The beam has a Gaussian shape close to the center, but shows a more complex structure at larger distances.

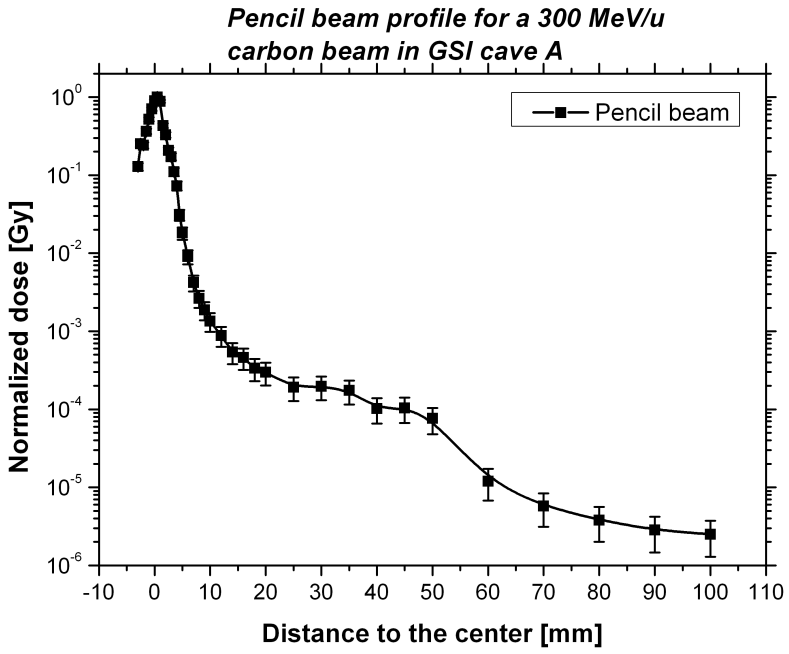

Figure 83: Pencil beam profile measured with a diamond detector for a 300 MeV/u carbon beam in GSI Cave A.

The bump at around 50 mm from the isocenter is most likely the cause of the trend of the lateral out-of-field dose profiles reported in Fig. 84. The dose distributions were measured for square fields with edge lengths of 2,4,5,6,8 and 10 cm but to give a clearer picture only selected results are shown. The profiles of the 2×2 and 5×5 cm^2 field show an increase in the dose at 3 and 2 cm distance to the edge respectively. The bump becomes smaller for bigger field sizes, indicating that the pencil beam shape is smoothed out when more points are irradiated. Overall, a clear increase in the out-of-field dose is measured with larger field sizes in agreement with the observations at PSI. The production of a bigger field requires a higher number of particles which undergo scattering and fragmentation and therefore add to the out-of-field dose.
The experiment was repeated with the diamond detector turned by 180 degrees to investigate whether it shows a directional dependence. The profiles showed no significant differences, proving that the results are independent of the direction the detector is positioned.

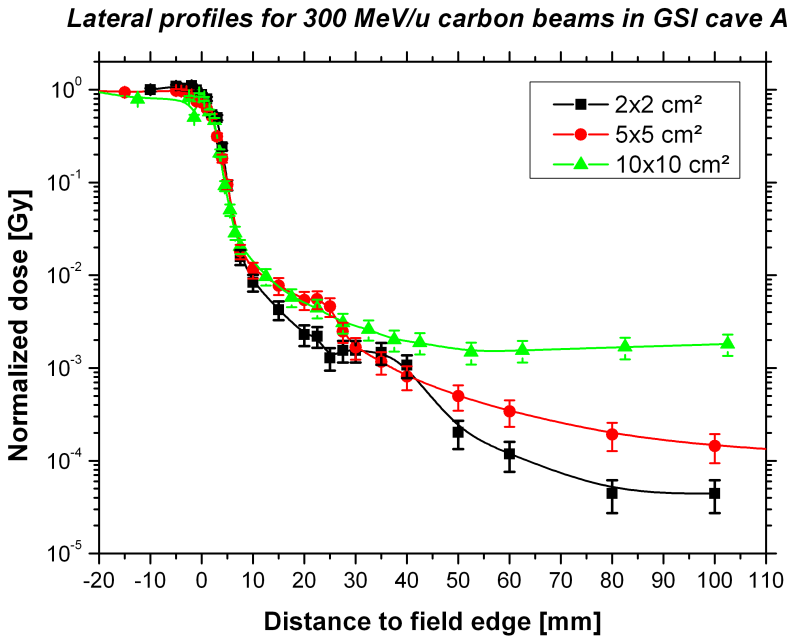

Figure 84: Out-of-field dose profiles measured with a diamond detector at GSI Cave A for a 300 MeV/u carbon beam with several field sizes.

Energy dependence

The main aim of the experiments performed at HIT was the comparison of the out-of-field dose for scanned protons and carbon ions. Measurements of the lateral dose profile were performed at various energies corresponding to ranges of 5, 12.5 and 20 cm in water. The results are shown in Figs. 85 to 87.

The penumbra of carbon ions is sharper than that for protons in all cases, a behavior that represents a well known advantage of carbon ions over protons. Since for low energies the carbon ions travel only a short path in the material, fragmentation is small and thus the out-of-field dose is lower than for protons in all positions measured.

At higher energies, the increased fragmentation of carbon ions plays a more important role. While the penumbra still is very sharp, an increase in the out-of-field dose is observed at 3 cm distance to the field edge, where the dose from protons and carbon ions is about equal. At further distances the fragmentation of carbon ions leads to a higher dose out-of-field than for protons.

Another conclusion can be drawn from these results. Only a little dependence of the dose profile on the energy is observed for protons with a slight increase at increasing energy; the penumbra for all energies is also almost constant. For carbon ions, on the other hand, the energy has a large influence on the dose profile. At the furthest point from the field edge, the dose increases more than one order of magnitude for carbon ions with a range of 20 cm compared to 5 cm. However, even in the "worst" case measured with high energetic carbon ions (330 MeV/u), the dose stays below 10^{-4} of the target at a distance of 10 cm.

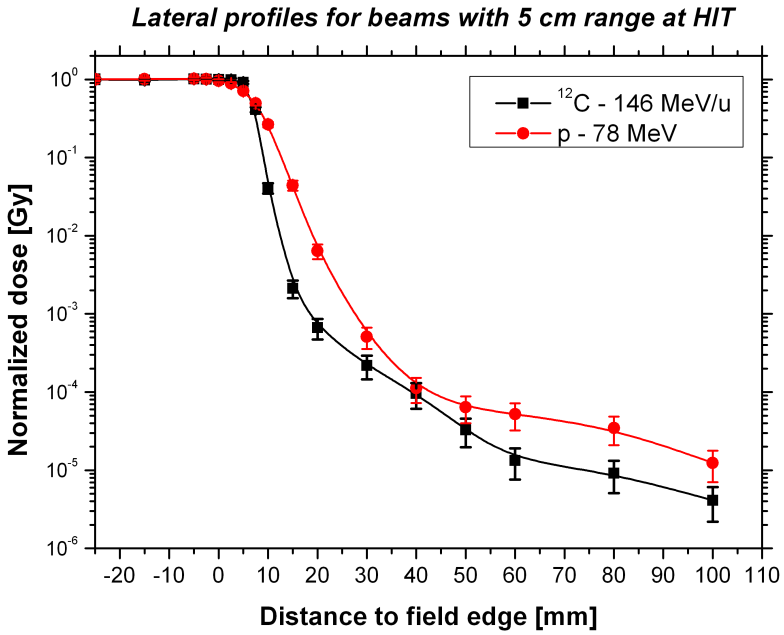

Figure 85: Lateral dose profiles for a 5×5 cm^2 field measured with a diamond detector for scanned protons and carbon ions with a range of 5 cm in water.

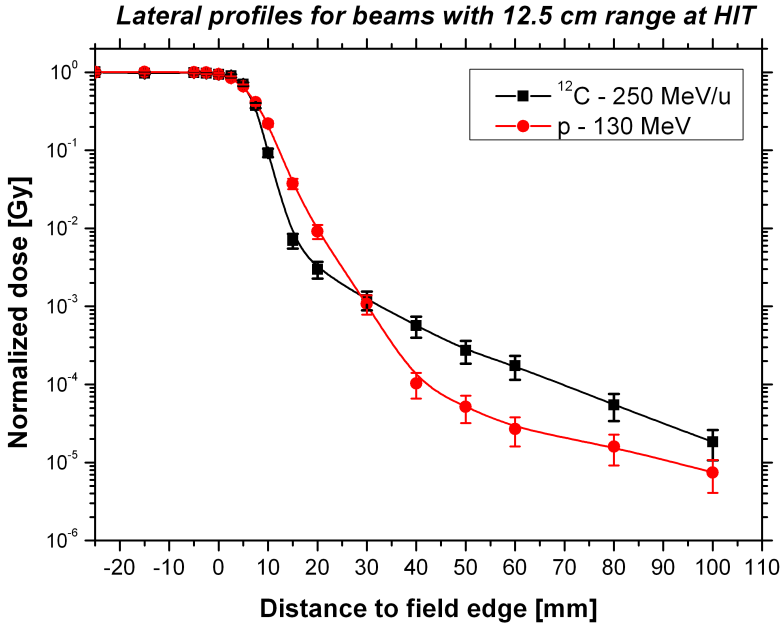

Figure 86: Lateral dose profiles for a 5×5 cm^2 field measured with a diamond detector for scanned protons and carbon ions with a range of 12.5 cm in water.

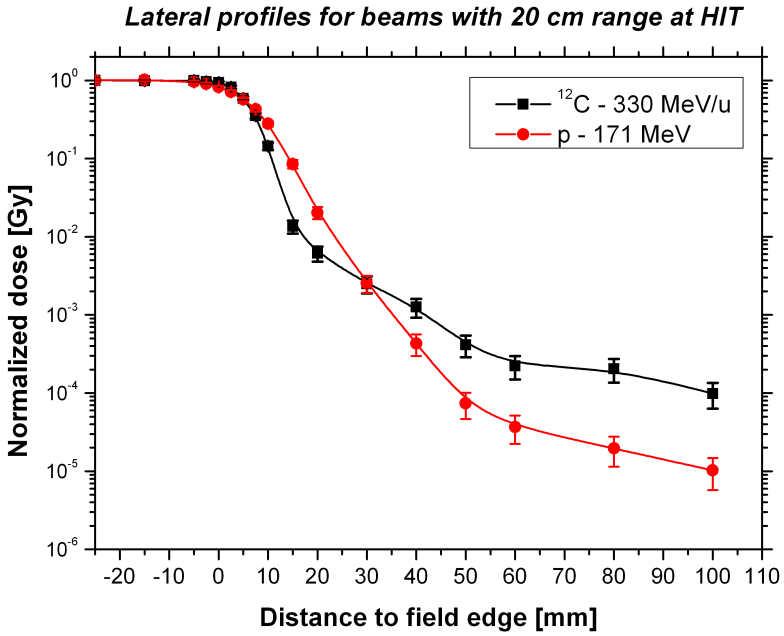

Figure 87: Lateral dose profiles for a 5×5 cm^2 field measured with a diamond detector for scanned protons and carbon ions with a range of 20 cm in water.

TLD results

Fig. 88 shows the comparison of the results from the diamond detector and the TLD 700. In the field the dose measured by TLDs is significantly lower than the one from the diamond detector. As described in section 3.2, the TLD 700 and 600 have a reduced efficiency to high-LET particles which characterize the region in-field. Outside the field lower-LET particles are present, thus the efficiency is close to 100% and the agreement is good. However, at distances larger than 10 cm to the field, the TLD 700 measures a higher dose at the 10^{-4} level. No diamond detector data were taken at these positions and the cause for this increase is unclear and not confirmed by any other detector.

The output from TLD 600 shows the same behavior in this region. It appears that the dose measured at this position is mainly from charged particles, since there is no visible difference between TLD 600 and 700. A small difference between the two detector types can be observed in the region between 3 and 10 cm distance to the field edge that can be attributed to neutrons produced through fragmentation.

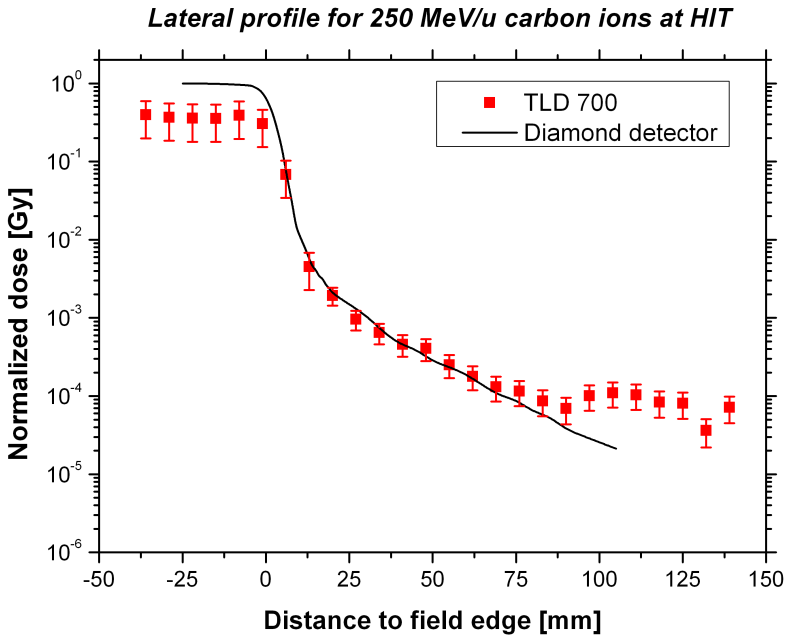

Figure 88: Comparison of TLD 700 data and diamond detector results for a 5×5 cm^2 field of 250 MeV/u scanned carbon ions at HIT.

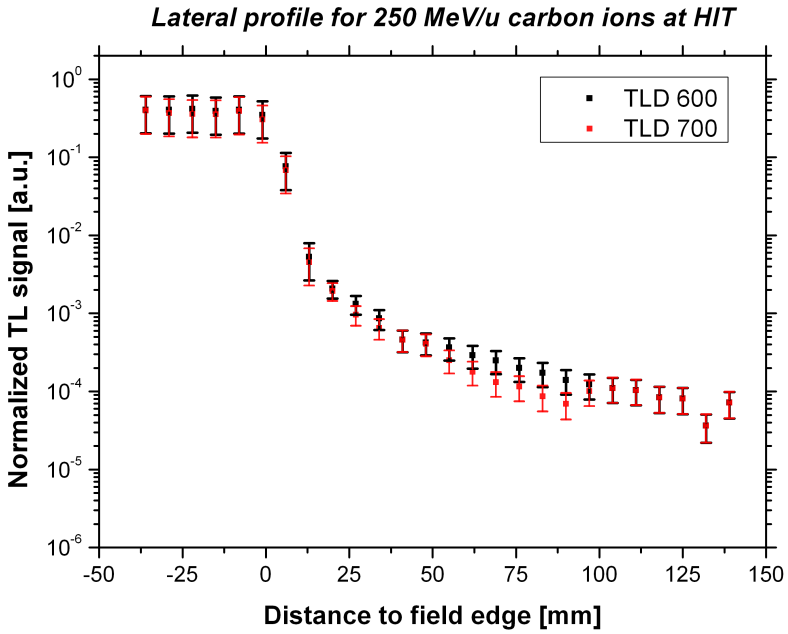

Figure 89: Thermoluminescence signal of TLD 600 and TLD 700 for a 5×5 cm^2 field of 250 MeV/u scanned carbon ions at HIT.

Further measurements

To confirm the reliability and reproducibility of these results a number of additional measurements was performed:

- comparison of profiles measured with a diamond detector and ionization chamber
- influence of the ripple filter for carbon ions
- effect of the air gap for protons
- reproducibility after accelerator maintenance

The lateral dose profiles measured by the ionization chamber and a diamond detector are compared in Fig. 90. The data show an excellent agreement of the ionization chamber and the diamond detector results after the sublinearity correction has been applied.

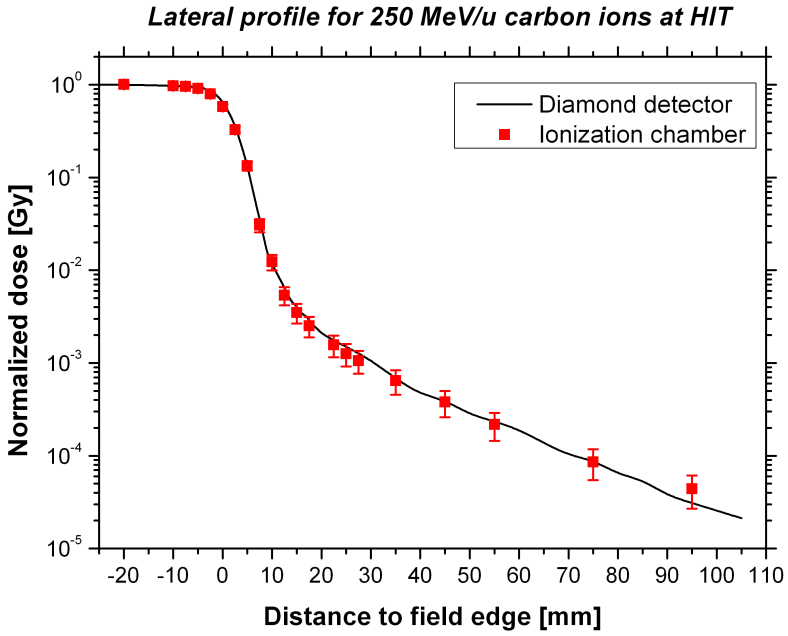

Figure 90: Lateral dose profiles for a 5×5 cm^2 field of 250 MeV/u scanned carbon ions at HIT measured with an ionization chamber and the diamond detector.

The influence of the ripple filter was also investigated at HIT. The out-of-field dose was measured twice for a 250 MeV/u carbon beam, with and without the ripple filter. No significant differences were observed. Furthermore, for carbon ions there was no significant difference of the out-of-field dose when the distance from the beam exit window to the water phantom was changed from 10.6 to 104 cm. For protons, on the other hand, a large effect could be observed (Fig. 91). Protons of 78 and 130 MeV energy were delivered with a distance of 10.6 cm of air between the BAMS and the phantom while the 115 MeV beam was delivered with an air gap of 104 cm, i.e. a

distance typical for carbon ions. It was shown above that the lateral dose profiles for protons are almost independent on the beam energy, even if the energies of the proton beams are different, they are therefore expected to be similar. A large increase of the penumbra is observed for the 115 MeV beam with a distance of 104 cm instead, proving that a large air gap following the lateral spread in the nozzle has a significant impact for protons. The results confirm the findings of (Weber and Kraft, 2009) and imply that for achieving a sharp penumbra for scanned protons the air gap should be kept as small as possible.

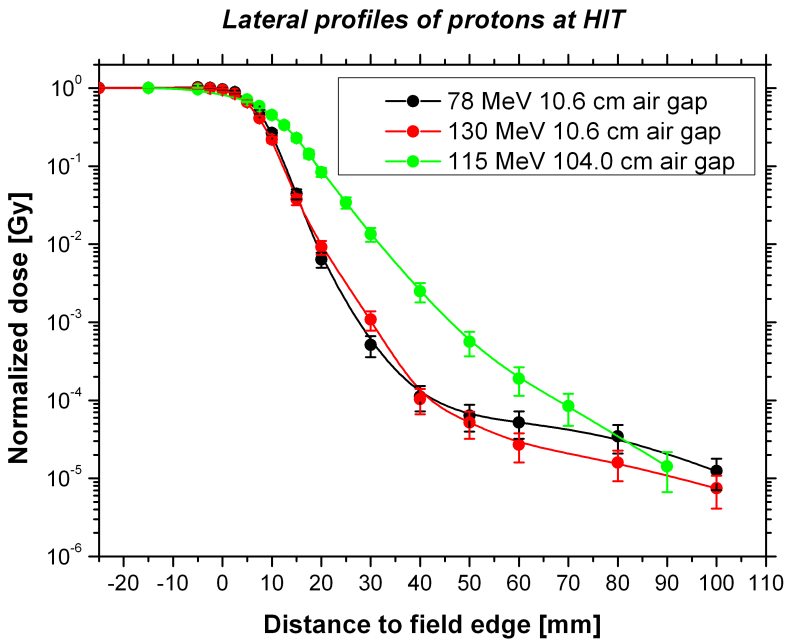

Figure 91: Lateral dose profiles measured with the diamond detector for a 5×5 cm^2 field of protons with different energies and air gaps.

Measurements with 250 MeV/u carbon ions were performed in two separate sessions in May and July 2010. Between the experiments, the accelerator had a shut down for maintenance where several parameters of the accelerator were slightly adjusted. Fig. 92 shows that the maintenance only had a minor influence on the profiles as the difference lies within the errors of the measurement.

During the irradiation of the anthropomorphic phantom at GSI, an additional experiment was performed with the water phantom in the treatment room Cave M under therapeutical conditions using carbon ions with a beam energy of 250 MeV/u. The measurements have a lower spatial resolution than the data collected at HIT but show very similar results (Fig. 93).

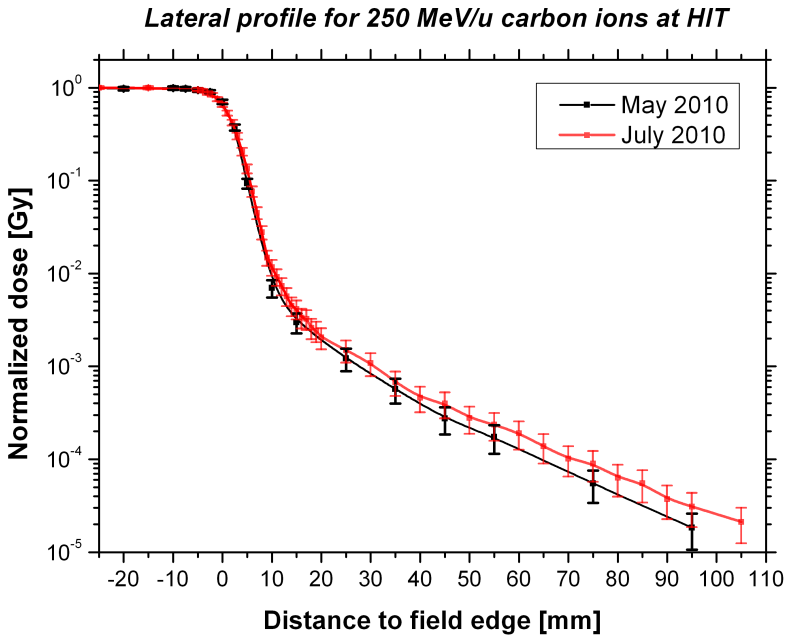

Figure 92: Lateral dose profiles for a 5×5 cm^2 field of 250 MeV/u scanned carbon ions measured at HIT with the diamond detector before and after a shutdown.

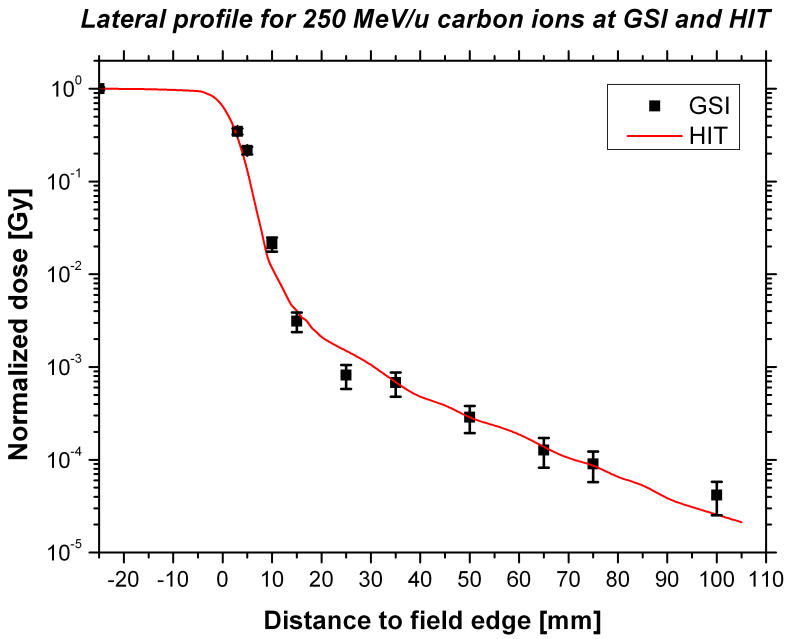

Figure 93: Lateral dose profiles for a 5×5 cm^2 field of 250 MeV/u scanned carbon ions measured at HIT and at GSI with the diamond detector.

6.6 Summary and conclusions

This section gives an overview of the results and the conclusions that can be drawn from the measurements of lateral dose profiles in a water phantom. The comparison with literature for the photon measurements has shown a reasonable agreement validating the experimental methods. For charged particles, no published data were found that allow a reasonable comparison with literature as these studies concentrate on the equivalent dose from neutrons which was not measured in this study for charged particles.

A comparison of the lateral dose profiles for a 5×5 cm^2 field measured in the dose maximum with the diamond detector is shown in Fig. 94. The logarithmic scale allows a comparison of the dose far away from the field. The dose fall-off near the field edge is similar for all irradiation types. At larger distances, the advantage of treating with ions rather than photons when considering the out-of-field dose profile becomes very clear. At 5 cm from the field edge ions deliver dose between one and two orders of magnitude lower than photons; the difference becomes even larger (at least two orders of magnitude) at 10 cm distance to the field edge.

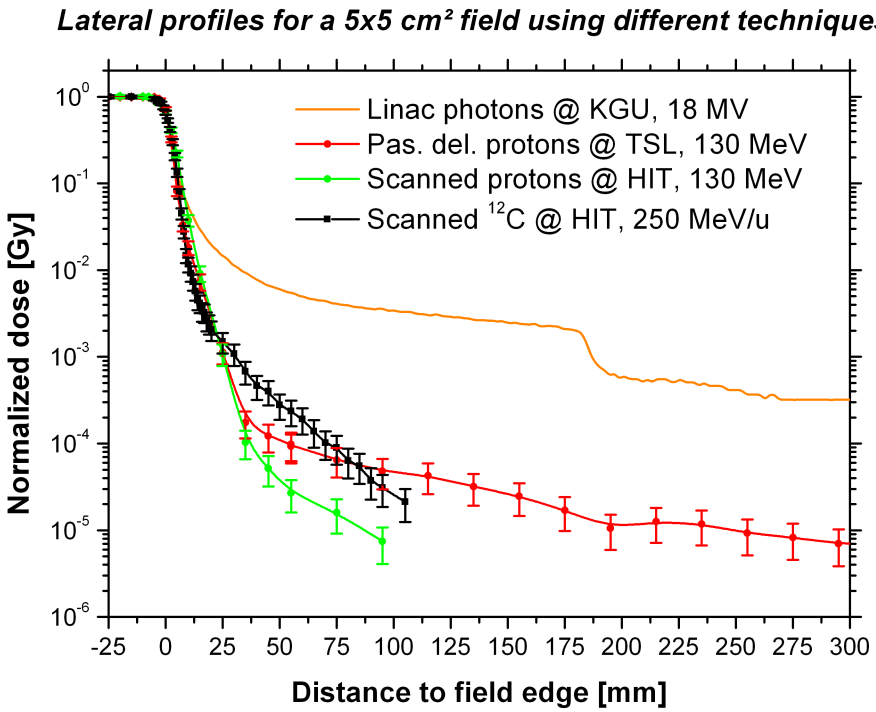

Figure 94: Lateral dose profiles measured with the diamond detector in the dose maximum depth for a 5×5 cm^2 field produced with photons, protons and carbon ions and different beam delivery techniques.

Irradiations with protons were performed at three different facilities. A comparison of the dose profiles measured with the diamond detector is shown in Fig. 95. The scanned protons at HIT and PSI show initially a very similar dose drop but deviate at approximately 2 cm distance to the field. When comparing the two facilities, it is important to keep in mind that the water phantom was placed at a distance of 10.6 cm to the BAMS for the irradiation at HIT. The experiment was set up to compare protons and carbon ions at a facility rather than comparing proton beams from different facilities. Patients treated with protons at HIT are positioned at larger distances, increasing the penumbra. Furthermore, Gantry 2 at PSI is not used for the treatment of patients yet, further beam optimization may change the results far from the field edge. The passive proton beam at TSL shows a sharper penumbra compared to the scanning technique as the collimator is placed directly in front of the water phantom producing a sharp edge and compensating the divergent beam after travelling in air. At larger distances, the dose delivered by passively modulated protons increases compared to the scanning technique, but at a level of $\leq 0.1\%$ of the in-field dose. It is important to note however, that the two-dimensional irradiation of a square field represents the ideal case for the passive modulation technique. Known problems such as the irradiation of normal tissue in the proximal part for complex geometries cannot be observed in this two-dimensional irradiation.

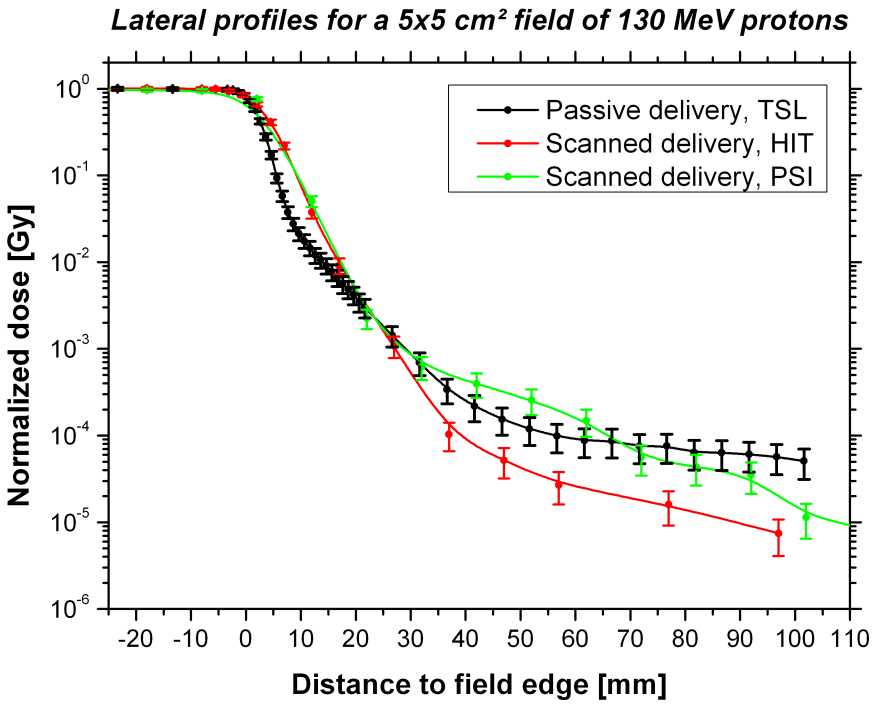

Figure 95: Lateral dose profile for a 5×5 cm^2 field of 130 MeV protons at three different proton facilities measured with the diamond detector.

The TLD results shown in Figs. 96 and 97 investigate further the out-of-field dose in passive and active delivery techniques. Taking into account the limitations described in section 3.2 such as the supralinearity or the low efficiency to high LET particles, Fig. 96 confirms the results from the diamond detector. The results from the TLD600 reported in Fig. 97 show a strong increase of the TL signal for the passive irradiation technique compared to scanned protons. This trend gives a clear indication of an increased neutron yield for passive delivery techniques. After the initial drop, the signal from the TLD 600 stays almost constant over the entire range investigated.

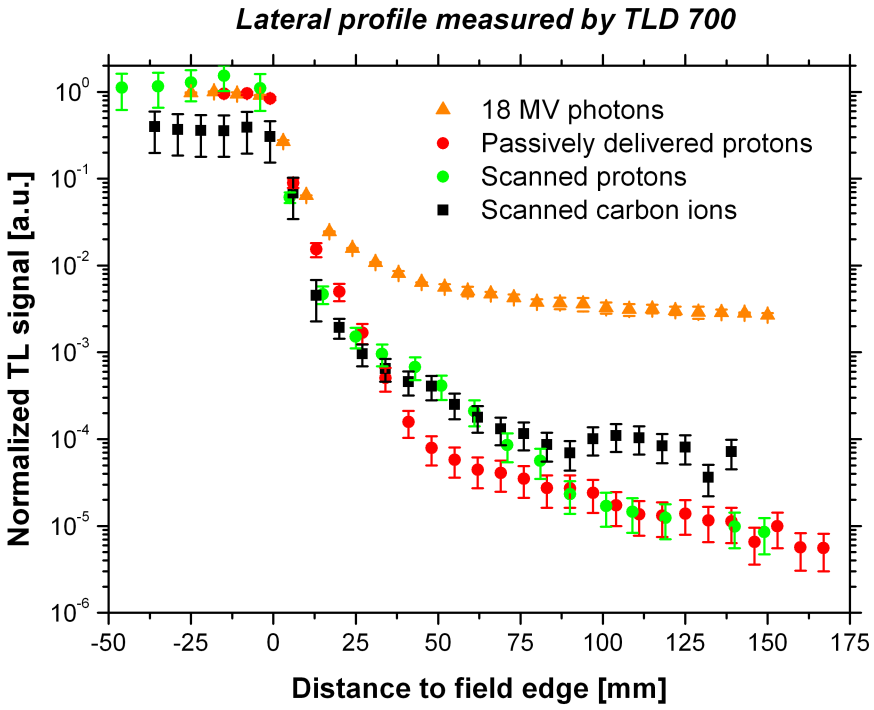

Figure 96: TL signal for the TLD 700 in all irradiation techniques for a 5×5 cm^2 field.

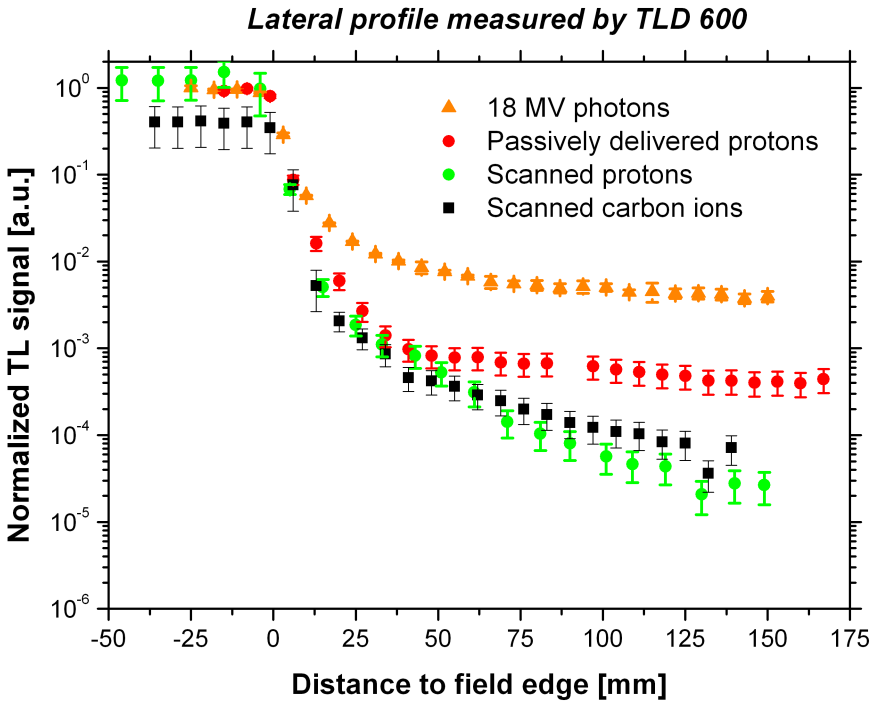

Figure 97: TL signal for the TLD 600 in all irradiation techniques for a 5×5 cm^2 field.

Summarising, the single field measurements lead to the following conclusions:

- the setup used for the experiments is able to reproduce data previously published for photon irradiations
- the out-of-field dose is a factor 50 to 400 lower for charged particles than for photons
- the bubble detector measurements show that on the water surface neutrons deposit an equivalent dose of 1 to 5 mSv / treatment Gray
- the neutron contribution outside the field is almost independent of the position in photon therapy
- the low neutron fluence at a water depth of 10 cm in photon therapy confirms that most neutrons are produced in the treatment head rather than in the patient itself
- the out-of-field dose of scanned particles increases with the field size (one order of magnitude for a 300 MeV/u carbon beam with field sizes of 5×5 and 10×10 cm^2)
- carbon ions have a sharper penumbra than protons (for a 5×5 cm^2 field of 130 MeV protons and 250 MeV/u carbon ions the dose drops from 90% to 10% within 12.5 mm for the former and 9.1 mm for the latter at HIT)

- for high energies the dose far out-of-field of carbon ions is higher than for protons at a dose range below 10^{-3} of the target
- the use of collimators for protons produces a sharper penumbra than the scanning technique (dose drop from 90% to 10% within 7.3 mm for protons at TSL and 12.5 mm for protons at HIT)
- the use of passive beam shaping yields a higher number of neutrons than scanning beams seen by the increased TL signal in TLD 600
- the out-of-field dose has a dependence on the facility

7 Results - 3D volume measurements

This chapter shows the dose profiles in an anthropomorphic phantom after irradiation using several treatment types. These results were obtained in collaboration with Thomas Berger, Christine Körner and Günter Reitz from DLR. All results are given in TL signal or absorbed dose normalized to 1 Gray in the target. If no error bar is visible for the TLD results, the standard error is within the size of the data points. It is significantly lower than for the water phantom measurements because of the increased number of TLDs used.
The two-dimensional plots use the same dose range for all treatments to enable a directly visible comparison. The spatial distribution of the dose is shown using a specific range for each treatment to make small differences within a slice for a treatment visible.

7.1 25 MV IMRT at KGU

The irradiation was delivered from seven fields. The results of the rod inside the phantom are reported in Fig. 98, where the dose from the TLD 700, the diamond detector as well as the absorbed and equivalent dose coming from neutrons measured by the bubble detector system are shown. The connected lines do not represent measured data and are only intended to guide the eye. The ratio of the neutron equivalent dose and absorbed dose is on average 18, the high ratio is explained by the fact that the peak of the neutron spectrum coincides with the peak of the weighting factors.

The dose reported by the TLD close to the target clearly show the high dose gradient around the irradiated volume: the detectors have a spatial resolution of 0.9 mm because of their thickness and each detector shows a significantly different readout than those surrounding it.
As already observed for the water phantom experiment, the photon dose drops rapidly at increasing distance to the target edge. The reasonable agreement between the TLD 700 and diamond detector data confirm the results. The comparison of the TL signal from TLD 600 and TLD 700 show an increase for the former indicating a high yield of low energetic neutrons.
The results from the bubble detectors in the rod show a high neutron fluence in the field. In agreement with the data from the water phantom, the highest neutron dose is measured in the field, but it is about two to three orders of magnitude lower in terms of equivalent dose when compared to photons. The out-of-field dose delivered by neutrons is lower than in-field, but remains almost constant with increasing distance to the target. The equivalent dose deposited by neutrons is higher compared to photons at about 20 cm distance to the field. For the water phantom, the equivalent dose deposited by neutrons at a water depth of 10 cm for an 18 MV photon beam was one order of magnitude lower. The difference in the anthropomorphic phantom is attributed to the higher photon energy.

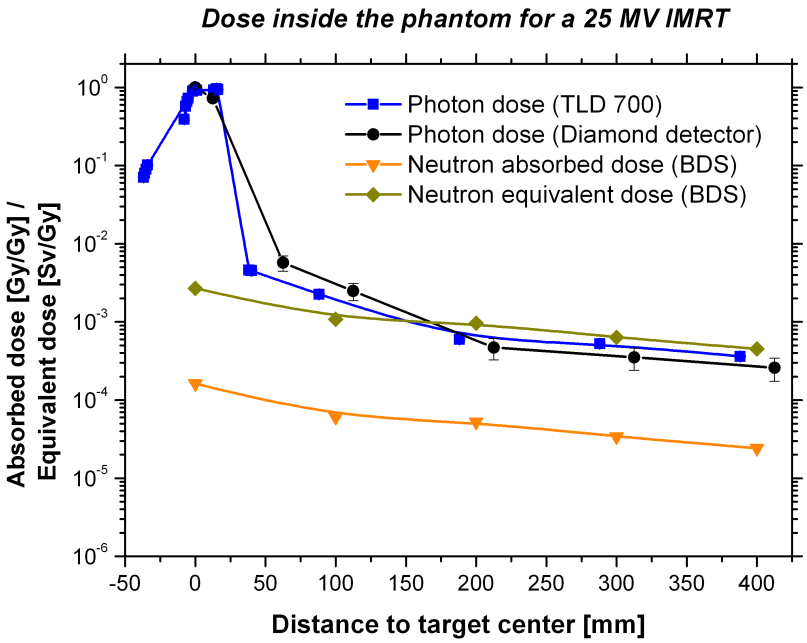

Figure 98: Measured lateral dose profile inside the anthropomorphic phantom treated with a 25 MV IMRT at KGU.

The surface dose was measured with the diamond detector placed on the ventral part of the body and compared with the corresponding values inside the phantom; the results are shown in Fig. 100. The dose measured in the field on the surface for the full treatment is about 12% of the target dose. The out-of-field dose then drops similarly to the water phantom measurements down to a level of around 5×10^{-4} Gy/treatment Gy at the furthest position. As expected, the dose in the field is higher inside the phantom than on its surface. Out-of-field, the dose is slightly higher on the surface than inside the phantom.

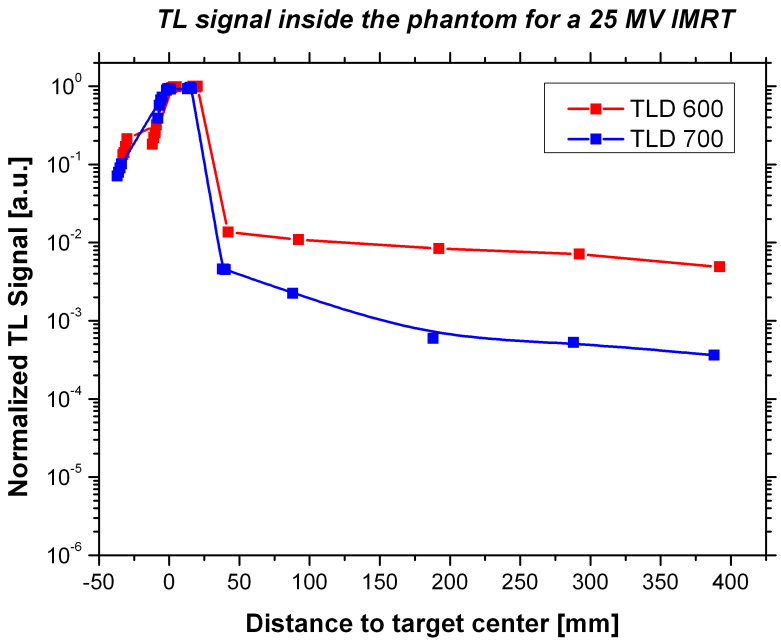

Figure 99: Normalized TL signal measured by TLD 600 and TLD 700 inside the anthropomorphic phantom treated with a 25 MV IMRT at KGU.

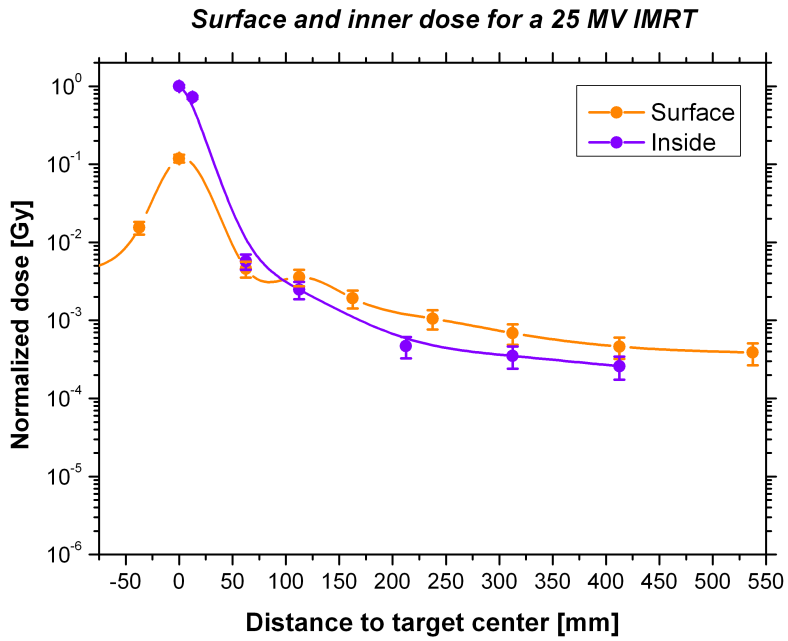

Figure 100: Surface and inner dose measured with the diamond detector along the phantom main axis with 25 MV IMRT photons

The neutron dose was determined from the neutron spectra measured with the bubble detectors in five positions after unfolding with the BUNTO code (Fig. 101). A high neutron fluence is observed in-field where the distribution shows two peaks at 2.3 MeV and 500 keV. The higher peak is mainly produced by the direction reaction in the accelerator head in agreement with the results from the water phantom. The lower peak was not observed in the water phantom and its origin is still being investigated. A photon energy of 25 MeV is high enough to excite giant resonances in Ca nuclei (bones). The produced neutrons would have a lower energy than those produced from tungsten in the accelerator head. The investigation of this process would however require a dedicated study and is beyond the scope of this thesis. Monte Carlo simulations could help clarifying whether the peak is an unfolding artifact or has a physical explanation.

Neutrons produced in the evaporation process explain the peak at 1 MeV neutron energy in the out-of-field detectors. As already indicated by the neutron dose profile shown in Fig. 98, the neutron fluence remains mostly constant with increasing distance to the field with little or no changes in absolute numbers and shape of the spectrum. This result agrees with the data collected in the water phantom.

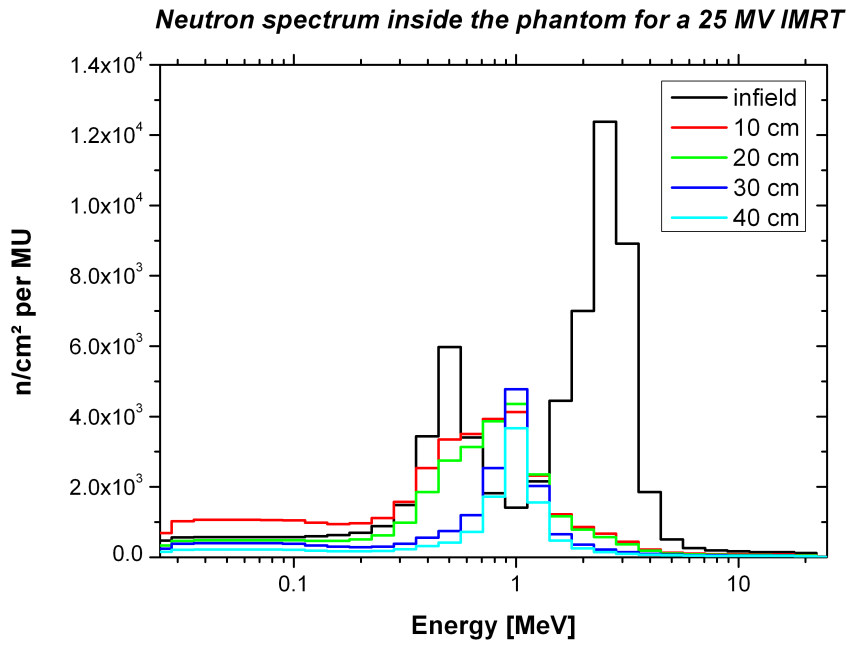

Figure 101: Neutron spectrum measured in the rod at 5 positions in the anthropomorphic phantom with increasing distance to the target for a 25 MV IMRT.

Spatial distribution

The 2D plot Fig. 102 shows the dose conformality in the transverse plane of slice 4 (the target slice). TLDs were positioned in a grid of 25.4 mm, each square representing the read out from one detector using a color scale; the area of the PTV is indicated in the plot. For better illustration, the squares shown are larger than the actual area of TLDs (3.2×3.2 cm^2). The data from the rod are not included in the Figure since they are offset by up to 12 mm in height compared to the detectors in the slices. Fig. 103 shows a photo of slice 4 seen in the same perspective as the color plots and specifies the anatomical directions.

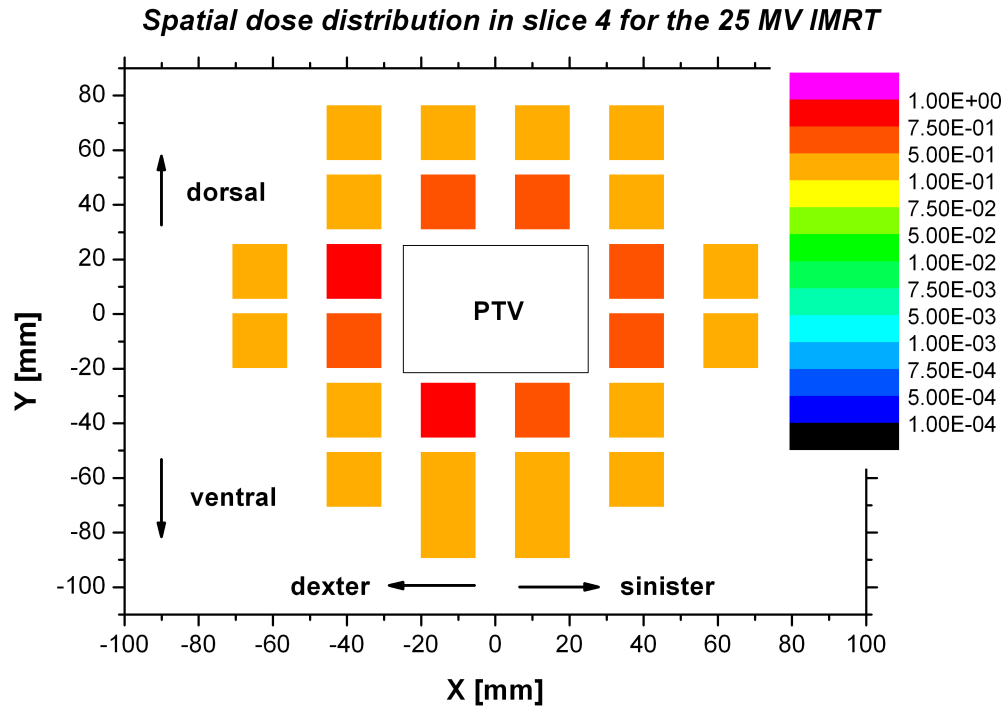

Figure 102: Dose measured by TLD 700 in slice 4 of the anthropomorphic phantom for the 25 MV IMRT.

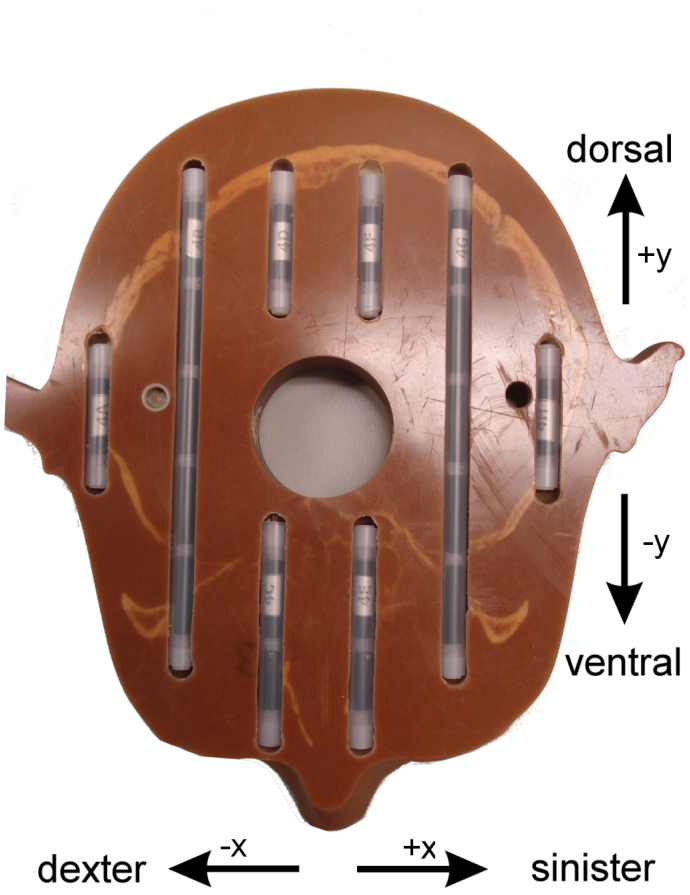

Figure 103: Photo of slice 4 (tumour slice) with anatomical directions seen in the same perspective as the TLD plots.

As expected, the highest dose region is observed around the target and the dose decreases in the lateral detectors. The dose distribution is relatively homogeneous at positions with the same distance to the target. The radial symmetry is caused by the irradiation from multiple fields at different angles.

The 2D dose profile of TLD 700 in slice 20 (plotted in Fig. 104) shows no preferred direction but rather a homogeneous distribution. In contrast, the TLD 600 readout for the same slice (Fig. 105) is higher at the dorsal side of the patient. An overall increase of the TL signal of TLD 600 compared to TLD 700 is also observed. In both plots the projection of the PTV is indicated, no data were measured in this area since the rod was positioned there.

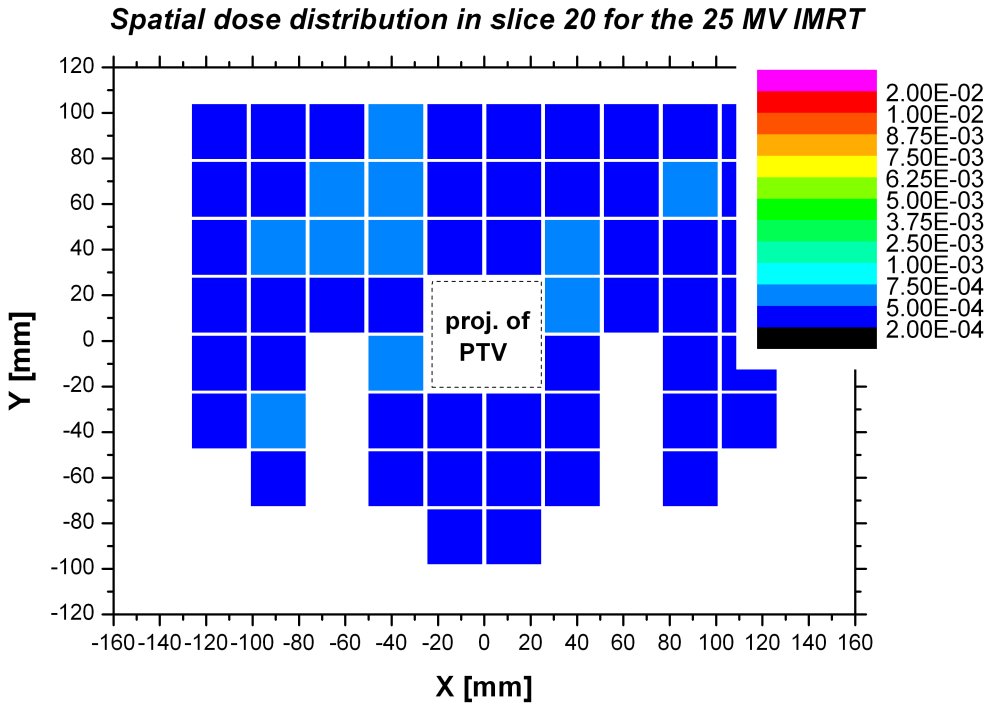

Figure 104: Dose measured by TLD 700 in slice 20 for the 25 MV IMRT.

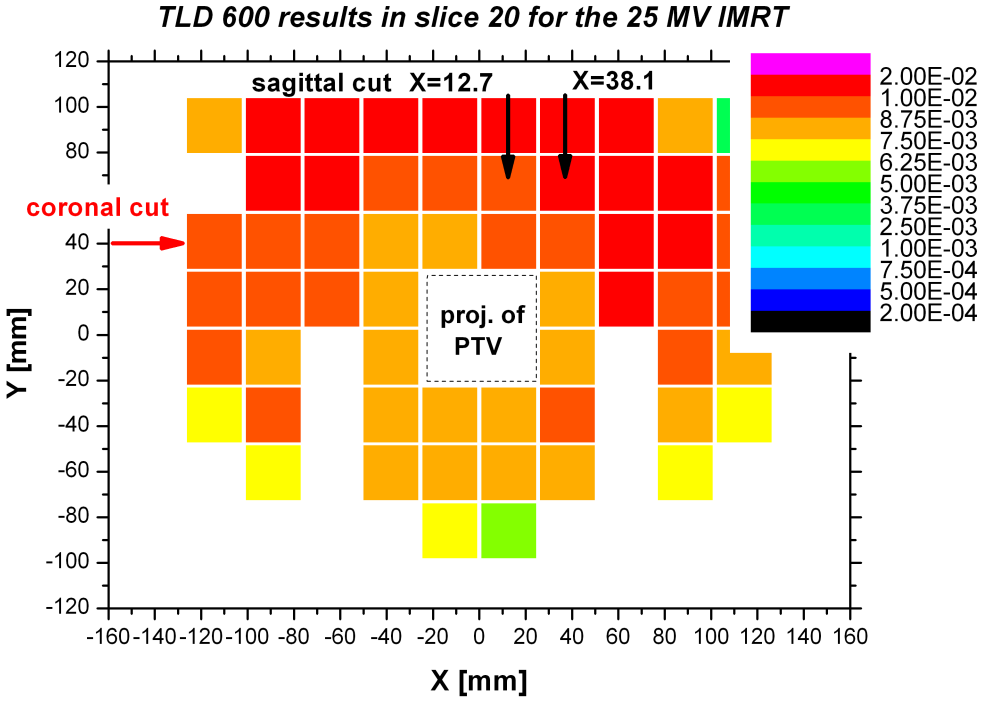

Figure 105: Normalized TL-signal measured by TLD 600 in slice 20 for the 25 MV IMRT

Fig. 105 includes three arrows which denote the positions of further investigations. For an easier comparison of the results from different positions, techniques and slices, the dose values are compared in several planes in the phantom. The red arrow denotes a cut which divides the body into left and right sections while the black arrows point to cuts in ventral and dorsal sections. The former is referred to as coronal cut and the latter as sagittal cut.
Dose profiles measured with the TLD 700 for coronal cuts are shown in Fig. 106. The dose is highest in Slice 4 and Slice 5, indicating a slight misalingment of the phantom so that also parts of slice 5 were directly irradiated. This would explain the mugh higher dose in slice 5 compared to slice 3 whereas rather a symmetrical distribution was expected from a perfect alignment. A gradient can be observed in the upper slices (3,4 and 5) while in the bottom slices (14 and 20) the differences are very small as already observed in the colour plots (Fig. 106).

The sagittal cuts (Fig. 107 and 108) show a similar behavior: the dose in the head changes significantly with the position whereas the dose far from the field is independent of the position.

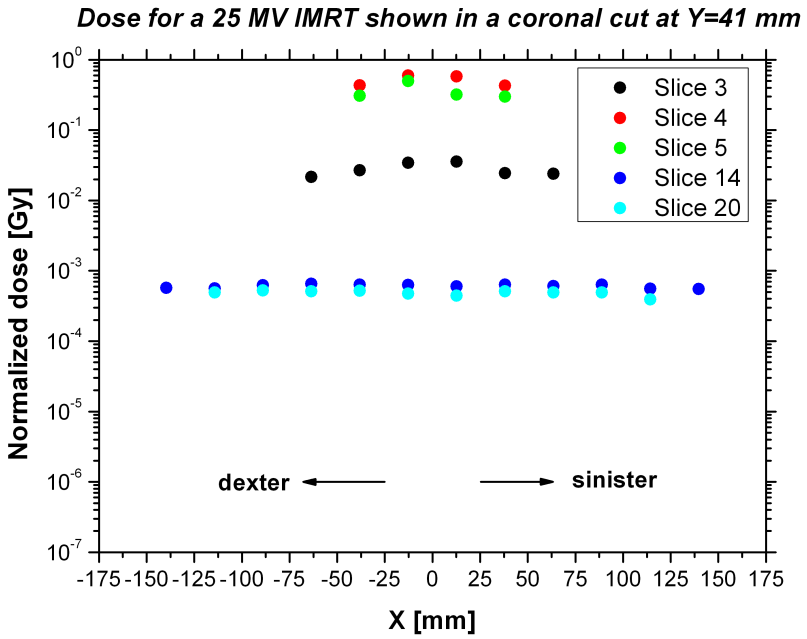

Figure 106: Relative dose from the TLD 700 shown in a coronal cut at Y=41 mm for the 25 MV IMRT irradiation.

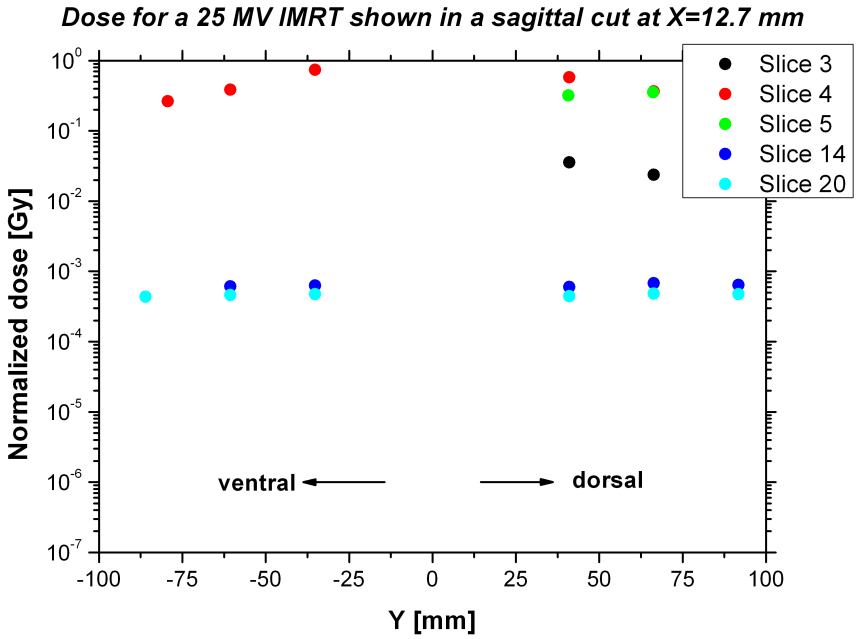

Figure 107: Relative dose from the TLD 700 shown in a sagittal cut at X=12.7 mm for the 25 MV IMRT irradiation.

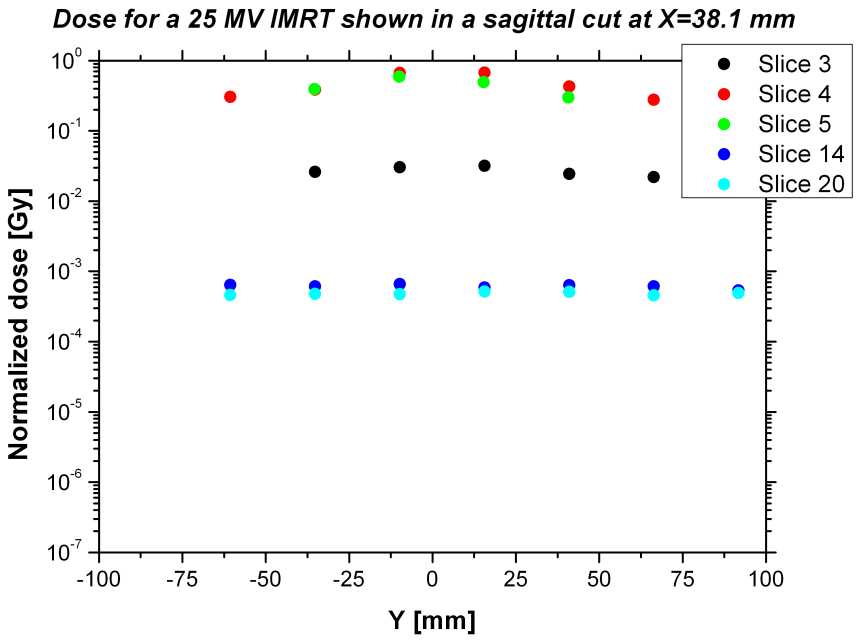

Figure 108: Relative dose from the TLD 700 shown in a sagittal cut at at X=38.1 mm for the 25 MV IMRT irradiation.

7.2 Irradiation with passively modulated protons (TSL)

The irradiation with passively modulated protons (TSL) was delivered in the posterior-anterior direction with a single field. Thus, the spatial distribution of the dose does not show a radial symmetry as for photons. The dose measured along the phantom main axis with TLD 700 is plotted in Fig. 109 together with the readout from the TLD 600.

As for photons, the data show a steep gradient close to the field. After only about 2 cm distance from the target center, the results from the TLD 600 and TLD 700 start to diverge. The sharp decrease close to the field becomes almost flat out-of-field where the dose is in the order of 10^{-4} to 10^{-5} Gy/treatment Gy for the TLD 700. The TL signal of TLD 600 is in the order of 10^{-2} to 10^{-3}. In agreement with the data collected in the water phantom, the delivery with passive modulation is characterized by a significant yield of low-energy neutrons produced along the beam line. A dedicated study is recommended for an accurate assessment of the neutron spectral fluence.

A small dose increase at 88 mm from the target center was detected with TLD 700. This position corresponds to the edge of the collimator. The collimator shields from the primary particles outside the field volume but some particles might scatter outside, thus leading to an increase of the dose at this position.

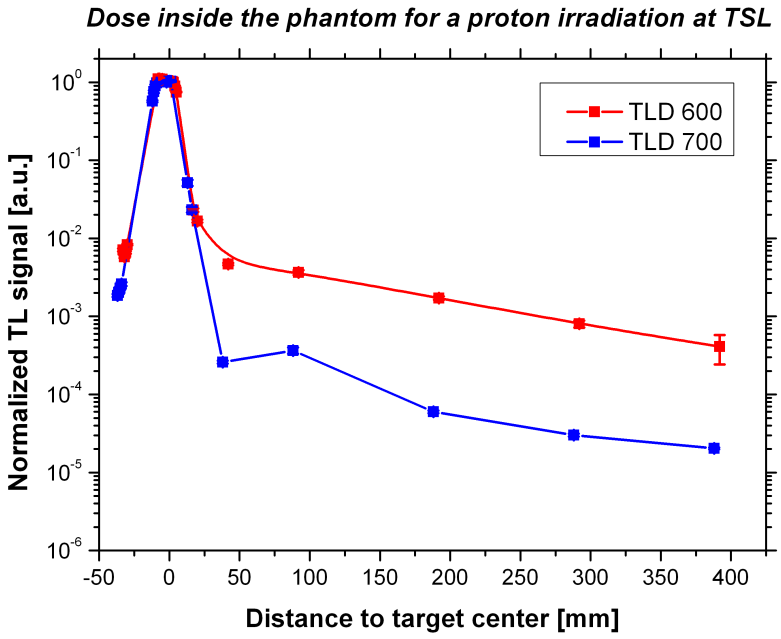

Figure 109: Dose and TL Signal measured with TLD 700 and TLD 600 in the rod of the anthropomorphic phantom treated with a passively shaped proton field (TSL).

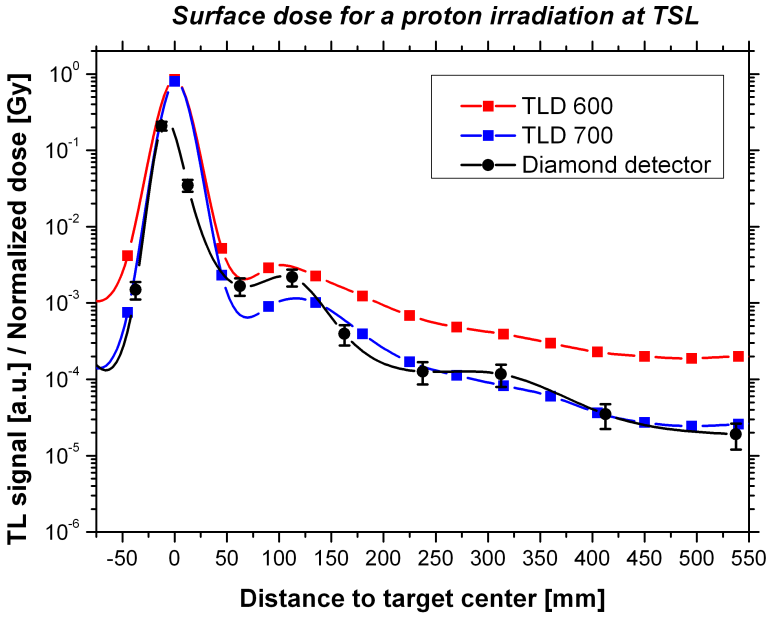

Figure 110: Dose on the surface of the anthropomorphic phantom treated with a passively shaped proton field at TSL.

Fig. 110 shows the measurement of the surface dose on the dorsal side of the body, where higher values were expected because of the irradiation direction. The data were collected both with the diamond detector and the TLDs attached to the back of the phantom. For the diamond detector results, the increased dose at the edge of the collimator can be observed.

Spatial distribution

As the phantom was treated only from one side, a more inhomogeneous spatial distribution of the dose is expected in this case. The Bragg curve for protons (and carbon ions) at therapeutic energies shows a higher dose in the plateau than in the tail, thus, for an irradiation in posterior-anterior direction a higher dose is expected in the dorsal part of the body.
This behavior is well observed in the dose profile measured with TLD 700 in slice 4 (Fig. 111). In contrast to the radial symmetry observed for the IMRT, the out-of-field dose is significantly higher in the entrance channel and lower in the tail of the field as well as in the lateral positions. Moreover, a rather asymmetrical dose distribution is observed in the left and right side.
The TLD 700 results for slice 5 are reported in Fig. 112. A higher dose is observed on the right side of the phantom (left side in the graph), indicating that the phantom was not perfectly aligned. The same trend was found from dose values in slice 3 (not shown).
When investigating the dose distribution further away from the field (slices 14 and 20) no asymetries in the left and right direction can be observed (Fig. 113 and 114), i.e. the misalignment of the phantom did not affect these regions. Furthermore, a slightly higher dose in the dorsal part of the body is measured.

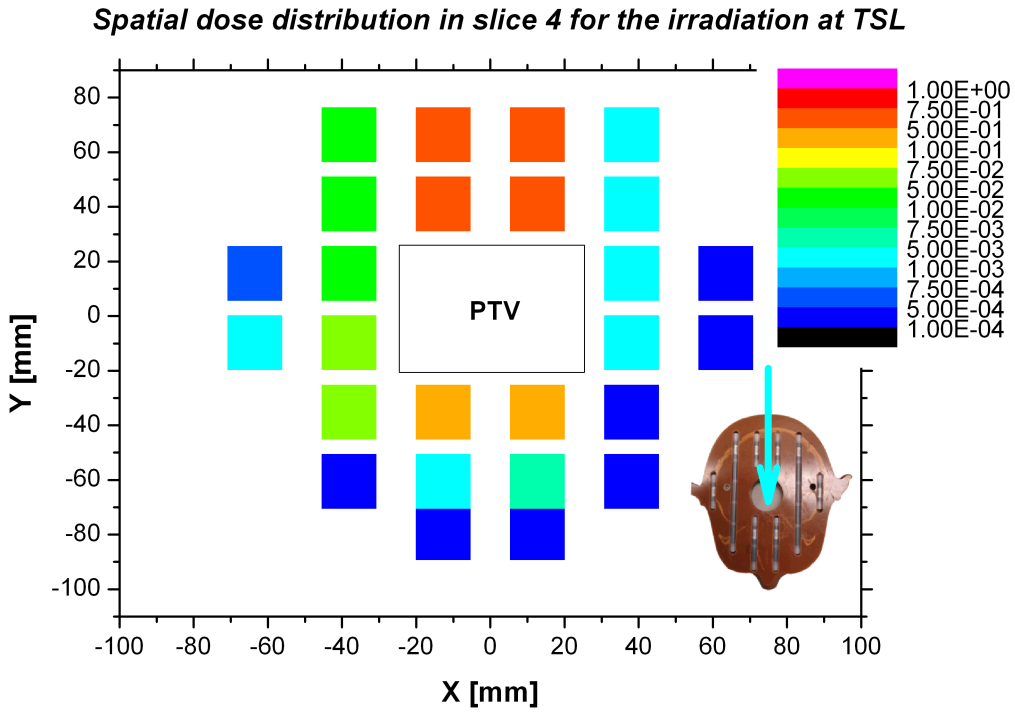

Figure 111: Dose distribution in slice 4 measured with TLD 700 for an irradiation with passively modulated protons. The small photo in the bottom right corner illustrates the irradiation direction for this treatment.

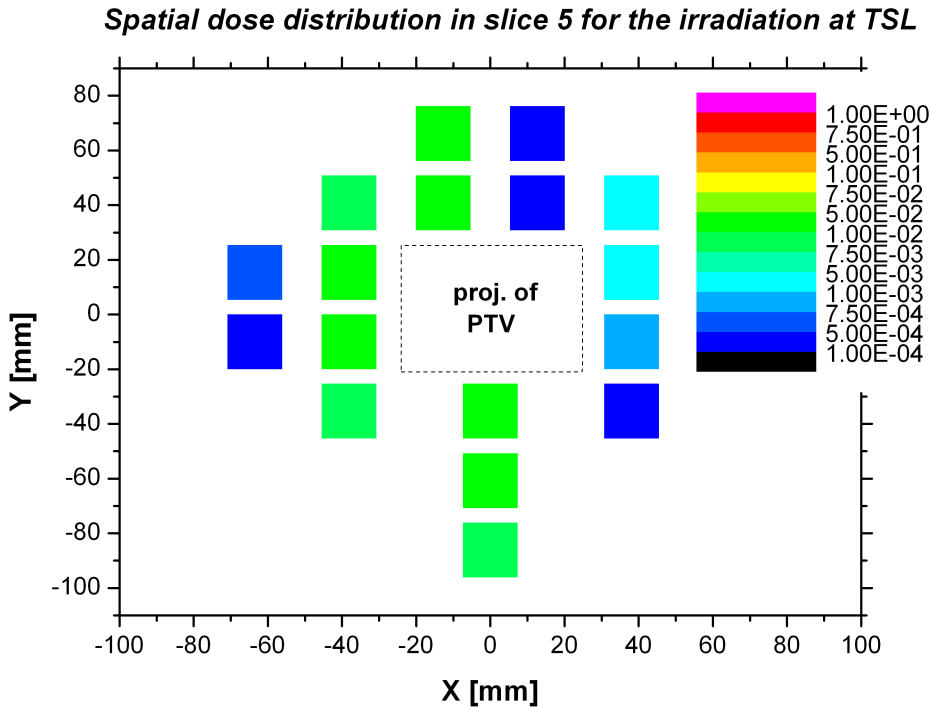

Figure 112: Dose distribution in slice 5 measured with TLD 700 for an irradiation with passively modulated protons.

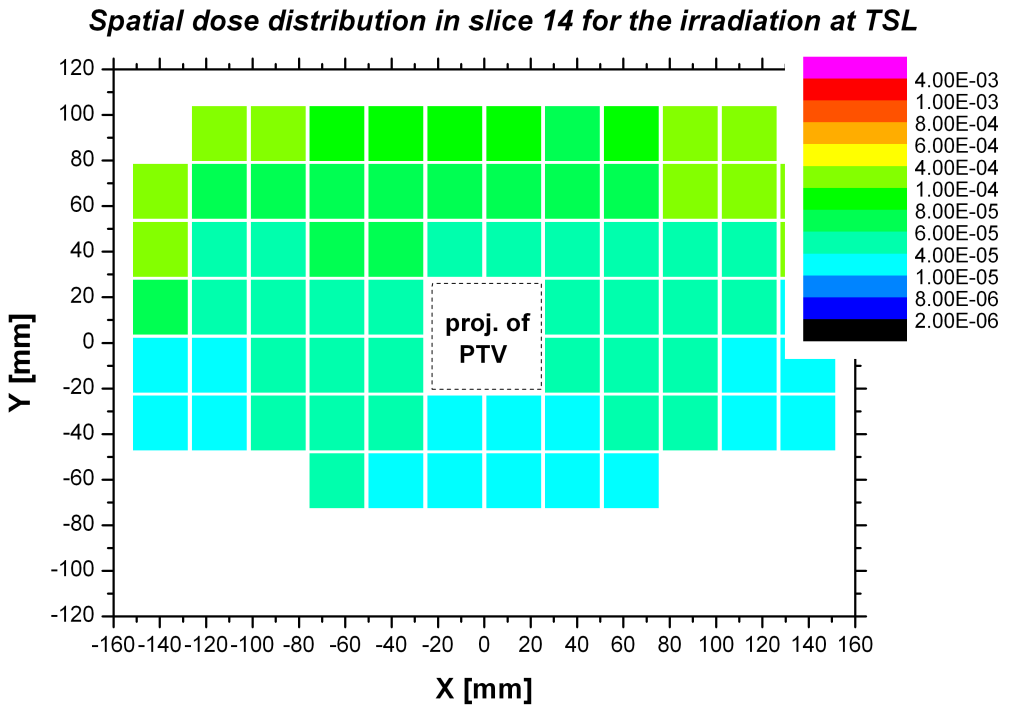

Figure 113: Dose distribution in slice 14 measured with TLD 700 for an irradiation with passively modulated protons.

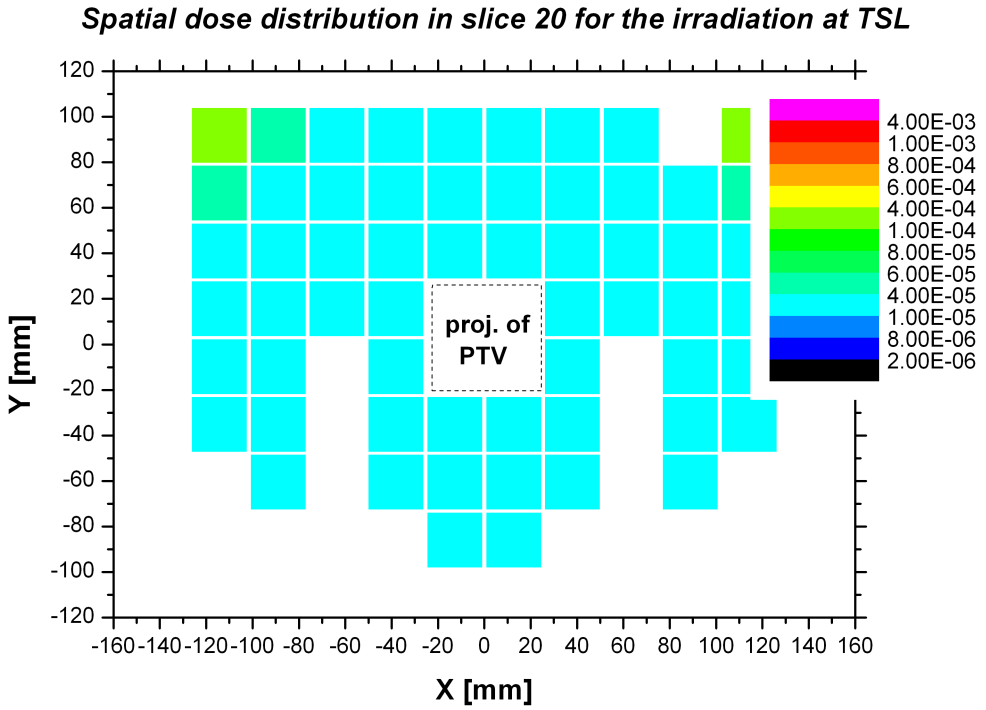

Figure 114: Dose distribution in slice 20 measured with TLD 700 for an irradiation with passively modulated protons.

As for photons, the data measured with the TLDs have been divided into coronal and sagittal cuts. The former selects the TLDs placed directly in front of the target area and its results are plotted in Fig. 115. The dose is highest in slice 4 for the middle two points that are positioned in the beam plateau. A substantially lower dose is observed laterally and for slices 3 and 5 confirming the high dose gradient expected for therapy with ions.

The dose is generally low in the order of 10^{-4} Gy/treatment Gy or less in the bottom slices and is slightly higher on the sides of the phantom rather than its center. A possible explanation is that scattered primary particles traverse less material to reach the positions on the edge, and therefore deposit a higher dose than in the center.

The sagittal cuts show agreement with the depth dose curves measured in the water phantom. A higher dose is found in the entrance channel than in the tail. This trend is observed especially in the sagittal cut in beam (Fig. 116) and in the cut one inch away from the beam (Fig. 117). The dose decrease from the back to the front of the phantom can be observed well in all slices.

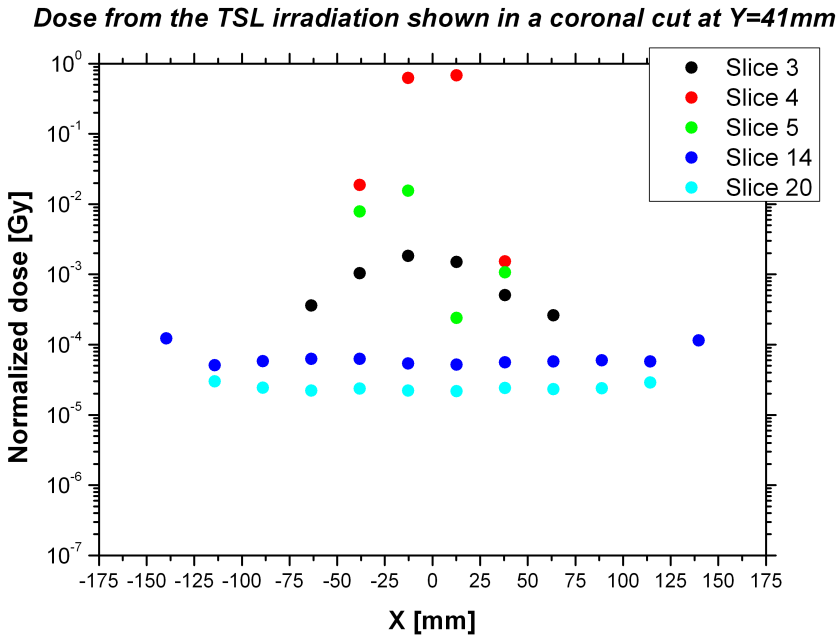

Figure 115: Coronal cut of the phantom at Y=41 mm, TLD 700 results for an irradiation with passively modulated protons at TSL.

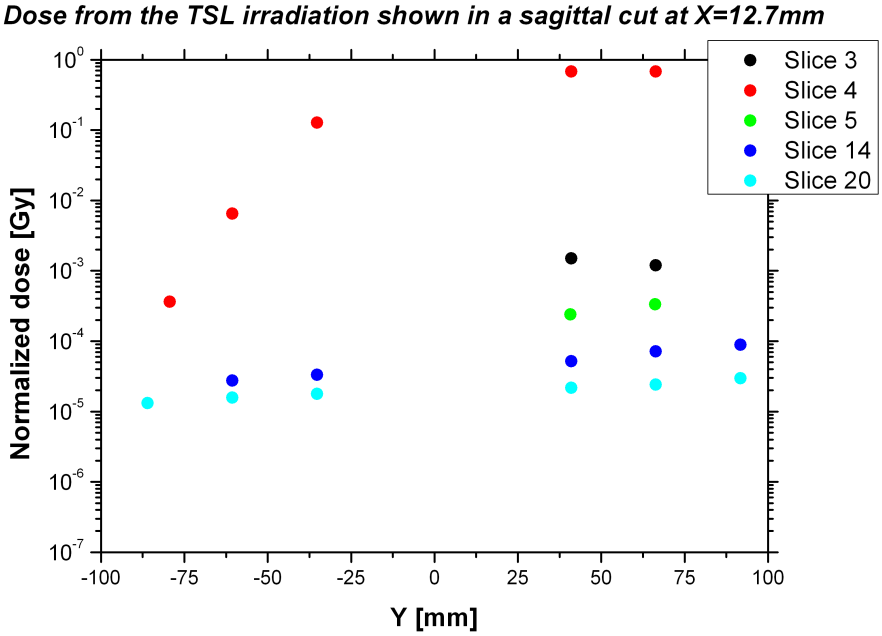

Figure 116: Normalized dose measured by the TLD 700 displayed in a sagittal cut at X=12.7 mm for an irradiation with passively modulated protons.

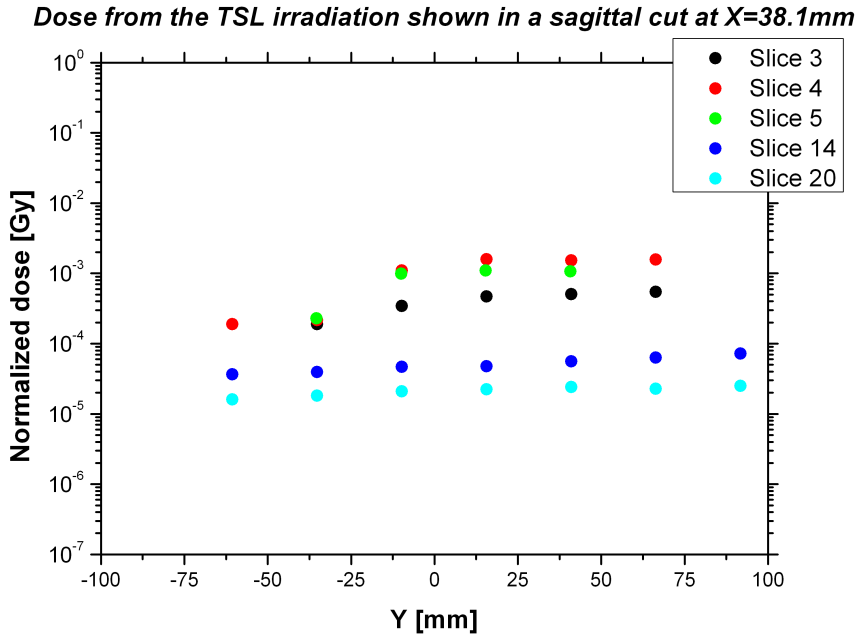

Figure 117: Normalized dose measured by the TLD 700 in a sagittal cut X=38.1 mm for an irradiation with passively modulated protons.

7.3 Irradiation with scanned protons (PSI)

The irradiation with scanned protons was performed at PSI Gantry 1 with the phantom lying with the face on the patient table (irradiation in posterior-anterior direction). The dose profile along the phantom main axis is plotted in Fig. 118.
The measurements show a sharp decrease close to the target and a smaller gradient out-of-field. The dose measured by the TLD 700 decreases almost six orders of magnitude compared to the target dose. The TLD 600 data show a slightly higher tail going down to about 10^{-5} in comparison to the 5×10^{-4} measured by the TLD 600 at TSL.

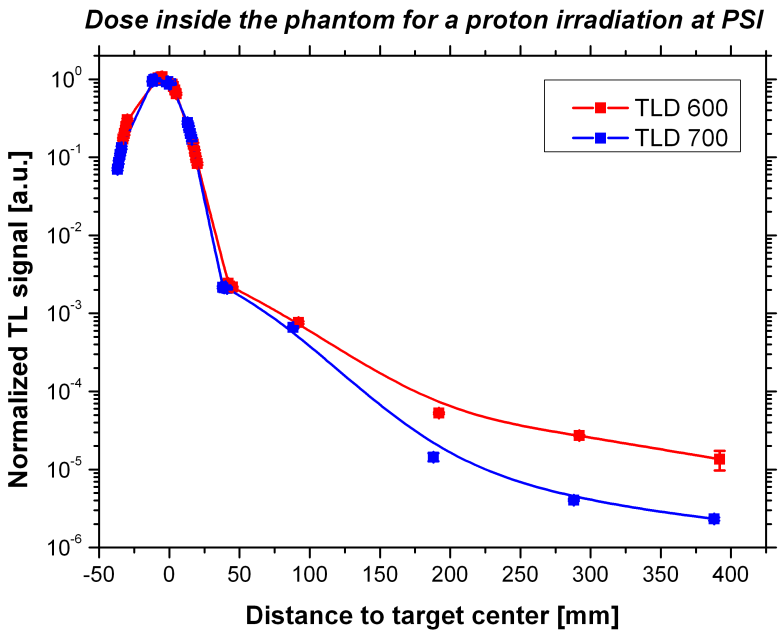

Figure 118: Dose in the main axis of the anthropomorphic phantom treated with scanned protons at PSI Gantry 1.

The results from the TLDs placed on the surface of the phantom are reported in Fig. 119. Out-of-field the dose is about one order of magnitude higher on the surface compared to the inner regions. However, this increase is in a dose region less than three orders of magnitude compared to the target dose. The difference between the TLD 600 and TLD 700 is almost negligible on the surface compared to the difference inside the phantom. Almost no slow neutrons are measured on the surface, indicating that either the neutrons measured inside are produced in the phantom or that fast neutrons produced in front of the patient are moderated to thermal energies.

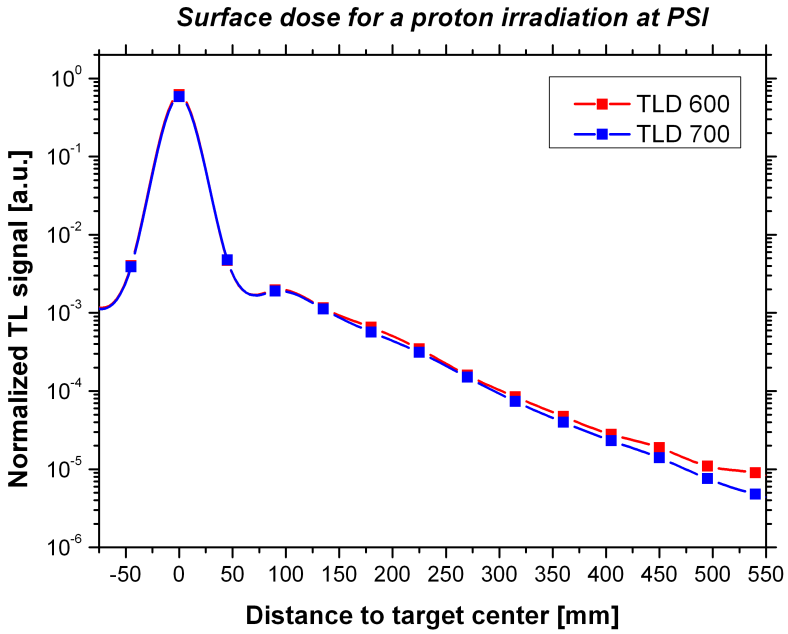

Figure 119: Surface dose along the phantom main axis measured with TLD 600 and TLD 700 for a treatment with scanned protons at PSI.

Spatial distribution

The spatial distribution of the dose measured by TLD 700 in slice 4 is plotted in Fig. 120. A slight asymmetry is observed suggesting a small tilt of the phantom during irradiation, which however has no effect on the dose far out-of-field. An increased dose in the dorsal part is observed in comparison to the ventral side, corresponding to the position of the plateau and the tail of the spread out Bragg peak respectively. The small misalignment is also indicated by the dose distribution in slice 5 (Fig. 121).

Slices 14 and 20 also show a higher dose in the dorsal part (entrance channel) than in the ventral (tail) (Figs. 122 and 123). The colour plots show a large decrease in the dose between slice 14 and 20.

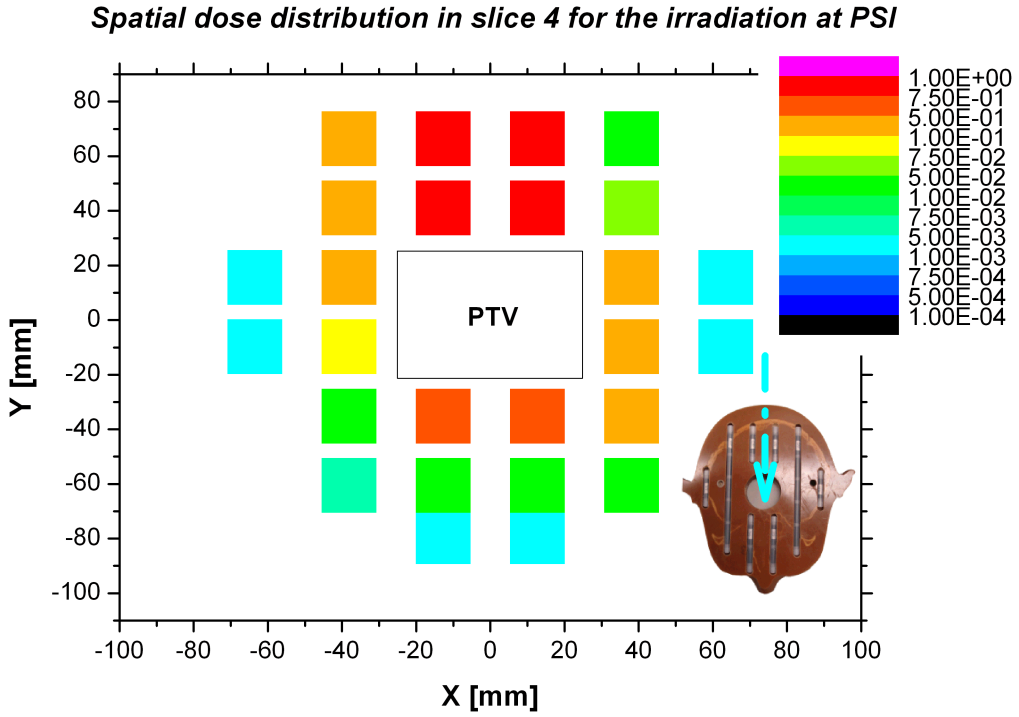

Figure 120: Spatial distribution of the dose measured by the TLD 700 in slice 4 for an irradiation with scanned protons at PSI. The small photo in the bottom right corner illustrates the irradiation direction for this treatment.

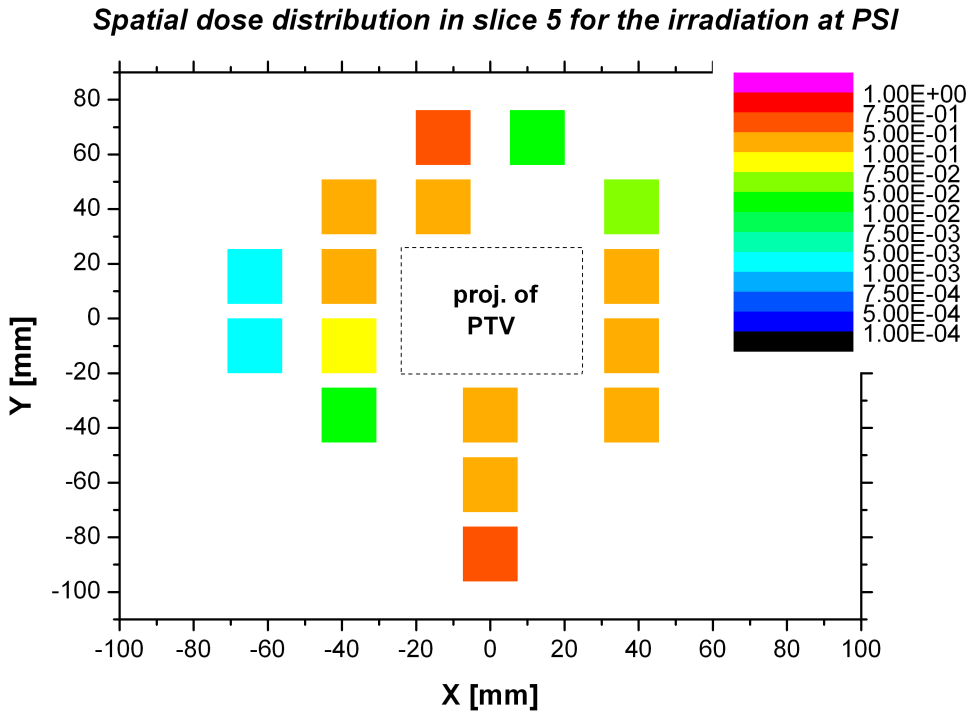

Figure 121: Spatial distribution of the dose measured by the TLD 700 in slice 5 for an irradiation with scanned protons at PSI.

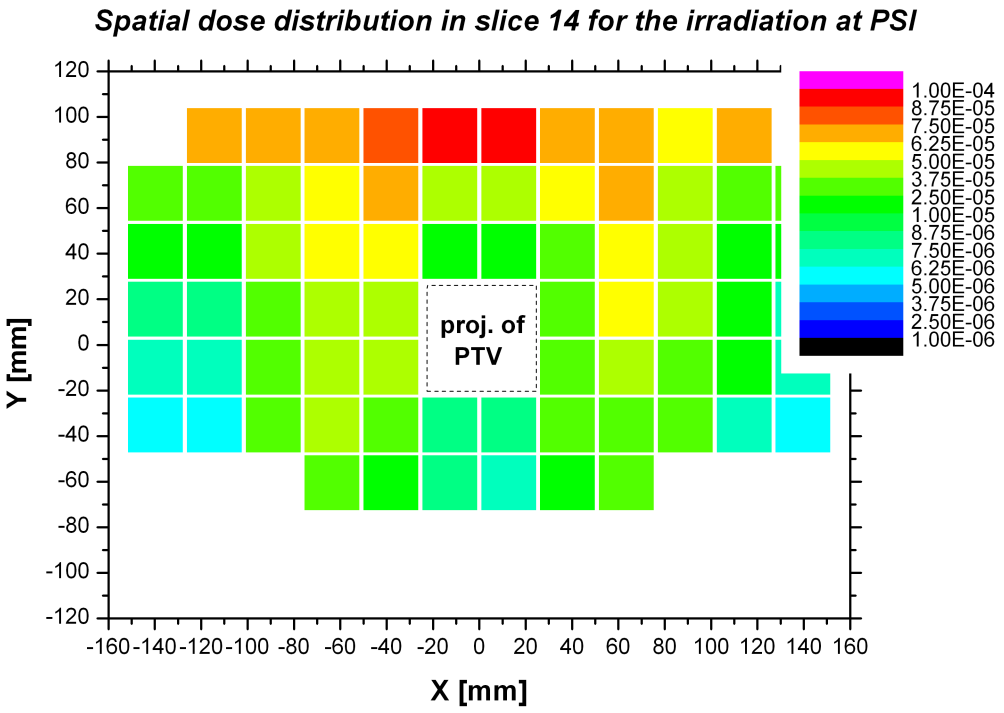

Figure 122: Spatial distribution of the dose measured by the TLD 700 in slice 14 for an irradiation with scanned protons at PSI.

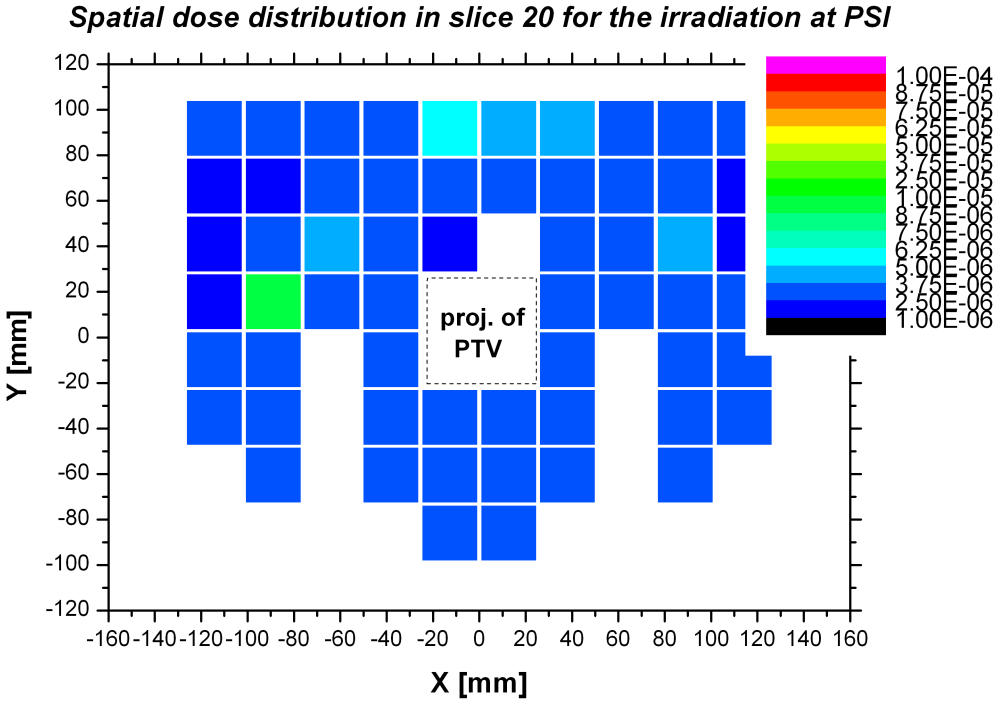

Figure 123: Spatial distribution of the dose measured by the TLD 700 in slice 20 for an irradiation with scanned protons at PSI.

In the coronal cut of the phantom (Fig. 124) a dose increase is seen in the medial parts of the body for slice 3,4 and 5 while a small decrease in the medial parts is observed for slice 14; in slice 20 the dose is almost constant.
The sagittal cuts depicted in Fig. 125 and 126 show the relation of the dose in the plateau and the tail in slice 4. However, the dose behaviour seems inverted in the upper slices (3,4 and 5) for X=38.1 mm. This effect might be caused by the misalignment of the phantom increasing the dose at the ventral parts of the cut.

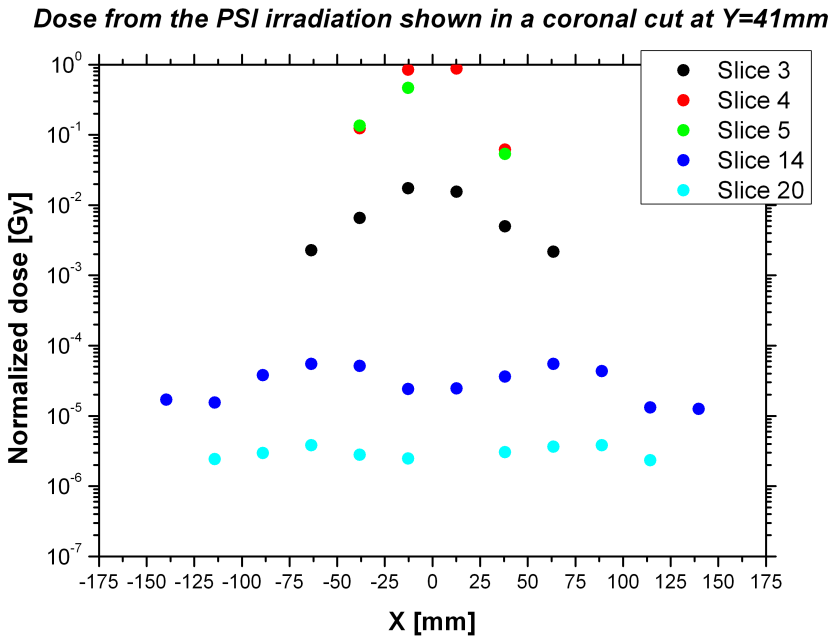

Figure 124: Coronal cut of the phantom at Y=40.8 mm, TLD 700 results for an irradiation with scanned protons at PSI.

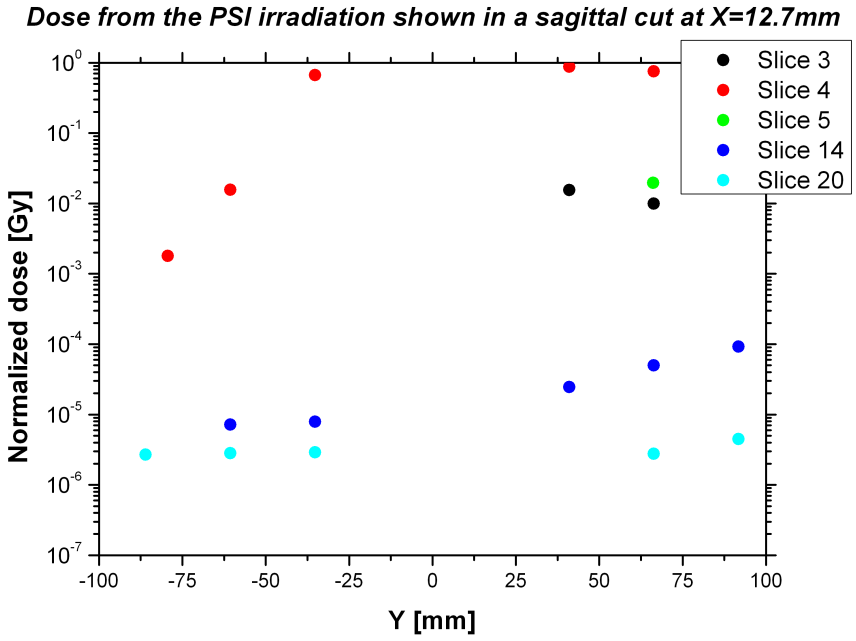

Figure 125: Normalized dose measured by the TLD 700 shown as a sagittal cut at X=12.7 mm for an irradiation with scanned protons at PSI.

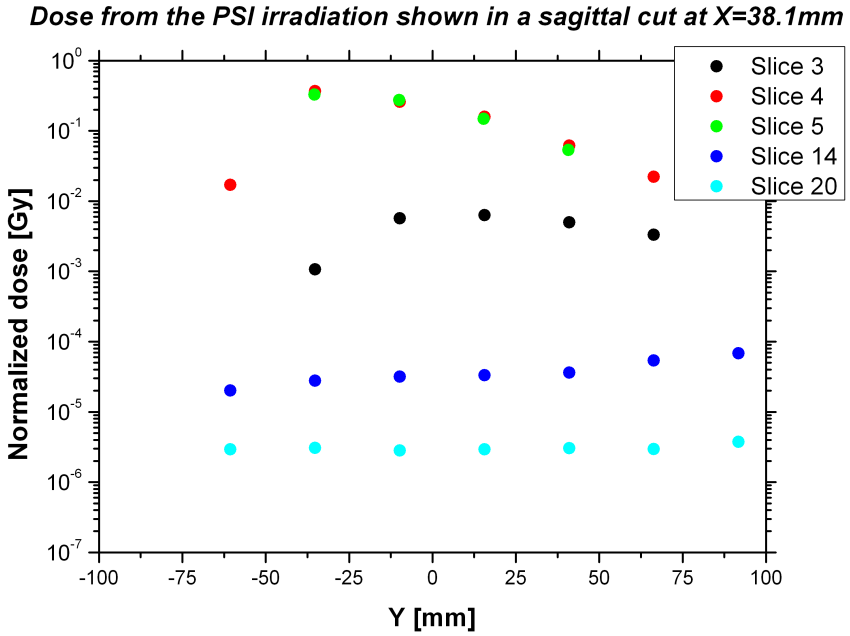

Figure 126: Normalized dose measured by the TLD 700 displayed as a sagittal cut at X=38.1 mm for an irradiation with scanned protons at PSI.

7.4 Irradiation with passively shaped carbon ions (HIMAC)

The irradiation with passively shaped carbon ions was performed at the vertical treatment room of HIMAC. For this treatment the phantom was lying on the back on the patient table, and irradiated in the anterior-posterior direction. The dose values along the phantom main axis are plotted in Fig. 127 for TLDs and the diamond detector.
In field the response from the TLDs is lower compared to the diamond detector because of the decreased relative TL efficiency due to the high LET particles. Outside the field the diamond detector shows a slightly higher dose than the TLD 700, maybe explained by the sensitivity of the diamond detector to neutrons in the region of several MeV. The TL signal from the TLD 600 is significantly higher than the TLD 700, indicating, as for passively modulated protons, an increased amount of low-energy neutrons. The dose observed with the TLD 700 drops down to about 10^{-4} of the target dose.

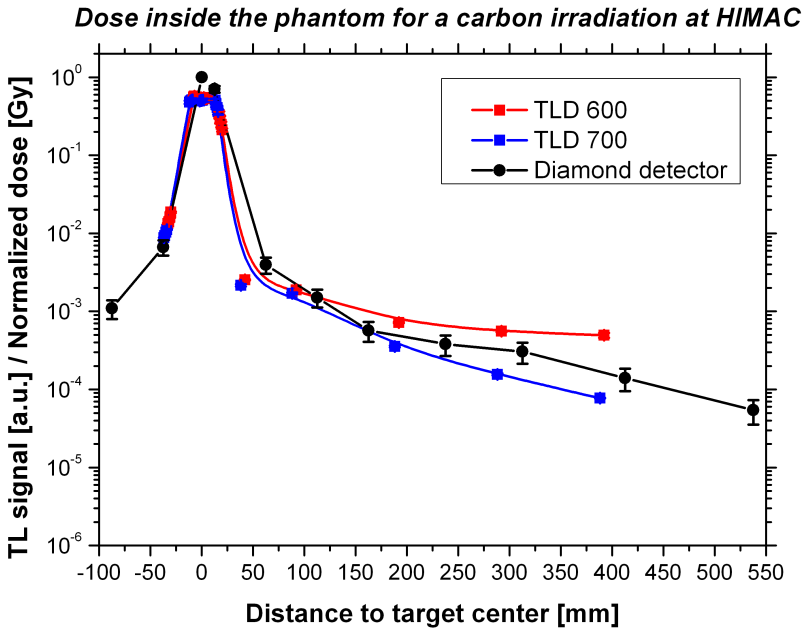

Figure 127: Dose inside the anthropomorphic phantom treated with passively shaped carbon ions at HIMAC.

The surface dose measurements for the TLD 600, TLD 700 and the diamond detector are plotted in Fig. 128. The difference in the field is explained by the fact that the TLDs were placed directly in the field whereas the diamond detector was placed on the edge. The source for the discrepancy between the TLD 700 and the diamond detector at 100 mm from the target is unknown. The data from both detectors agree very well in the out-of-field region. As for measurements inside the phantom, a visible increase of the TLD 600 over the TLD 700 TL signal is observed.

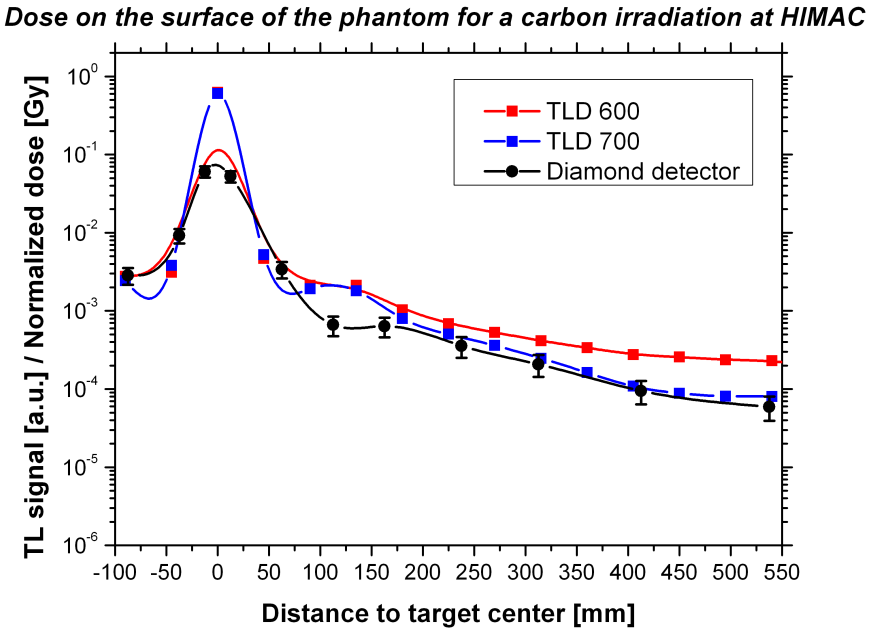

Figure 128: Surface dose measured with TLDs and the diamond detector for an irradiation with passively modulated carbon ions at HIMAC.

Spatial distribution

The irradiation in anterior-posterior direction is clearly visible in the spatial distribution of the dose. The results for the TLD 700 placed in slice 4 are shown in Fig. 129. Contrary to the irradiation at TSL and PSI (irradiation in posterior-anterior direction), the dose is higher in the ventral part of the head. No misalignment can be observed in this irradiation. The colour plot of TLD 700 in slice 5 depicted in Fig. 130 shows no large dose fluctuations within the slice.

In the colour plots for TLD 700 in slices 14 and 20 a higher dose is observed in the ventral part (Figs. 131 and 132), corresponding to the entrance channel in slice 4. A relatively small dose decrease is observed with increasing slice number.

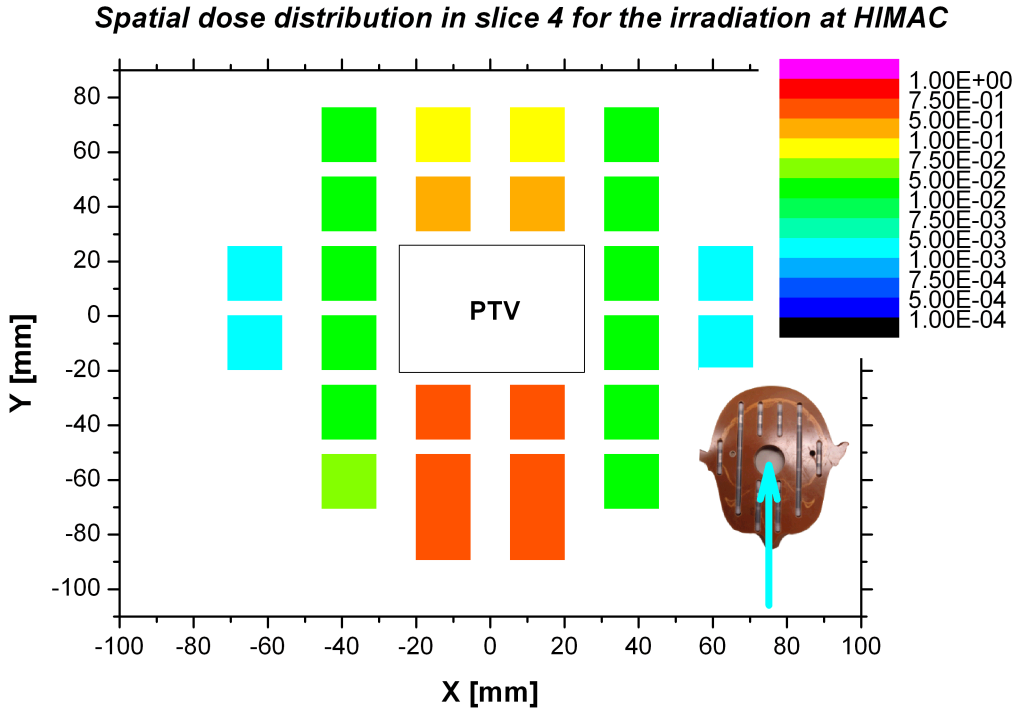

Figure 129: Spatial distribution of the dose measured by the TLD 700 in slice 4 for an irradiation with passively modulated carbon ions at HIMAC. The small photo in the bottom right corner illustrates the irradiation direction for this treatment.

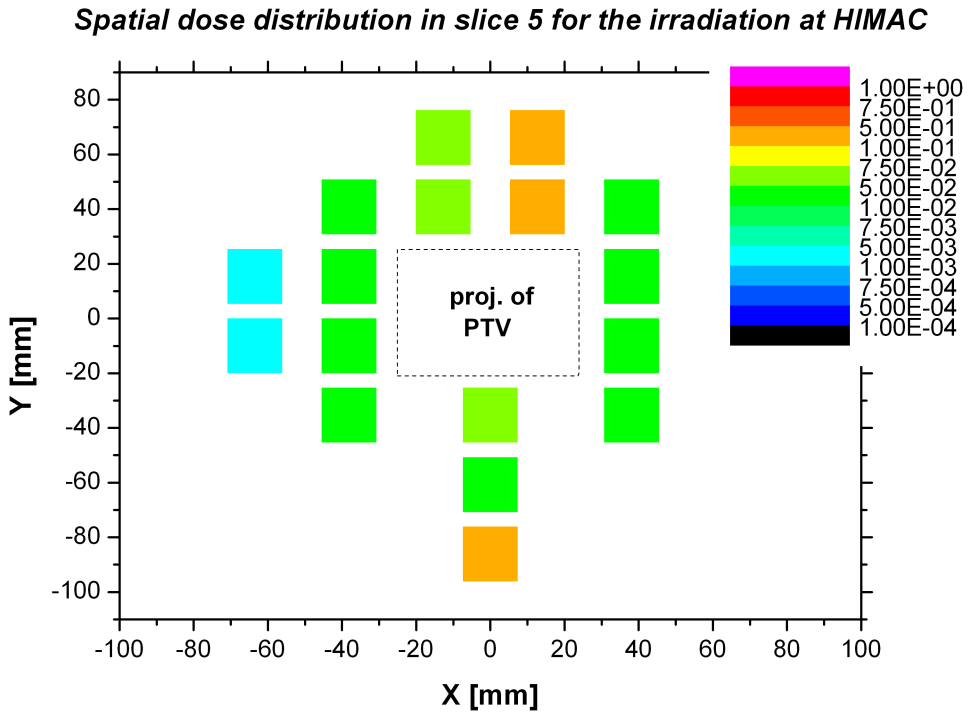

Figure 130: Spatial distribution of the dose measured by the TLD 700 in slice 5 for an irradiation with passively modulated carbon ions at HIMAC.

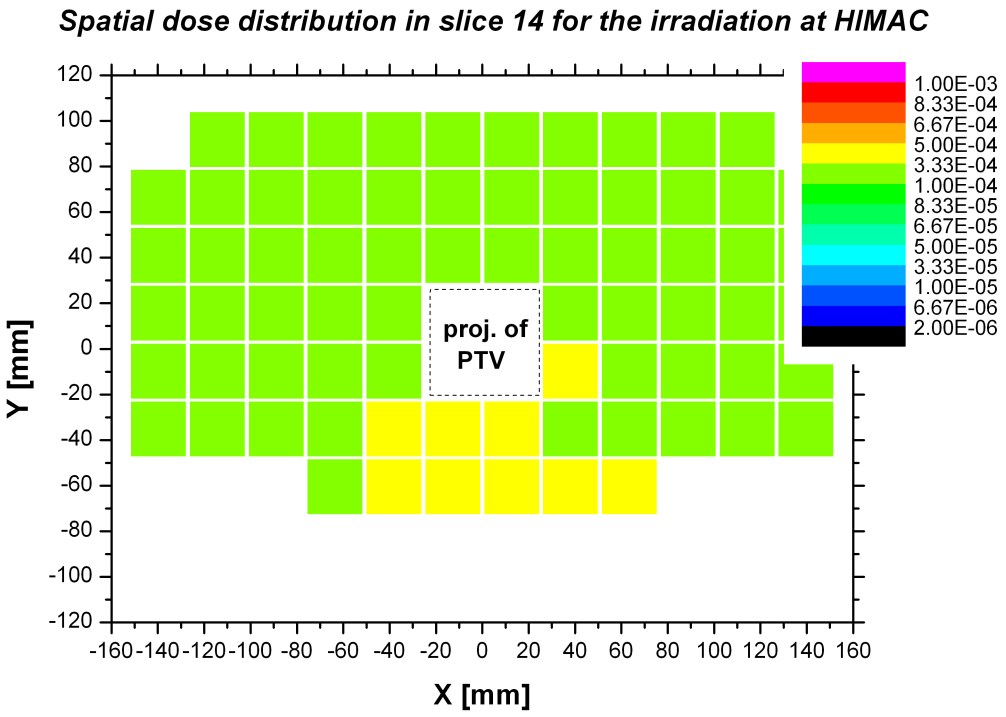

Figure 131: Spatial distribution of the dose measured by the TLD 700 in slice 14 for an irradiation with passively modulated carbon ions at HIMAC.

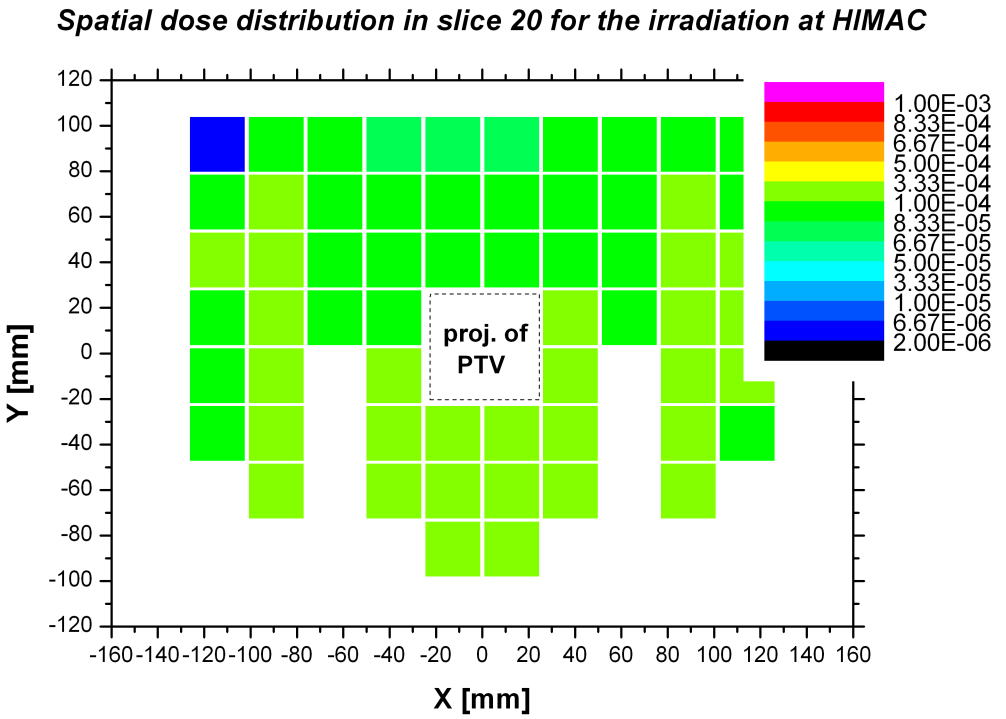

Figure 132: Spatial distribution of the dose measured by the TLD 700 in slice 20 for an irradiation with passively modulated carbon ions at HIMAC.

The coronal cut of the phantom (Fig. 133) shows an increase of the dose in the medial parts. Since the irradiation at HIMAC was the only facility where the irradiation was performed in anterior-posterior direction, an additional coronal cut was performed in the ventral side of the body at Y=-35.2 mm for the two lowest slices and included in the figure. No significant difference can be observed in the lower slices between the dorsal and ventral positions, indicating that there is only a small dependence of the dose on the irradiation direction far from the target.

The sagittal cuts (Figs. 134 and 135) confirm a higher dose in the ventral parts of the body for the slices in the head, while at large distances from the target (i.e. slices 14 and 20) no significant changes are observed between the dorsal and ventral positions.

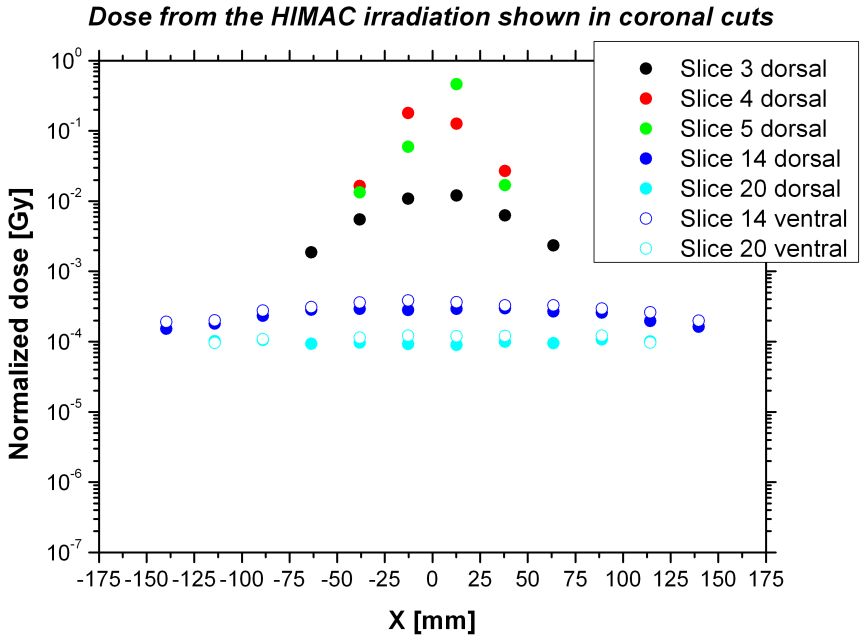

Figure 133: Coronal cut of the phantom at Y=40.8 mm (dorsal part of the body) and at Y=35.2 mm (ventral part of the body), TLD 700 results for an irradiation with passively modulated carbon ions at HIMAC.

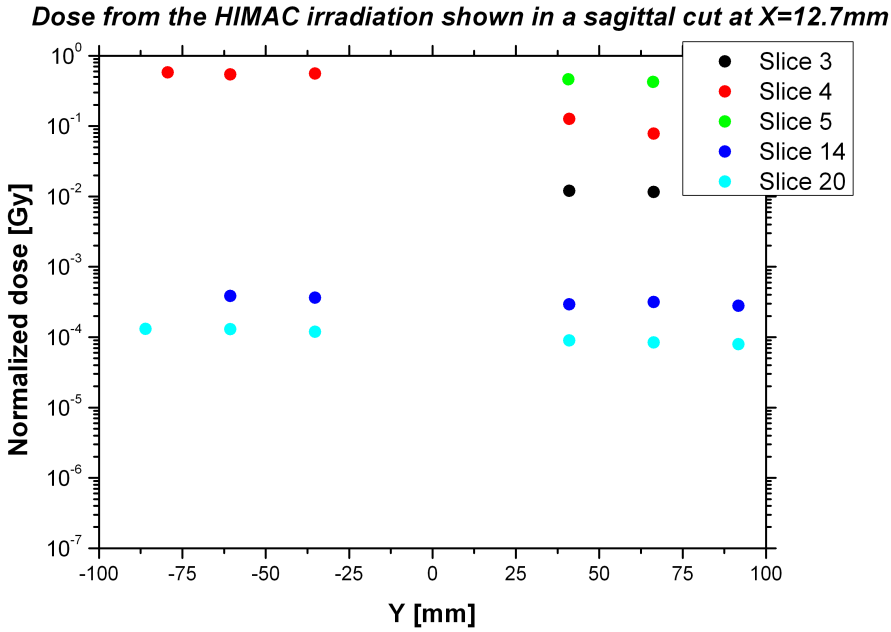

Figure 134: TLD 700 results, sagittal cut at X=12.7 mm for an irradiation with passively modulated carbon ions at HIMAC.

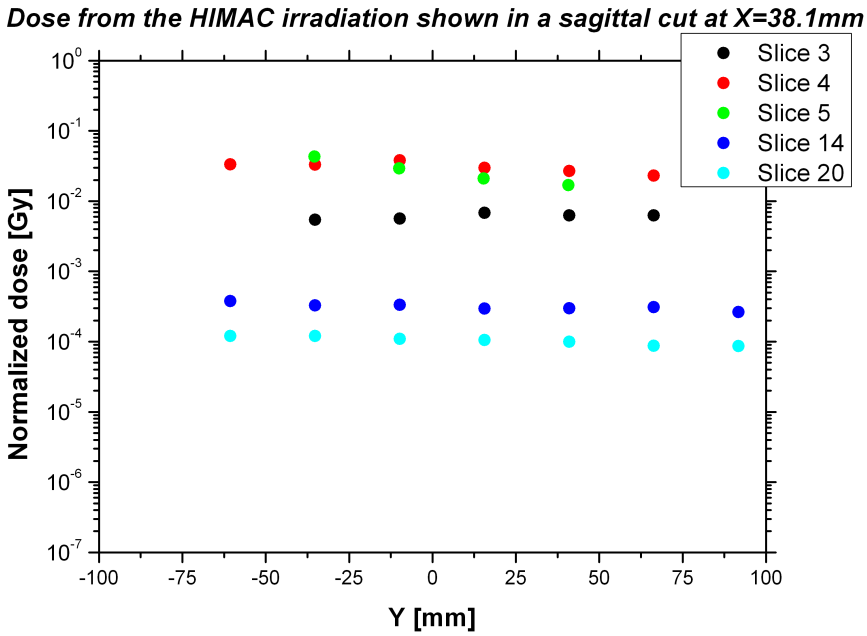

Figure 135: TLD 700 results, sagittal cut at X=38.1 mm for an irradiation with passively modulated carbon ions at HIMAC.

The dose values collected with TLD 600 and TLD 700 along the phantom main axis following irradiation with scanned carbon ions in posterior-anterior direction at GSI are reported in Fig. 136.

As for all experiments, a high dose gradient is measured by the TLDs close to the field while outside a slower drop down to about 10^{-6} of the target dose is seen. Only a small difference can be observed between the TLD 600 and TLD 700 indicating a low production of slow neutrons.

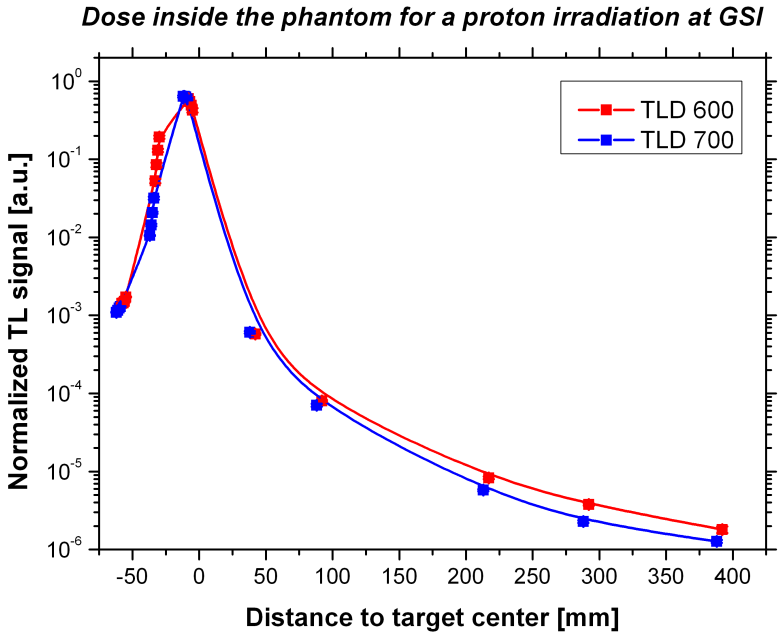

Figure 136: Dose inside the anthropomorphic phantom after irradiation with scanned carbon ions at GSI.

Spatial distribution

The irradiation in posterior-anterior yields a higher dose in the entrance channel in the dorsal part of slice 4 compared to the tail in the ventral part (Fig. 137). A relatively homogeneous dose distribution is seen in slice 5 (Fig. 138) and in the lower slices (Figs. 139 and 140).

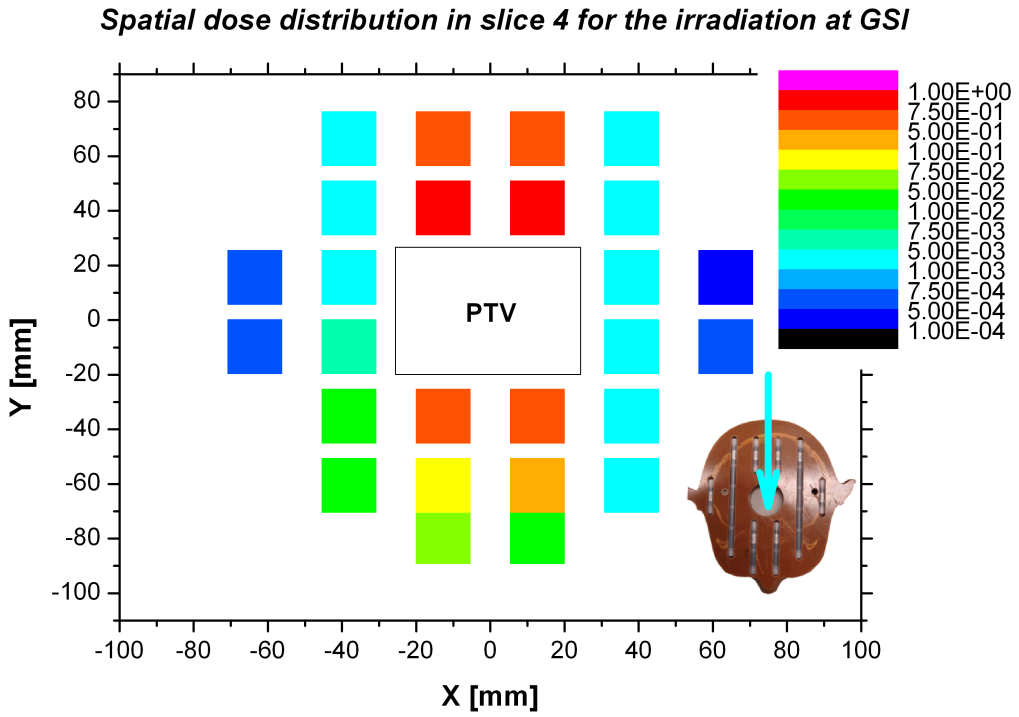

Figure 137: Spatial distribution of the dose measured by the TLD 700 in slice 4 after irradiation with scanned carbon ions at GSI. The small photo in the bottom right corner illustrates the irradiation direction for this treatment.

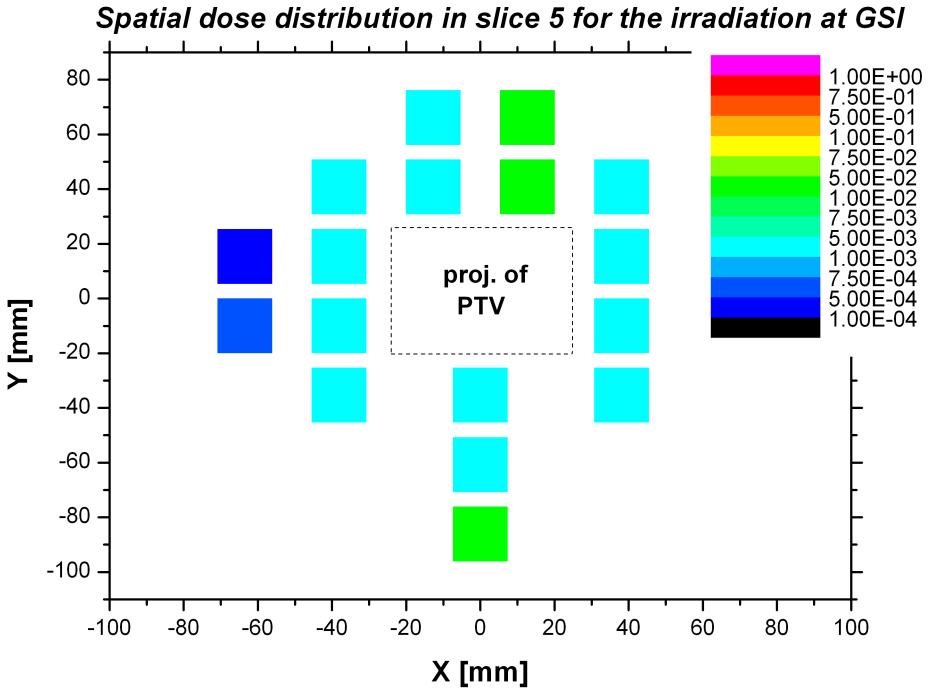

Figure 138: Spatial distribution of the dose measured by the TLD 700 in slice 5 after irradiation with scanned carbon ions at GSI.

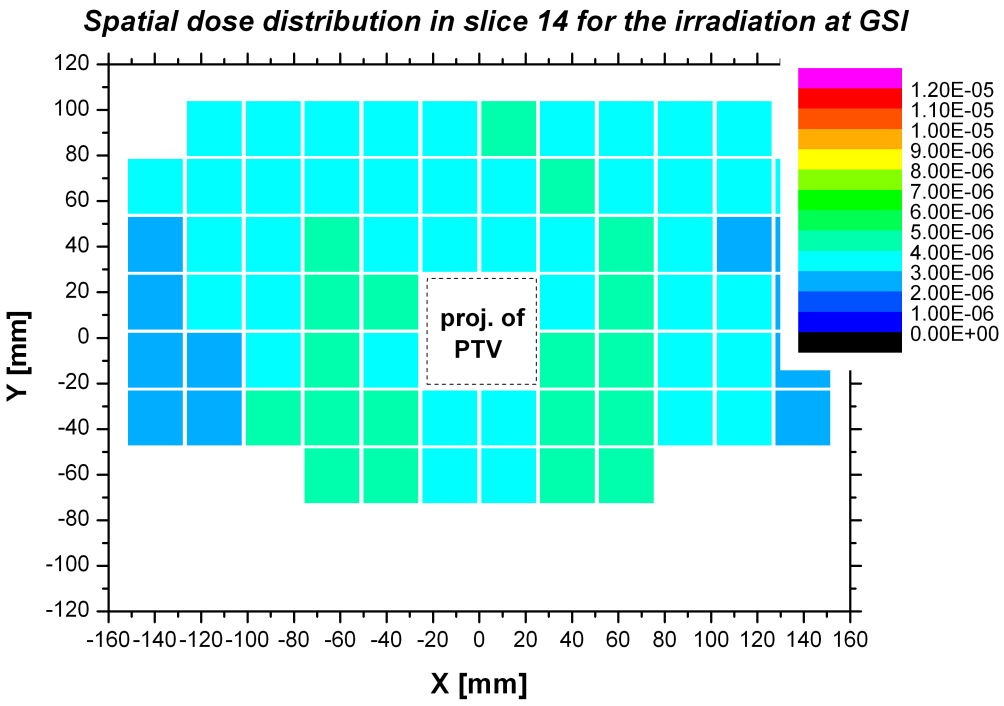

Figure 139: Spatial distribution of the dose measured by the TLD 700 in slice 14 after irradiation with scanned carbon ions at GSI.

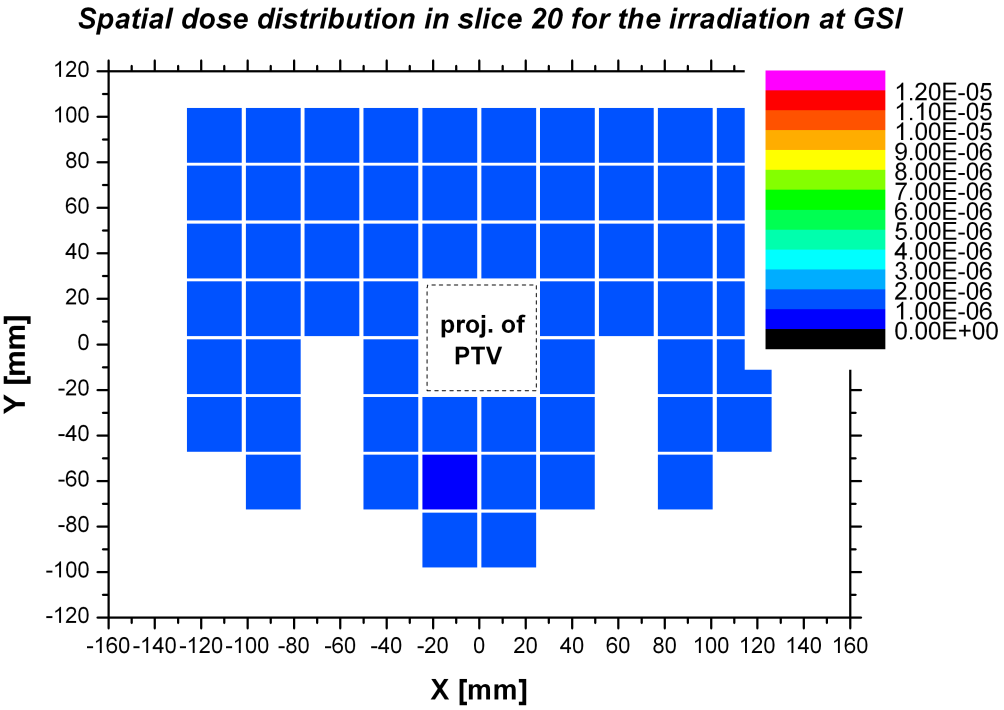

Figure 140: Spatial distribution of the dose measured by the TLD 700 in slice 20 after irradiation with scanned carbon ions at GSI.

The coronal cut is reported in Fig. 141 and the sagittal cuts in Figs. 142 and 143. When going to slices further away from the target the dose decreases. The dose in the upper slices is increased when close to the entrance channel; no large differences in the dose distribution can be seen within the bottom slices.

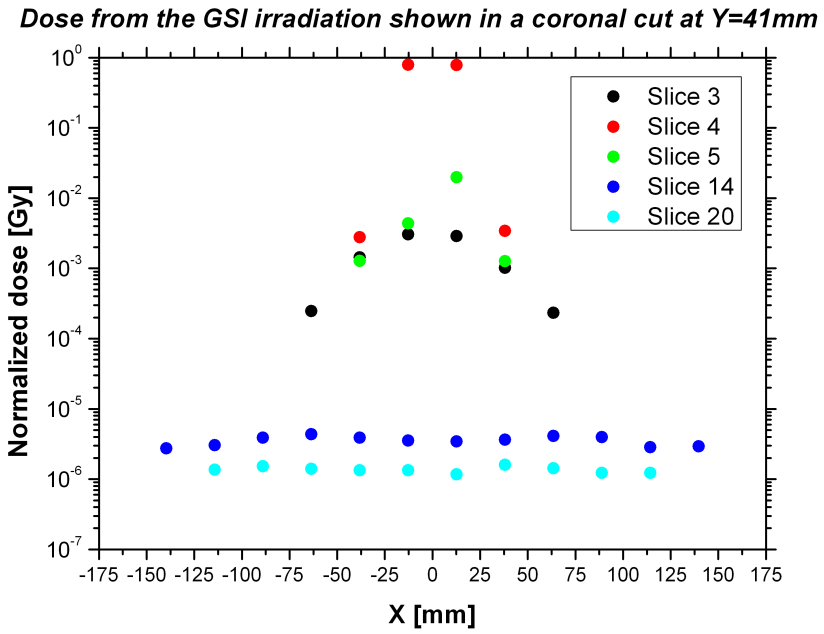

Figure 141: Coronal cut of the phantom at Y=40.8 mm, TLD 700 results after irradiation with scanned carbon ions at GSI.

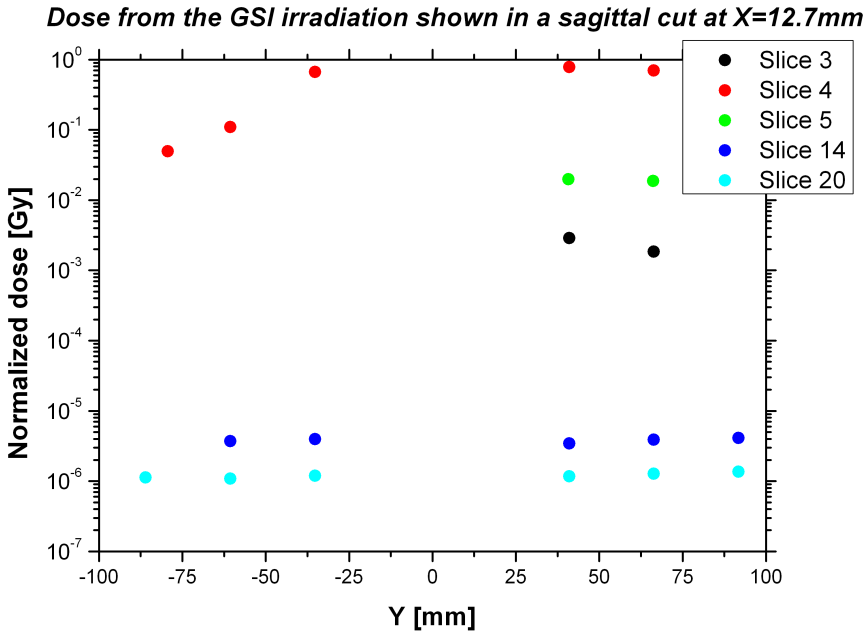

Figure 142: Sagittal cut of the GSI results at X=12.7 mm after irradiation with scanned carbon ions at GSI.

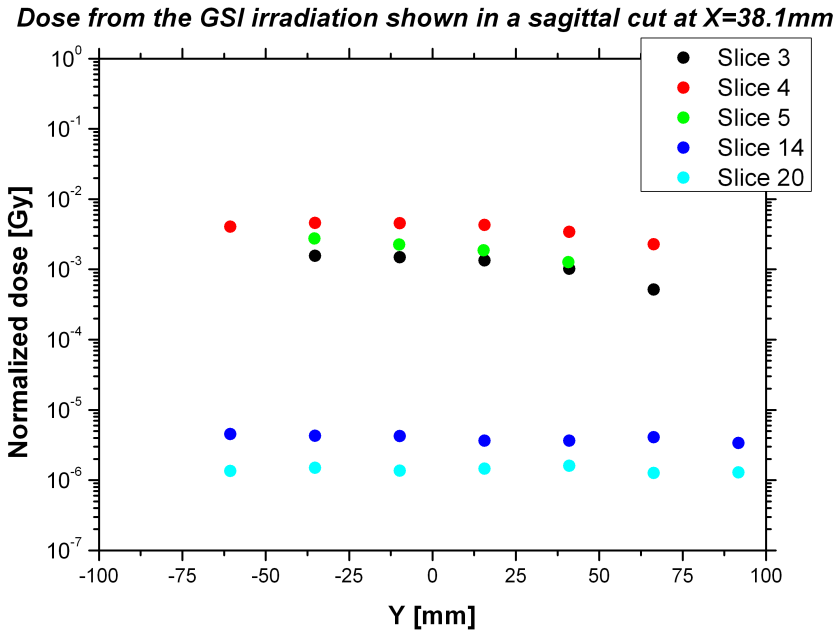

Figure 143: Sagittal cut of the GSI results at X=38.1 mm after irradiation with scanned carbon ions at GSI.

Inside the phantom

This section summarizes the findings of the irradiation of a rectangular cuboid in the anthropomorphic phantom using several treatment types. The dose profiles measured along the phantom main axis with TLD 700 are summarized and compared for all treatment types in Fig. 144. The results of the TLD 700 represent directly the absorbed dose and agree well with the diamond detector results. The difference of the TL signal for TLD 600 and TLD 700 is plotted in Fig. 145 and can be used to qualitatively compare the low-energy neutron yield of all techniques.

The small dose differences registered in Fig. 144 for the TLD 700 in the regions nearby the target can be mainly attributed to slight misalignments of the phantom during the irradiations; however, the positioning errors are negligible out-of-field.
Overall, the IMRT treatment yields the highest out-of-field dose delivered by leaked and scattered photons and photoneutrons. The irradiation with passively delivered carbon ions has the second highest out-of-field dose, where fragmentation of the primary particles in the bolus is expected to give the major contribution.
As for the data measured in the water phantom, the comparison of the results of protons passively modulated and scanned does not lead to a final conclusion. While the out-of-field dose close to target is lower when using a collimator, the dose far out-of-field is smaller when applying the scanning technique. The latter difference might be even more pronounced when the contribution from neutrons is considered. One also has to note that in this experiment a rectangular cuboid was chosen as target. When irradiating an irregularly shaped target (as it is typical for tumours), the normal tissue in the proximal part of the patient receives additional dose when using passive modulation, resulting in a higher integral dose for the patient compared to the scanning technique.
When comparing the dose measured by TLD 700 for scanned protons and carbon ions, the difference decreases with increasing distance to the target: the large difference close to the field is caused by the larger lateral straggling of protons compared to heavier ions. Several considerations need to be taken into account for a correct interpretation of the data collected in the out-of-field sites: as observed from the measurements in the water phantom, the lateral dose profile far from the field for carbon ions is strongly dependent on the beam energy because of fragmentation. The out-of-field dose for protons was found to have only a small dependence on the energy at large distances to the target. In particular, it was proven that the out-of-field dose delivered by a carbon beam is lower than for protons at small ranges, whereas the opposite is true for higher energies. Thus, for a deep seated tumour, for example in the prostate, higher energies would be required increasing the out-of-field dose deposited by carbon ions.

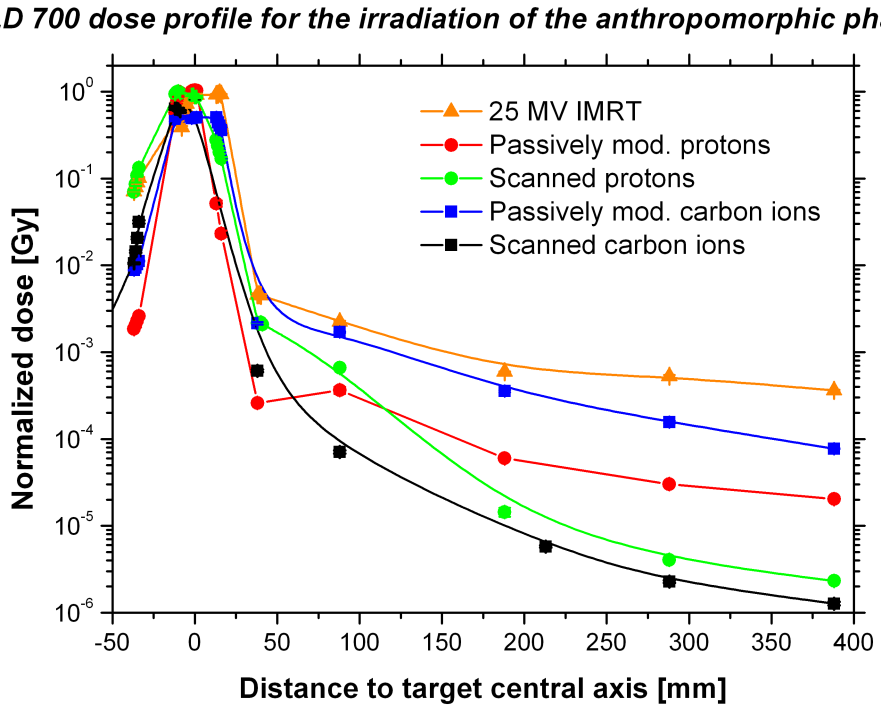

Figure 144: Comparison of the TLD 700 results inside the anthropomorphic phantom for all treatment techniques.

On the other hand, the measured absorbed dose profile may represent the worst case scenario for carbon ions as it does not include their biological effectiveness. In fact, the treatment was not optimized biologically. It is known that the RBE in the target is elevated compared to the surrounding tissue. Thus, when considering the biological dose in a patient for risk determination, the ratio between the dose in the target and the out-of-field positions is increased for carbon ions.

The evaluation of the difference of TLD 600 and TLD 700 leads to similar conclusions as for the TLD 700 only: the highest TL signal attributed to slow neutrons was obtained for IMRT photons followed by protons and carbon ions in passive delivery techniques. A low TL signal from TLD 600 is found for scanned protons and an even lower one for carbon ions. This result proves that the lowest yield of low-energy neutrons is provided by scanned carbon ions. However, it should be remembered that TLD 600 are only sensitive to neutrons with an energy of up to 200 keV and therefore will not detect the largest fraction of secondary neutrons produced by photons (in the order of 1 MeV) or charged particles (energy up to hundreds of MeV).

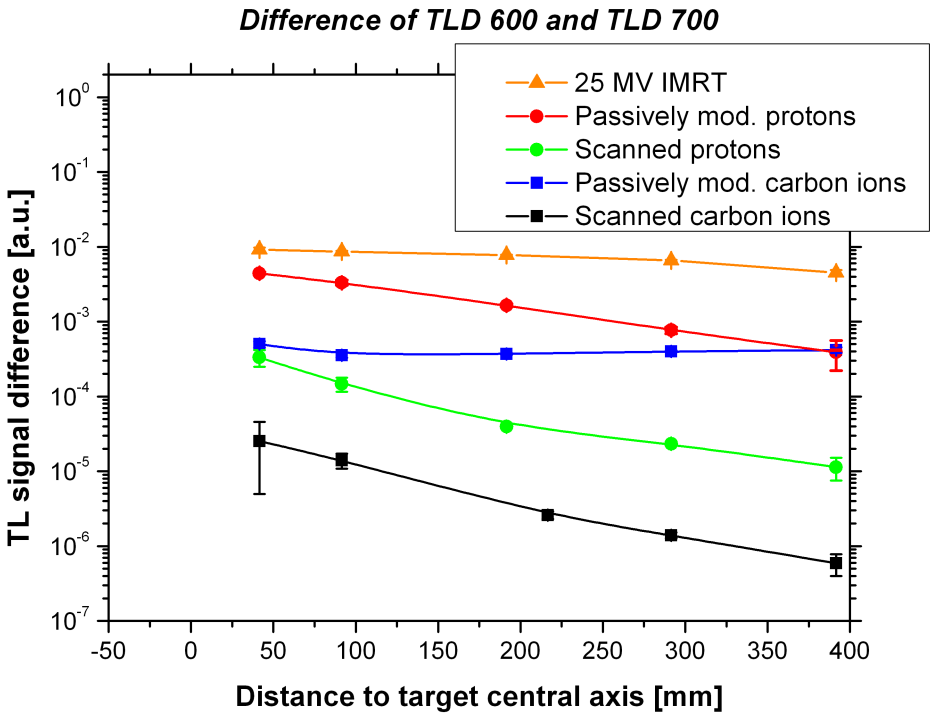

Figure 145: Comparison of the difference of the TLD 600 and TLD 700 TL signal inside the anthropomorphic phantom for all treatment techniques.

Surface dose

The surface dose was measured with TLDs and the diamond detector (Fig. 146). The surface dose in field from passive protons seems highest, however one has to keep in mind that in the field small differences in the positioning may lead to large changes of the results because of the high gradient. The data in the field therefore have to be taken with care.
For photons, the dose on the surface is small in-field, since the IMRT irradiation is performed using seven fields, thus distributing the surface dose to more positions.
Out-of-field, the dose is lowest in most positions for the passive proton technique and highest for the IMRT. The differences between the techniques are about one order of magnitude on a dose level of 10^{-3} to 10^{-5} of the dose in the target. The collimator, which is placed directly in front of the bolus, produces a sharp field edge stopping the primary protons that have scattered laterally and would contribute to the surface dose. Correlating with the outer edge of the collimator, an increase of the dose for the passively modulated protons is observed with the diamond detector at a distance of 12 cm to the target edge. However, the stopping of high-energy protons in the collimator and other parts of the beamline generates high energetic neutrons that can not be measured using the TLDs. A dedicated study is recommended to address this issue.

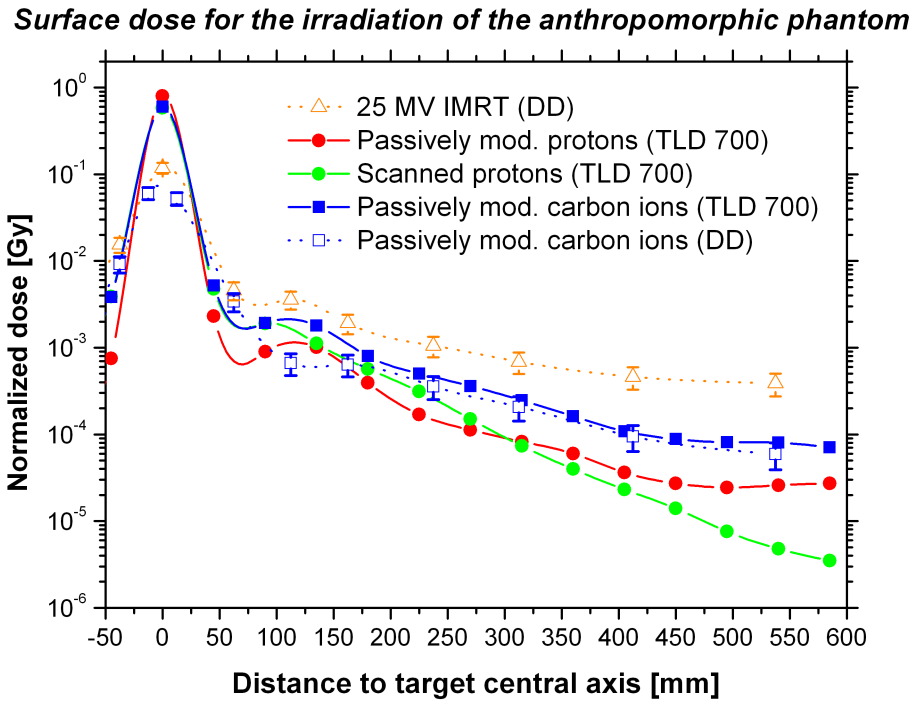

Figure 146: Surface dose measured with the TLD 700 and the diamond detector in the irradiation of the anthropomorphic phantom.

Spatial distribution

The 2D dose distributions were shown before for all delivery techniques according to sagittal and coronal cuts. The data measured with TLD 700 in slice 4 are plotted in a coronal cut in Fig. 147. For all charged particle therapies the central points are comparable and lie in the entrance channel except for the irradiation at HIMAC where they lie in the tail of the SOBP, where the dose is known to be lower than in the plateau.
The plot also demonstrates the high target conformality that can be achieved with a single field with charged particles. In contrast, to achieve a homogeneous dose distribution in the target requires many fields for photons. Thus, an IMRT treatment delivers a higher dose to more positions around the target.
Furthermore, a low dose is registered in the lateral points for carbon ions and passively modulated protons, caused by the small scattering of carbon ions and the sharp edge produced by the collimator respectively. Both carbon ions and passively modulated protons are characterized by a lower dose in the lateral points than IMRT and scanned protons.

The data selected by the coronal cut in slice 20 (Fig. 148) agree with the profile measured along the phantom main axis, where the IMRT provided the highest out-of-field dose and scanned carbon ions the lowest.
The sagittal cut in slice 4 at X=12.7 mm is shown in Fig. 149. The data reflect the Bragg curves in the irradiation direction. Passively shaped carbon ions deliver a higher dose in the ventral part, whereas the other charged particles show an inverse dose distribution. For photons the dose distribution is relatively symmetric as the irradiation was delivered from 7 fields.

In a further sagittal cut at X=38.1 mm, the Bragg curve of the primary beam can still be seen (Fig. 150). For carbon ions and photons, the dose deposition is generally homogeneous; a small peak in the medial part is seen for the latter. The difference between photons and charged particles is more pronounced in this case than in the entry channel.

The sagittal cut at X=12.7 in slice 20 (Fig. 151) gives similar results to the coronal cut (Fig. 148). The results relative to the phantom main axis are confirmed.

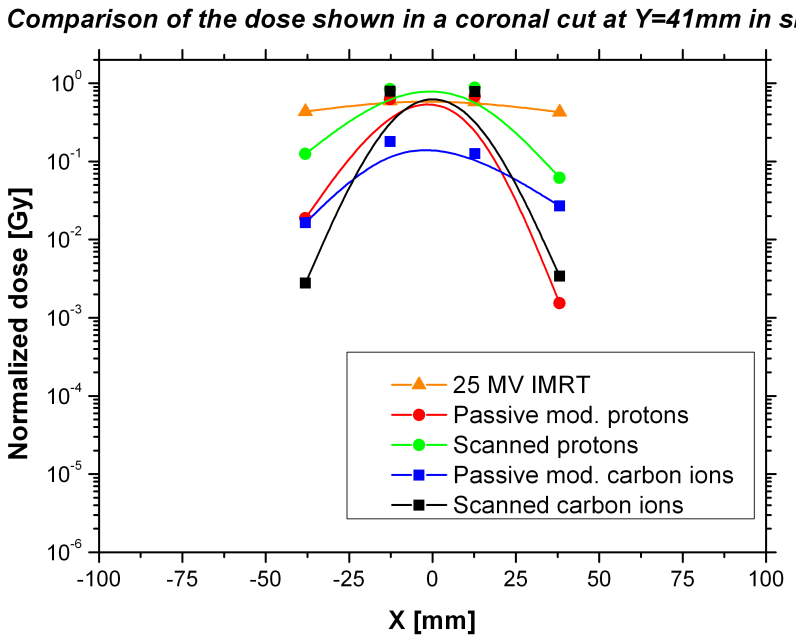

Figure 147: TLD 700 results shown in a coronal cut at Y=41 mm in slice 4 (target slice).

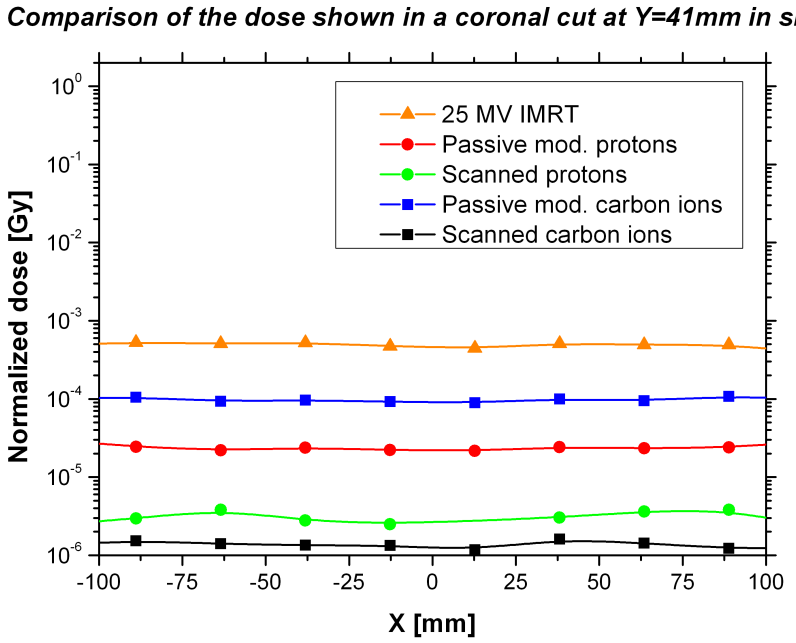

Figure 148: TLD 700 results shown in a coronal cut at Y=41 mm in slice 20.

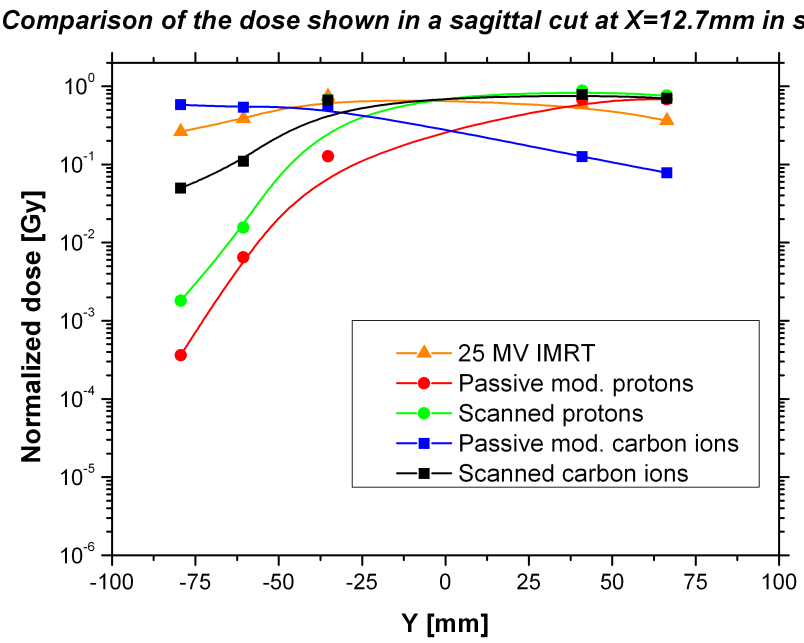

Figure 149: TLD 700 results shown in a sagittal cut at X=12.7 mm in slice 4(the target slice).

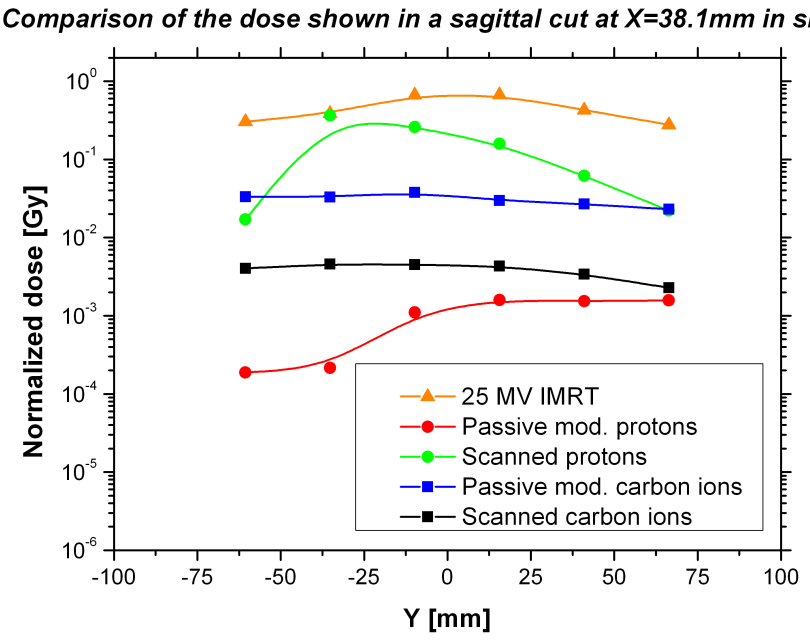

Figure 150: TLD 700 results shown in a sagittal cut at X=38.1 mm in slice 4.

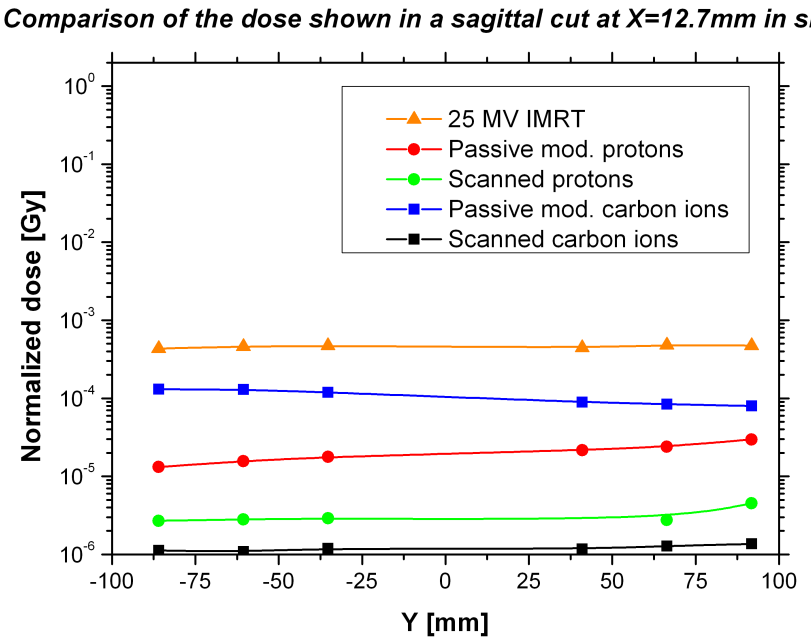

Figure 151: TLD 700 results shown in a sagittal cut at X=12.7 mm in slice 20.

Conclusions

The following conclusions can be drawn from all results collected in the irradiation of the anthropomorphic phantom:

- far out-of-field, the dose measured by TLD 700 along the phantom main axis is highest in IMRT, decreasing for passively modulated carbon ions and protons and being lowest for scanned protons and carbon ions;
- for all treatments the dose inside the phantom at 40 cm distance to the field is below 10^{-3} of the target and drops to 10^{-6} for scanned ions;
- the results obtained with TLD 600 show a large increase of the TL signal in photon therapy and passive modulation techniques attributed to an increased (low-energy) neutron yield;
- the data collected with the diamond detector along the main axis show good agreement with the TLD 700 results;
- the surface dose is highest for the IMRT treatment and is comparable for passive shaping and scanning in ion therapy;
- around the target, the 2D dose distribution is relatively homogeneous for photons while it is highly dependent on the irradiation direction for charged particles (i.e. the Bragg curve);
- the 2D dose profile is distributed homogeneously for all techniques in slices far away from the target volume;
- the dose measured in the far out-of-field slices is similar to the results obtained along the phantom main axis

Conclusions and outlook

The experiments described in this study provide a large database for the evaluation and comparison of different radiotherapy techniques in the view of out-of-field dose and secondary cancer risk. Furthermore, it raised questions that require further investigation to be answered.

The measurements performed with the water phantom (simple geometry) have proven that photon therapy is characterized in general by a higher overall out-of-field dose than ion therapy. When comparing the particle therapy techniques, many parameters like beam energy and target size have to be considered. When using the scanning technique, the out-of-field dose is higher when the target size increases, i.e. when more primary particles are required to deliver the dose. For passively shaped protons, an increase of the neutron dose is expected for smaller field sizes since more particles are stopped in the collimator, but no detailed measurements of the field size influence could be performed in this case.
No significant energy dependence of the lateral dose profile far out-of-field was found for protons. The energy dependence found in carbon therapy is mainly related to the fragmentation of the primary particles and is translated into an increased dose deposition with increasing beam energy. However, the raise is on a low level and the clinical relevance is questionable.
In photon therapy, the out-of-field dose deposited by photoneutrons was found to be relatively small (in the order of 1 mSv/treatment Gy). However, the isotropicity and the small lateral fall-off are of concern. On the other hand, the strong moderation of neutrons in water suggests simple solutions for shielding at least outside the field. In the field, a neutron dose of around 5 mSv per Gy in the target was measured on the water surface dropping rapidly at a depth of 10 cm. A neutron depth dose curve would be interesting to evaluate the dose they deliver to critical organs close to the target. Furthermore, the data with the anthropomorphic phantom suggest an enhanced photoneutron production in bones, which would require a dedicated investigation for risk analysis. The bubble detectors were found to represent a suitable but time-consuming tool for these purposes.
The aforementioned considerations indicate clearly the recommendations to manufacturers of linacs: the neutron dose can be further reduced by placing moderators on the outer walls of the treatment head. Their presence will not perturbate the treatment fields but, on the other hand, will not reduce the neutron dose in the target volume.
A further result observed from the water phantom data is the sharper penumbra of passively delivered protons compared to scanned protons. This result raises several questions. One could consider whether the sharper penumbra achievable by collimators would further improve scanning beam delivery; on the other hand, in medical applications the field irradiated is chosen somewhat larger than the clinically relevant target, and therefore a sharper gradient may not have any advantages. However, it may prove advantageous for the irradiation near organs at

risk. The use of collimators would require the solution of technical and physical issues. To benefit from sharper edges, a collimator would be necessary for each single energy slice in scanned treatment plans, i.e. an MLC would need to be implemented into the beamline. However, the benefit of the sharper edges may be largely outweighed by the biologically dangerous fragments produced in the collimator. Since carbon ions already have a sharp penumbra, this question is especially relevant for treatment with scanned protons, where the clinical benefit of sharper edges and the risk coming from the secondary neutron production have to be compared.

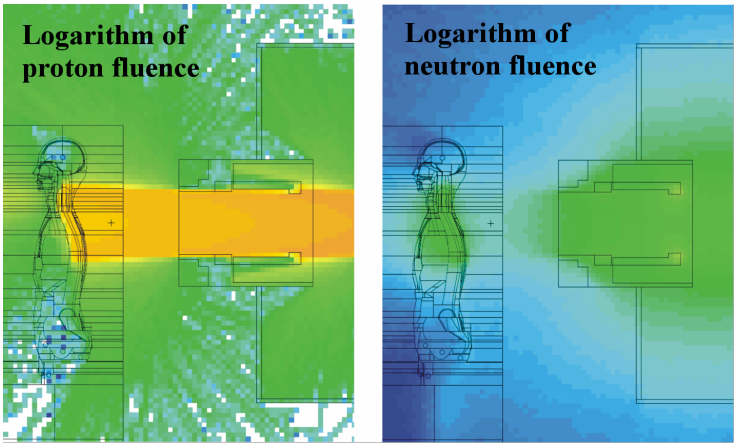

Figure 152: Monte Carlo simulation by (Newhauser et al., 2009) illustrating the therapeutically wanted proton beam on the left. The right side shows the potentially harmful "neutron bath" affecting a large volume of the body.

The last consideration states one of the most important issues to investigate in the near future in particle therapy. While the benefits of the scanning technique in tumour conformality are clear and are accepted by the community, the debate on the health risk caused by fast neutrons especially in passive beam shaping is still ongoing. The question arises, whether the improved dose conformality can justify the potential risks from the unwanted neutron bath the patient takes (Fig. 152). A significantly lower secondary cancer risk would represent another strong argument for the implementation of scanning delivery systems at existing facilities. In this study the difference of the TLD 600 and TLD 700 was used to compare qualitatively the low-energy neutron dose for passive and scanning beam delivery. For characterizing the fast neutron component so far only few experimental data are available such as (Yan et al., 2002; Schneider et al., 2002; Gunzert-Marx et al., 2008; Yonai et al., 2008) and Monte Carlo studies such as (Newhauser et al., 2009; Pshenichnov et al., 2005). While the increased number of low-energy neutrons was observed from the TLDs in passive therapy, a complete systematic comparison of the neutron spectrum and dose in both techniques is lacking. A follow-up of the ALLEGRO project might address this problem. A measurement of the neutron spectrum in passive and active beam delivery is recommended for example using the time of flight technique. Further investigations on the bubble detectors' sensitivity to charged particles as well as to high energetic neutrons may also help in this study. Ideally such a comparison could be performed at a

facility that provides both techniques with the same accelerator, thus the influence of other factors on the comparison could be minimized. At the present stage, the proton therapy facilities at MD Anderson and MGH in the US could be suitable candidates as they both provide passive and scanning modulations in clinical practice. As stated above, the biological effect of neutrons is energy dependent and therefore their energy spectrum is necessary for an accurate risk assessment.

Similar conclusions as for the water phantom can be drawn from the measurements with the anthropomorphic phantom. The lateral dose profile is higher for the treatment with IMRT than for charged particle therapy. Since the IMRT treatment is delivered from more fields than for ions, the spatial dose distribution in the former is relatively homogeneous while for the latter it is dependent on the direction of the irradiation. When comparing the results of charged particles, it should be noted that most irradiations are performed with two fields and not only one as in this study. In this way, the dose distribution is more homogeneous and the dose in the entrance channel is reduced. Furthermore, the RBE must be taken into account when translating the data to clinical risks. The RBE is elevated in the target for carbon ions improving the ratio of the dose in the target and in the surrounding tissue when considering the biological effects.
The 2D dose distribution measured in slices far from the treatment agree with the values collected along the phantom main axis enabling an extrapolation of the dose in the main axis to lateral organs.
Future measurements are recommended for further evaluating the LET spectrum of the radiation field outside the target and therefore to translate the physical data into a biological effect. At the present stage, only Monte Carlo simulations provide a detailed characterization of the field outside the treatment volume and could be verified using the dose measured in this study. Further experiments should also consider the investigation of the 3D dose profile following irradiation of different targets. The target in the head was chosen because of its clinical relevance especially for ion therapy, but the application of charged particles is expanding to more cases. For example, prostate cancer patients are treated with charged particles. The prostate is in close vicinity to many sensitive organs and represents a rather different scenario than the head and neck target investigated in this study as the target lies deeper requiring higher energies. Moreover, the beam has to traverse massive structure like thick bones in comparison with the thin layer in the head. The effects of bone on the therapeutic beam should be further investigated to account for neutron production (photon therapy) or increased beam spreading and fragmentation (ion therapy). Furthermore, the beam in treatments for prostate cancer sometimes has to traverse artificial hip joints, often made of titanium which is rather different from tissue. Repeating the experiment with the anthropomorphic phantom for a prostate would shed some light on the potential benefits of charged particles over IMRT. Moreover, experiments with simple geometries should be set up to measure the effect of bone and other materials on the beam.

In summary, this work represents the first systematic experimental comparison of conventional radiotherapy and ion therapy using the same conditions and detectors. The water phantom measurements helped to determine all parameters influencing the out-of-field dose profile allowing a more accurate understanding of their advantages and disadvantages than before. The detailed understanding of the parameters influencing the out-of-field dose will help to employ counter measures in the design of future treatment units.
Additionally, the comparison was repeated in the more realistic geometry of the anthropomorphic phantom which was never accomplished before. Using the same target for all treatment types will help answering the question whether particle therapy can reduce the secondary cancer incidence after irradiation. The main investigation of the health risks in radiotherapy will now have to concentrate on the biological and clinical aspects. The biological effect of low and very high doses delivered by photons and particles is the main question that needs to be answered as the uncertainties of the biological effects largely outweigh the precision of the physical measurements. In particular, for a complete understanding of the risk of developing a secondary cancer from radiotherapy more accurate dose-to-risk conversion factors are required. Both in-vitro and in-vivo biological studies are being performed and need to be completed in the future. The clinical analysis of data collected in the past decades will also help to evaluate this risk. It is obvious that this issue has started to receive some answers but will remain a hot and interesting topic in the years to come. The improved risk assessment and mitigation measures will be beneficial for many patients in the future.

References

[Barkas 1963] Barkas, H. W.: *Nuclear Research Emulsions*. Bd. Vol. 1. Academic, New York, 1963

[Bassler 2006] Bassler, N.: *Experimental Studies Relevant for Antiproton Cancer Therapy*, University of Aarhus, Denmark, PhD Thesis, 2006

[BEIR 2006] BEIR: Health risks from exposure to low levels of ionizing radiation *BEIR VII, Phase 2 /* National Research Council, National Academy of Science. 2006

[Berger 2003] Berger, T.: *Dose assessment in mixed radiation fields - special emphasis on space dosimetry*, Vienna University of Technology, PhD Thesis, 2003

[Berger and Hajek 2008] Berger, T. ; Hajek, M.: TL-efficiency – Overview and experimental results over the years. *Radiat. Meas.* 43 (2-6) (2008), 146–156

[Berman and Fultz 1975] Berman, B. L. ; Fultz, S. C.: Measurements of the giant dipole resonance with monoenergetic photons. *Rev. Mod. Phys.* 47 (1975), 713–761

[Bethe 1930] Bethe, H.: Zur Theorie des Durchgangs schneller Korpuskularstrahlen durch Materie. *Ann. Phys.* 397 (1930), 325–400

[Bloch 1933a] Bloch, F.: Bremsvermögen von Atomen mit mehreren Elektronen. *Z. Phys. A: Hadron Nucl.* 81 (1933), 363–376

[Bloch 1933b] Bloch, F.: Zur Bremsung rasch bewegter Teilchen beim Durchgang durch Materie. *Ann. Phys.* 408 (1933), 285–320

[Bos 2007] Bos, A. J. J.: Theory of thermoluminescence. *Radiat. Meas.* 41 (Supplement 1) (2007), 45–56

[Bragg 1905] Bragg, W.: On the a-particles of radium and their loss of range in pasing through various atoms and molecules. *Philos. Mag.* 10 (1905), 318–340

[Bramblett et al. 1964] Bramblett, R. L. ; Caldwell, J. T. ; Harvey, R. R. ; Fultz, S. C.: Photoneutron cross sections of Tb^{159} and O^{16}. *Phys. Rev.* 133 (4) (1964), 869–873

[Cahan et al. 1948] Cahan, W. G. ; Woodard, H. Q. ; Higonbotham, N. L. ; Coley, F. W. S. B. L.: Sarcoma arising in irradiated bone: report of eleven cases. *Cancer* 1 (1) (1948), 3–29

[Chaturvedi et al. 2007] Chaturvedi, A. K. ; Engels, E. A. ; Gilbert, E. S. ; Chen, B. E. ; Storm, H. ; Lynch, C. F. ; Hall, P. ; Langmark, F. ; Pukkala, E. ; Kaijser, M. ; Andersson, M. ; Fosså, S. D. ; Joensuu, H. ; Boice, J. D. ; Kleinerman, R. A. ; Travis, L. B.: Second cancers among

104760 survivors of cervical cancer: evaluation of long term risk. *J. Natl. Cancer. I.* 99 (21) (2007), 1634–1643

[Chen et al. 1981] Chen, G. T. Y. ; Castro, J. R. ; Quivey, J. M.: Heavy charged particle radiotherapy. *Annu. Rev. Biophys. Bioeng.* 10 (1981), 499–529

[Chu et al. 1993] Chu, W. T. ; Ludewigt, B. A. ; Renner, T. R.: Instrumentation for treatment of cancer using proton and light-ion beams. *Rev. Sci. Instrum.* 64 (1993), 2055–2122

[Combs et al. 2010] Combs, S. ; Jäkel, O. ; Haberer, T. ; Debus, J.: Particle therapy at the Heidelberg Ion Therapy Center (HIT) - Integrated research-driven university-hospital-based radiation oncology service in Heidelberg, Germany. *Radiother. Oncol.* 95 (1) (2010), 41–44

[d'Errico 1999] d'Errico, F.: Fundamental properties of superheated drop (bubble) detectors. *Rad. Prot. Dos.* 83 (1-4) (1999), 55–62

[d'Errico and Matzke 2003] d'Errico, F. ; Matzke, M.: Neutron spectrometry in mixed fields: superheated drop (bubble) detectors. *Rad. Prot. Dos.* 107 (1-3) (2003), 111–124

[Dörr and Herrmann 2002] Dörr, W. ; Herrmann, T.: Second Primary Tumors after Radiotherapy for Malignancies, Treatment-Related Parameters. *Strahlenther. Onkol.* 178 (7) (2002), 357–362

[Enghardt et al. 2004] Enghardt, W. ; Crespo, P. ; Fiedler, F. ; Hinz, R. ; Parodi, K. ; Pawelke, J. ; Poenisch, F.: Charged hadron tumour therapy monitoring by means of PET. *Nucl. Instrum. Meth. A* 525 (1-2) (2004), 284–288

[Foulon et al. 2002] Foulon, F. ; Bergonzoa, P. ; Amosovb, V. ; Kaschuckb, Y. ; Frunzeb, V. ; Tromsona, D. ; Brambillaa, A.: Characterisation of CVD diamond detectors used for fast neutron flux monitoring. *Nucl. Instrum. Meth. A* 476 (1-2) (2002), 495–499

[Fowler 1963] Fowler, J. F.: Solid State Dosimetry. *Phys. Med. Biol.* 8 (1) (1963), 1–32

[Friedman et al. 2010] Friedman, D. ; Whitton, J. ; Leisenring, W. ; Mertens, A. ; Hammond, S. ; Stovall, M. ; Donaldson, S. ; Meadows, A. ; Robison, L. ; Neglia, J.: Subsequent neoplasms in 5-year survivors of childhood cancer: the Childhood Cancer Survivor Study. *J. Natl. Cancer. I.* 102 (14) (2010), 1083–1095

[Garnica-Garza 2005] Garnica-Garza, H. M.: Characteristics of the photoneutron contamination present in a high-energy radiotherapy treatment room. *Phys. Med. Biol.* 50 (3) (2005), 531

[Geiß1997] Geiss, O. B.: *Strahleninduzierte Prozesse in LiF Kristallen und Verifikation dreidimensionaler Dosisverteilungen nach Schwerionenbestrahlung*, University GhK Kassel, PhD Thesis, 1997

[Goldhaber and Teller 1948] Goldhaber, M. ; Teller, E.: On Nuclear Dipole Vibrations. *Phys. Rev.* 74 (9) (1948), 1046–1049

[Goryachev et al. 1973] Goryachev, A. M. ; Zalenyi, G. N. ; Semenko, S. F. ; Tulupov, B. A.: Giant dipole resonance on nuclei of transition region. *Yad. Fiz.* 17 (1973), 463

[Gunzert-Marx et al. 2008] Gunzert-Marx, K. ; Iwase, H. ; Schardt, D. ; Simon, R. S.: Secondary beam fragments produced by 200 MeV/u ^{12}C ions in water and their dose contributions in carbon ion radiotherapy. *New J. Phys.* 10 (7) (2008), 7, 075003

[Haberer et al. 1993] Haberer, T. ; Becher, W. ; Schardt, D. ; Kraft, G.: Magnetic scanning system for heavy ion therapy. *Nucl. Instrum. Meth. A* 330 (1-2) (1993), 296–305

[Haettner et al. 2006] Haettner, E. ; Iwase, H. ; Schardt, D.: Experimental fragmentation studies with 12C therapy beams. *Rad. Prot. Dos.* 122 (1-4) (2006), 485–487

[Hall 2004] Hall, E. J.: Henry S Kaplan Distinguished Scientist Award 2003: the crooked shall be made straigt – dose response relationships for carcinogenesis. *Int. J. Radiat. Biol.* 80 (5) (2004), 327–337

[Hoban et al. 1994] Hoban, P. W. ; Heydarian, M. ; Beckham, W. A. ; Beddoe, A. H.: Dose rate dependence of a PTW diamond detector in the dosimetry of a 6 MV photon beam. *Phys. Med. Biol.* 39 (8) (1994), 1219–1229

[Holthusen 1936] Holthusen, H.: Erfahrungen über die Verträglichkeitsgrenze für Röntgenstrahlung und deren Nutzanwendung zur Verhütung von Schäden. *Strahlenther. Onkol.* 57 (1936), 30–36

[Horowitz 1981] Horowitz, Y. S.: The theoretical and microdosimetric basis of thermoluminescence and applications to dosimetry. *Phys. Med. Biol.* 26 (5) (1981), 765–824

[Horowitz et al. 2006] Horowitz, Y. S. ; Belaish, Y. ; Oster, L.: Theories of TL systems: failures, successes, conflicts, trends: insights into possible future materials and techniques. *Rad. Prot. Dos.* 119 (1-4) (2006), 124–129

[Howell et al. 2005] Howell, R. M. ; Ferenci, M. S. ; Hertel, N. E. ; Fullerton, G. D.: Investigation of secondary neutron dose for 18 MV dynamic MLC IMRT delivery. *Med. Phys.* 32 (3) (2005), 786–793

[Howell et al. 2009] Howell, R. M. ; Kry, S. F. ; Burgett, E. ; Hertel, N. E. ; Followill, D. S.: Secondary neutron spectra from modern Varian, Siemens, and Elekta linacs with multileaf collimators. *Med. Phys.* 36 (9) (2009), 4027–4038

[ICRP103 2008] ICRP103: Recommendations of the International Commission on Radiological Protection *ICRP Publication Vol. 103 /* Pergamon Oxford. 2008

[ICRP60 1990] ICRP60: Recommendations of the International Commission on Radiological Protection *ICRP Publication Vol. 60* / Pergamon Oxford. 1990

[ICRU51 1993] ICRU51: Quantities and Units in Radiation Protection Dosimetry / International Commission on Radiation Units and Measurements, Bethesda, MD. 1993

[Jäkel et al. 2001] Jäkel, O. ; Krämer, M. ; Karger, C. P. ; Debus, J.: Treatment planning for heavy ion radiotherapy: Clinical implementation and application. *Phys. Med. Biol.* 46 (4) (2001), 1101–1116

[Kalez-Ezra and Horowitz 1982] Kalez-Ezra, J. ; Horowitz, Y. S.: Heavy charged particle thermoluminescence dosimetry: track structure theory and experiments. *Int. J. Appl. Radiat. Isot.* 33 (11) (1982), 1085–1100

[Knoll 2010] Knoll, G. F.: *Radiation detection and measurement, Fourth Edition*. John Wiley and Sons, 2010

[Kozlov et al. 1975] Kozlov, S. F. ; Stuck, R. ; Hage-Ali, M. ; Siffert, P.: Preparation and Characteristics of Natural Diamond Nuclear Radiation Detectors. *IEEE Trans. Nucl. Sci.* 22 (1) (1975), 160–170

[Krämer et al. 2000] Krämer, M. ; Jäkel, O. ; Haberer, T. ; Kraft, G. ; Schardt, D. ; Weber, U.: Treatment planning for heavy-ion radiotherapy: Physical beam model and dose optimization. *Phys. Med. Biol.* 45 (11) (2000), 3299–3317

[Krämer and Scholz 2000] Krämer, M. ; Scholz, M.: Treatment planning for heavy-ion radiotherapy: physical beam model and dose optimization. *Phys. Med. Biol.* 45 (11) (2000), 3319–3330

[Laub et al. 1997] Laub, W. U. ; Kaulich, T. ; Nüsslin, F.: Energy and dose rate dependence of a diamond detector in the dosimetry of 4-25 MV photon beams. *Med. Phys.* 24 (4) (1997), 535–536

[McKeever 1985] McKeever, S. W. S.: *Thermoluminescence of Solids*. Cambridge University Press, 1985

[Min et al. 1963] Min, K. ; Bolen, L. N. ; Whitehead, W. D.: Neutron photoproduction cross section of calcium. *Phys. Rev.* 132 (2) (1963), 749–751

[MIT] MIT: http://ocw.mit.edu/courses/nuclear-engineering/22-101-applied-nuclear-physics-fall-2006/. *Internet source accessed on April 28th, 2011*

[Molière 1948] Molière: Theorie der Streuung schneller geladener Teilchen II, Mehrfach- und Vielfachstreuung. *Z. Naturforsch. A* 3A (1948), 78–97

[Newhauser and Durante 2011] Newhauser, W. D. ; Durante, M.: Assessing the risk of second malignancies after modern radiotherapy. *Nat. Rev. Cancer* 11 (6) (2011), in press

[Newhauser et al. 2009] Newhauser, W. D. ; Fontenot, J. D. ; Mahajan, A. ; Kornguth, D. ; Stovall, M. ; Zheng, Y. ; Taddei, P. J. ; Mirkovic, D. ; Mohan, R. R. ; Cox, J. D. ; Woo, S.: The risk of developing a second cancer after receiving craniospinal proton irradiation. *Phys. Med. Biol.* 54 (8) (2009), 2277–2291

[Oeffinger et al. 2006] Oeffinger, K. C. ; Mertens, A. C. ; Sklar, C. A. ; Kawashima, T. ; Hudson, M. M. ; Meadows, A. T. ; Friedman, D. L. ; Marina, N. ; Hobbie, W. ; Kadan-Lottick, N. S. ; Schwartz, C. L. ; Leisenring, W. ; Robison, L. L.: Chronic Health Conditions in Adult Survivors of Childhood Cancer. *New Engl. J. Med.* 355 (15) (2006), 1572–1582

[Olko 2004] Olko, P.: Microdosimetric modelling of the relative efficiency of thermoluminescent materials. *Radiat. Meas.* 38 (4-6) (2004), 781–786

[Olko 2007] Olko, P.: Microdosimetry, track structure and the response of thermoluminescence detectors. *Radiat. Meas.* 41 (Supplement 1) (2007), 57–70

[Olko et al. 2002] Olko, P. ; Bilski, P. ; Budzanowski, M. ; Waligórski, M. ; Reitz, G.: Modeling the response of thermoluminescence detectors exposed to low- and high-LET radiation fields. *J. Radiat. Res.* 43 (2002), 59–62

[Ongaro et al. 2000] Ongaro, C. ; Zanini, A. ; Nastasi, U. ; Ródenas, J. ; Ottaviano, G. ; Manfredotti, C.: Analysis of photoneutron spectra produced in medical accelerators. *Phys. Med. Biol.* 45 (3) (2000), 55–61

[Ongaro et al. 2001] Ongaro, C. ; Zanini, A. ; Tommasino, L.: Unfolding technique with passive detectors in neutron dosimetry. *Proc. of the Workshop 'Neutron Spectrometry and Dosimetry: Experimental Techniques and MC Calculations' Stockholm, October 18 to 20, 2001* (2001), 117–128

[Paganetti et al. 2002] Paganetti, H. ; Niemierko, A. ; Ancukiewicz, M. ; Gerweck, L. E. ; Goitein, M. ; Loeffler, J. S. ; Suit, H. D.: Relative biological effectiveness (RBE) values for proton beam therapy. *Int. J. Radiat. Oncol.* 53 (2) (2002), 407–421

[Parodi et al. 2010] Parodi, K. ; Mairani, A. ; Brons, S. ; Naumann, J. ; Krämer, M. ; Sommerer, F. ; Haberer, T.: The influence of lateral beam profile modifications in scanned proton and carbon ion therapy: a Monte Carlo study. *Phys. Med. Biol.* 55 (17) (2010), 5169–5187

[Parodi et al. 2005] Parodi, K. ; Pönisch, F. ; Enghardt, W.: Experimental study on the feasibility of in-beam PET for accurate monitoring of proton therapy. *IEEE Trans. Nucl. Sci.* 52 (3) (2005), 778–786

[Pedroni et al. 1989] Pedroni, E. ; Bacher, R. ; Blattmann, H. ; Böhringer, T. ; Coray, A. ; Lomax, A. ; Lin, S. ; Munkel, G. ; Scheib, S. ; Schneider, U.: Proton therapy status reports, PSI Life Sciences Newsletter 1989/1990. *PSI Annual Report* Annex II, (unpublished) (1989), 5–12

[Pedroni et al. 1995] Pedroni, E. ; Bacher, R. ; Blattmann, H. ; Böhringer, T. ; Coray, A. ; Lomax, A. ; Lin, S. ; Munkel, G. ; Scheib, S. ; Schneider, U.: The 200 MeV proton therapy project at the Paul Scherrer Institute: Conceptual design and practical realization. *Med. Phys.* 22 (1) (1995), 37–53

[Petti and Lennox 1994] Petti, P. L. ; Lennox, A. J.: Hadronic radiotherapy. *Annu. Rev. Nucl. Part. Sci.* 44 (1994), 155–197

[Pierce et al. 1996] Pierce, D. A. ; Shimizu, Y. ; Preston, D. L. ; Vaeth, M. ; Mabuchi, K.: Studies of the mortality of atomic bomb survivors. *Radiat. Res.* 146 (1) (1996), 1–27

[Planskoy 1980] Planskoy, B.: Evaluation of diamond radiation dosemeters. *Phys. Med. Biol.* 25 (3) (1980), 519–532

[Podgorsak 2005] Podgorsak, E. B.: *Radiation Oncology Physics: A Handbook for Teachers and Students*. International Atomic Energy Agency, 2005

[Preston et al. 2003] Preston, D. ; Shimizu, Y. ; Pierce, D. ; Suyama, A. ; Mabuchi, K.: Studies of mortality of atomic bomb survivors. *Radiat. Res.* 160 (4) (2003), 381–407

[Pshenichnov et al. 2005] Pshenichnov, I. ; Mishustin, I. ; Greiner, W.: Neutrons from fragmentation of light nuclei in tissue-like media: a study with the GEANT4 toolkit. *Phys. Med. Biol.* 50 (23) (2005), 23, 5493–5507

[Ranogajec-Komor 2002] Ranogajec-Komor, M.: Thermoluminescence Dosimetry - Application in Environmental Monitoring. *Rad. Saf. Man.* 2 (1) (2002), 2–16

[Reitz and Berger 2006] Reitz, G. ; Berger, T.: The Matroshka facility - dose determination during an EVA. *Rad. Prot. Dos.* 120 (1-4) (2006), 442–445

[Reitz et al. 2009] Reitz, G. ; Berger, T. ; Bilski, P. ; Facius, R. ; Hajek, M. ; Petrov, V. ; Puchalska, M. ; Zhou, D. ; Bossler, J. ; Akatov, Y. ; Shurshakov, V. ; Olko, P. ; Ptaszkiewicz, M. ; Bergmann, R. ; Fugger, M. ; Vana, N. ; Beaujean, R. ; Burmeister, S. ; Bartlett, D. ; Hager, L. ; Pálfalvi, J. ; Szabó, J. ; O'Sullivan, D. ; Kitamura, H. ; Uchihori, Y. ; Yasuda, N. ; Nagamatsu, A. ; Tawara, H. ; Benton, E. ; Gaza, R. ; McKeever, S. ; Sawakuchi, G. ; Yukihara, E. ; Cucinotta, F. ; Semones, E. ; Zapp, N. ; Miller, J. ; Dettmann, J.: Astronaut's organ doses inferred from measurements in a human phantom outside the International Space Station. *Radiat. Res.* 171 (2) (2009), 225–235

[Rossi 1952] Rossi, B.: *High-Energy Particles*. Prentice-Hall, Englewood Cliffs, NJ, 1952

[Saeed et al. 2009] Saeed, M. K. ; Moustafa, O. ; Yasin, O. A. ; Tuniz, C. ; Habbani, F. I.: Doses to patients from photoneutrons emitted in a medical linear accelerator. *Rad. Prot. Dos.* 133 (3) (2009), 130–135

[Sawamura et al. 2003] Sawamura, T. ; Joji, T. ; Homma, A.: Measurement of the neutron detection sensitivity of a liquid in metastable states. *Rad. Prot. Dos.* 103 (2) (2003), 117–124

[Schardt et al. 2010] Schardt, D. ; Elsässer, T. ; Schulz-Ertner, D.: Heavy-ion tumor therapy: Physical and radiobiologicel benefits. *Rev. Mod. Phys.* 82 (1) (2010), 383–425

[Schippers et al. 2007] Schippers, J. ; Dölling, R. ; Duppich, J. ; Goitein, G. ; Jermann, M. ; Mezger, A. ; Pedroni, E. ; Reist, H. ; Vrankovic, V.: The SC cyclotron and beam lines of PSI's new proton-therapy facility PROSCAN. *Nucl. Instrum. Meth. B* 261 (1-2) (2007), 773–776

[Schneider et al. 2002] Schneider, U. ; Agosteo, S. ; Pedroni, E. ; Besserer, J.: Secondary neutron dose during proton therapy using spot scanning. *Int. J. Radiat. Oncol.* 53 (1) (2002), 244–251

[Scholz and Kraft 1996] Scholz, M. ; Kraft, G.: Track structure and the calculation of biological effects of heavy charged particles. *Adv. Space Res.* 18 (1-2) (1996), 5–14

[Serber 1947] Serber, R.: Nuclear reactions at high energies. *Phys. Rev.* 72 (11) (1947), 1114–1115

[Skripov 1974] Skripov, V. P.: *Metastable Liquids*. New York: John Wiley, 1974

[Takada et al. 2004] Takada, M. ; Kitamura, H. ; Koi, T. ; Nakamura, T. ; Fujitaka, K.: Measured proton sensitivities of bubble detectors. *Rad. Prot. Dos.* 111 (2) (2004), 181–189

[Tapper 2000] Tapper, R. J.: Diamond detector in particle physics. *Rep. Prog. Phys.* 63 (8) (2000), 1273–1316

[Torikoshi et al. 2007] Torikoshi, M. ; Minohara, S. ; Kanematsu, N. ; Komori, M. ; Kanazawa, M. ; Noda, K. ; Miyahara, N. ; Itoh, H. ; Endo, M. ; Kanai, T.: Irradiation system for HIMAC. *J. Radiat. Res.* 48 (2007), 15–25

[de Vathaire et al. 1989] Vathaire, F. de ; François, P. ; Hill, C. ; Schweisguth, O. ; Rodary, C. ; Sarrazin, D. ; Oberlin, O. ; Beurtheret, C. ; Dutreix, A. ; Flamant, R.: Role of radiotherapy and chemotherapy in the risk of second malignant neoplasms after cancer in childhood. *Br. J. Cancer* 59 (5) (1989), 792–796

[Waligórski and Katz 1980a] Waligórski, M. P. R. ; Katz, R.: Supralinearity of peak 5 and 6 in TLD-700. *Nucl. Instrum. Methods* 175 (1) (1980), 48–50

[Waligórski and Katz 1980b] Waligórski, M. P. R. ; Katz, R.: Supralinearity of peak 5 and 6 in TLD-700. *Nucl. Instrum. Methods* 172 (3) (1980), 463–470

[Weber and Kraft 1999] Weber, U. ; Kraft, G.: Design and construction of a ripple filter for a smoothed depth dose distribution in conformal particle therapy. *Phys. Med. Biol.* 44 (11) (1999), 2765–2775

[Weber and Kraft 2009] Weber, U. ; Kraft, G.: Comparison of carbon ions versus protons. *Cancer J.* 15 (4) (2009), 325–332

[WHO] WHO: http://www.who.int/cancer/en/index.html. *Internet source accessed on March 24th, 2011*

[Wilson 1946] Wilson, R. R.: Radiological use of fast protons. *Radiology* 47 (5) (1946), 487–491

[Xu et al. 2008] Xu, X. G. ; Bednarz, B. ; Paganetti, H.: A review of dosimetry studies on external-beam radiation treatment with respect to second cancer induction. *Phys. Med. Biol.* 53 (13) (2008), 193–241

[Yan et al. 2002] Yan, X. ; Titt, U. ; Koehler, A. ; Newhauser, W.: Measurement of neutron dose equivalent to proton therapy patients outside of the proton radiation field. *Nucl. Instrum. Meth. A* 476 (1-2) (2002), 429–434

[Yonai et al. 2008] Yonai, S. ; Matsufuji, N. ; Kanai, T. ; Matsui, Y. ; Matsushita, K. ; Yamashita, H. ; Numano, M. ; Sakae, T. ; Terunuma, T. ; Nishio, T. ; Kohno, R. ; Akagi, T.: Measurement of neutron ambient dose equivalent in passive carbon-ion and proton radiotherapies. *Med. Phys.* 35 (2008), 11, 4782–4792

[Zanini et al. 2005] Zanini, A. ; Fasolo, F. ; Visca, L. ; Durisi, E. ; Perosino, M. ; Annand, J. R. M. ; Burn, K. W.: Test of a bubble passive spectrometer for neutron dosimetry. *Phys. Med. Biol.* 50 (18) (2005), 4287–4297

Acknowledgements

I would like to thank all the people that helped in the course of this thesis. The experiments were only possible thanks to the tremendous amount of help I have received in form of scientific discussions and suggestions, the operating of the accelerators at the facilities, the data analysis, the technical side and of course the psychological support.
A big thank you goes to Ulla Ramm, Jörg Licher and Janett Liebich from KGU for the help and especially for being so patient during the neverending bubble detector experiments. To Christina Vallhagen-Dahlgren and Erik Grussell, thank you for the warm reception in Uppsala and letting us come again after parts of the experiment had to be cancelled because of volcano eruptions in Iceland... I humbly thank Matsufuji-san and the staff from NIRS for the opportunity of measuring at HIMAC in the middle of a hot Japanese summer night. Many thanks also go to Sairos Safai and David Meer for their help during the measurements at PSI. For the measurements and support 24h around the clock at HIT I would like to sincerely thank Stephan Brons!
Another big thank you goes to Oscar Borla and Alba Zanini from INFN Torino for allowing me the use of the BUNTO code for unfolding the neutron spectra.

Of course a very large thanks goes to our friends at DLR, Thomas Berger, Christine Körner and Günter Reitz for the great cooperation with GSI. For me personally it was not only very fruitful, but also very enjoyable and I hope to still see you often in the future.

Many thanks to the members of "Dieter's group": Giovanna, Christoph, Radek, Elko, thank you for the scientific, technical and especially for the fun and friendly atmosphere at work. Another thanks to the people from my daily 11:30 and 15:00 dates.

Chiara and Dieter, thank you very very much for the wonderful time at GSI with you! It is a great pleasure working with you, no matter what the time of the day. I couldn't have asked for better supervisors, both scientifically and personally. I would also like to thank you for the tremendous effort you made proofreading the thesis, I really appreciate the time I stole you...

On the scientific side, I would lastly like to thank my referees Gerhard Kraft and Marco Durante for the ideas for experiments, the discussions and the effort proofreading the thesis. I would like to thank Professor Durante for giving me the opportunity to work on this interesting experimental topic, even though I came with a theoretical background and no experimental experience. I am looking forward to continuing work in this field!

Julia möchte ich für die große Unterstützung und das Verständnis während der experimentellen Zeit danken. Meinen Freunden sei gedankt für die Ablenkung und Unterstützung besonders in den vergangenen Monaten. Den Volleyballern danke ich für ihre Möbelpackerdienste, Geburtstags- und Erntewitze und natürlich für alles was so passieren kann.
Zuletzt möchte ich herzlich meinen Eltern danken, diese haben das Studium überhaupt erst durch ihre Unterstützung und mahnende Worte zum rechten Zeitpunkt möglich gemacht. Ich danke Euch mehr, als ich es in Worten ausdrücken kann!

Lebenslauf und Werdegang

Persönliche Daten

	Geboren am 14.11.1983 in Offenbach am Main

Schulische Ausbildung

1990-1993	Gartenstadtschule in Rodgau
1993-1999	Einhardgymnasium in Seligenstadt
1999-2000	Highschool Jahr in Kansas, USA
2000-2002	Abitur an der Claus-von-Stauffenberg Schule in Rodgau

Grundwehrdienst

2002-2003	Grundwehrdienst in Münsingen und Darmstadt-Eberstadt

Universitäre Ausbildung

2003-2008	Mathematik und Physik Studium an der Johann Wolfgang Goethe-Universität Frankfurt am Main
2005	Vordiplom Mathematik und Physik
2008	Diplom in Physik Diplomarbeit mit Titel "Einführung in die bosonische und fermionische Deformationsquantisierung" betreut von Prof. Dirk Rischke
2009-2011	Promotion an der GSI in Darmstadt unter Prof. Marco Durante Titel der Arbeit "Out-of-field dose measurements in radiotherapy"

Sonstiges

	Hobbies: Volleyball, Musik, Kino
2005	Stipendium der Studienstiftung des deutschen Volkes
2004-2008	Wissenschaftliche Hilfskraft in Mathematik und Physik

Erklärung zur Dissertation

Hiermit versichere ich, die vorliegende Dissertation ohne Hilfe Dritter nur mit den angegebenen Quellen und Hilfsmitteln angefertigt zu haben. Alle Stellen, die aus Quellen entnommen wurden, sind als solche kenntlich gemacht. Diese Arbeit hat in gleicher oder ähnlicher Form noch keiner Prüfungsbehörde vorgelegen.

Darmstadt, den 3. Mai 2011

_____

(Robert Kaderka)